THE UNIVERSITY OF ASTON IN BIRMINGHAM

A STUDY OF THE GAMMA-RAYS ASSOCIATED WITH THE INELASTIC SCATTERING OF NEUTRONS IN EXTENDED TARGET SAMPLES

Thesis Submitted for the Degree of

Doctor of Philosophy

by

Bassam A.R. Al-Shalabi B.Sc., M.Sc.

Department of Physics

June, 1981

A STUDY OF THE GAMMA-RAYS ASSOCIATED WITH THE INELASTIC SCATTERING OF NEUTRONS IN EXTENDED TARGET SAMPLES

Thesis for Degree of Ph.D.

by

Bassam Al-Shalabi

The University of Aston in Birmingham

SUMMARY

The gamma-rays produced in the inelastic scattering of 14 MeV neutrons have been studied using a gamma-ray spectrometer employing a sodium iodide scintillation detector. The source neutrons are produced by the $T(d,n)^4He$ reaction using the Radiation Centre Dynamitron and the SAMES accelerator. In order to overcome the large gamma-ray background and large stray neutron signal due to the sensitivity of the sodium iodide detector to neutrons, heavy shielding around the gamma-ray detector is used together with a particle time of flight discrimination system based on the associated particle time of flight method. The instant of production of a source neutron is defined by detecting the associated alpha-particle which enables discrimination between the neutrons and gamma-rays because of their different time of flight times. The electronic system used for measuring the time of flight of the neutrons and gamma-rays over the fixed flight path is described.

The materials studied in this work were iron and concrete because of their importance as structural and shielding materials in the construction of both fission and fusion reactors. Several sample thicknesses were studied to determine the multiple scattering effects in large sample. The observed gamma-ray spectra from each sample at several scattering angles in the angular range 0^o-90^o enabled absolute differential gamma-ray production cross-sections and angular distributions of the resolved gamma-rays from iron to be measured and compared with published data where available. For the concrete sample, the absolute differential gamma-ray production cross-sections for discrete 1 MeV ranges and the angular distributions were measured and compared with cross-sections synthesized from the published cross-section data for the elements constituting concrete.

The number of gamma-rays produced from each sample in the angular range studied were compared with the predictions of a theoretical model based on the continuous slowing down model and Fermi-Age equation. Good agreement between experiment and theory is obtained and a single parameter found which describes the effects of multiple scattering in both materials.

Inelastic Scattering of Fast Neutrons/Gamma-Ray Production Cross-Sections/ Iron and Concrete Extended Samples.

BA/AJC/LCR
7.5.81

ACKNOWLEDGEMENTS

I wish to express my gratitude to my Supervisor, Dr. A.J. Cox, for the continued help and guidance offered throughout the project. I would also like to thank Professor S.E. Hunt, the Head of the Physics Department, for his interest in the project and I am grateful to Dr. P.N. Cooper of the Nuclear Physics Group for his advice during the work. Thanks are also due to Mr. J. Phull of the Nuclear Research Laboratory and Mr. F. Lane and other members of the Physics Workshop for their assistance.

I also wish to thank Mr. T. Kennedy, the Physics Department Superintendent and the secretarial staff for their assistance; and also Miss L. Riding of the Combined Honours Unit for her help.

I do appreciate the two years British Council Award for paying part of the University fees.

I am very indebted and grateful to my family for their moral and financial support throughout the whole project.

Finally, I wish to thank my wife, Karen, and my son, Abder-Rahim, for their patience and understanding throughout the period.

B. Al-Shalabi

University of Aston in Birmingham

June, 1981

To my parents, Aysha and Abder-Rahim

CONTENTS

PAGE

CHAPTER 3 (continued..)

CHAPTER 5 (continued...)

CHAPTER 5 (continued...) PAGE

LIST OF TABLES

LIST OF TABLES (Continued..)

LIST OF TABLES (continued...) Page

LIST OF TABLES (continued...)

LIST OF FIGURES

CHAPTER ONE

GENERAL INTRODUCTION

Introduction

Proposed fusion reactor blanket designs and shields bring into focus a large number of problems dealing with the interaction of 14 MeV neutrons with different materials, eg. Carbon, oxygen, aluminium, titanium and iron are among the materials possibly to be used in the blanket. The gamma-rays produced from neutron interactions are an important aspect of many problems concerned with nuclear reactor shielding and with radiation induced heating.

As the present work is concerned with the interaction of 14 MeV neutrons which are produced in the fusion reaction $T(d,n)^4He$ which is closely linked to the possible future nuclear fusion reactors, an outline of these reactions and reactors will be given in the following sections.

1.1. Nuclear Fusion Reactions

Nuclear fusion is a nuclear reaction in which light atomic nuclei combine or fuse together to produce more tightly bound heavier isotopes. An example of such a reaction is that which occurs between the two heavier isotopes of hydrogen, deuterium ${}^2_1D$ and tritium ${}^3_1T$:

$$ {}^2_1D + {}^3_1T \longrightarrow {}^4_2He + {}^1_0n + 17.5 \text{ MeV} $$

This reaction releases 17.5 MeV of energy which appears as kinetic

energy of the reaction products (14 MeV with the neutron, 3.5 MeV with the alpha particle).

The fusion reactions of particular interest to fusion reactors involve only the very light nuclei, because the larger the charges of the fusing nuclei, the greater the amount of energy required to bring them together. The main problem in using the fusion reactions in a nuclear reactor is the question of how to get these nuclei to overcome the repulsive interaction among themselves and to induce nuclear fusion? The straightforward answer would be to accelerate one particle (say deuteron) to several 100 KeV energy and direct it onto a target consisting of the other particle (tritium), after all, this is the reaction used in the laboratory to produce 14 MeV neutrons. The main problem with this is the fact that the scattering cross-section which determines the number of scattering interactions is a million times higher than the fusion cross-section which determines the number of fusion interactions; it would therefore, be necessary to arrange for the nuclei to collide with one another millions of times or they will probably not fuse together. This leads to the fact that a different approach is necessary.

One way to bring the nuclei to the speeds required for fusion reactions is to heat them up, since temperature is a measure of the average kinetic energy of the atoms in a material. In fact, a gas at a temperature T is characterized by an average particle energy of 3/2 KT where K is Boltzmann's constant. Hence, it is required to heat the fuel

mixture (e.g. tritium and deuterium) such that the average atom velocities are 100 KeV or so. As 1 eV corresponds to 1.3×10^4 °C, the fuel must be heated to the enormous temperature of 10^{9}°C, but since there will be a spread of energies about 3/2 KT, even at temperatures of 10^{8}°C there will be enough energetic nuclei to produce an appreciable number of fusion reactions. This scheme of heating the fuel to a sufficiently high temperature to induce a nuclear fusion is called "thermo- nuclear fusion".

The second problem concerning the utilization of the thermo - nuclear reactions is that the nuclei must collide with eachother millions of times before fusion reaction is likely to take place. Hence, the fuel must be contained at this very high temperature for a period of time if an appreciable amount of fusion energy is to be released. The twin requirements to achieve thermonuclear fusion energy release are:

1. To produce and heat a plasma fuel to thermonuclear temperatures (10 KeV or 10^{8}°C) and
2. Confine it for a sufficiently long time in order to get out more fusion energy that initially invested in heating the fuel to that temperature in the first place.

These two requirements are usually expressed by a mathematical relation known as the Lawson Criterion which can be expressed as a condition on the product of the fuel density times the time of plasma fuel confinement:

D-T	:	$n\tau$	>	10^{14} S/cm^3	T = 10 KeV
D-D	:	$n\tau$	>	10^{16} S/cm^3	T = 100 KeV

Lawson criterion is simply a balance between fusion and thermal energy and as seen above it depends on the type of fusion reaction.

1.2. Fusion Reactor System

The basic principles of the main confinement systems has been used to provide conceptual design of fusion reactor assuming that sufficient plasma confinement can be achieved. In all these conceptual designs, the D-T fuel with an associated blanket containing some form of lithium are considered as the main features of the system. Figure (1-1) shows a generalised illustration of the cross-section of a possible fusion reactor. The plasma at a temperature of 10^8 to 6×10^9 ^oK depending on the confinement concept is surrounded by a vacuum and a magnetic field which confines it and holds it away from the first wall. This wall is surrounded by a coolant (possibly liquid lithium or potassium moving in niobium tubes) which is usually part of the tritium breeding moderator. The moderator function is to slow the 14 MeV neutrons from the fusion reaction in the plasma and convert their kinetic energy to heat which is used to power the energy conversion equipment in order to produce electricity. In addition the moderator (where lithium is used) breeds tritium for refueling the plasma through the disintegration of lithium by neutron capture according to the equations

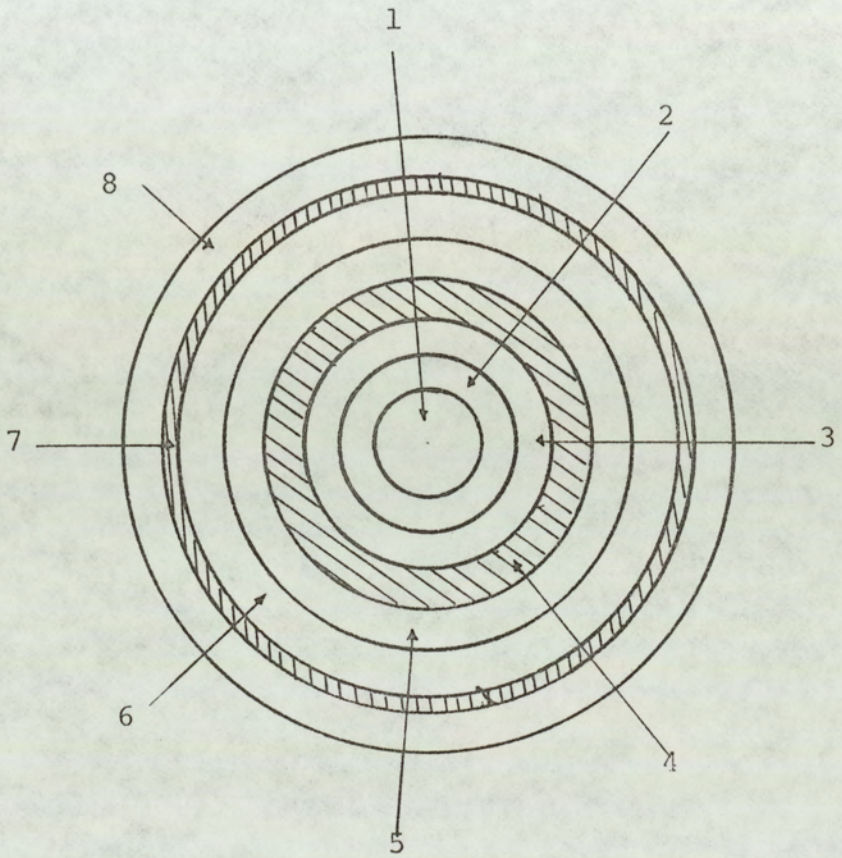

1- Plasma 10^{8} ° K

2- Vacuum

3- Lithium Planket

4- Graphite or Lithium

5- Lithium Coolant

6- Neutron Shielding ,Water or Suitable Material

7- Lead Gamma-ray Shield .

8- Magnet (Super -conducting Coils at -268^{O} K)

Figure (1-1) Section of possible fusion reactor based on Tokamak[1].

$$^{7}_{3}Li + ^{1}_{o}n \longrightarrow ^{3}_{1}T + ^{4}_{2}He + ^{1}_{o}n$$

and $$^{6}_{3}Li + ^{1}_{o}n \longrightarrow ^{3}_{1}T + ^{4}_{2}He$$

The magnet coil is shielded from the 14 MeV neutrons firstly by a lithium blanket and moderator and secondly by specially designed neutron and gamma-ray shields. The neutron shield should contain mainly light elements to be effective against high energy neutrons, therefore, water and different types of concrete are used while the gamma-ray shield usually consists of lead for its high Z atomic number which makes it ideal as a gamma-ray shield.

1.3. Reactor Shielding :-

In the design of a nuclear facility, thought must be given to the protection of personnel, materials and equipment from the radiations associated with the nuclear materials used. Radiation shielding used to reduce the radiation exposure to people in the vicinity of the radiation sources is called "biological shielding", while other types of shielding, e.g. equipment and apparatus shielding are used to protect the core etc., or electronic apparatus, i.e. like the Cryogenic magnet coils.

In the design of nuclear power plants, the gamma-rays and the neutrons are the important radiations from the standpoint of shielding.

1.3.1. Neutron Shielding :

Neutrons are produced in reactors with relatively high energy,

(average 2 MeV in fission reactors and much higher in future fusion reactors), and since the absorption cross-sections are extremely small in the MeV region, neutron shielding thus involves the process of slowing down fast neutrons to the thermal range where the absorption cross-sections are high. For this purpose, two processes are available :

1. Inelastic scattering by medium and heavy elements for neutrons above the (0.1 - 1) MeV range, and,

2. Elastic scattering by light elements for neutrons below the (0.1 - 1) MeV range.

A good neutron shield must thus contain heavy elements as well as light material. This brings into focus the importance of the present work which is the study of the interaction of 14 MeV neutrons in iron and concrete with particular emphasis on the inelastic scattering and the cross-sections for the production of gamma-rays following the inelastic scattering.

Concrete is considered to be the most important shielding material [2,3]. Ordinary concrete with density (2.2 - 2.5 gm/cm^3) is the most extensively used shielding material for several reasons. Concrete beside serving as a shielding material often serves also as a structural material. It is also inexpensive compared to other shielding materials and is a good shield against all kinds of radiation. However, the generation of nuclear radiation heat within the shielding concrete can be a problem (due to the low heat conductivity of this material) since

abnormal stress concentration can develop inside the material. This problem could be solved by cooling the concrete either using water tubes embedded in the concrete or air flowing outside the concrete. Further discussion about neutron shielding is given in Chapter 4.

1.3.2. Gamma-rays Shielding :-

Gamma-rays are produced in the reactor materials by the interaction of 14 MeV neutrons via the inelastic scattering process as well as through the capture of neutrons that have been slowed down to thermal energies. A detailed knowledge of these interaction mechanisms as well as the reaction cross-section would lead to the correct calculation of the gamma-ray fluxes produced in the different parts of the reactor. The gamma-ray interactions with matter are discussed in detail in Chapter 4, but generally the heavier the element (high atomic number Z), the better it is as a gamma-ray shield.

Iron and concrete are extensively used for shielding purposes and they would be an excellent combination for shielding fusion reactors, as the neutron slowing down could be achieved by inelastic scattering by the moderately heavy iron atoms as well as by elastic scattering with the light atoms of the concrete constituents. It can be shown, however, when a shield is suitably divided into alternating regions of iron and concrete in such a way that the attenuation of gamma-rays and neutrons proceeds at more or less the same rate through successive layers, the overall size and weight of the shield is reduced over that of concrete

shield alone [4].

1.4. The Research Programme

The aim of the research programme is to study the differential cross-sections for gamma-ray production following the inelastic scattering of 14 MeV neutrons in possible shielding materials for future fusion reactors. Since it is experimentally impossible to study all the relevant materials, attention is focussed on two materials, viz. iron and concrete since they represent the most favoured shielding materials as can be seen from the previous sections. Although several measurements [5,6,7] have been reported on iron differential cross-sections measurements for gamma-ray production and corresponding angular distributions, these measurements broadly fall into two categories: a) those using very thin scattering samples, and hence do not include the multiple scattering effects which are encountered in thick reactor shields, b) those specially designed experiments for fission reactor shields where the average neutron energy is about 2 MeV, hence the inelastic scattering processes do not predominate. From the literature survey undertaken at the beginning of the work, limited experimental data only was available concerning the effects of multiple scattering on the measured cross-sections, although the theoretical work on the subject using complex analysis with Monte-Carlo techniques has been reported in many papers [8,9].

For iron, the differential cross-sections for gamma-ray production and the effect of multiple scattering at a neutron energy of 2.56

MeV has been measured by Day[10] and later by Kellie, et al.,[11] for neutron energies of up to 9 MeV. The scattering sample thickness in these experiments did not exceed 0.5 mean free paths of the incident neutrons. Pourmansouri[12] studied the gamma-ray production cross-sections and the multiple scattering processes in flat iron plate sample with thickness of 4 cm corresponding to about one mean free path of a 14 MeV neutron in iron and reported the gamma-ray production differential cross-sections per MeV.

For concrete there is an absence of data available on the differential gamma-ray production cross-sections and most of the reported work is in the form of the measured dose or flux behind concrete shields[13,14] Also information is given on the attenuation of neutrons in concrete shields[15,16].

Schmidt[17] has reported analytical radiation shielding calculations for concrete based on removal diffusion theory. The macroscopic removal cross-sections were synthesized from the published cross-section data for the elements constituting concrete.

The aim of the present work is to provide data on the angular distributions for iron and the effect of the multiple scattering in thick samples on these angular distributions. It also provides data on the differential cross-sections per MeV for gamma-ray production from concrete. In addition, it tests the possibility of producing a simple mathematical model based on slowing down theory and the use of the

published cross-sections for the published data on concrete constituents to synthesize the cross-sections for the neutron interactions in concrete.

To obtain the required data, a time of flight spectrometer was used and it is described fully in Chapter 3.

CHAPTER TWO

INTRODUCTION TO NEUTRON INTERACTIONS AND SPECTROMETRY

2.1. Interaction of Neutrons with Matter

Since the neutron is electrically neutral, it interacts directly with the nucleus without being affected by the atomic electrons or by the positive charge of the nucleus, even when its velocity (or energy) is very low. Neutrons may interact with nuclei in one or more different ways, if the nucleus remains unchanged in either isotopic composition or internal energy after interacting with the neutron, the process is called "elastic scattering" abbreviated by the symbol (n,n), while if the nucleus is left in an excited state after the interaction, then the process is called "inelastic scattering" denoted by (n,n') symbol. Since the neutron reappears after the interaction, it is common to say that the neutron has been scattered elastically or inelastically when referring to the above processes although the emerging neutron may not be the same neutron that was incident on the target nucleus.

Another class of interactions is known as absorption reactions in which the incident neutron is absorbed by the nucleus leading to the emission of one or more gamma-ray photons. This type of reaction is known as "radiative capture" denoted by (n, γ). The neutron capture may also lead to the emission of a charged particle such as a proton or an alpha-particle. Such interactions are known as the charged particle reactions and are denoted by (n), and the symbol of the charged particle

produced, e.g. (n, p) reaction and (n,α) reaction.

At higher neutron energies, i.e. 10 MeV, neutron producing reactions of the type (n, 2n) and (n, 3n) occur, these reactions are clearly endothermic reactions since one neutron in the (n,2n) reaction and two neutrons in the (n, 3n) reaction are extracted from the target nucleus.

2.2. Theories of Neutron Interactions with Nuclei

2.2.1. The Compound Nucleus Theory

This theory proposed by Bohr[17] is based on the postulate that nuclear reactions proceed in two stages: i) the formation of a compound nucleus by the fusion of the incident neutron and the target nucleus, followed by (ii) its decay into the reaction products in a manner independent of the method of compound nucleus formation, and excitation depending only on the properties such as the spin and parity of the compound nucleus system. During the first stage, the energy of the incident neutron and its binding is shared between all the nucleons by a series of multiple collisions inside the nucleus resulting in high excitation of the compound system, eventually all or part of the incident energy is concentrated in a particle near to the nuclear surface leading to the decay of the compound system by the emission of the particle concerned.

At incident neutron energies of less than about 10 MeV, this theory has been found to yield good fits to experimental data,[18,19] for example, it is able to account for large capture cross-sections and narrowly spaced resonances shown by nuclei under bombardment by

neutrons having energies of a few MeV.

As the shapes and anisotropies of the angular distributions of the gamma-rays emitted in neutron inelastic scattering depend strongly on the properties of the relevant nuclear levels, it is possible to obtain unambiguous values by comparing the experimental measurements of the angular distributions with the theoretical predictions. For example, Benjamin et al., [20] have found the spin and parities of the isotope ^{56}Fe.

In spite of the success of the compound nucleus theory mentioned above, it does not provide an explanation of the diffraction structure including forward peaking as observed in experimental results for nucleon scattering at energies as low as even 6 MeV.

2.2.2. The Direct Interaction Theory

The shortcomings of the compound nucleus theory gave rise to the direct interaction theory. Here an incident neutron would interact with the nucleus via the nuclear potential and the probability of absorption into a compound nucleus would be relatively small. Consequently, direct interaction may take place within the time period taken by the neutron to traverse the nucleus (10^{-21} sec). Direct interaction theory has successfully accounted for nucleon scattering of neutrons having an energy of $\geqslant 10$ MeV. The fits to the experimental neutron data are also good.[21,22,23]

In the range of incident neutron energies from 10 to 20 MeV., the neutron interactions are best expressed by a mixture of the two theories, hence Hauser and Fesbach[24] unified the different aspects of the nuclear reaction into a single theory. This theory was developed further by Weisskopf [25] and by Feshbach[26,27,28] as discussed briefly below.

2.2.3. Unified Theory for Nuclear Reactions :

Weisskopf proposed that any nuclear reaction proceeds through a series of stages illustrated in Figure (2.1) where one or more of the indicated reactions can take place. The first interaction called shape elastic scattering will be a partial reflection of the wave function. The part of the wave function which enters the nucleus undergoes absorption. Feshbash suggested that the first step in the absorption process consists of a two body collision, i.e., the incident neutron interacts with one nucleon in the nucleus and raises it to an unfilled level. If the struck nucleon then leaves the nucleus, a direct reaction has occurred. This process becomes more probable at higher energies because in this case a given nucleon would have a good chance of receiving enough energy to leave the nucleus. If the struck nucleon does not leave, the incident neutron (or the struck nucleon) may interact with a second nucleon in the nucleus thus raising this to a unfilled level and under proper conditions, the nucleus could be excited to a collective state after which one of the nucleons could leave.

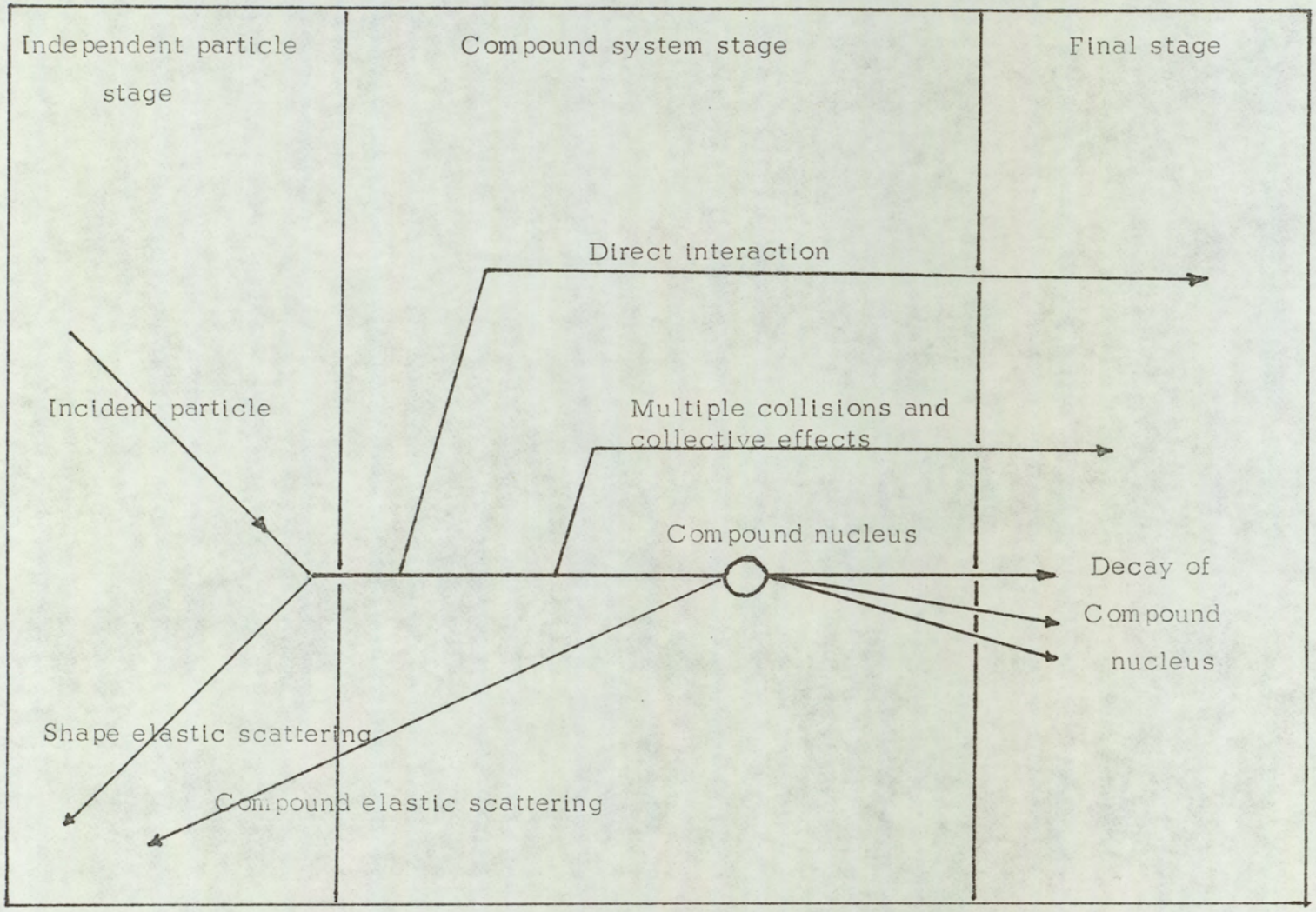

Figure (2-1) Sequence of stages in a nuclear reaction according to Weisskopf.

However, if this does not occur, each of the three nucleons can then interact with other nucleons until finally the energy sharing envisaged by the compound nucleus theory has occurred.

2.3. The Time of Flight Technique

The determination of neutron energy by measuring the time it takes to traverse a fixed flight path is a well known method of neutron spectroscopy. Although the method is straight-forward, when dealing with slow neutrons, a greater precision is required with fast neutrons as nano-second timing will be necessary. The time of flight technique can be used to produce suitable gating pulses in the study of the gamma-rays associated with the inelastic scattering of neutrons to separate the gamma-ray and neutron events and to reduce background.

This technique requires the establishment of two time signals (START, STOP) relating to the neutron production and detection respectively. An essential part of the time of flight measurement is the precise determination of the time of origin of the neutron production. Two possible methods for time of flight measurement for neutron energies above 1 MeV are the "pulsed beam method" and the "Associated particle method". These methods differ in the manner in which the start pulse is obtained, while the "STOP" signal is produced when a gamma-ray or neutron is detected.

The main advantage in applying the time of flight method to the study of the gamma-rays associated with the inelastic scattering of neutrons

is the marked reduction in the background radiation contributing to the gamma-ray energy spectrum, which in turn leads to a marked improvement in the signal to background ratio.

2.3.1. The Pulsed Beam Method

In this method the neutrons are produced in bursts of time of duration Δt_b, a specific neutron can then be said to have originated at the given point at a certain time with an uncertainty Δt_b. If the neutrons are produced by positive ion bombarding a target to induce a nuclear reaction, it is sufficient to produce the positive ions in bursts of time Δt_b. Consequently, the discussion can be carried out in terms of ion beam burst duration with the understanding that at the same time the discussion is meant to be about the neutron burst duration.

Several means of producing the required bursts of ions are possible, viz (a) plasma pulsing, (b) beam chopping, and (c) beam bunching. The first method is perhaps the most direct since it has been found that the rf excited ion source itself produces bunches of ions at the excitation frequency.[30] However, this method suffers from the disadvantage that it is rather inflexible and not susceptible to precise analysis and design since it is built around a gas discharge phenomenon.

The beam chopping method has been the most commonly employed, it has been the first step even for the beam bunching method because with the sacrifice in beam required by (b), it is possible to achieve clean pulse definition before beam bunching.

2.3.1.1. The Beam Chopping Method

A. Post acceleration beam pulsing :-

Figure (2 - 2) illustrates a simple technique used by Turner[31] et al., to "chop" out short segments of a steady beam produced by an electrostatic accelerator. A sinusoidal rf voltage applied across a pair of plates P sweeps the ion beam across a collimating slit S, so that a short burst of ions passes through at each crossing. Typically a 5 MHZ signal with a peak voltage of several Kv volts is used for the production of neutrons by positive ions in bursts of one or two nano-second duration.

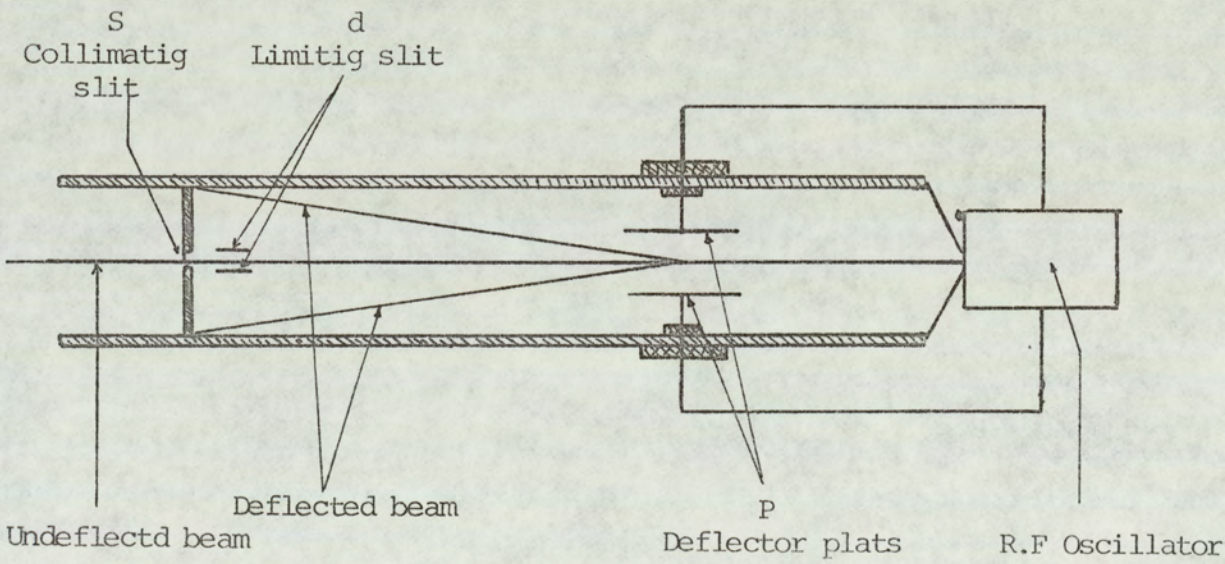

Figure (2.2) Schematic representation of RF sweeping method for producing 10 ns pulses in the nano- second range.

(From referance (31)

The flight of particles from the bombarded target to a detector may then be timed relative to the phase of deflecting voltage[32] or relative to the current pulse of the target itself.[33] This method suffers from the fact i) that efficiency of utilization of a steady ion beam decreases with decreasing pulse length with the minimum usable pulse length being determined by the intensity of the initial beam and deflection efficiency and ii) the large background contribution created by the large fraction of ions which are discarded from the beam.

The main advantage of applying this method is that in addition to defining the production of a neutron with uncertainty of $\pm$ 1 ns, it provides a time interval of about 100 ns during which the beam is held off the targe for the scattering and possible subsequent detection of gamma-ray or neutron.

B. Pre-acceleration beam pulsing:

In this method developed concurrently by Parker et al.,[34] and Turner et al.,[31] the beam "chopper" is introduced between the ion source and the acceleration tube. Since essentially no beam will be accelerated with such a system other than the short pulses produced, the background problem associated with the post-acceleration type is greatly reduced. Furthermore, this method is more efficient and greater ion burst peak currents can be achieved. The main disadvantages of the method is that pulse duration is longer than for post-acceleration beam chopping and the fact that the pulsing instrumentation lies within the

terminal produces special problems such as the power requirements (high voltages) and axial space to release an adequate sweep lever arm.

2.3.1.2. The Beam Bunching Method

This method was first applied for producing burst of electrons by klystron bunching. A similar technique may also be applied to positive ion beams. However, in most important applications of pulses of ions, there is a premium on clearly defined pulses with few ions between pulses. Consequently, most attempts to achieve bursts of positive ions by bunching consisted of employing bunching to increase the density of the ions in pre-existing pulses. This means that the beam utilization is less than 100%, with the exact amount depending in the attempts made on convenience or arbitrary choice.

Bunching always consists of changing in a time correlated manner, the energy (or momentum) of a burst of ions in such a way that all the ions in the burst regardless of their relative original positions arrive at the same instant at some point on which all such ions converge to a focus. The ion beam is first chopped to produce relatively long ion bursts of about 30 n s duration, then these ion bursts are bunched into intense short bursts of about 1 ns duration by either a Mobley-type [35] magnet [36] or Klystron buncher as it has been described by Stelson et al., for use with concroft-Walton accelerator, and by Oliver et al., [37] who used a Klystron buncher with Liverpool HVC 12 MeV Tandem Van de Graaf.

In Stelson et al., [36] system, a 250 uA deuteron beam was

chopped into bursts of 30 ns duration at a frequency 4.5 MHZ. The beam was accelerated to 140 KeV. The pulsed beam then passed through a hollow tube which served as a signal pickup. The induced signal was delayed, amplified and then used to drive a three-stage tuned amplifier to provide a sine wave output which was amplified further by a one-stage power amplifier. The in turn drove a remote tuned circuit connected directly to the Klystron buncher electrode. The beam was then velocity modulated in the Klystron tube to less than 2 ns duration with a peak pulse intensity of between 3 μA and 4 μA.

Oliver et al.,[37] reported that under typical conditions with the high energy chopper slits opened wide so that they did not interfere with the d.c. transmission, 10-12% of the beam is obtained in a 2 ns wide pulse with a repetition rate of 5 MHZ. The corresponding figures for a 1 ns wide pulse was 6%. The above efficiencies were found to be essentially independent of beam energy.

A full discussion of the methods discussed above has been made by Neiler and Good.[38] More recent work employing the pulsed beam methods can be found in the references[39,40,41] where pulses have been produced with duration < 1 ns with a pulse frequency of 2 MHZ.

2.3.2. The Associated Particle Method.

The associated particle method can be used to define the instant of neutron production if the neutrons are produced from highly exoergic reaction. Two such reactions for the production of monoenergic neutrons

are the $T(d,n)^4He$ reaction and the $D(d,n)^3He$ reaction. In each of these reactions the charged particle is produced with sufficient energy to be detected hence providing a "zero time" signal for the neutron time of flight measurement. The uncertainty in the neutron production time from the $T(d,n)^4He$ reaction is usually less than 1 ns. The timing uncertainty is a function of the energy loss of the alpha-particles in escaping the target and the time resolution of the alpha-particle detector.

Scherrer et al.,[42] pioneered using $T(d,n)^4He_2$ associated particle method, and they were unable to separate scattered neutrons from gamma-rays produced in the sample. The method has been used by several workers[22,44,45] to observe the gamma-rays produced in the inelastic scattering of 14 MeV neutrons. The method has three distinct advantages: i) a d.c. accelerator is used hence, eliminating the complications required by the pulsing methods, ii) with the scattering sample positioned such that it subtends all the defined neutron beam, a neutron start pulse is obtained only when a neutron penetrates the sample and this gives a better signal to background ratio and iii) with the $T(d,n)^4He$ and the $D(d,n)^4He$ reactions two particles only are produced, resulting in the two detector angles being no longer independent hance the direction and flux of the neutrons are accurately known if the position and efficiency of the associated particle detector are known.[45]

The limitations of this method are not so easy to analyze since several sources of background must be taken into account and the exact details of geometry and room scattering must be considered. A disadvant-

age of the method is that the neutron yield is restricted by the high count rate in the alpha-particle detector.

The application of pulsed beam method depends primarily on producing target current burst of high peak value to give a workable signal to background ratio. To produce intense ion bursts of 1 ns duration requires sophisticated apparatus like those described by Huber et al., [46] Haught et al.,[47] and Dickens et al.,[7] . For the present work, since neither space nor facilities were available, the associated particle method was adopted for the time of flight discrimination technique used. The experimental arrangement is discussed in Chapter 3.

2.4. Survey of the Experimental Methods

The experimental methods available for differential gamma-ray production cross-section measurements in first neutron interactions are governed by the experimental conditions. The dimensions and construction of the scattering room determine the amount of shielding required in order to achieve a workable signal to background ratio. There are two basic techniques i) open geometry which refers to the case where the minimum amount of shielding is used in contrast to the ii) closed geometry method where fairly massive shielding is used around either the neutron source, or the gamma-ray detector or both.

2.4.1. The Open Geometry :

The experiments using the open geometry arrangement need to be carried out in a large scattering room to minimize the scattered back-

ground from the walls and the floor of the scattering room. With this method, a large scattering sample in the form of ring is used with its axis on the line passing through the source and the detector. A shadow bar is placed along this line to remove the direct beam. Figure (2-3) shows a plane view of a typical ring geometry arrangement.

The scattering angle is varied either by moving the scatterer or the detector along the axis or by using rings with different diameters. The main advantage of this arrangement is that greater scattered intensity can be obtained for a given angular resolution and scatterer thickness, however, the angular resolution for this geometry is generally poor. The open geometry has been used by many workers[48,49] but it is mainly limited to pulsed beam spectrometers where time related neutrons are produced in all directions.

2.4.2. The Closed Geometry

This geometry is usedwhere a limited space only is available for the experimental arrangement. Usually, the detector is heavily shielded from the neutron source, the scattered neutrons and the spurious gamma-ray radiations. The scattering sample is in the form of a cylinder or flat plate. The associated particle time of flight technique is used with this geometry to provide a further reduction in the background as discussed earlier.

This closed geometry method has been used by several workers[50,51] as

the scattering room which was available for the present work is relatively small, hence the closed geometry method was adopted in the present experiments. The scattering samples used were rectangular plates which results in a simplification of the calculation of the correction terms in the general equation for the differential cross-section. Figure (2-4) shows closed geometry arrangment with flat plate plate scattering sample .

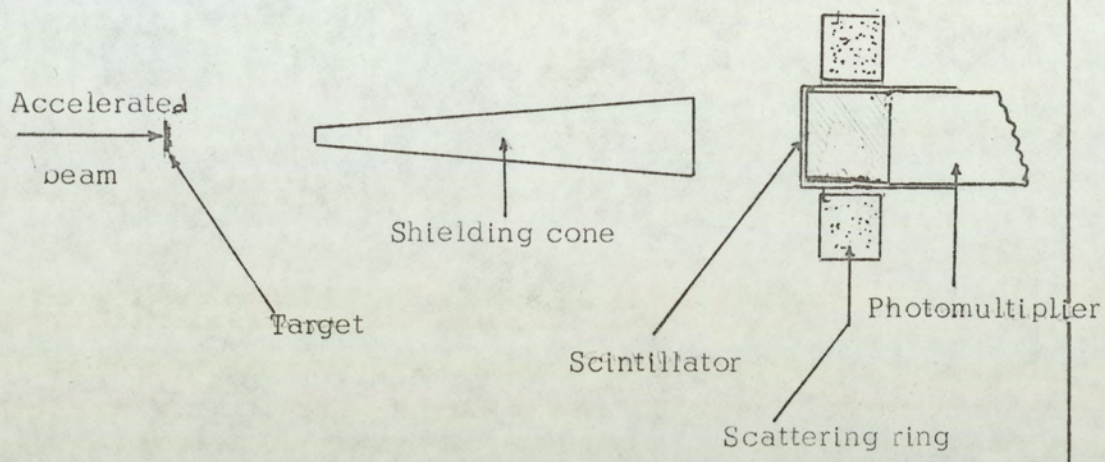

Figure (2-3) Plane view of a typical ring geometry arrangement for studying -rays from neutron inelastic scattering

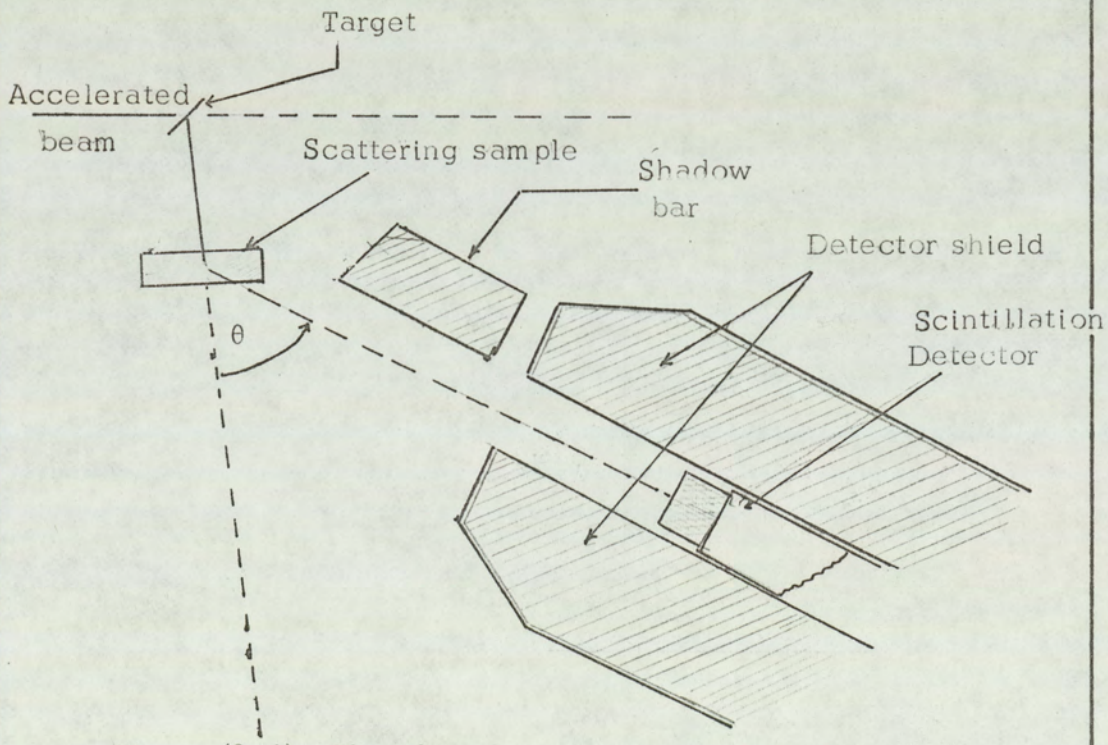

Figure (2-4) The closed geometry arrangement with flat plate scattering sample.

CHAPTER THREE

THE EXPERIMENTAL SYSTEM

As the work is concerned with the measurement of the differential cross-section of the gamma-ray production following the inelastic scattering of 14 MeV neutrons from concrete and iron samples, the present Chapter is devoted to the experimental system. The production of neutrons, neutron monitoring, the electronic system and the scattering samples will be discussed.

3.1. The Experimental Arrangement for the Associated Particle Method Using the T (d,n) ^{4}He Reaction :

Neutrons were produced from the T(d,n)^{4}He reaction by bombarding a titanium-tritide target with deuterons having an energy of about 140 KeV produced by the S.A.M.E.S. type J accelerator described below.

3.1.1. The S.A.M.E.S. Accelerator

The accelerating voltage was supplied by a d.c. electrostatic generator hermetically sealed in a hydrogen atmosphere. The accelerating voltage can be varied continuously from zero to 160 KV. The voltage stability as quoted by the manufacturers is about 1% at 150 KV, the observed stability is about 4% depending on humidity and temperature during the runs.

The ion source, is a 100 MHZ R. F. source supplied with

deuterium gas through a thermally activated palladium leak. The ions were extracted by a potential variable from zero to 6 KV and the maximum ion source output current is 600 μ A. The extracted beam has a two stage potential drop to earth, the focus electrode is adjustable from zero to 50 KV and an oil immersed Cockroft-Wallton generator supplies the power for the focus electrode. The control consul is connected to the ion source, deuterium gas leak, beam extraction and the focussing inside the high voltage terminal via a 150 KV isolation transformer. The S.A.M.E.S. accelerator is shown in Figure (3-1).

3.1.2. The Beam Tube and The Target Assembly

The accelerated deuterons were passed through a 6 metre long evacuated tube to the tritiated - titanium target in the scattering room. The tube was evacuated to a pressure of about 5×10^{-6} torr with the main pumping stage being part of the accelerator and additional pumping stage being provided at the target end. The pumps consisted of a backed oil diffusion pump with liquid nitrogen refrigerated baffels. A cold finger was positioned above the auxiliary pumping-stage to maintain a good vacuum in the target assembly and to stop oil and other contaminants being deposited onto the target.

Additional beam focussing was necessary due to the length of the beam tube, and this was accomplished by a pair of electrostatic quadrupole which have been discussed in detail by Baynham[52]
A pair of electrostatic deflector plates further down the tube enabled the

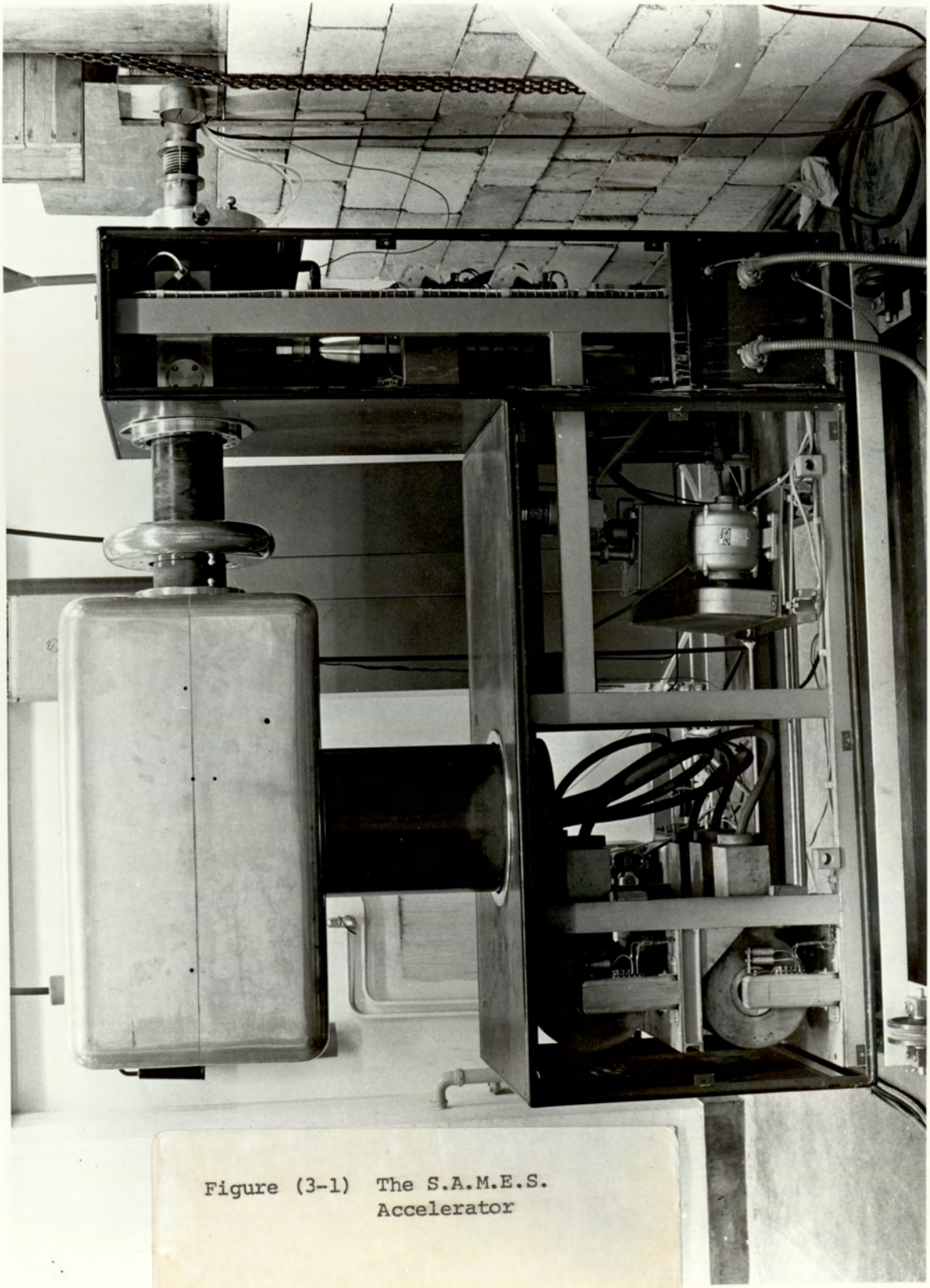

Figure (3-1) The S.A.M.E.S. Accelerator

target current to be optimised. A typical deflector peak voltage was - 1 KV, and the voltage on the quadrupoles was $\pm$ 1.8 KV. Figure (3.2) shows the quadrupole lenses and the deflector plates. The target assembly was supplied by Multivolt Limited, and a full description of it was reported by previous workers [44, 50]. The target assembly is shown in Figure (3.3). An aperture slit was used to limit the area of the target bombarded by the deutrons. The target was water cooled to minimize the evaporation of tritium due to the heating effect of the deutron bombarding.

The target consists of an annular disc of titanium loaded with tritium, the whole assembly being contained in a stainless steel case incorporating a water cooling system. The target had an outer diameter of 143 mm was 31.8 mm wide and contained about 6.2 mCi of tritium per cm^2.

Since the bombarding deuterons eject electrons from the target and the diaphram, it was necessary to prevent these electrons back-streaming to the accelerator, this was achieved by raising the target and diaphram potentials to + 200 volts. As shown in Figure (3.4), the target, the aperture flange and the main beam tube were insulated by araldite spacers in order to maintain the suppression potentials which were produced by taking the target and diaphram currents to earth via large resistors. An avometer in series with the target and diaphram suppression resistors enabled the currents to be monitored.

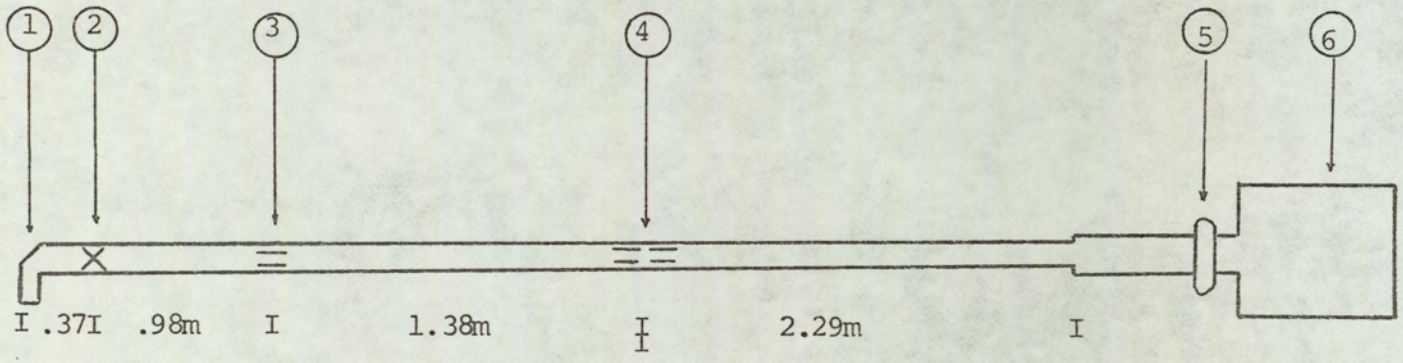

Figure (3-2) The Accelerator beam tube showing the quadrupole lenses , the deflector plate and the target end .

1- The Tritium target

2- Pumping stage

3- Deflector plate

4- Quadrupole lenses

5- The focous electrode

6- The H.V. terminal .

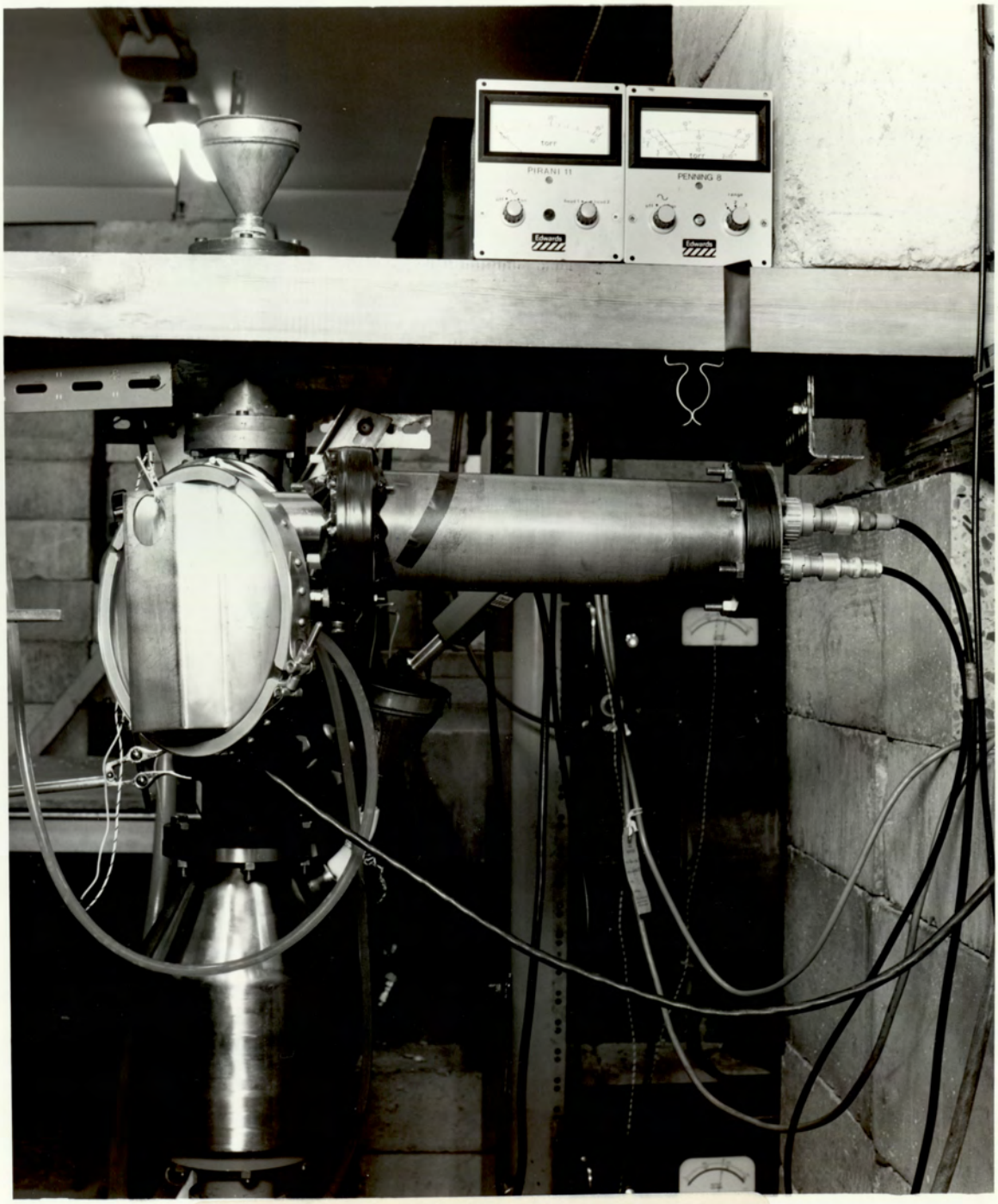

Figure (3-3) The target assembly

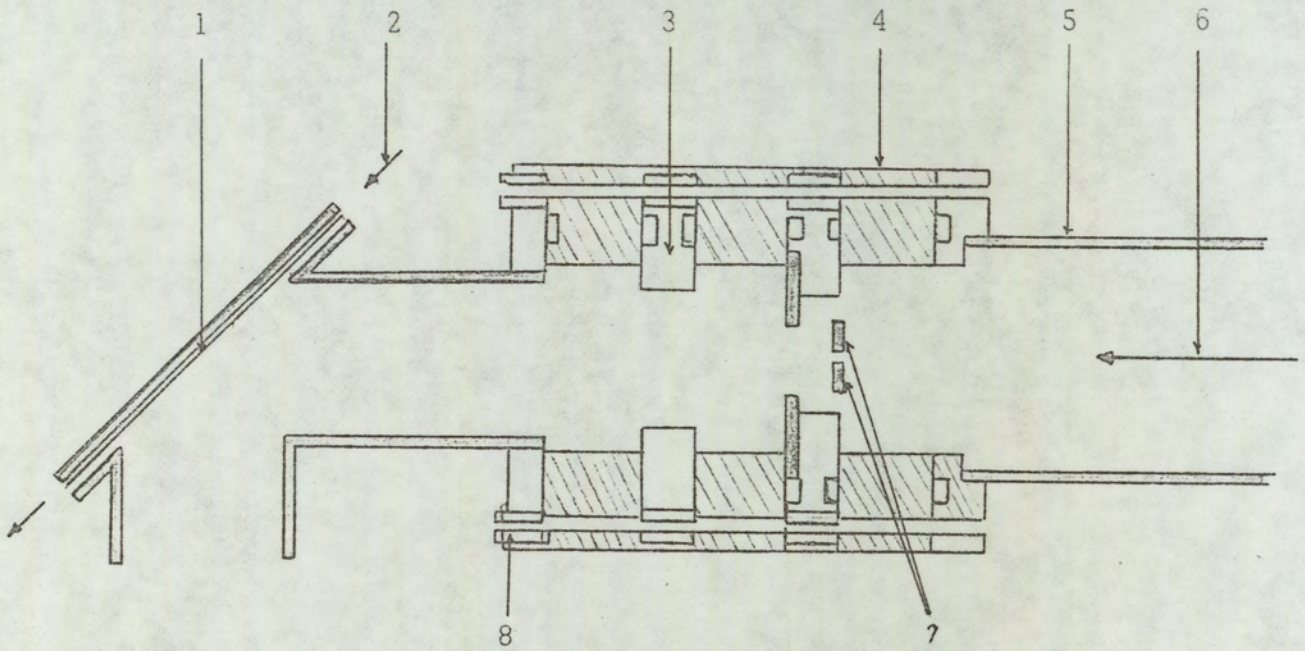

Figure (3-4) Sketch of the target assembly .

1- Tritium target

2- Water cooling

3-Suppressor

4- Araldite

5- Main beam tube .

6- Deuteron beam .

7- Aperture plate .

8-Insulating sleves

3.1.3. The Alpha Particle Detector

Alpha-particles can be detected with 100% efficiency because they are highly ionizing particles due to the fact that they are relatively heavy, doubly charged particles. For the present application, the detector had to meet the following requirements;

a - A high alpha particle detection efficiency

b - A low neutron and gamma-ray detection efficiency

c - A fast response time and

d - Insensitivity to radiation damage.

It was possible to use either a semi-conductor detector or scintillation detector and a detailed consideration of the properties of each of the two detectors has been given by Baynham[52].

The main two advantages of the plastic scintillation detector compared with the semi-conductor detector are :

1. The Plastic scintillator is less susceptible to radiation damage under long irradiation times and

2. The plastic scintillator has a better response time than that of the semi-conductor detector, the rise time in the plastic scintillator being about 1 ns compared with about 6 ns in the semi-conductor detector.[52] With modern electronics , this can be reduced to considerably less than this value .

These two properties make the plastic scintillator more suitable for the nano-second timing required in the time of flight technique

employed in this work. The alpha-particles were detected using an 0.5 mm thick sheet of plastic scintillator (N 102 A) mounted on a perspex flange which acted as a light pipe and a vacuum seal, the perspex was optically coupled to a "Phillips" 56 AVP Photomultiplier tube. The scintillator was a disc 25 mm in diameter mounted behind an aluminium plate 1 mm thick. A rectangular aperture in the plate (11 mm x 19 mm) was used to define the solid angle of the detected alpha-particles. The scintillator was placed 90 mm from the target this geometry defines the beam of alpha-particles detected with semi-angles 3.5° and 6° in the vertical and the horizontal planes respectively.

A thin aluminium foil (0.0044 mm thickness) was used to stop the beta-particles produced in the decay of tritium and the deuterons which had been scattered through 90° reaching the detector.

The dynode resistor chain which supplies the dynode voltages is shown in Figure (3.5). Equal voltages are applied between the dynodes, a design recommended by the manufacturers, for high gain. The photomultiplier tube was operated with the anode at zero potential while the cathode was kept at -ve H.T., the output pulses were taken from the anode via a 50 Ω resistor. This arrangement eliminated the necessity of an emitter follower amplifier to match the signals through the cable to the electronic system.

Figure (3.6) shows the alpha-particle detector which was positioned in the arm of the target assembly at 90° to the deutron beam

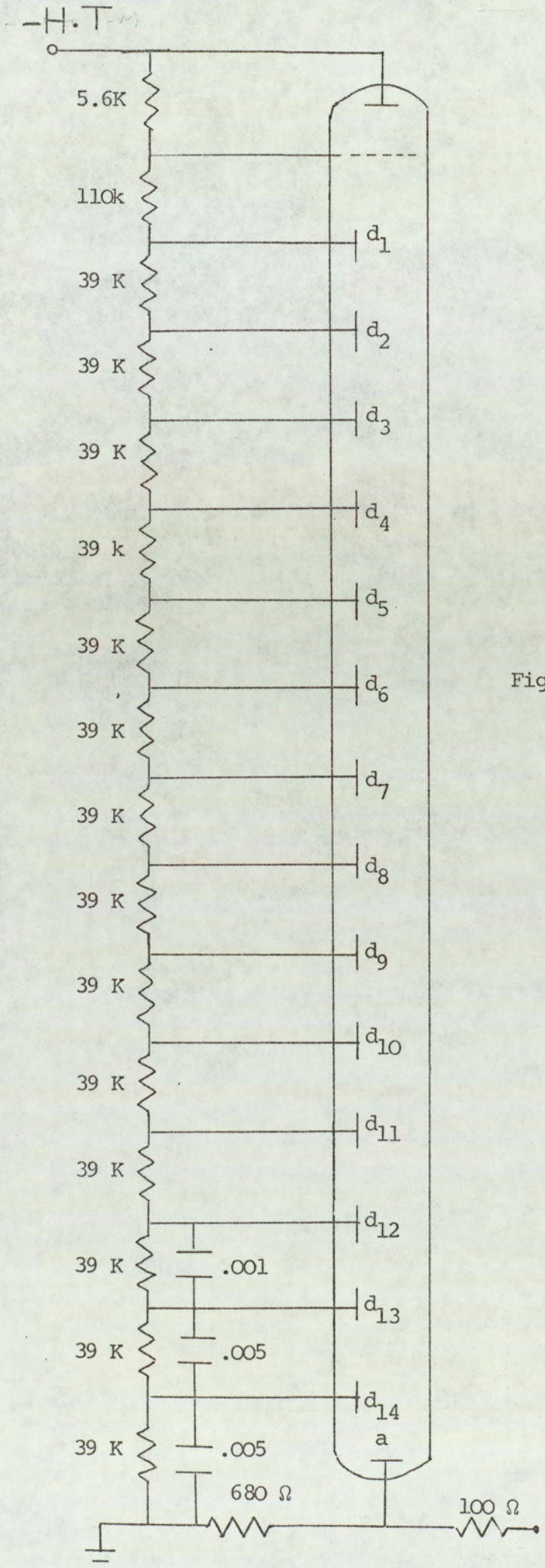

Figure (3-5) The dynode resister chain of the 56 AVP photomu-tiplier tube for alpha detector .

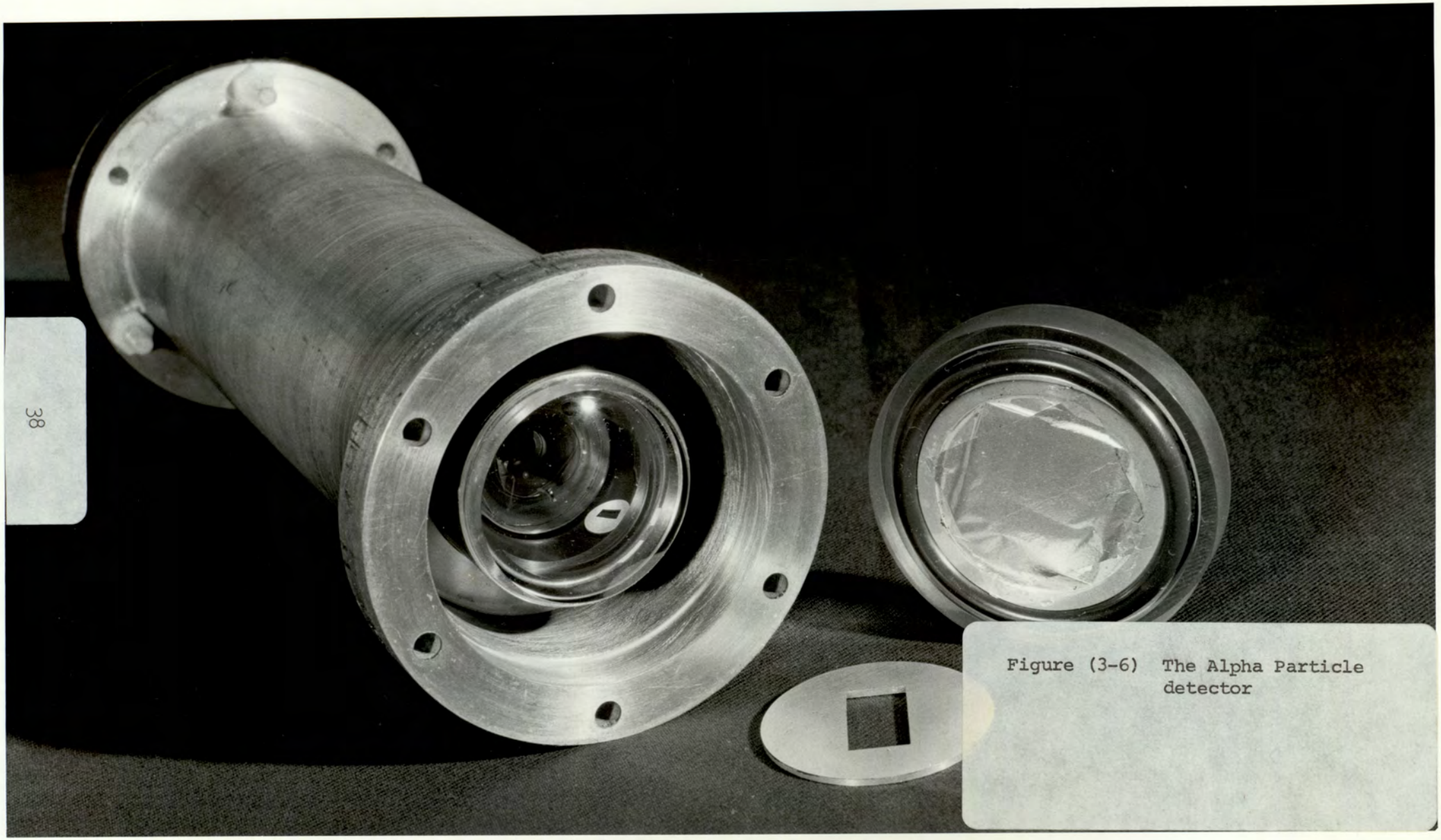

Figure (3-6) The Alpha Particle detector

as shown in Figure (3.3).

3.2. The Neutron Source :-

3.2.1. The Kinetics of The T(d,n) ^{4}He Reaction :-

For any nuclear reaction the following conservation laws apply in the centre of mass system of coordinates.

i) Conservation of charge,

ii) Conservation of the total energy,

iii) Conservation of linear and angular momentum, and

iv) Conservation of parity (strong reactions only).

The T (d,n) ^{4}He reaction can be represented by a two-body collision in both the laboratory and the centre of mass system as shown in Figure (3.7). The mathematical equations relevant to the reaction are given in Appendix A.

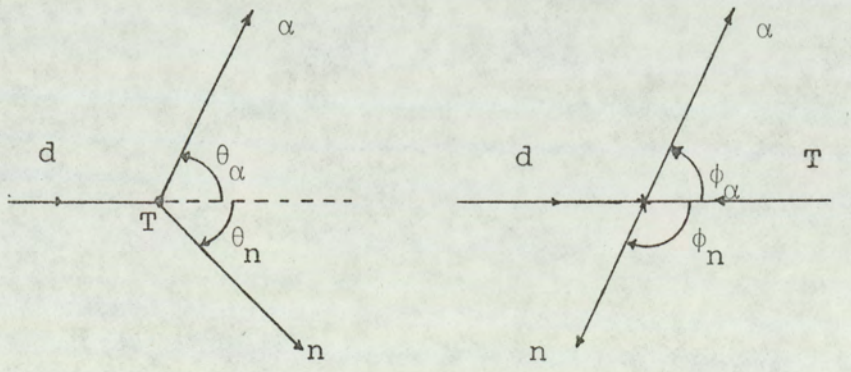

Figure (3.7) The T(d,n) ^{4}He reaction in the laboratory and the center of mass systems.

3.2.2. The Angular Range of Neutrons In The T (d,n)^{4}He Reaction :-

As mentioned in Section (3.1.3), the alpha-particles emitted at right angles to the incident beam, i.e. ($\phi_\alpha = 90^\circ$) were observed by the alpha-detector which remained fixed in the target assembly, therefore, it was necessary to consider neutron emission angles associated with an alpha-particle detector centred at $\phi_\alpha = 90^\circ$.

Due to energy loss by deutrons encountered in penetrating the target, neutrons were produced in collisions with the deuterons having energies in the range $(E_d)_{min.} = 0$ to $(E_d)_{max.} = 140$ KeV.

The general relationship between ϕ_n and ϕ_α in the laboratory system is given by

$$\tan \phi_\alpha \quad \frac{-\frac{1}{2} \operatorname{Sin} 2\phi_n + \operatorname{Sin} \phi_n \sqrt{(1/\gamma)^2 - \operatorname{Sin}^2 \phi_n}}{-\operatorname{Sin}^2 \phi_n + \operatorname{Cos} \phi_n \sqrt{(1/\gamma^2) - \operatorname{Sin}^2 \phi_n - (\frac{m\alpha}{mn})}} \qquad (3.1)$$

where $\gamma = \frac{V_{C.M}}{V'_n}$ where $V_{c.M}$ and V_n' denotes the velocities of the centre of mass and that of the neutron in the centre of the mass respectively.

For the special case of $E_d = 0$, the relation becomes

$$\phi_\alpha = 180 - \phi_n \qquad (3.1.a)$$

In figure (3.8), ϕ_α is plotted vs. ϕ_n for different values of deuteron

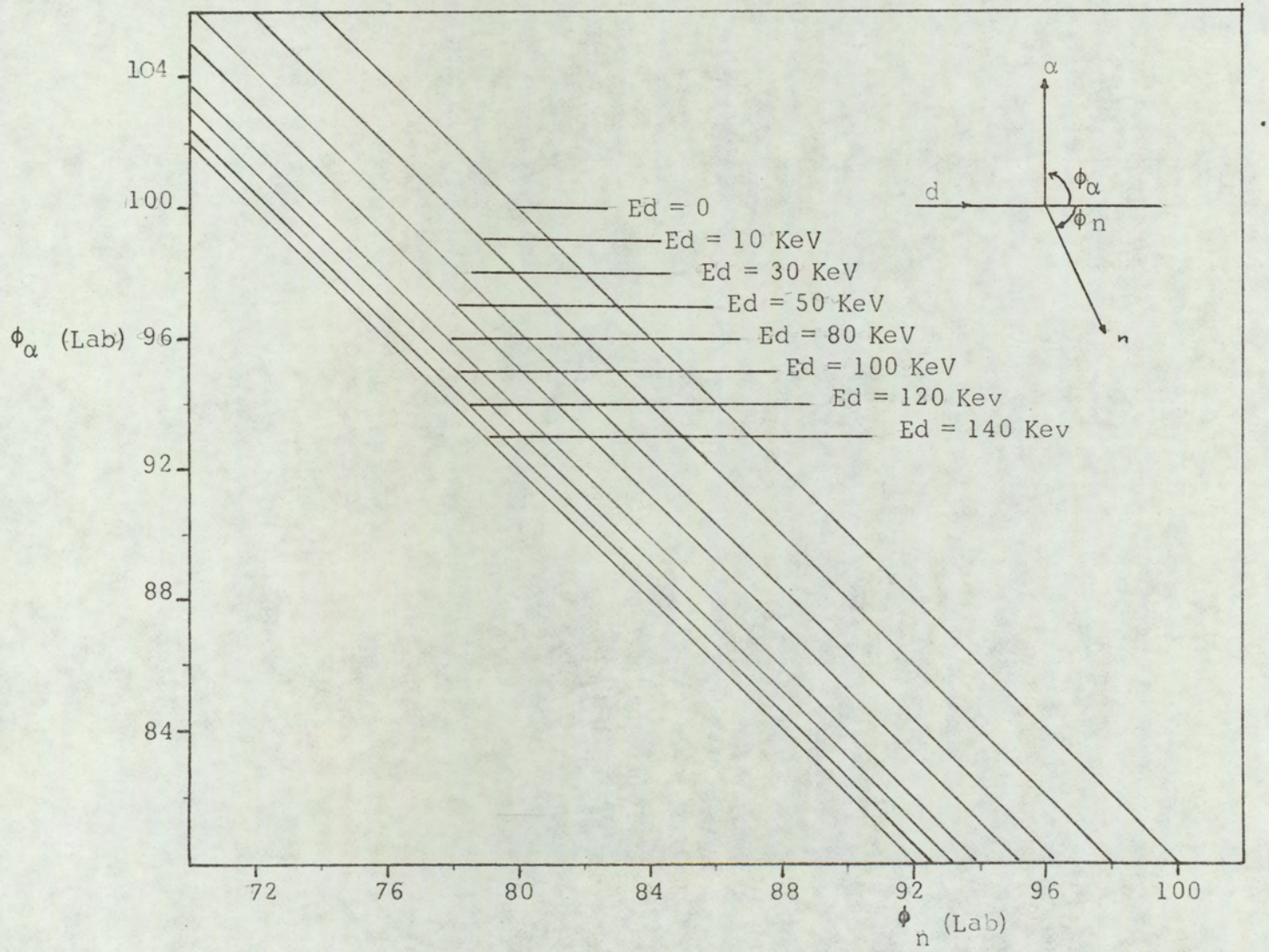

Figure (3-8) The alpha-particle and neutron emission angles (ϕ_α, ϕ_n) for various

energies between 0 and 140 KeV, from which for any specified angular spread of alpha-particles in the reaction plane, the angular limits of the associated neutron can be determined.

3.3. The Neutron Beam Profile

The cross-section of the $T(d,n)^4He$ reaction depends on the deutron energy E_d as shown in Figure (3.9). Since different values of E_d produce different values of ϕ_n, the neutron yield varies with ϕ_n. This is described by the neutron beam profile which can be calculated if the variation of the neutron yield with the deuteron energy E_d is known.

3.3.1. The Neutron Yield :-

The different cross-section for the $T(d,n)^4He$ reaction has been measured by several workers[53,54,55] for different deuteron energies. The angular dependence of the differential cross-section of the $T(d,n)^4He$ reaction in the centre of mass system was found to be isotropic for E_d upto 200 KeV by Allan and Poole [55] and for E_d upto 570 KeV by Argo et al.[54] The total neutron yield from a thick target per incident deuteron of energy Ed per unit solid angle is given by

$$Y = \int_o^{E_d} \frac{n_t \left(\frac{d\sigma}{dw}\right)}{(d E_d/dx)} \, d E_d \qquad (3.2)$$

where

n_t = no of tritium atoms / cm^3.

$(d\sigma/dw')$ = The differential cross-section for the $T(d,n)^4He$ reaction

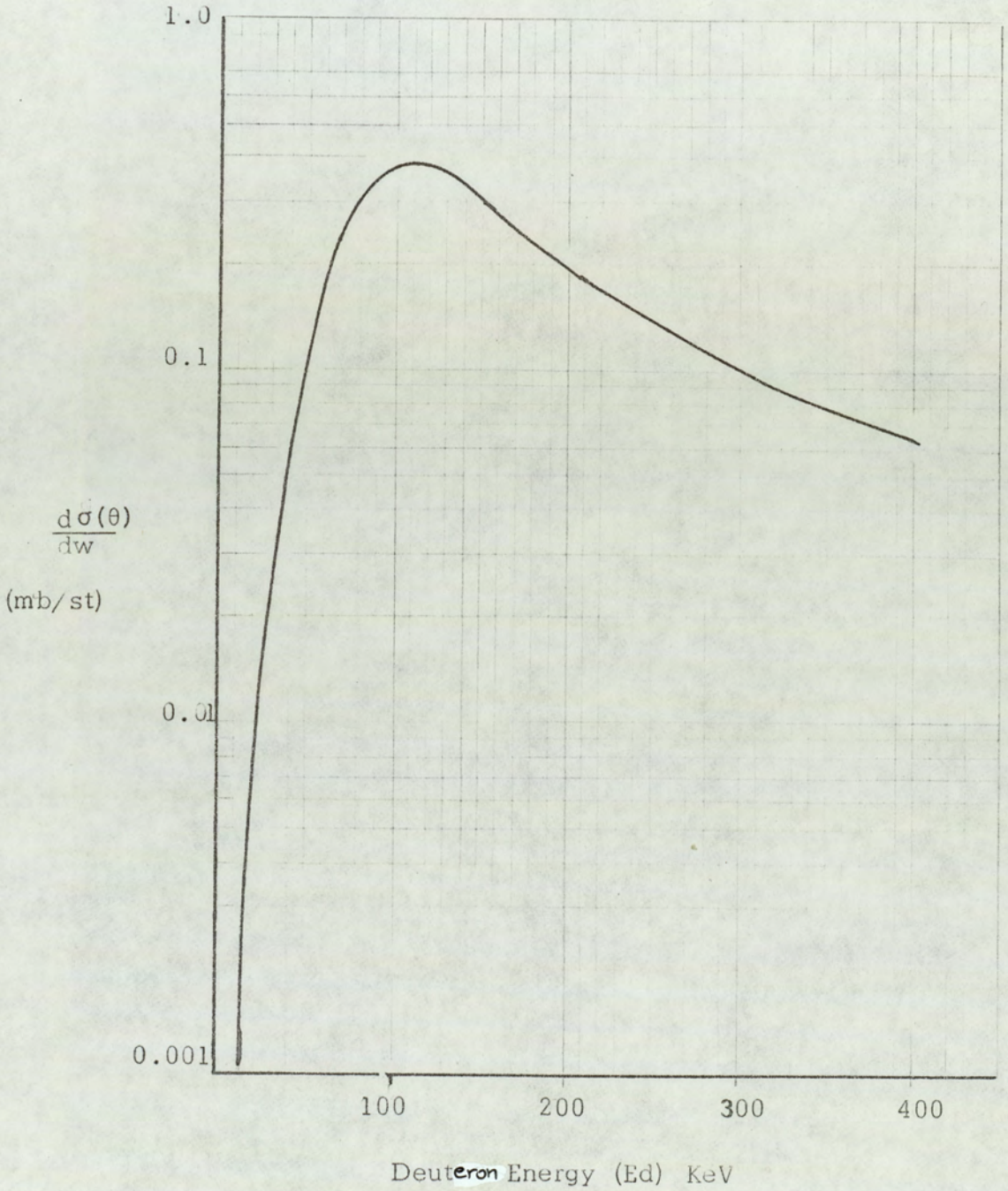

Figure (3-9) The differential cross section for the $T(d,n)^4He$ reaction vs deuteron energy

in the centre of mass system, and

$(d E_d/dx)$ = The rate of energy loss of deuterons of energy Ed in the titanium tritiated target.

Equation (3.2) assumes that the incident deuteron flux is constant throughout the target which is an acceptable approximation since only a small fraction of the dueterons interact with the tritium in the target.

3.3.1.a. Calculation of n_t :

In calculating the number of tritium atoms/cm^2, the loading factor in the target was considered to be unity. The density of titanium is 4.54 gm/cm^3 and since the volume expansion of the hydride is about 15%, the density of the loaded titanium can be calculated from

$$\rho_{TiT} = \frac{(M.w)_{TiT}}{A_{Ti}} \times \rho_{Ti} \times (1 - \text{volume expansion}) \quad (3.3)$$

So the density of the loaded titanium is

$$\rho_{TiT} = \frac{48 + 3}{48} \times 4.8 \times 0.85 = 4.1 \text{ gm/cm}^3 \quad (3.3.a)$$

The percentage error in the calculated density is about 5% [56]. Hence the number of tritium atoms per cm^3 in the target is

$$n_t = \frac{\rho_{TiT} \times N_o}{A_{TiT}}$$

$$= \frac{4.1 \times 6.023 \times 10^{23}}{48} = 5.146 \times 10^{22} \text{ atoms/cm}^3$$

3.3.1.b. The Stopping Power of the Deuterons in the Target

The rate of energy loss of deuterons in the titanium-tritium target is given by :-

$$\left(\frac{-dE}{dx}\right)_{TiT} = \left(\frac{A_{Ti}}{(M.w)_{TiT}}\right)\left(\frac{dE}{dx}\right)_{Ti} + \left(\frac{A_{T}}{(M.w)_{TiT}}\right)\left(\frac{dE}{dx}\right)_{T} \qquad (3.5)$$

where (d E/dX) represents the rate of energy loss and the subscripts TiT, Ti, and T represent titanium-tritium target, titanium and tritium respectively.

Benvensite et al.,[56] obtained (d E/dX) by using Warshaw's measurements on the rate of energy loss of protons in various elements in the energy range 50 to 350 KeV and assuming that the energy loss is a function of the velocity of the particle only, i.e.

$$(dE/dX)_{p}\ (E) = (dE/dX)_{d}\ (2E) \qquad (3.6)$$

The stopping power for deuterons in tritium has been found from the rate of energy loss data in hydrogen by Reynolds et al.,[57] and also from Phillips measurements on proton energy losses in hydrogen and helium.

The stopping power in the titanium-tritium target was found by combining the stopping powers in both materials using equation (3.5), and the result is shown in Figure (3.10).

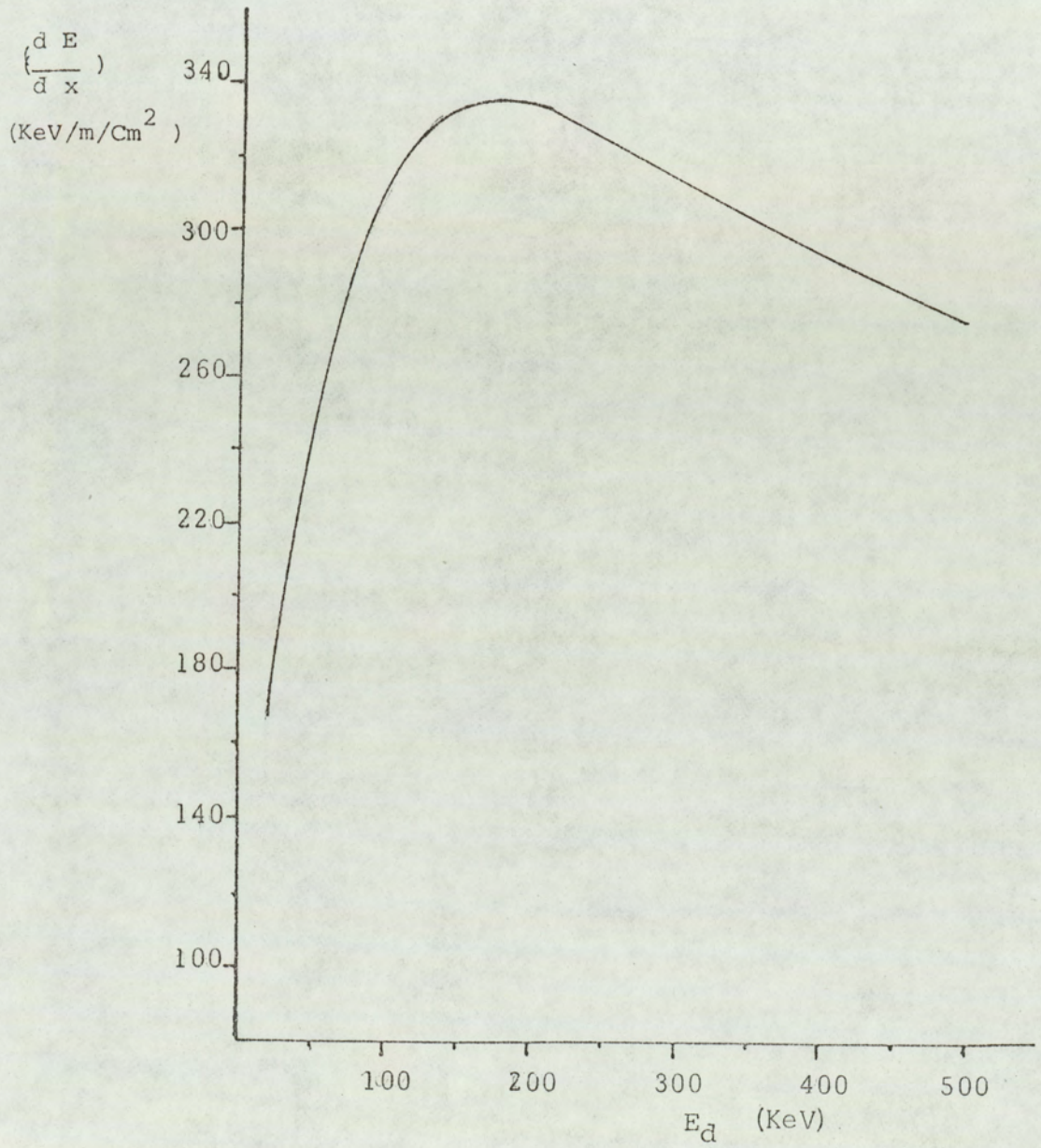

Figure (3-10) The stopping power of deuterons in titanium-tritide.

Using the above, the neutron yield per incident deuteron per unit solid angle can be calculated from equation (3.2) and applying numerical integration, ie.

$$Y = n_t \sum_E \left\{ \left(\frac{d\sigma}{dw}\right) \Big/ \left(\frac{dE}{dx}\right) \right\} \Delta E \qquad (3.2.a)$$

This has been evaluated numerically in 25 KeV steps from $E_d = 0$ to $E_d =$ 500 KeV [56] and the result is shown in Figure (3.11).

The neutron beam profile is finally calculated from Figures (3.10) and (3.11). The calculation is performed in one degree (1^o) steps for each value of ϕ_n in the range $\phi_n = 76^o$ to $\phi_n = 96^o$.

Figure (3.10) was used to determine the yield that this range of values of deuteron energy can produce. This was done using the area under the curve in the relevant range of Ed, the areas are then normalized so that the maximum yield is unity. The resultant neutron beam profile is shown in Figure (3.12). The full width at half maximum is about 12 degrees and the total width of the beam of the associated neutrons is 17 degrees.

3.3.2. The Anisotropy Factor

The relation between the solid angles in the centre of mass and the laboratory systems is called the anisotropy factor, i.e.,

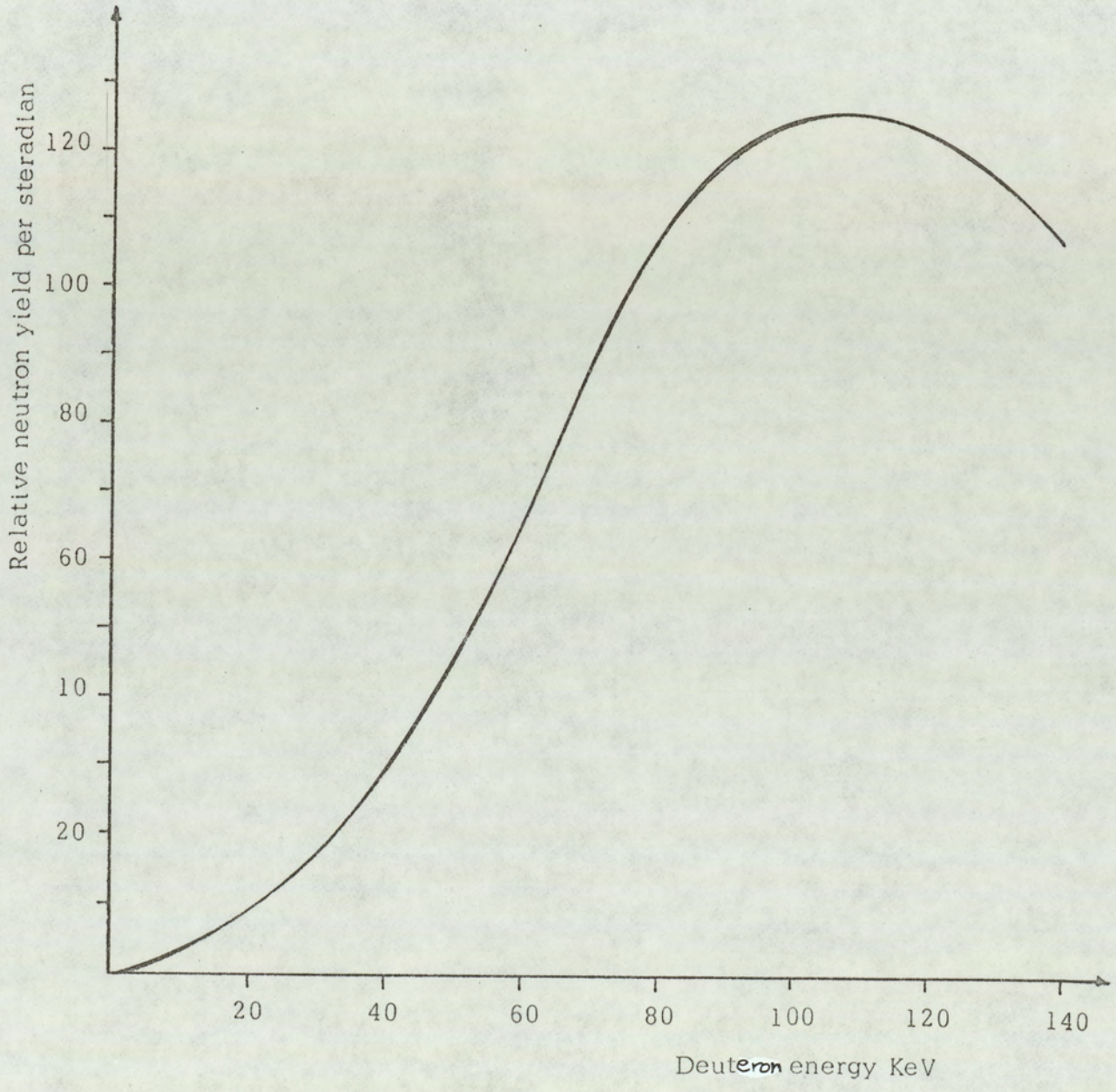

Figure (3-11) The relative neutron yield as a function of deuteron Energy Ed

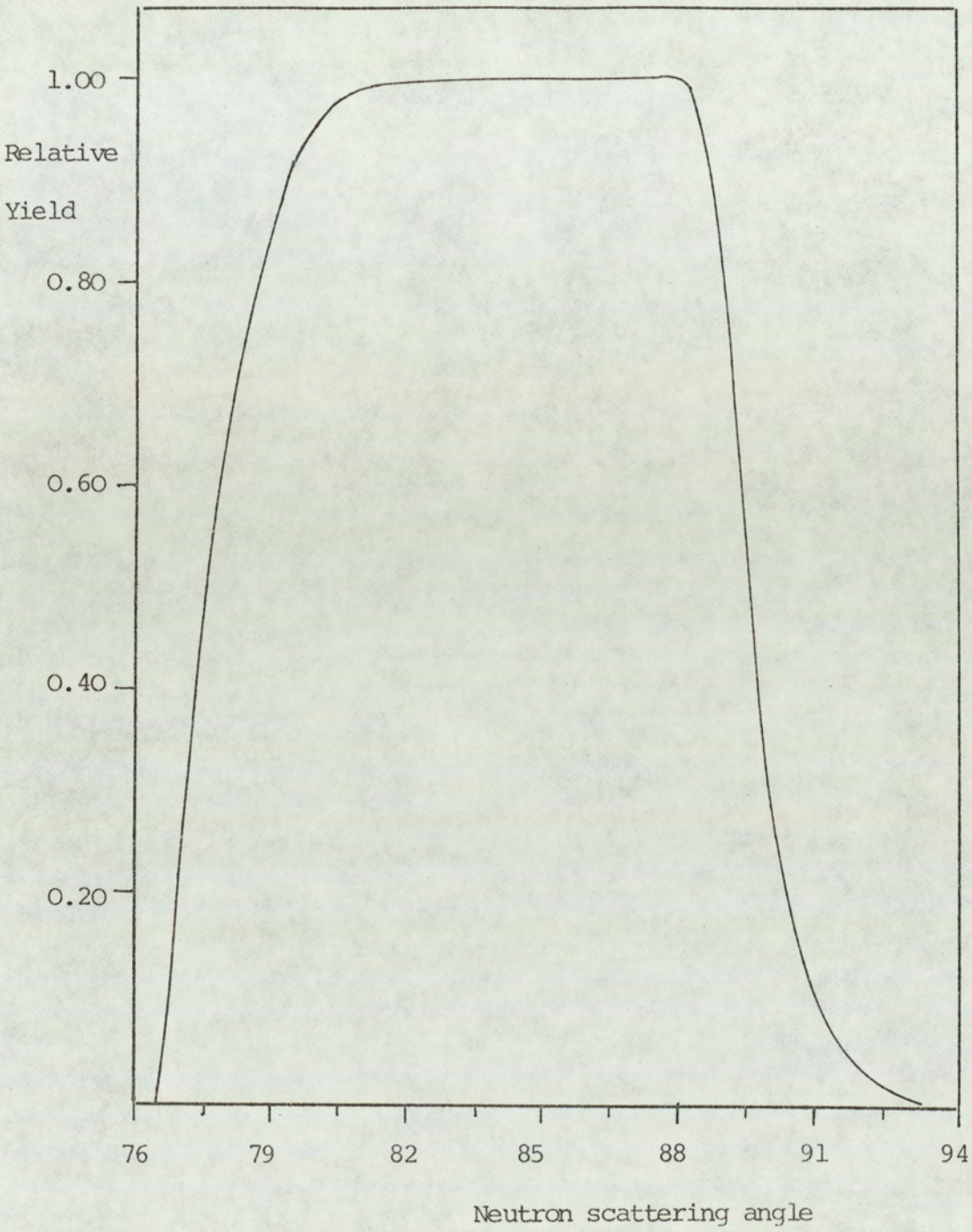

Figure (3-12) Neutron Beam Profile .

$$\frac{dw'}{dw} = \frac{\sin\ \theta\ \ d\ \theta}{\sin\ \phi\ \ d\ \phi} \qquad \frac{(C.M.)}{(Lab.)} \tag{3.7}$$

The relationship between θ and ϕ is given by

$$= \text{Cos}^{-1} \left\{ -\gamma^2\ \text{Sin}^2\theta \quad \pm \quad \text{Cos}\ \phi\ \sqrt{1 - \text{Sin}^2\phi} \right\} \tag{3.8}$$

where

$$\frac{1}{\gamma^2} = \left(\frac{V'_n}{V_{C.M}} \right)^2 = \frac{m_\alpha}{m_n} \cdot \frac{(m_d + m_T)}{m_d} \quad \frac{m_T}{m_d + m_T} + \frac{Q}{Ed} \tag{3.9}$$

From equation (3.7) and (3.8)

$$\left(\frac{dw'}{dw} \right)_n = \frac{\gamma\ (\text{Cos}\ \phi + \sqrt{(1/\gamma)^2 - \text{Sin}^2\ \phi}\ )}{\sqrt{(\frac{1}{\gamma^2}) - \text{Sin}^2\ \phi}} \tag{3.10}$$

To find $\left(\frac{dw'}{dw}\right)$ for the alpha-particles, ie. $\left(\frac{dw'}{dw}\right)_\alpha$ equation (3.10) can be used with

$$(1/\gamma^2) = \frac{m_n}{m_\alpha} \left(\frac{m_d + m_T}{m_d} \right) \left\{ \frac{m_T + Q}{E_d} \right\} \tag{3.9.a}$$

Equation (3.10) has been evaluated as a function of ϕ_n and E_d the results are shown in Figure (3.13) from which it can be seen that in the deuteron energy employed in these experiments, the anisotropy factor can be taken as equal to unity. The error introduced by this approximation

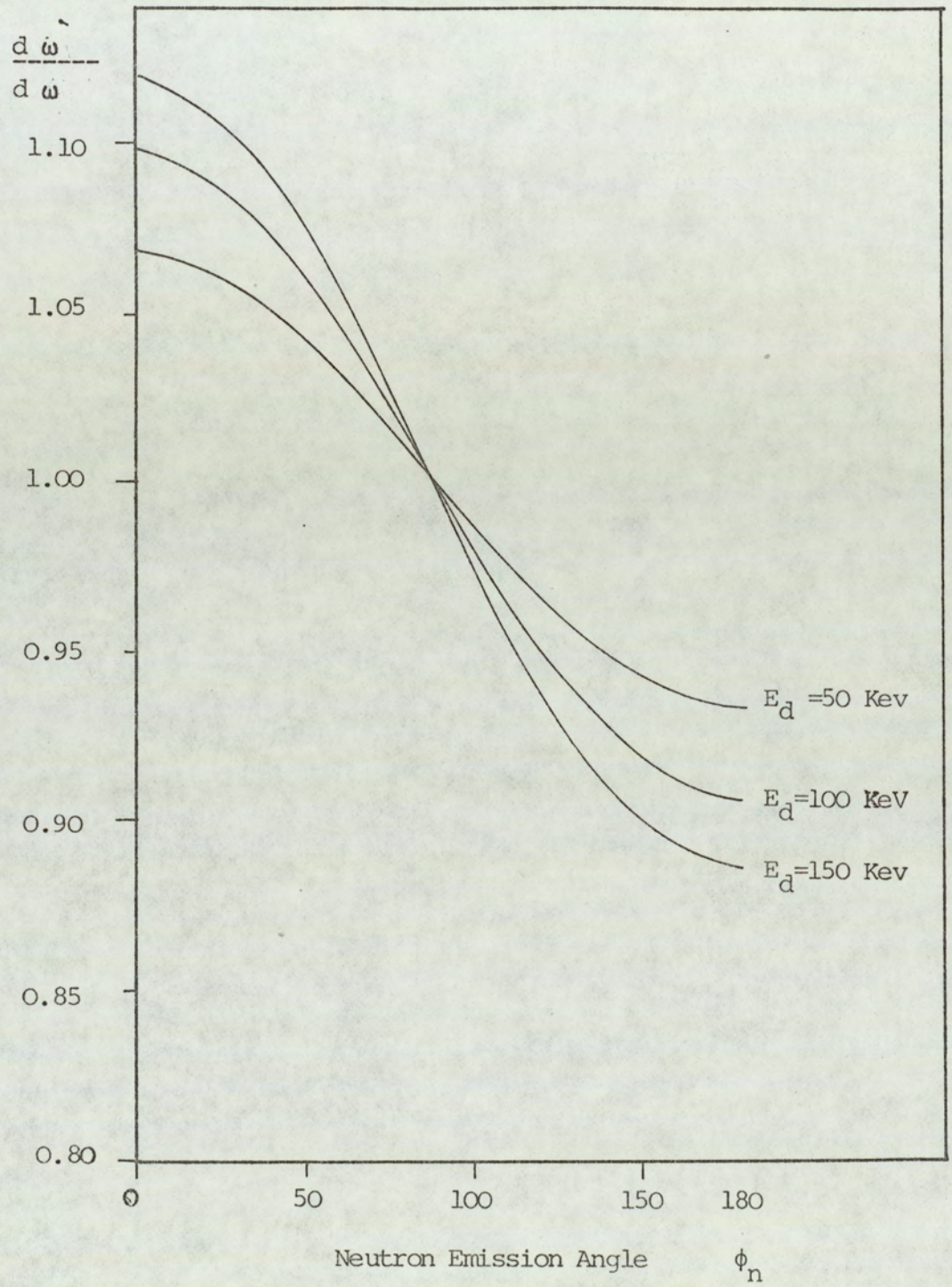

Figure (3-13) The Anisotropy Factor .

is less than 1%, especially in the calculation of the neutron line shape to be discussed in the following Section.

3.3.3. The Neutron Line Shape :

The energy distribution of the neutrons at any particular laboratory angle is referred to as the neutron line shape, and is of a particular interest since it shows for a specific experimental geometry, the energy spread of the neutrons striking the sample. The dependence of the neutron energy on the angle of emission ϕ_n and the energy of the incident deutron is given by,

$$E_n(E_d, \phi_n) = \left(\frac{m_d}{m_d + m_T}\right)^2 \frac{m_n}{m_d} E_d \cos(2\phi_n) + \left(\frac{m_\alpha}{m_n + m_\alpha}\right)\left(\frac{m_T E_d}{m_d + m_T} + Q\right) \pm \frac{2\cos\phi_n}{m_d + m_T} \cdot$$

$$\left\{\frac{m_d m_n m_\alpha}{(m_n + m_\alpha)} \cdot E_d \frac{m_T E_d}{(m_d + m_T)} + Q\right\}^{\frac{1}{2}} \left\{1 - \frac{m_d m_n E_d \sin^2\phi_n}{m_\alpha m_d E_d + Q.(m_d + m_T)}\right\}^{\frac{1}{2}} \qquad (3.11)$$

When the values of the masses and Q are substituted in (3.11) the resulting formula is

$$E_n(E_d, \phi_n) = 0.08 E_d \cos(2\phi_n) + 0.8 (0.6 E_d + 17.6) \pm 0.4 \cos\phi_n \cdot \sqrt{1.6 E_d (0.6 E_d + 17.6).\left(1 - \frac{E_d \sin^2\phi_n}{10 (0.6 E_d + 17.6)}\right)} \qquad (3.12)$$

The ordinate of the line shape can be either the evaluated neutron yeild or the relative neutron yield, ie. a quantity proportional to the yield. The quantity plotted as the ordinate is

$$A\ (\phi_n, E_\theta) = \left\{ \frac{(d\sigma(E)\ /\ dw')}{(d\ E\ /\ d\ x)} \right\} \left(\frac{dw'}{dw} \right) \quad (3.13)$$

Figure (3.14) shows the resulting neutron line shape for different values of ϕ_n, Figure (3.15) shows the same parameter for $\phi_n = 83^o$.

3.3.4. The Scattering Sample

3.3.4.1. The Iron Samples

The iron samples used were alloys containing 90% iron, the other elements present in these samples were nickel, and impurities such as carbon and oxygen, but these materials introduce no interference with the experiment due to the small amounts present and the different γ-rays they produce as it can be seen in Table (3.1).

Table (3-1) Gamma-ray energy levels from iron, carbon and oxygen

Element	Gamma-ray energy levels MeV		
	1st	2nd	3rd
^{56}Fe	0.84	1.24	1.81
^{12}C	4.43	7.6	9.1
^{16}O	6.05	6.14	7.

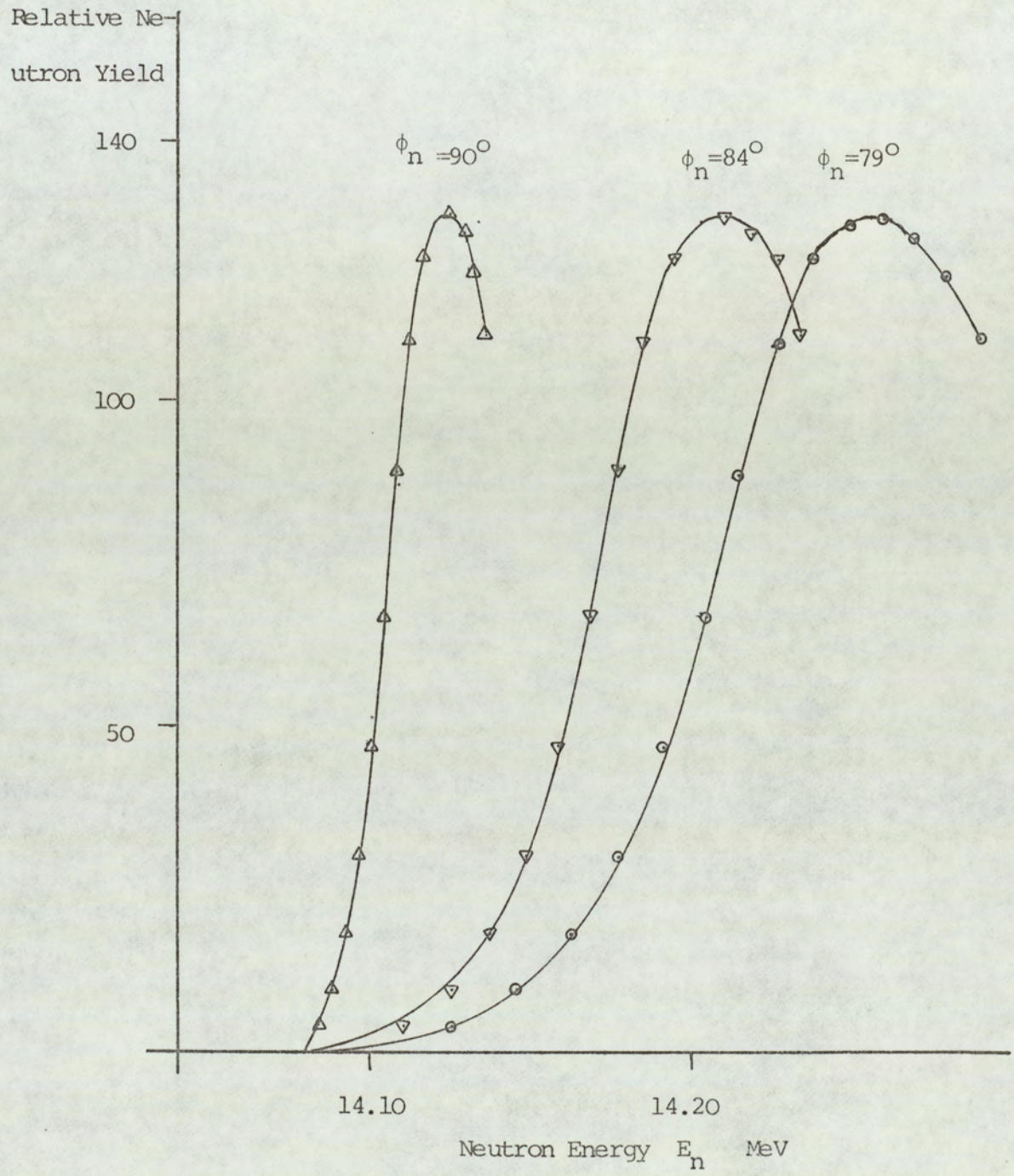

Figure (3-14) The Neutron Line Shape For Different Values Of ϕ_n

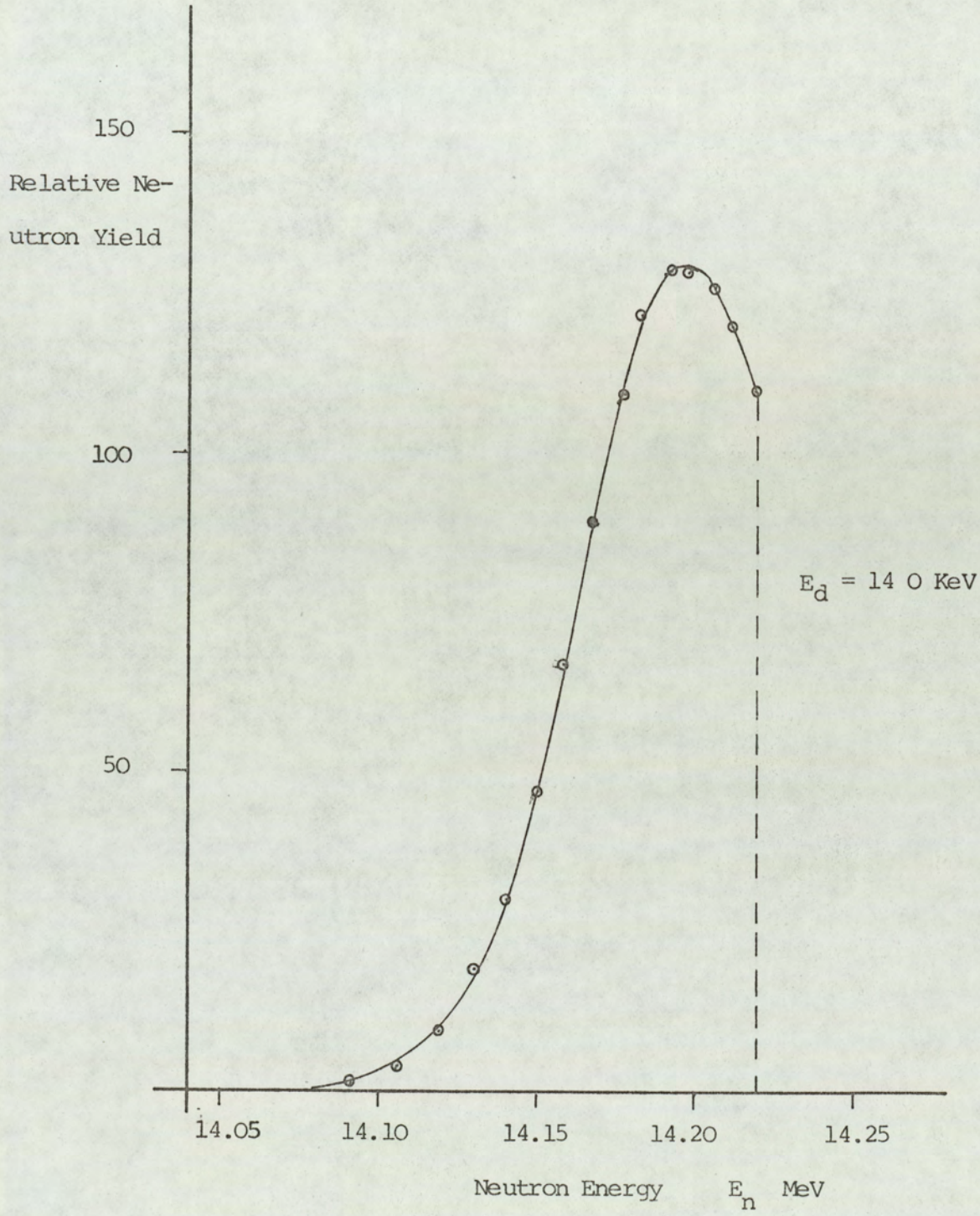

Figure (3-15) The Neutron Line Shape For $\phi_n = 83^o$

The samples were rectangular in shape with dimensions 20 x 17 cm and thicknesses of 2, 7.6 and 10.4 cm for the three samples used corresponding to 0.5 , 1.66 and 2.33 mean free paths respectively at the neutron incident energy of 14 MeV.

The density of these samples was taken as 7.6 gm/cm^3.

3.4.4.2. The Concrete Samples

The concrete samples used were ordinary concrete specially treated by ultrasonic waves to increase the density to 2.5 gm/cm^3. This treatment has no effect on the chemical composition of the concrete. The chemical composition of concrete is so complicated that it is rather impossible to predict a chemical formula that would describe a hypothetical concrete molecule.

Table (3-2) below gives the main compounds entering in the composition of Portland Cement which is only one of four materials which constitute portland concrete namely cement, gravel, sand and water.

Table (3-2) The chemical composition of Portland Cement as given in reference (86).

Description + Abbreviation	Chemical Formula	% in Cement	Composition Percent			
			C_aO	SiO_2	Al_2O_3	Fe_2O_3
Tricalcium Silicate (C_3S)	3 Ca 0.SiO_2	54.1	73.7	26.3	-	-

Continued.

Di calcium Silicate (C_2S)	2 Ca 0.SiO_2	16.6	65.1	34.9	-	-
Tri calcium Aluminate (C_3A)	3 Ca 0.Al_2O_3	10.8	62.3	-	37.3	-
Tri calcium Alumino-ferrite (C_4AF)		9.1				

The samples were rectangular plates in shape with dimensions 23 x 15 cm and the thickness of each plate was 2.5 cm. The different samples consisted of 2, 5, 8 and 10 plates giving sample thickness of 5, 12.5, 20 and 25 cm respectively.

3.5. The Electronic System

As the time of flight technique was used to discriminate between neutrons and gamma-rays, the electronic system used consisted of two main parts, namely,

1. The time of flight electronics, i.e. (Timing Line)
2. The Y-ray energy measurements, i.e. (Linear Line)

3.5.1. The Time of Flight Electronics

The original timing circuitary has been reported by Connel[50] then modified by Allenby[44] to give better time resolution, the circuit

used by Allenby is shown in Figure (3.16a) while the circuit used in the present work is shown in Figure (3.16b).

The gamma-timing pulse was taken from the anode and fed through coaxial table to the (Ortec 463) unit which incorporates a discrimination level and a constant fraction discriminator circuit which triggers at a constant fraction f of the input pulse height, thus eliminating the "walk" problem as the circuit triggers on the same phase point on each pulse [58,59]. This timing pulse was used to start the time convertor.

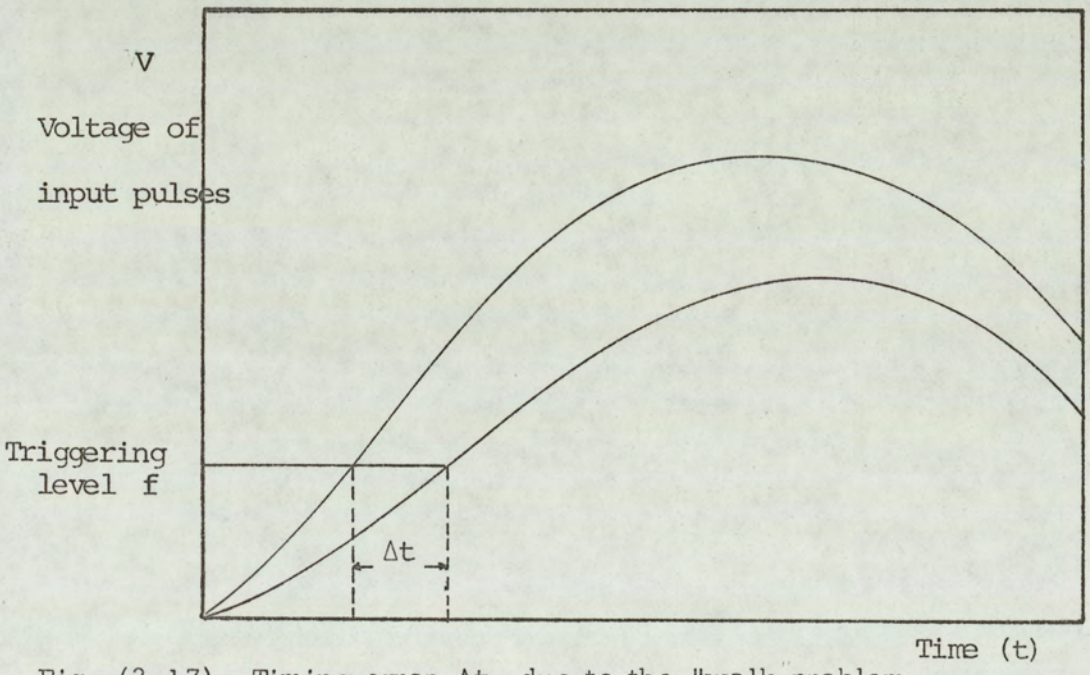

Fig. (3.17) Timing error Δt due to the "walk problem.

The alpha detector has been altered as discussed in Section 3.1.3, the second timing pulse was taken from the alpha detector (anode pulse), and fed to delay generator which can provide a continuously

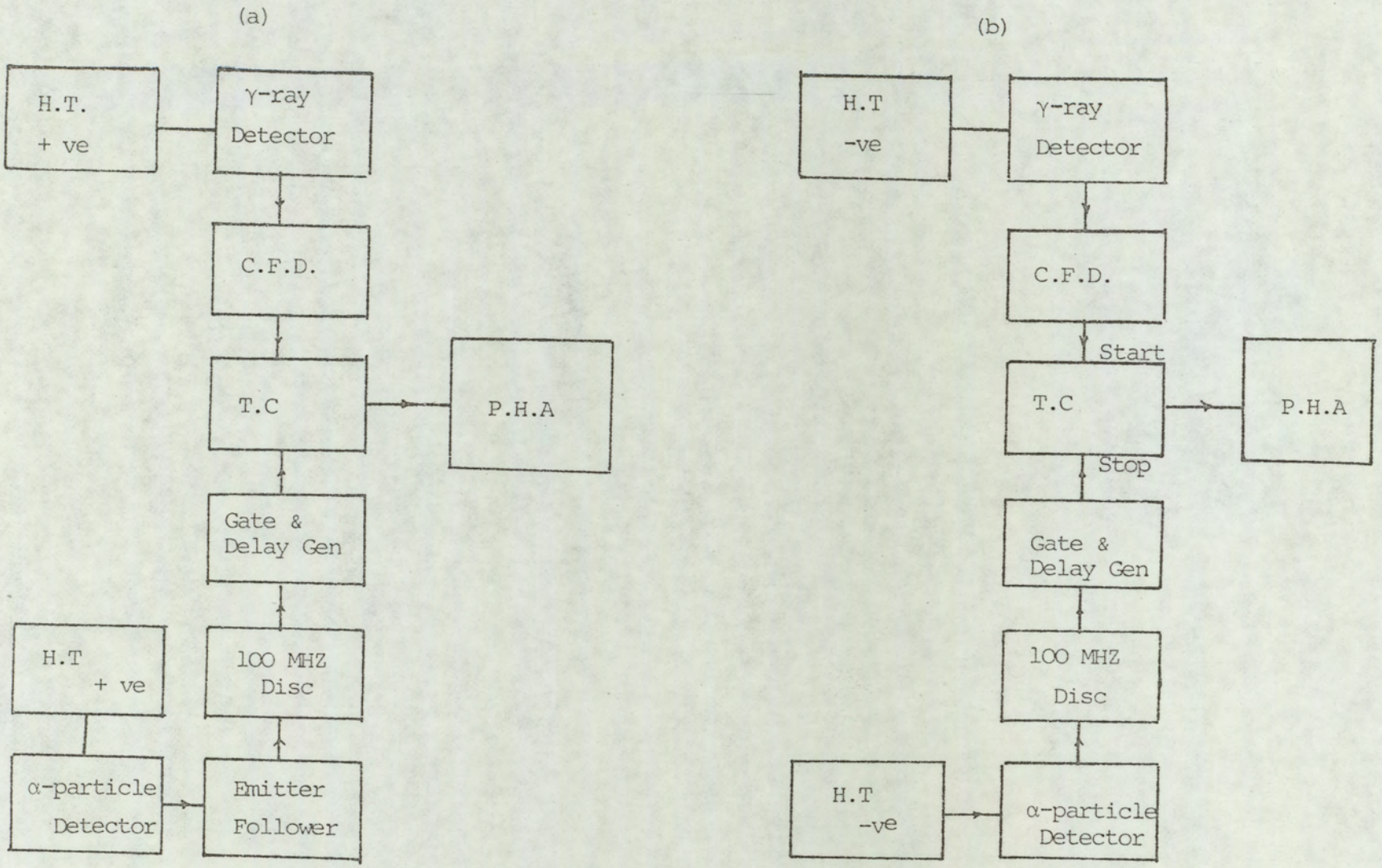

Figure (3-16) The T.O.F. Electronis

a - The original timing circuit

b - The circuit used in the present work

variable delay from 100 nS to 110 μ S. This delayed signal was used to stop the time convertor.

The time convertor used (NE 4670) manufactured by Nuclear Enterprises had a variable time conversion range which could be varied between (0-50) nS to (0 - 200μ S). The output provided from this time convertor ranged from 0 to $\pm$ 10 volts depending on the output polarity required.

The γ-ray pulse was used to start the time convertor as the γ-ray line has the lower count rate than the alpha line (10^4 counts/ sec. compared with 8×10^4 count/sec), so the dead time of the time convertor is reduced and consequently the random coincidences are reduced. The time resolution obtainable with this system is shown in Figures (3 - 18) through to Figure (3-20), and the results are shown in Table (3-3)

TABLE (3-3)

Sample	Scattering angle	F.W.H.M.		F.W.T.H.	
		I/T	T.M.C.	I/T	T.M.C.
-	0	3.9 ns		9 ns	
Iron 2 cm	50°	5.7	7.5	9.5	12.5
" "	40	10	15	16	24
Concrete 2"	30°	7	10	17	21
Concrete 3"	70°	12	12.5	17	21

Table 3.3 Time resolution obtained using the electronic system

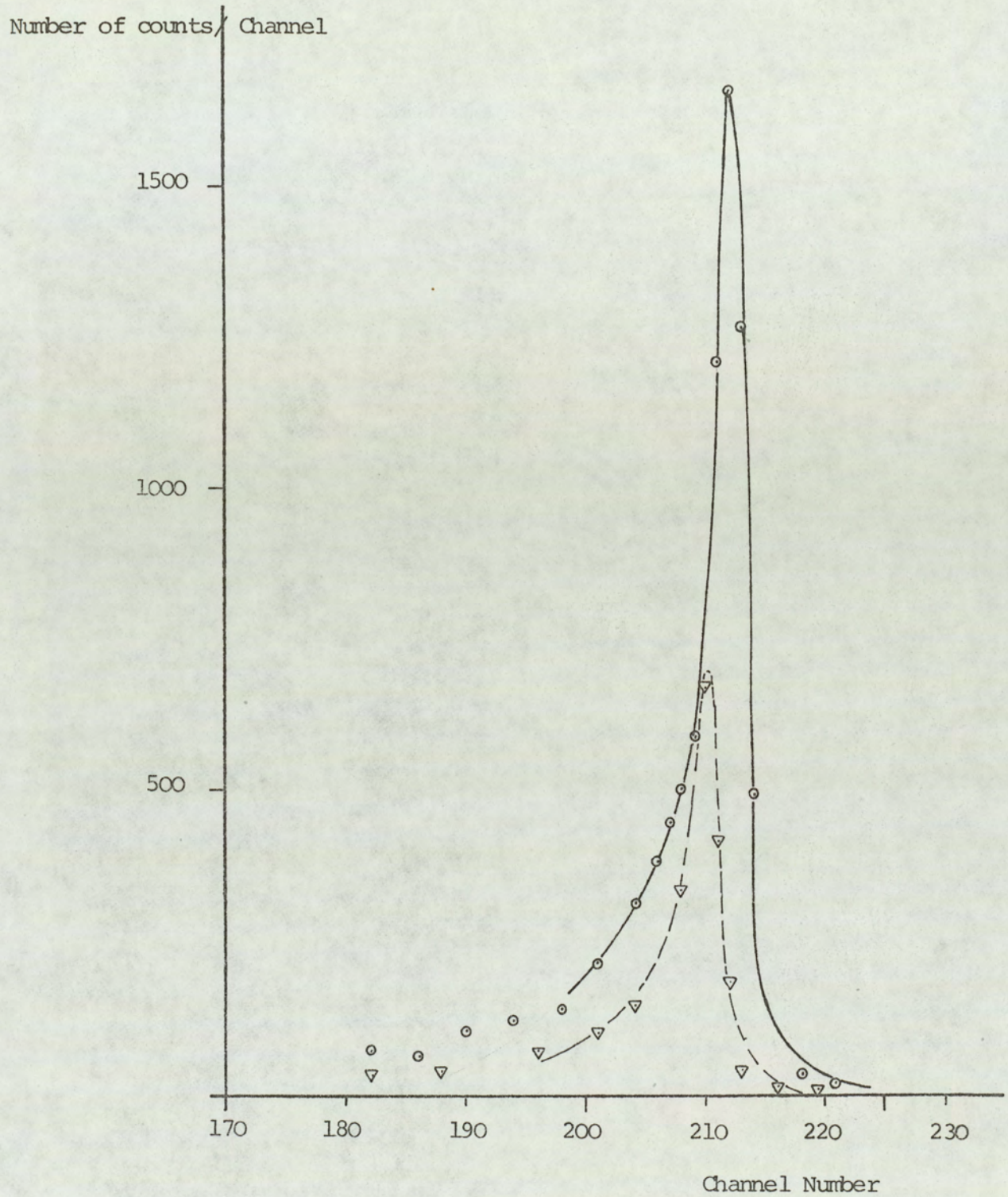

Figure (3-18) Time spectrum with no scattering sample , scattering angle 0^{o} .

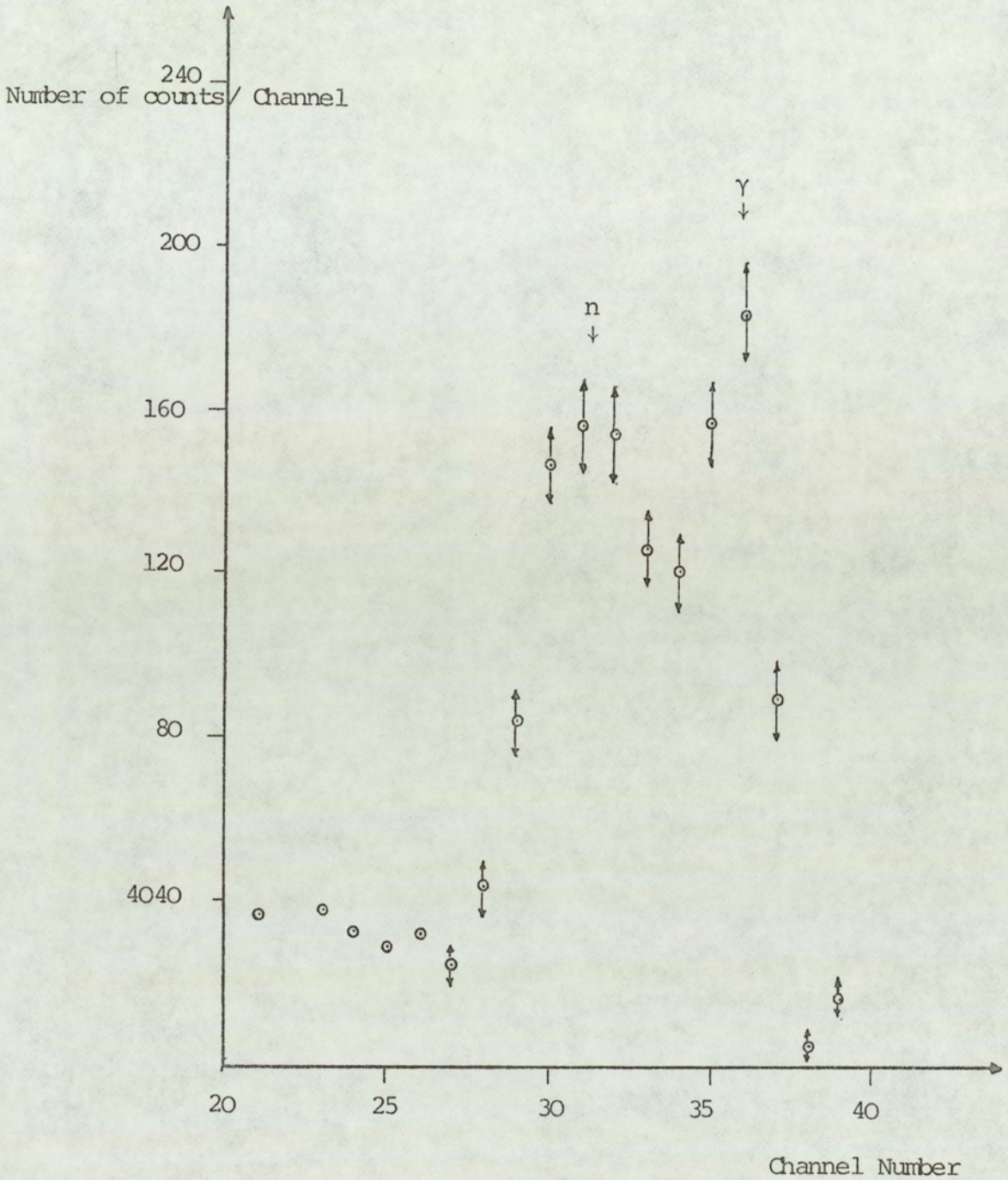

Figure (3-19) Typical time-spectrum from thin iron sample at scattering angle of 40^{o} . Sample thickness= 2 cm.

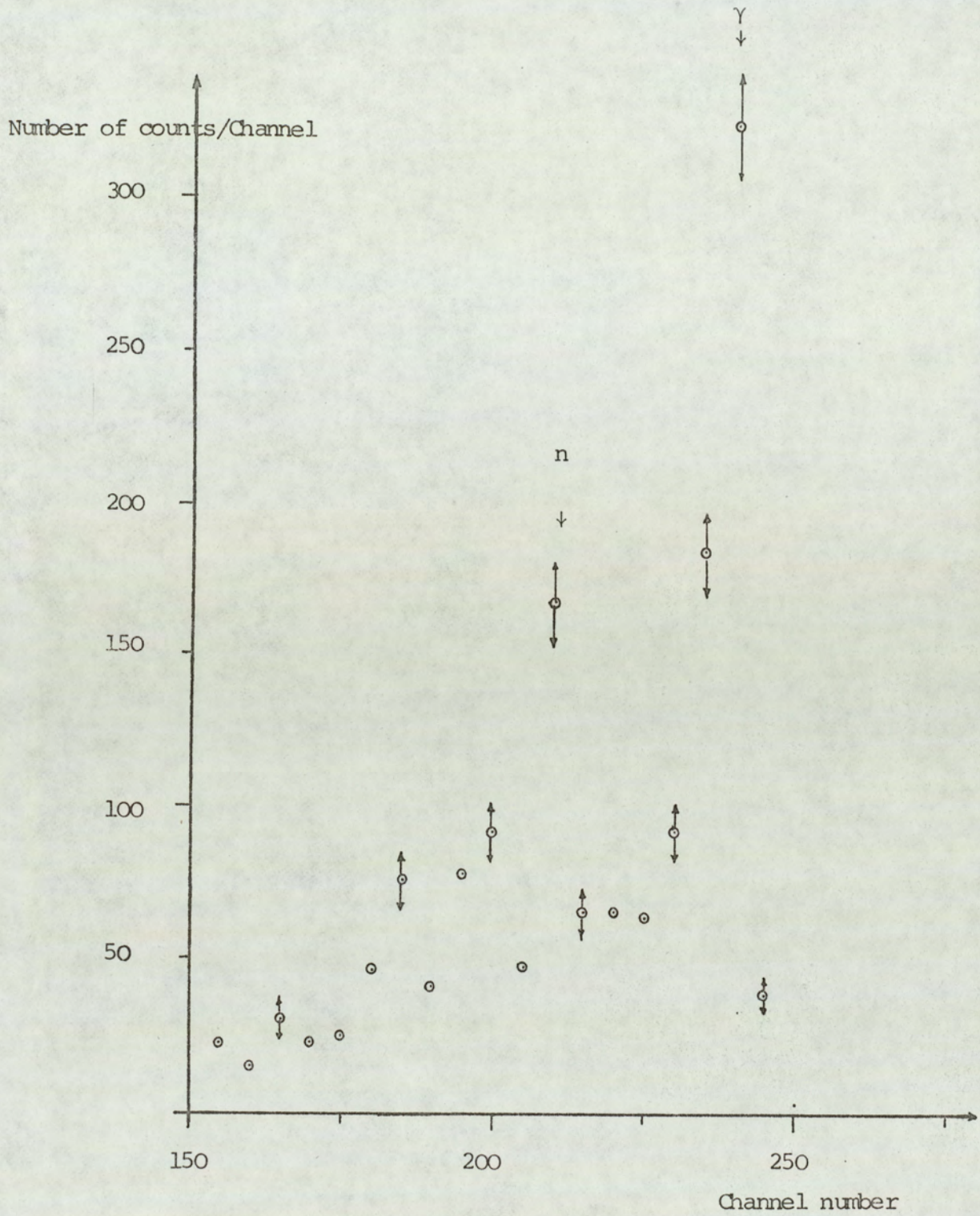

Figure (3-20) Time -spectrum from thin concrete sample at scattering angle of 30^{o} . Sample thickness = 5 cm.

The pulses due to the detection of neutrons can be seen also to form several peaks, with the main peak due to the elastically scattered neutrons with an energy of 14 MeV as can be verified from the time difference relative to the gamma-ray peak.

As the detector sample distance was kept constant through all the measurements at 140 cm, the obtained resolution was adequate to allow the gamma and neutron peaks to be completely resolved.

3.5.2. Setting the Discriminator Levels

Figure (3 -21) shows the spectrum obtained from the alpha-particle detector before applying any discrimination level. The (ORTEC 436) unit was used to eliminate the low energy noise and to pass the 3 MeV α-particle pulses from the $T(d,n)^4He$ reaction.

The detector output was amplified by using the ORTEC 485 linear amplifier and then gating the resulting pulses by the discriminator output which is governed by the discriminator's level as shown in Figure (3-22). As the discriminator's level was increased pulses below this level were not passed and therefore, the linear gate remains closed, thus, the low energy end was removed. Figure (3 -21) the dashed line shows the resulting spectrum with the discriminator's level set at 1.5.

The gamma-ray discrimination level was set in a similar way using the circuit shown in Figure (3-23), gamma-ray sources were

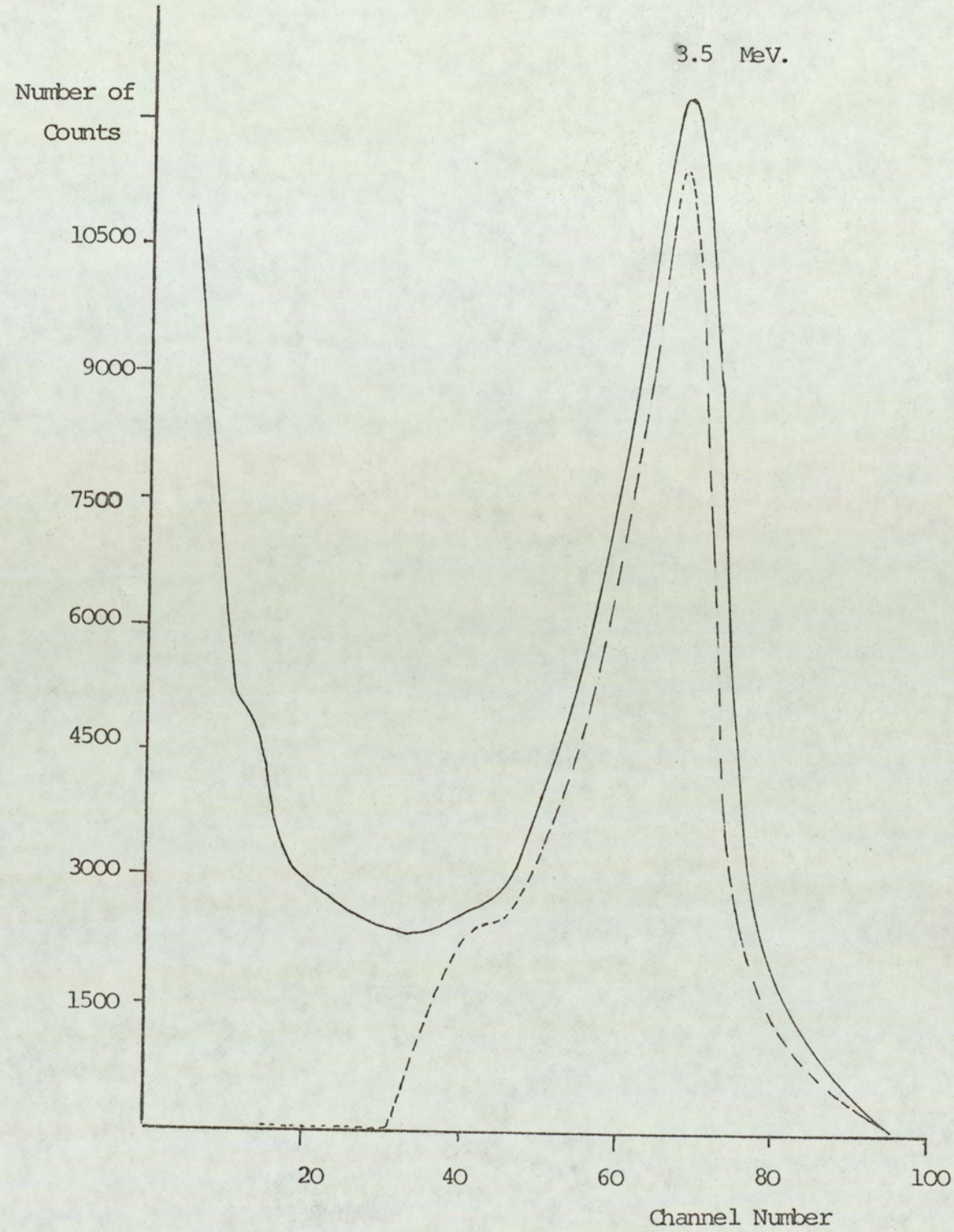

Figure (3-21) The alpha-particle pulse height spectrum from the T (d,n) ^{4}He reaction .

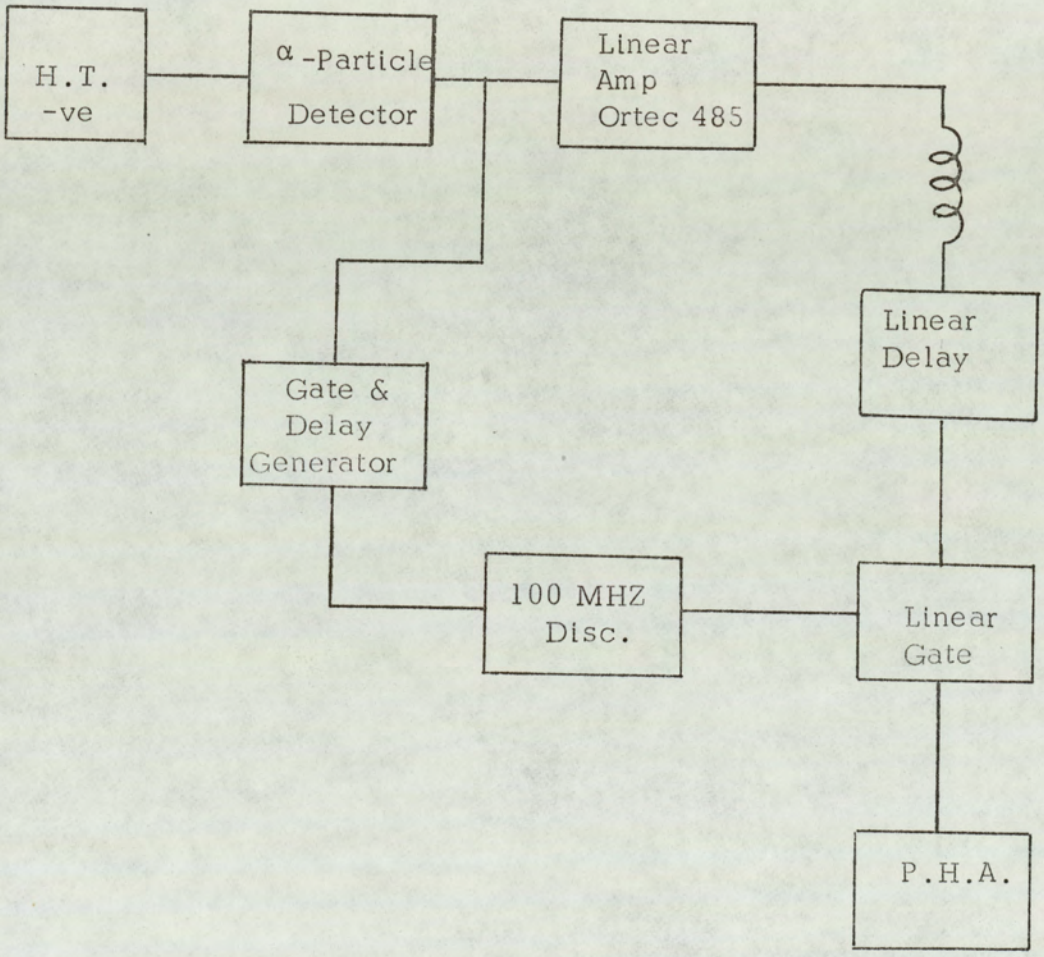

Figure (3-22) Setting α-particle discrimination level

used to set the discrimination level at a value appropriate to the gamma-ray energies being investigated. ^{137}Cs γ-ray source emitting 0.66 MeV γ -rays was used to set the discriminator level for the iron measurements and ^{60}Co 1.17 MeV γ-ray peak was used to set the discriminator level for the concrete measurements.

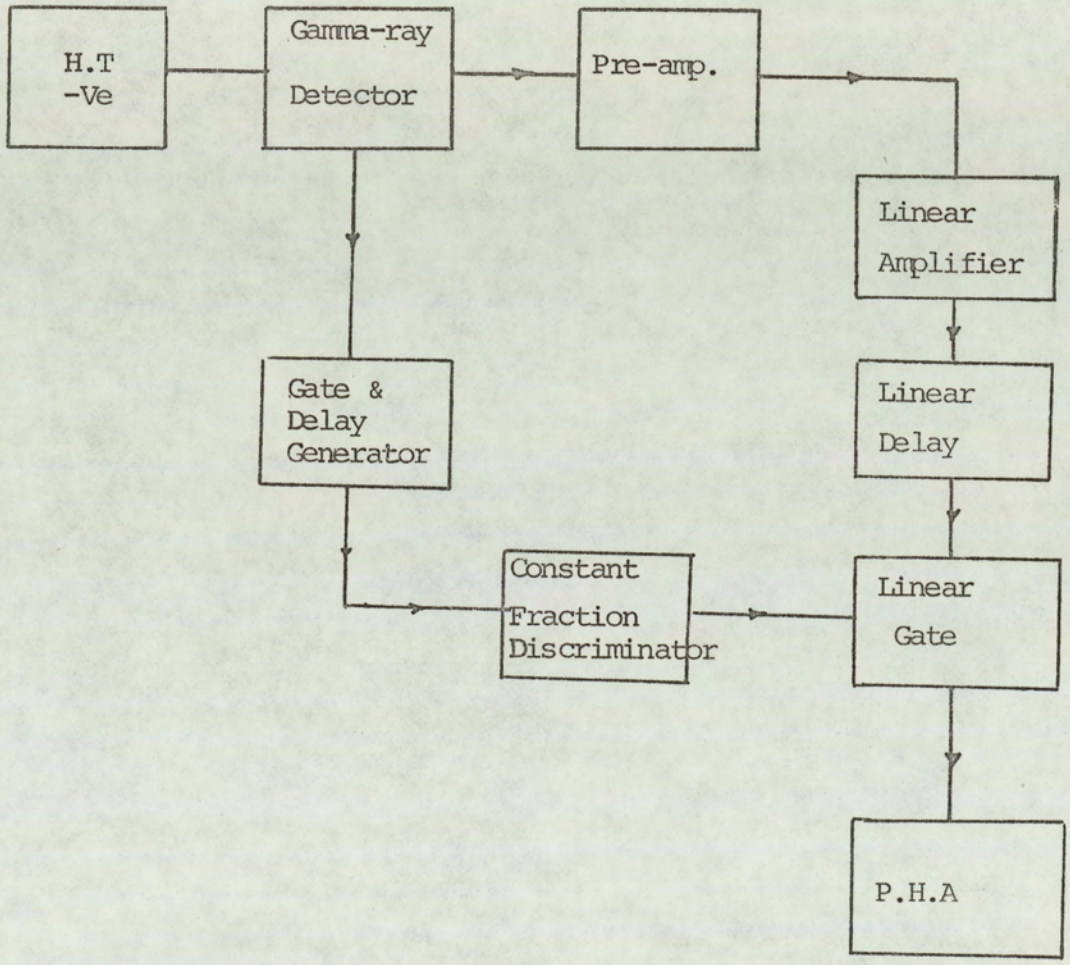

Figure (3.23) Setting the gamma-ray discriminator level.

3.5.3. The Linear Line (Energy) Electronics

The γ-ray pulses for energy measurements were taken from the 12th dynode and matched into a coaxial cable by an (ORTEC 113) preamplifier. The output of the preamplifier was then amplified by a linear amplifier (ORTEC 485). The pulses are then gated by the output of an (ORTEC 420 A) single channel analyser which has its window set over the gamma-ray peak in the time spectrum and finally analysed by the pulse height analyser.

The complete electronic system is shown in Figure (3.24)

3.5.4. Energy Scale Calibration

The radioactive sources listed below were used to calibrate the energy scale, the circuit used for the calibration is that shown in Figure (3-23) , with the discriminator level set at minimum.

Source	Gamma-ray Energy (MeV)
^{137}Cs	0.662
^{22}Na	0.511, 1.28
^{60}Co	1.173, 1.332
Am-Be	4.43 (3.92, 3.41 escape peaks)

Table (3-4) List of radioactive sources used for energy scale calibration.

A linear calibration relating the channel number to the gamma-ray energy was obtained .

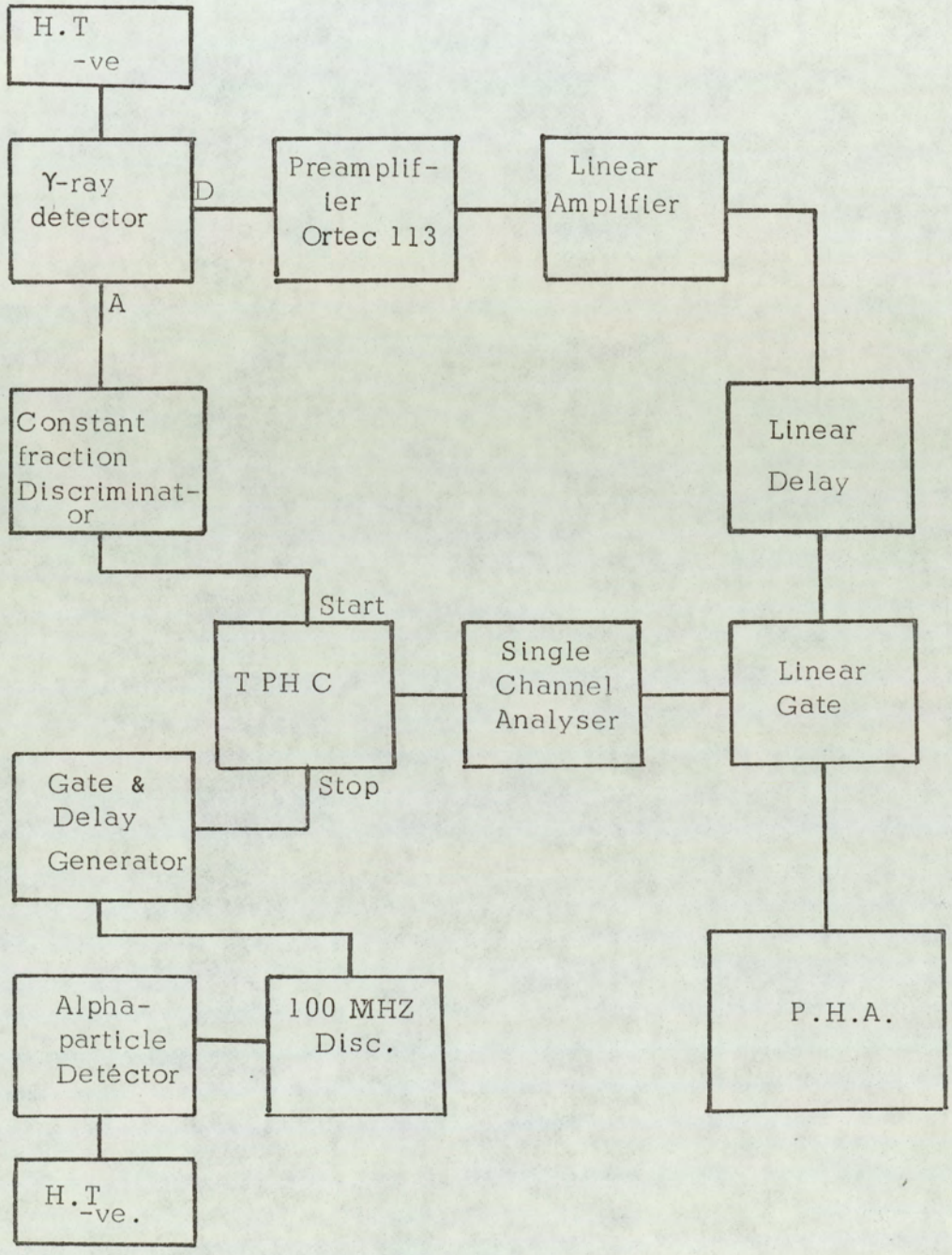

Figure (3-24) The complete electronic systed used to accumulate the γ-ray energy spectra.

3.5.5. The Energy Resolution :-

The energy resolution of sodium iodide detector is measured by the peak to valley ratio obtained in the energy spectrum of ^{60}Co. The energy resolution depends on the crystal size and the photomultiplier tube employed. The detector used in the present work employed a 76.2 x 76.2mm NaI (TI) crystal optically coupled via a 100 mm long converging light pipe of perspex to a 56 AVP photomultiplier tube which has a 55 mm (2") diameter photocathode. The system achieved a peak to valley ratio of 1.17 : 1 as shown in Figure (3.25). A full account of the gamma-ray detection system is given in Chapter (4).

3.5.6. The Energy Spectrum

The complete electronic system used to accumulate the gamma-ray energy spectra is shown in Figure (3.24). The single channel analyser was set such that only the pulses in the γ -ray peak in the time spectrum produces output pulses from this unit to open the linear gate, thus pulses due to neutrons are cut-out anddo not contribute to the background except in random coincidences.

The number of incidentneutrons was obtained by counting the associated alpha particle pulses on a scaler, at the same time, the gamma-ray energy spectrum was accumulated on the pulse height analyser. The process is then repeated for the same alpha count (total) with the sample removed and the P.H.A. in the subtract mode in order to subtract the background.

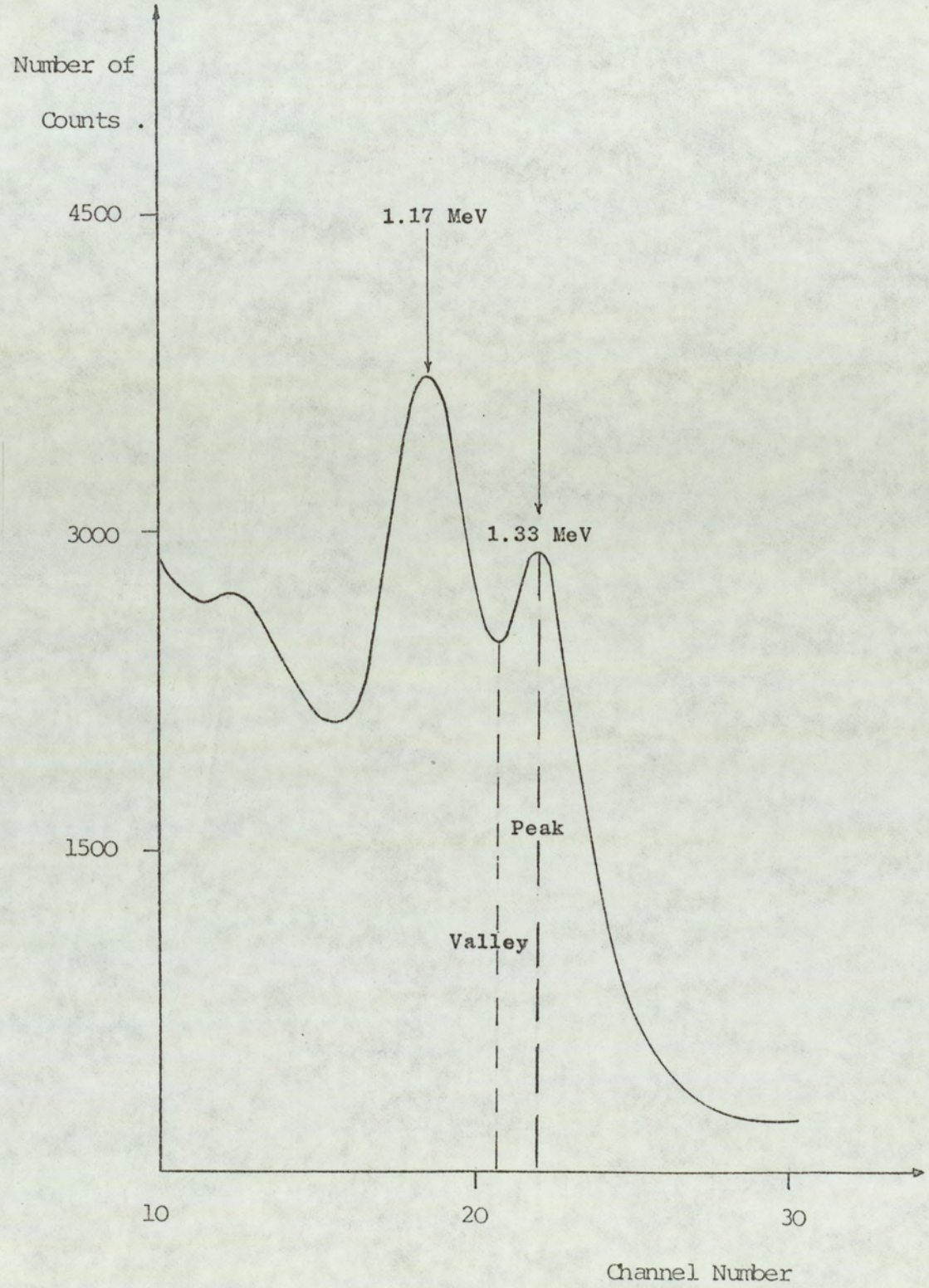

Figure (3.25) Gamma-ray spectrum from Co-60 source showing the Peak-to-Valleyratio .

The process is repeated until the number of counts in the accumulated energy spectra is high enough to reduce the statistical error to an acceptable level.

The gain of the system was checked between each run and there was no appreciable shift in the gain over a period of 12 hours.

CHAPTER FOUR

GAMMA-RAY INTERACTIONS AND DETECTION

INTRODUCTION

A gamma-ray photon is uncharged and creates no direct ionization or excitation of the material through which it passes, the gamma-ray detection is therefore, critically dependent on causing the gamma-ray photon to undergo an interaction that transfers all or a part of the photon energy to the electron in the absorbing material. The photon interactions in the context of their influence on the response of gamma-ray detectors are discussed in the following sections of Part I of this Chapter, while Part II, deals with the gamma-ray detection system.

PART 1

4.1 Interaction of gamma-rays with Matter

Although a large number of possible interaction mechanisms are known for gamma-rays in matter, only three major types play an important role in radiation measurements, namely, photoelectric absorption, Compton Scattering and Pair Production. All these interactions lead to the partial or complete transfer of the gamma-ray photon energy to electron energy. The result of this energy transfer is that the photon either disappears entirely or is scattered through a large angle losing a large fraction of its energy. The behaviour is in marked contrast to charged particle behaviour which slow down gradually through continuous, consecutive interactions with many absorber atoms.

4.1.1 Photoelectric Absorption :

The photoelectric absorption is an interaction in which the incident photon gives all of its energy to one of the atomic electrons; the gamma-ray photon disappears and the electron called "Photo-electron" is produced with an energy E_e given by

$$E_e = h\nu - E_b \qquad (4\text{-}1)$$

where $h\nu$ = the incident photon energy and E_b is the binding energy of the electron in its original shell.

For typical gamma-ray energies the photoelectron is most likely to emerge from the K-shell for which typical binding energies range from a few eV for low atomic number (Z) materials and tens of KeV for materials with higher atomic number, for example, the binding energy E_b for K-shell electron in hydrogen is 13.6 eV and in neon E_b = 20 KeV.

The vacancy created in the electron shell as a result of the photoelectron emission is quickly filled by electron rearrangement. In the process, the binding energy is librated either in the form of a characteristic X-ray or Auger electron. The characteristic X-ray may travel some distance (typically < 1 mm) before being absorbed through photoelectric interactions with less tightly bound electron shells of the absorber atoms.

The photoelectric process is the predominant mode of interaction of gamma-rays (or X-rays) of relatively low energy (400KeV) and it is enhanced for absorber materials of high atomic number (Z) An approximation for an analytical expression for the probability of photoelectric absorption per atom over all ranges of E_γ and Z is given by

$$\tau \simeq (\text{Constant}) \times \frac{Z^n}{E_\gamma^{\,3}} \qquad (4\text{-}2)$$

where n varies between 4 and 5 over the gamma-ray region of [60] interest. The severe dependence of the photoelectric absorption probability on the atomic number of the absorber is a primary reason for the predominance of high-atomic number constituents in many detectors for gamma-ray spectroscopy and in gamma-ray shields.

Photoelectric absorption is an ideal process for measuring the energy of the incident gamma-ray, the total electron kinetic energy equals the incident gamma-ray energy. For mono-energetic gamma-rays, the differential distribution of electron kinetic energy for a series of photoelectric absorption events will be a simple sharp gaussian as shown below in Figure (4-1). The single peak appears at a total electron energy corresponding to the energy of the incident gamma-rays.

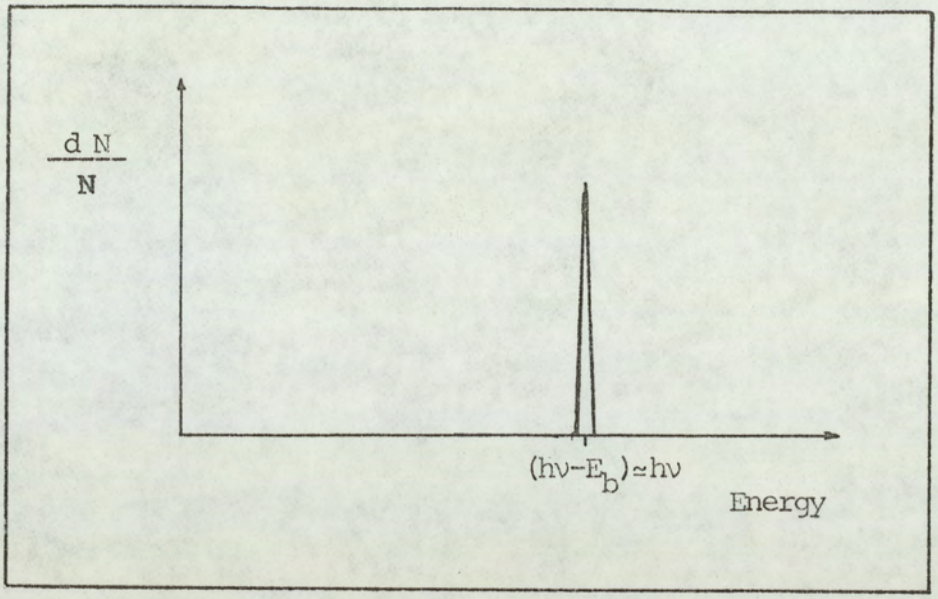

Figure (4-1) The pulse height spectrum from mono-energetic gamma-ray source as a result of photoelectric absorption process.

4.2 Compton Scattering

Compton scattering is the predominant interaction mechanism for gamma-ray energies typical of radio-isotope sources (0.5-2 MeV), and it takes place between the incident gamma-ray photon and an unbound or free electron in the absorbing material.

As it can be seen in Figure (4-2), the incident photon is deflected through an angle θ with respect to its original direction after transferring some of its energy to the electron which is assumed to be initially at rest, and is then known as the recoil electron.

Because all angles of scattering are possible, the energy of

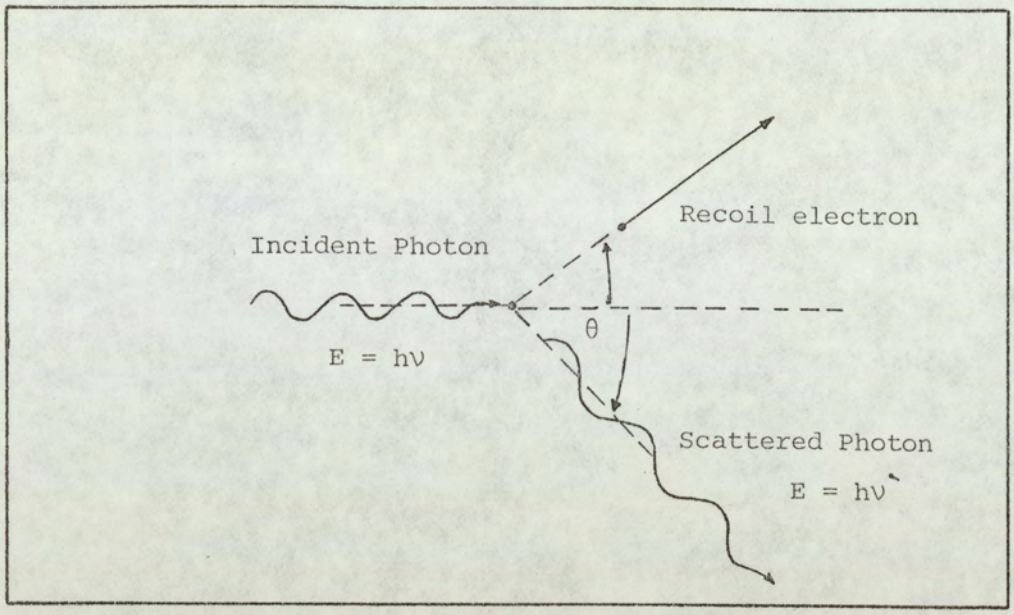

Figure (4-2) A sketch illustrating the Compton Scattering.

the recoil electron can vary from zero to a large fraction of the gamma-ray energy. The expressions relating the energy transfer and the scattering angle for any given interaction can be derived by writing simultaneous equations for the conservation of energy and momentum using the notation defined in Figure (4-2), it can be shown that

$$h\nu' = h\nu \Big/ \left(1 + \frac{h\nu}{m_o C^2} (1 - \text{Cos } \theta) \right) \quad (4\text{-}3)$$

where $m_o c^2$ is the rest mass energy of the electron = 0.511 MeV. Figure (4-3) shows the variation of the scattered gamma-ray energy with the Scattering angle.

The energy of the recoil electron is therefore

$$E_e = h\nu - h\nu' = h\nu \left(\frac{(h\nu / m_o c^2)(1 - \text{Cos } \theta)}{1 + (h\nu / m_o c^2)(1 - \text{Cos } \theta)} \right) \quad (4.4)$$

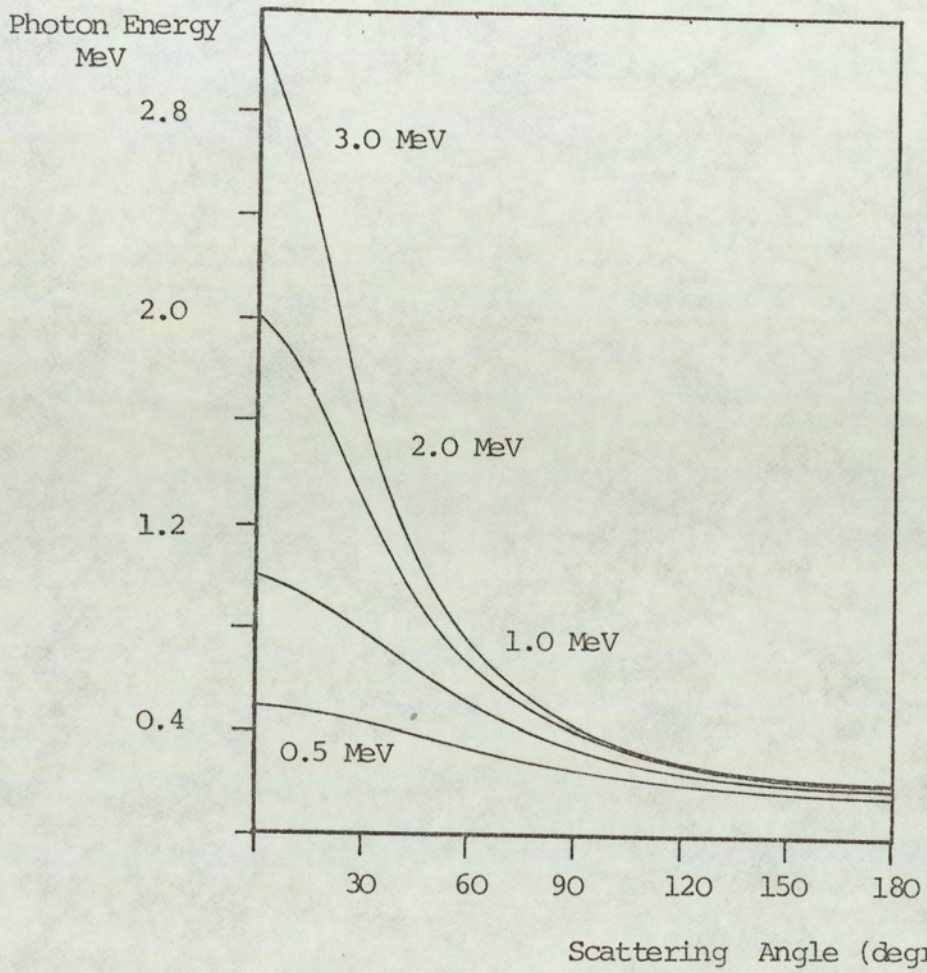

Figure (4-3) Variation of scattered gamma-ray energy with scattering angle .

The minimum energy transfer occurs for the case of grazing angle scattering in which $\theta = O$ where equations (4-3) and (4-4) predict $h\nu' = h\nu$ and $E_e = O$ while the maximum energy transfer occurs for $\theta = \pi$ and using the same equations yield

$$\left.\begin{aligned} h\nu'_{(min)} &= \frac{h\nu}{1 + 2\,(h\nu / m_o c^2)} \quad (a) \\ E_{e\ (max)} &= h\nu\left\{\frac{2\,h\nu / m_o c^2}{1 + 2\,h\nu / m_o c^2}\right\} \quad (b) \end{aligned}\right]_{\theta=\pi} \qquad (4\text{-}5)$$

In normal circumstances, all scattering angle will occur in the detector, therefore, a continuum of energies can be transferred to the electron ranging from zero upto a maximum energy predicted by equation (4-5-b).

The angular distribution of scattered gamma-rays is predicted by the Klein-Nishina formula for the differential scattering cross section $(d\sigma / d\Omega)$:

$$\frac{d\sigma}{d\Omega} = r_o^2 \left(1/(1 + \alpha\,(1-\cos\theta))\right)^3 \times \left(\tfrac{1}{2}\,.\,(1 + \cos^2\theta)\right) \times \left\{1 + \frac{\alpha^2\,(1-\cos\theta)^2}{(1+\cos^2\theta)\,(1+\alpha\,(1-\cos\theta))}\right\} \qquad (4\text{-}6)$$

where $\alpha = (h\nu / m_o c^2)$ and r_o is classical electron radius ($r_o = 2.82 \times 10^{-13}$ cm).

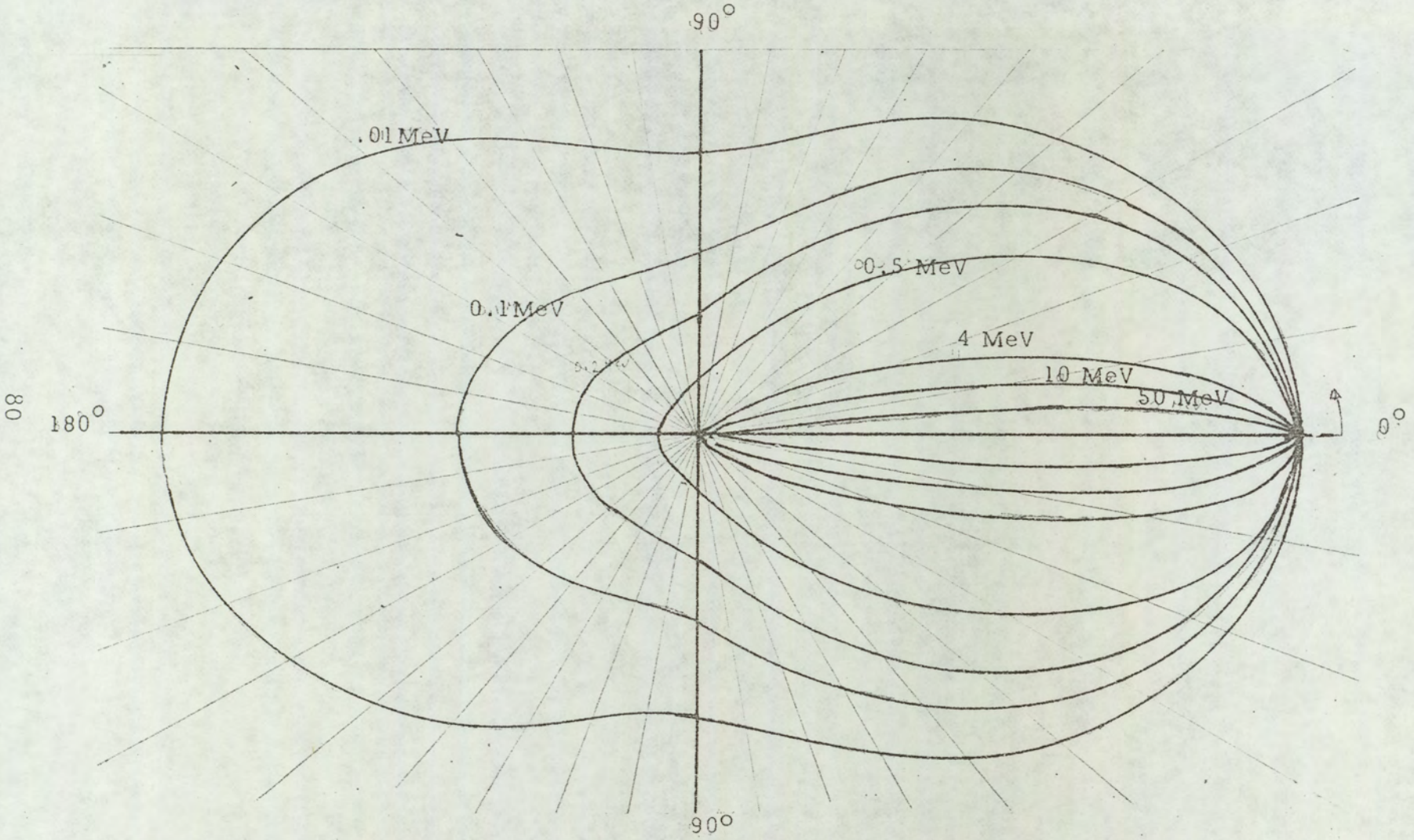

Figure (4.4). A polar plot of the number of photons (incident from the left) Compton scattered into a unit solid angle at the angle θ, the curves are shown for the incident initial energies.

The above angular distribution was evaluated for a set of gamma-ray energies and the result is shown in Figure (4-4) which illustrates the strong tendency for forward scattering at high values of the gamma-ray energy.

Figure (4-5) shows the shape of the distribution of the recoil electrons predicted by Klein-Nishina cross-section (equation 4-6) for several values of incident gamma-ray energy.

For any one specific gamma-ray energy, the electron energy distribution has the general shape shown in Figure (4-6).

The energy difference between the maximum Compton recoil electron energy and the incident gamma-ray energy is given by

$$E_c = h\nu - E_e \Big\}_{\theta=\pi} = h\nu / [1 + 2 (h\nu/m_o c^2)] \quad (4\text{-}7)$$

For $h\nu >> (m_o c^2/2)$, this difference tends towards a constant value given by

$$E_c = \frac{m_o c^2}{2} = 0.256 \text{ MeV} \quad (4\text{-}8)$$

The above analysis is based on the assumption that Compton scattering involves free electrons which is not the case in actual detector materials where the binding energy of the electron prior to the scattering process can have a measurable effect on the shape of the Compton continuum especially for low incident gamma-ray energies. These effects involve a rounding-off of the rise in the continuum near

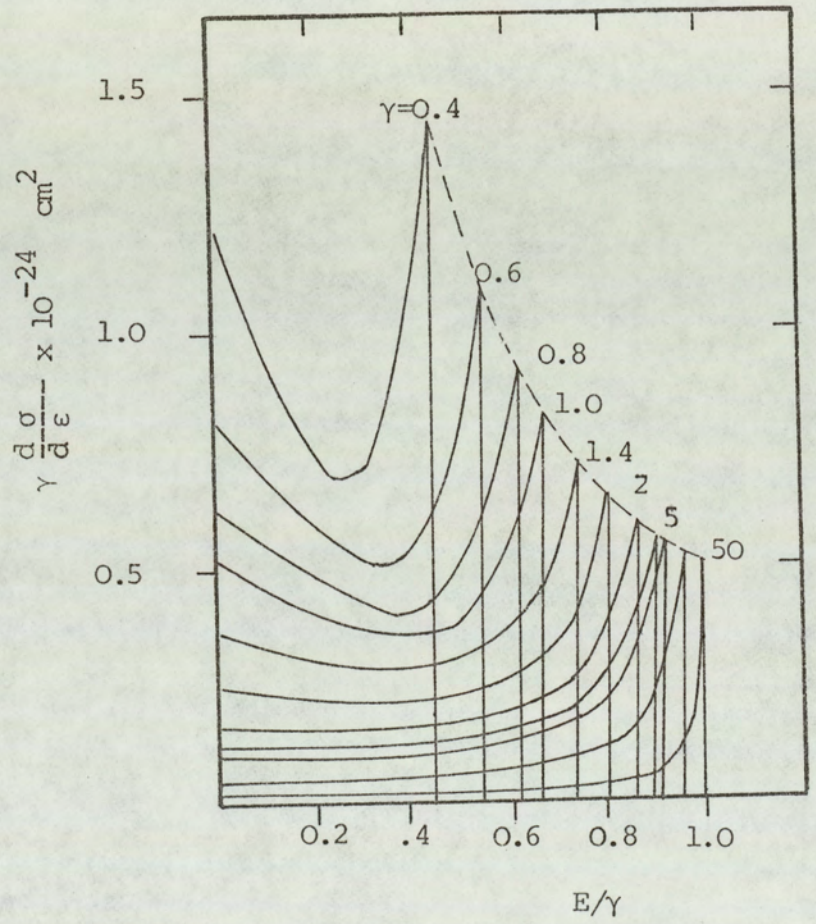

Figure (4-5) The shape of Compton continuum for various gamma-ray energies[61].

$$\gamma = E_\gamma / m_o c^2$$

$$\varepsilon = E_e / m_o c^2$$

its upper extremity and the introduction of a finite slope to the abrupt drop of the Compton edge. These effects are often masked by the finite energy resolution of the detector, but can be evident in the spectra from detectors with high energy resolution.

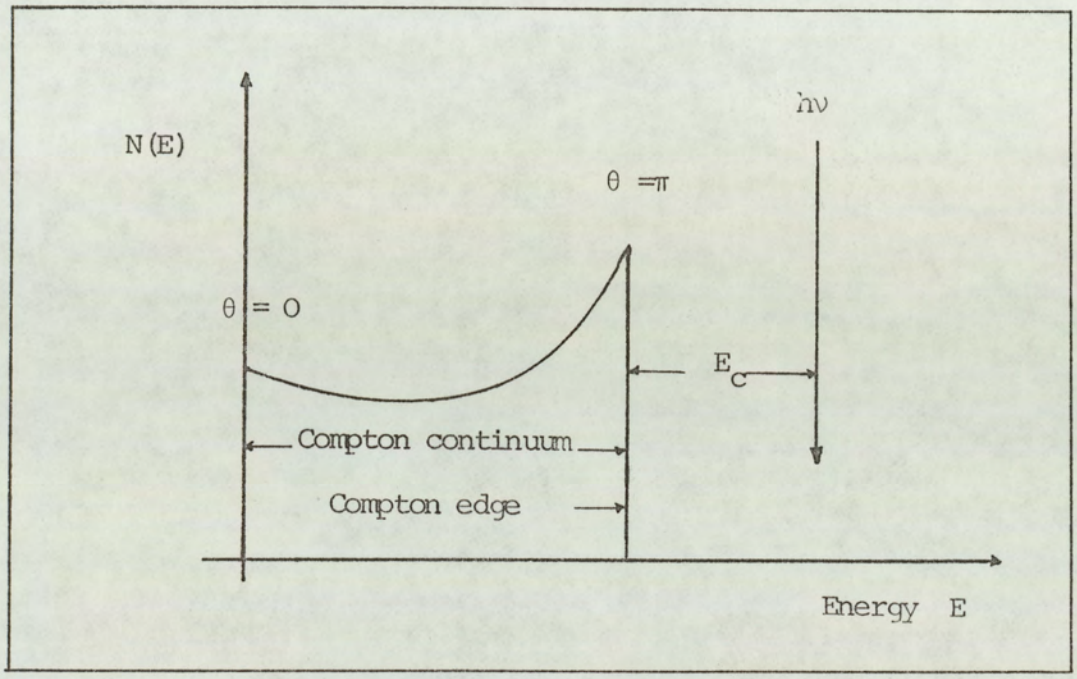

Figure (4-6) The general shape of the electron energy distribution for Compton scattering

4.3 Pair Production

The pair production process corresponds to the gamma-ray giving all its energy to the creation of an electron-positron pair and it must occur in the field of a nucleus of the absorbing material (in order to conserve the momentum of the system).

Because an energy of $2 m_o c^2$ is required to create the electron-positron pair, the pair production process has a threshold energy of

1.022 MeV below which it cannot take place. For gamma-ray photons with energy above the threshold, the excess energy appears as kinetic energy shared by the electron-positron pair. The process therefore essentially converts the incident gamma-ray photon into an electron and a positron with kinetic energies.

$$E_{e^-} + E_{e^+} = h\nu - 2 m_o c^2 \qquad (4\text{-}9)$$

For typical gamma-ray energies, both the electron and the positron travel a few millimeters at most before losing all their kinetic energy to the absorbing medium. The sketch below shows a plot of the total charged particle (electron + positron) kinetic energy created by the incident gamma-ray.

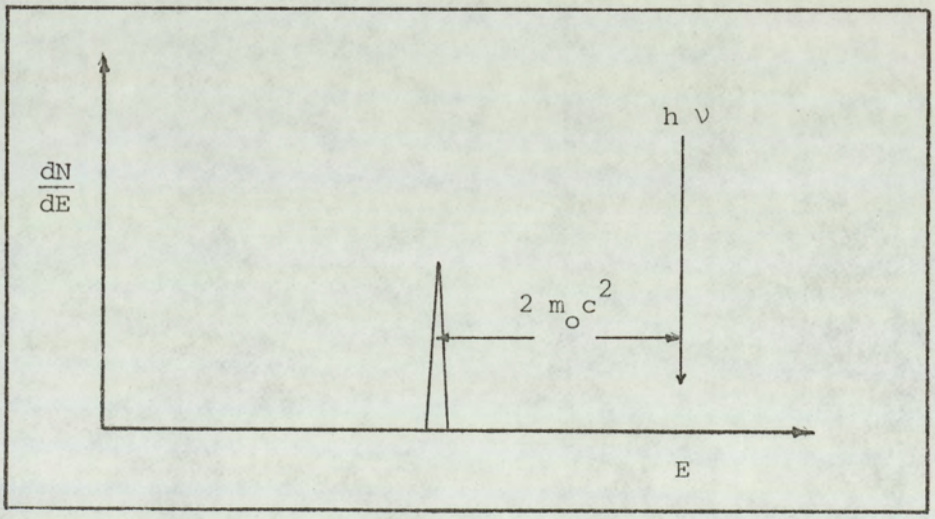

The pair production is complicated by the fact that the positron is an unstable particle, and once its kinetic energy becomes very low (comparable to the thermal energy of normal electrons in the absorbing material), the positron will annihilate with a normal electron and at this

point both disappear to be replaced by two annihilation gamma-ray photons each of energy of 0.511 MeV. ($m_o c^2$).

The annihilation radiation appears in virtual coincidence with the original pair production interaction since the time required by the positron to slow down is very small.

There is no simple expression for the probability of pair production per nucleus, but is magnitude varies approximately as the square of the absorber atomic number (Z) and rises rapidly as a function of energy above the threshold in the region below 10 MeV.

The relative importance of the three processes described above for different absorber materials and gamma-ray energies is illustrated in Figure (4-7), the lines at the left represent the energy at which photoelectric absorption and Compton scattering are equally probable as a function of the absorber atomic number. The line on the right represents the energy at which the Compton scattering and the pair production are equally probable. Thus, three areas are defined on the plot within which one of the processes is predominant.

Figure (4-8) shows the scattering and absorption cross-sections per electron for light and heavy elements as a function of energy.

4.4. The attenuation of gamma-rays in matter

As discussed in the preceeding sections, the cross-sections for gamma-ray interactions are determined primarily by the atomic number of

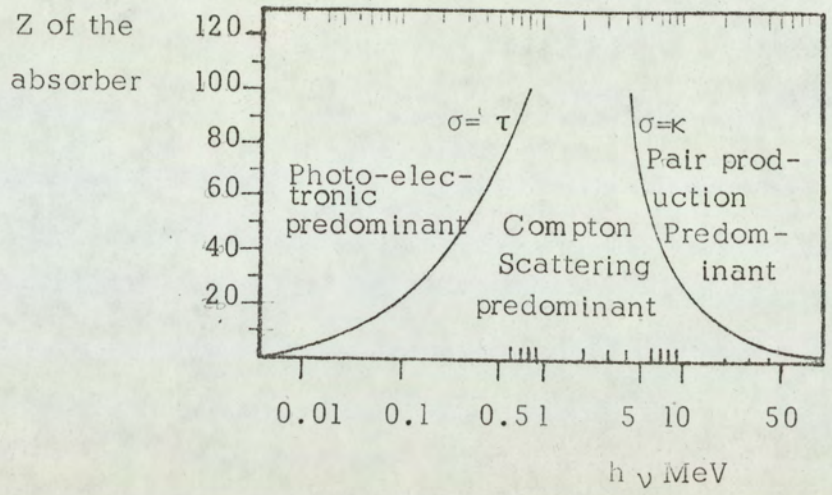

Figure (4-7) The relative importance of the three major types of gamma-ray interaction.

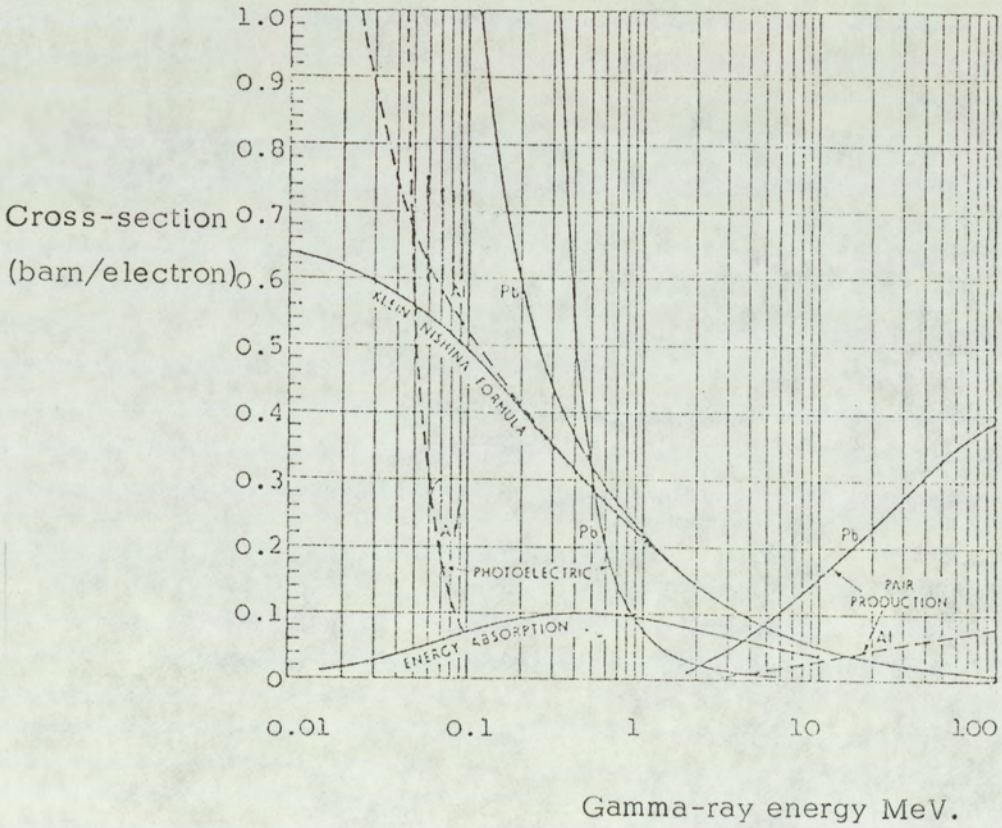

Figure (4-8) Scattering and absorption cross-sections per electron for light and heavy elements as function of gamma-ray energy.

the absorber, and the gamma-ray energy.

The total cross-section for gamma-ray interaction is the sum of the cross-sections for the above mentioned processes, i.e.

$$\sigma = \sigma_{pe} + \sigma_{c} + \sigma_{pp} \qquad (4\text{-}10)$$

A macroscopic cross-section can be defined by multiplying in equation (4-10) by the atom density N which is the number of absorber atoms per unit volume, and traditionally this macroscopic cross-section is called the attenuation coefficient of the material and denoted by μ . Thus,

$$\mu = N\sigma = \mu_{pe} + \mu_{c} + \mu_{pp} \qquad (4\text{-}11)$$

where μ is the total attenuation coefficient and has units (unit length $^{-1}$) and μ_{pe}, μ_{c} and μ_{pp} are the attenuation coefficients of the three interaction processes.

Use of the linear attenuation coefficient is limited by the fact that it varies with the density of the absorber even though the material is the same, so it is more convenient to introduce the mass absorption coefficient defined as the linear attenuation coefficient per unit density ie., (μ/ρ) and given by

$$(\mu/\rho) = \left(\frac{\mu_{pe}}{\rho}\right) + (\mu_{c}/\rho) + (\mu_{pp}/\rho) \qquad (3\text{-}12)$$

where ρ is the density of the absorber.

Since μ and ρ have units of (length $^{-1}$) and (mass/length^3) respectively, it follows that (μ/ρ) has the units of (length^3/mass) in the c.g.s. system the units of (μ/ρ) are (Cm^2/gm) while in the M.K.S system it has the units of (m^2/kgm).

Extensive tabulation of the linear and mass attenuation coefficients for various elements and materials can be found in the literature [3,4,62,63]. Figures (4-9) and (4-10) show the mass attenuation coefficients for some elements in the gamma-ray energy range (0.01 - 100 MeV). The mass attenuation coefficient of a compound or mixture of elements is given by

$$\left(\frac{\mu}{\rho}\right)_{\substack{\text{Mixture}\\ \text{or compound}}} = \sum_i w_i \left(\frac{\mu}{\rho}\right)_i \qquad (4\text{-}13)$$

where w factors represent the weight fraction of element i in the compound or mixture. For example, the mass attenuation coefficient of water (H_2O) is given by

$$(\mu/\rho)_{H_2O} = \frac{2}{18}(\mu/\rho)_H + \frac{16}{18}(\mu/\rho)_O \qquad (4\text{-}14)$$

In the case of perfect geometry, i.e. narrow beam of monoenergetic gamma-rays incident onto an absorber with attenuation coefficient μ, if I_o is the intensity (gamma-rays per unit area per unit time) of a monoenergetic gamma-ray beam striking a target of thickness x, then the intensity of the photons that penetrate the target without having a collision is given by

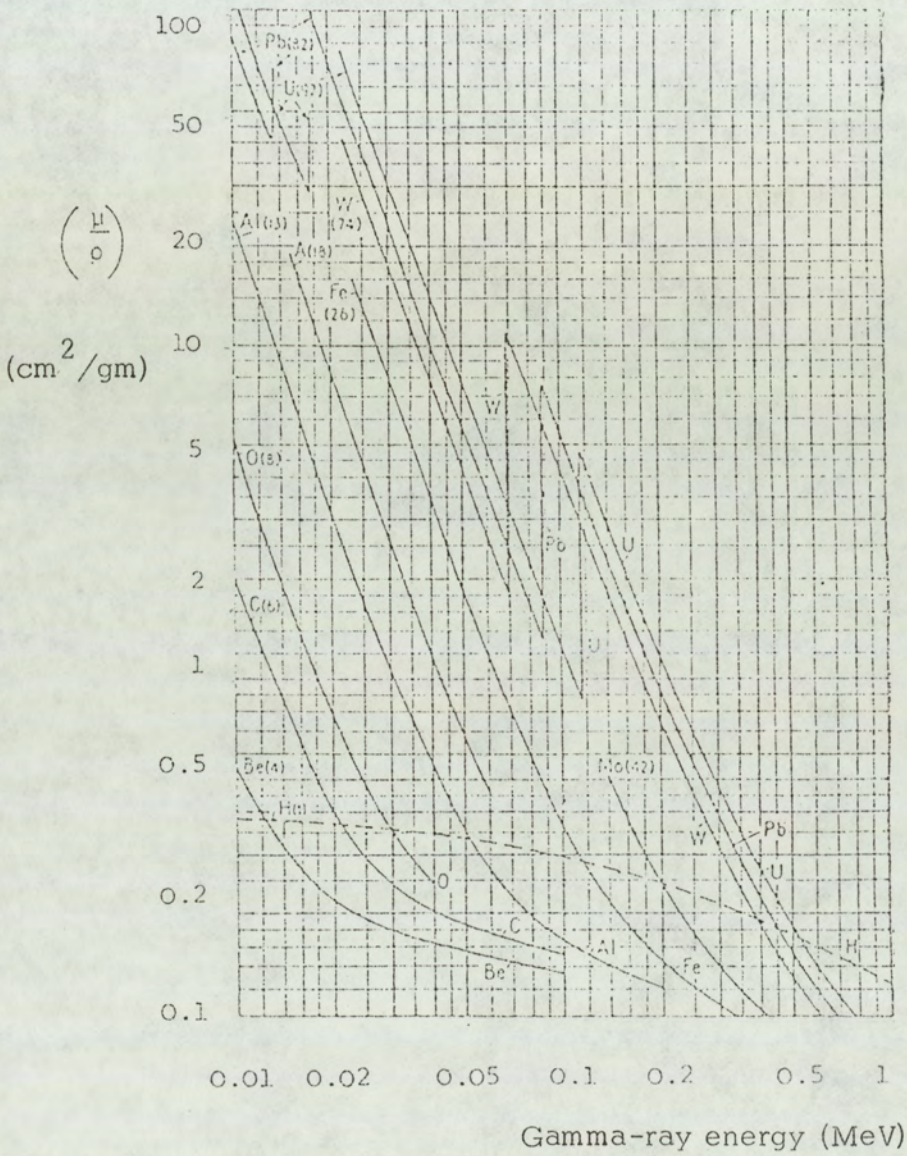

Figure (4-9) Mass absorption coefficients as as a function of atomic number and gamma-ray energy for

(E_γ = 0.01 - 1 MeV)

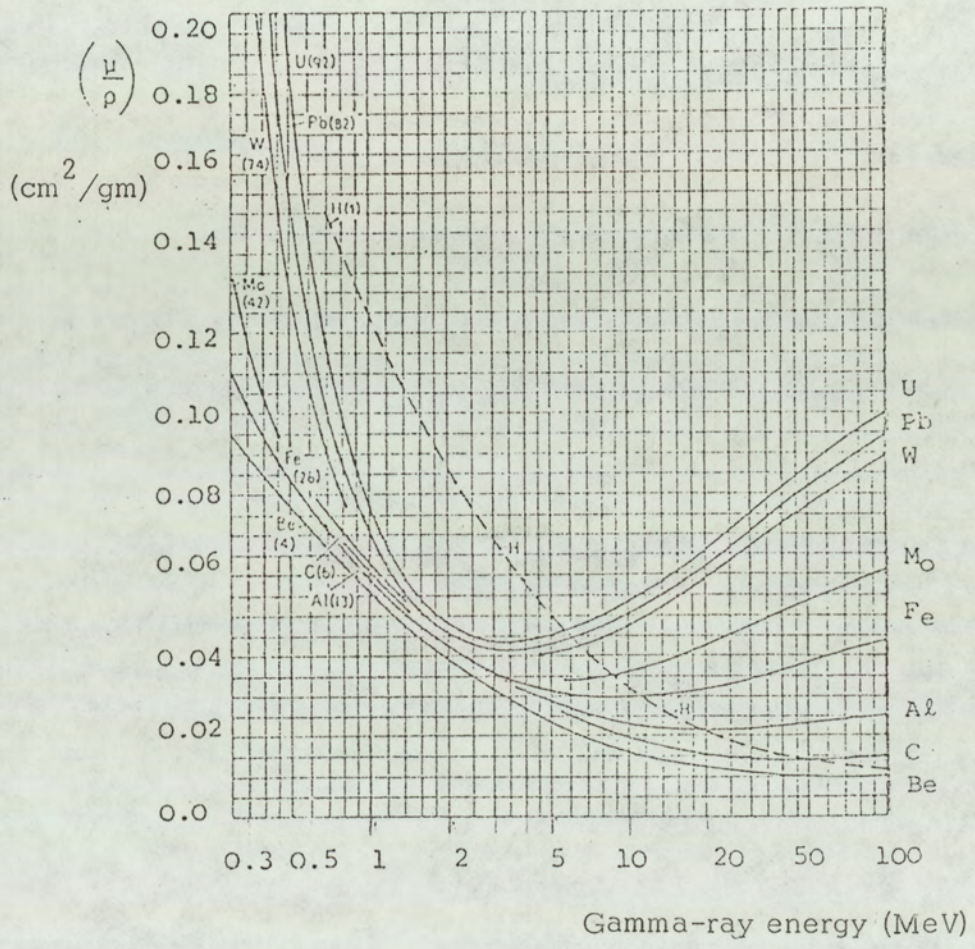

Figure 4-10 Mass absorption coefficient as a function of atomic number and gamma-ray energy for

E_γ = 0.3 - 100 MeV

$$I = I_o \quad e^{-\mu X} \tag{4-15}$$

or in terms of the mass attenuation coefficient

$$I = I_o \quad e^{-(\mu/\rho)\,\rho X} \tag{4-16}$$

The quantity (ρ X) is known as the mass thickness of the absorber and is equal to the number of (unit mass) contained in (unit area) of the target using the M.K.S units (ρX) has the units of (Kgm/meter ^{2}).

Under poor geometry (broad beam), the attenuation law becomes

$$I = I_o \quad B\,(X, E_\gamma) \cdot e^{-(\mu/\rho).\rho X} \tag{4-17}$$

where the factor $B(X, E_\gamma)$ is called the build-up factor which is dependent on the type of gamma-ray detector used because this will affect the relative weight given to the direct and scattered gamma-rays. The build-up factor also depends on the specific geometry of the experiment. However, as an approximate rule, the build-up factor for a thick slab of material (absorber) tend to be about equal to the thickness of the absorber measured in units of mean free path [62] of the incident gamma-rays, provided that the detector responds to a broad range of gamma-rays.

PART II

4.5. Gamma-Ray Detection

The properties to be considered in the choice of a suitable gamma-ray detector are, the detection efficiency, the spectral response,

the energy resolution, the response time and in the case of the study of gamma-rays produced by the inelastic scattering of neutrons, an additional proerty to be considered is the neutron response.

4.5.1. Possible gamma-ray detectors

The two most commonly used detectors for gamma-ray spectroscopy are :

A- The sodium iodide (thallium activated) scintillation detector and B- the lithium drifted germanium. (GeLi) semiconductor detector.

A detailed discussion of the properties of each of these two detectors can be found in the references[60,62,64] since the gamma-ray yield from the inelastic scattering of neutrons is small as estimated from the calculated values of the reaction rate, the detection efficiency was considered of a prime importance in the detector choice. The detector response and sensitivity to neutrons was the second major property to be considered because of the high neutron flux used throughout the experiments. The two detectors mentioned above are considered briefly from the view point of detection efficiency and neutron response.

a. Detection efficiency :

As the interaction processes which lead to the subsequent gamma-ray detection are strongly dependent on atomic number (Z), it follows that the sodium iodide crystal containing iodine with atomic

number 53 is more efficient than the Ge-Li detector containing germanium which has an atomic number of 32.

The photoelectric, Compton and pair production cross-sections are proportional to $N Z^5$, $N Z$ and $N Z^2$ respectively, so as the interaction probability (cross-section) are on average proportional to $N Z^2$, it follows that for the same detector size the ratio of the detection efficiency of the Na I (Tl) detector to that of Ge-Li detector is $\frac{N 1}{N 2} \left(\frac{53}{32} \right)^2$. On consideration of the number of atoms per unit volume (N), which is larger for NaI, and the fact that Ge-Li detectors are manufactured in small sizes only (maximum size 100 cm^3), then the sodium iodide produces the better detection efficiency. The detector manufacturers quote the Peak efficiency of a 30 cm^3 Ge (Li) detector as being 3% that of a 7.62 cm (3") NaI (Tl) crystal for a point 1.33 MeV gamma-ray source 25 cm from the detector face.

b. Neutron response

Both the NaI (Tl) and (Ge-Li) detectors are sensitive not only to gamma-rays, but also to neutrons which are detected by the ionising products of a neutron reaction. The neutron response is very energy dependent because of the variation of the neutron reaction cross-section with energy. Although the neutron source produces nearly monoenergetic neutrons, it is important to consider the detector response to a wide spectrum of neutron energies because the neutron energies can be greatly modified by the scattering sample and the detector shielding material.

b.1. The neutron response of NaI (Tl) detector

For neutrons with energies below 0.5 MeV, the neutron response is dominated by the radiative capture process. In NaI(Tl) the major response is from the radiative capture in iodine where the ^{128}I is formed. ^{128}I has a high level density so the prompt gamma-ray emission consists of many gamma-rays due to cascade transitions between the many levels. The resulting pulse height spectrum is almost continuous with a maximum pulse height corresponding to the binding energy of the neutron in the ^{128}I at 6.71 meV.

Less than 10% of the slow neutron response of NaI (Tl) is due to capture in the sodium [50]. The sodium capture gamma-rays has been observed by Groshev [67], as in the case of iodine, the spectrum is almost continuous with a maximum energy of 6.96 MeV which is the neutron binding energy in ^{24}Na. Table (4-1) gives the radiative capture cross-sections at two neutron energies for the NaI (Tl) crystal constituents taken from the barn book [66].

Table (4-1) Radiative capture cross-section at two neutron energies for iodine, sodium and thallium

Element	$\sigma(n, \gamma)$	
	E_n = 0.025	E_n = 0.1 MeV
^{23}Na	0.525 b	1.3 b
^{127}I	7.000 b	0.43 b
^{169}Tl	3.500 b	-

For neutron energies above 0.5 MeV, the radiative capture reaction becomes less significant, and the predominant reaction is the inelastic scattering. This (n, nγ) process in NaI (Tl) has been studied by Day [2] and Van Loef [65] for neutron energies in the range 0.52 to 3.15 MeV. The Peaks in the spectra correspond to the excited levels of sodium and iodine. As the neutron energy increases, new peaks arise as higher levels are excited. For neutron energies of $\geq$ 10 MeV, the pulse height spectrum becomes almost continuous due to the large number of levels excited. Throughout the energy range the inelastic scattering cross-section for iodine is larger than that for sodium.

At higher energies, charged particle reaction and the (n, 2n) reaction becomes energetically possible. The cross-sections for the main reactions at different neutron energies is shown in Table 4-2.

Table 4-2 The cross-sections for main reactions in iodine and sodium at neutron energies (14-14.8 MeV)

Neutron Energy	$^{127}_{53}I$			$^{23}_{11}Na$		
	(n,2n)	(n,α)	(n,p)	(n,2n)	(n,α)	(n,p)
14	1.6	0.800mb	0.5 mb	13.8 mb	29 mb	0.05 b
14.1		1.39 mb	17 mb		147 mb	
14.2	1.95b					
14.4	1.65		11.7 mb			
14.5	1.12b	1 mb		20 mb	180 m	33.9 mb
14.6	1.487b			49.5 mb		
14.7	1.128b				141 mb	41.0 mb
14.8	1.660b	1.8 mb				45.0 mb

Fast neutron interactions in the NaI (Tl) scintillator are then dominated by the inelastic scattering process giving rise to prompt detection, but at both ends of the energy range 0.025 to 15 MeV, reactions take place introducing long lived activity in the crystal. At the lower energy end, the induced activity is mainly due to the (n,γ) reaction with iodine which produces unstable ^{128}I which has a 25 min. half life. It can decay to ^{128}Xe by β^- emission or by electron capture of β^+ emission, to ^{128}Te. At the high energy end, the induced activity results from the (n, 2n) reaction and the (n, p) reaction with the iodine. The ^{127}I (n, 2n) reaction produces ^{126}I which has a 13 day half life decaying to ^{126}Te by β^+ emission and to ^{126}Xe by β^- emission. The ^{127}I (n,p) reaction produces ^{127}Te with a half life of 9.3 hrs and decays to ^{127}I by β^- emission.

b.2. <u>The neutron response of the Ge(Li) detector</u> :-

For the Ge(Li) detector, the situation is similar to that in NaI(Tl) detector. The (n, γ) cross-section for germanium is $(2.30 \pm .2)$ b for thermal neutrons[68] and there is a little information on the variation of this cross-section with energy.

The energy released in a single capture reaction in each of the germanium isotopes is about 9 MeV, and due to the density of excited nuclear levels, many gamma-rays are emitted in a single capture reaction.

The main fast neutron detection processes are by the $(n, n'\gamma)$,

(n,p) and (n,α) reactions. All the germanium isotopes have closely spaced excited nuclear levels and consequently, very many different gamma-rays are produced by the inelastic scattering of neutrons of only a few MeV. Study of the (n, α) reaction in germanium by Aitken and Dixon [69] by bombarding a Ge(Li) detector with 14 MeV neutrons revealed that the pulse height spectrum was almost continuous up to energies of about 13 MeV. The spectrum extended to approximately 17 MeV because the ^{73}Ge (n,α) ^{70}Zn has a positive Q-value of 3.79 MeV. There is little information available on the cross-sections of these reactions, the non-elastic cross-section has been measured as 1.97 barns for 3.66 MeV neutrons [80]. Chagman et al., [70] investigated the response of a Ge(Li) detector to monoenergetic neutrons in the range 1.2 to 16.3 MeV. Lines were observed that resulted from the inelastic excitation of four germanium isotopes as well as from the neutron excitation of other materials in the detector vacuum enclosure and cryostat. At neutron energies above 3 MeV, additional peaks were detected due to the neutron-induced charged particles created in reactions with germanium nuclei. A spectrum showing many of the neutron-induced peaks is given in Figure (4-11). The operation of any semiconductor detector depends on the near perfection of the crystalline lattice to prevent defects that can trap charge carriers and lead to incomplete charge collection. Any extensive use of these detectors, however, ensures that some damage to the lattice will take place due to the disruptive effect of the radiation being measured as it passes through

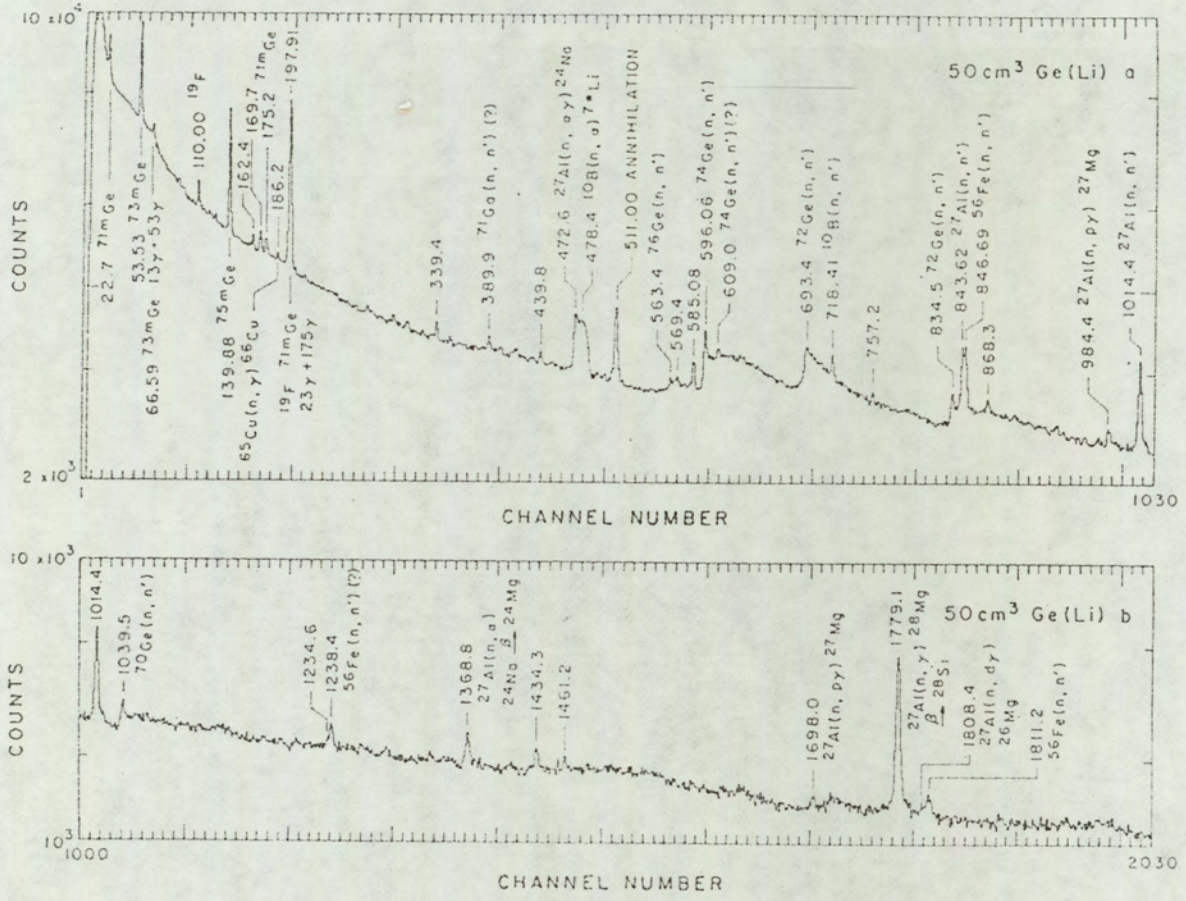

Figure 4-11 Prompt pulse height spectrum produced by fast neutron irradiation of a 50 cm^3 Ge(Li) detector [71]

the crystal. The radiation damage appears as a significant loss in the energy resolution and multiple peaking in the pulse height spectra recorded for monoenergetic particles. Furthermore the time characteristic of the detector may be degraded even at doses that are too low to show measurable spectral effects [73]. These effects are minor for lightly ionizing radiations (β and γ -radiations), but can become quite significant under typical conditions of use for neutron and heavy charged particles.

Exposure to fast neutron fluxes of about 3×10^{11} neutrons/cm^2 [74] is sufficient to lead to significant performance degredation. The principal effect of radiation damage is to increase the amount of hole trapping in the intrinsic region of the Ge(Li) detectors. Figure (4-12) illustrates the gradual broadening of measured gamma-ray peaks as the fast neutron exposure is increased.

Other experiments [75,76] confirm the general observation that significant performance degradation begins with a neutron fluence of approximately 10^9 neutron/cm^2. Procedures have been described in which the effect of radiation damage can be reversed [72,77] through annealing the damage by warming the detector and subsequent redrifting. This redrifting process is expensive and time consuming.

4.5.2. Choice of Detector

The most favourable property of the NaI(Tl) scintillator is its high detection efficiency, while the significant points favouring the

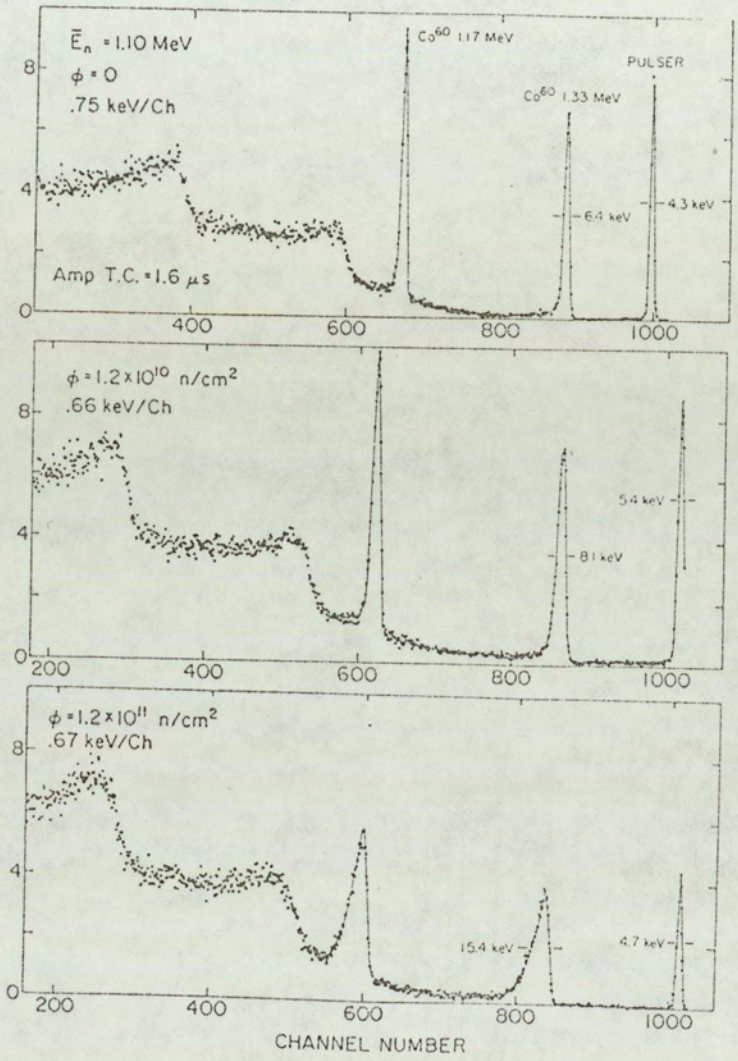

Figure 4-12. The deterioration of a Ge(Li) γ -spectrum with increasing neutron fluence, only the upper part of the spectrum is shown (62).

Ge-Li detector are its excellent energy resolution and fast rising output pulses well suited for fast timing.

Both detectors are sensitive to neutrons which also cause a build-up of activity in the detectors. The large reaction cross-section for iodine makes the NaI(Tl) the more sensitive of the two detectors to neutrons, however, the use of the time of flight technique reduces the neutron background to manageable proportions for the observation of the prompt gamma-rays emitted following the inelastic scattering of the 14 MeV neutrons.

As discussed in Section 4.5.1, the radiation damage suffered by the Ge-Li detector under fast neutron bombardment causes a severe effect on the energy resolution and the timing properties of this detector which are the major advantages of the Ge-Li detector. On the other hand, the gamma-ray yield from the scattering sample is relatively weak, so high detection efficiency is of prime importance to reduce the statistical (uncertainty) particularly for high energy gamma-rays.

It was decided to sacrifice energy resolution for high detection efficiency and the NaI(Tl) scintillation detector was chosen.

4.6. Sodium Iodide Scintillation Detector Design

The gamma-ray detector used in the present work employed a 76.2 mm x 76.2 mm NaI(Tl) crystal which was supplied by Nuclear Enterprises. Since a 76.2 mm photocathode tube is not manufactured,

the photomultiplier tube used was Mullard's 56 AVP tube with 50.8 mm diameter photocathode. This tube is a high gain linear focussed tube with good time resolution having an electron transit time spread of < 0.5 ns.

As the crystal used had a larger diameter than the photomultiplier tube, a perspex light pipe was used to ensure an efficient optical coupling. A 76.2 mm diameter rod of perspex was machined so that it tapered at one end to a diameter of 46 mm. The light pipe was 100 mm long and the angle of convergence was 9^{o}.

The performance of a photomultiplier tube, especially the focoused tubes with focussed dynode structure is sensitive to magnetic field as reported by Engstrom [78] and by Conner [79]. They have shown that even weak magnetic fields can cause a marked reduction in the gain of the tube. The earth's mangetic field is not troublesome if the tube is operated at a fixed position throughout the experiments, however, this is not so in the present case, so that shielding from the earth's magnetic field was essential for stable performance. The photomultiplier tube was placed in a mu-metal shield so that the first dynode stages were properly shielded.

The use of a mu-metal shield, besides giving optimum tube gain, gives minimum transit time spread. The 56 AVP tube is a high gain photomultiplier tube with a current gain $\geq 10^{8}$ capable of producing peak anode current between 500 and 1000 mA according to the

manufacturers.

The manufacturers recommended two voltage divider chains (a) has an equal voltage across the last twelve dynode stages and type (b) has progressively increasing voltage across the last nine dynode stages Voltage divider type (a) gives a higher gain but a higher anode current with better time characteristics than type (a) can be obtained with type (b). Divider type (b) reduces space charge effects around the later dynodes which are coupled with capacitors to stabilize the dynode potential and also provide a charge store when high electron current is produced.

A dynode chain of type (b) was used and it is shown in Figure (4-13). The current through the dynode chain was ~ 2.7 mA at an operating voltage of (-1750) volts. Two output signals were taken from the gamma-ray detector as shown in Figure (4-13). The timing signal was taken from the anode and the energy line pulses were taken from the 12^{th} dynode via a 50 Ω resistor.

Figure (4-13a) shows a photograph of the complete gamma-ray detector.

4.7 Detector Shielding

4.7.1. Principles of Neutron Shielding and Materials Used

As the NaI (Tl) scintillation detector is sensitive to neutrons, adequate detector shielding is required. In addition to the direct

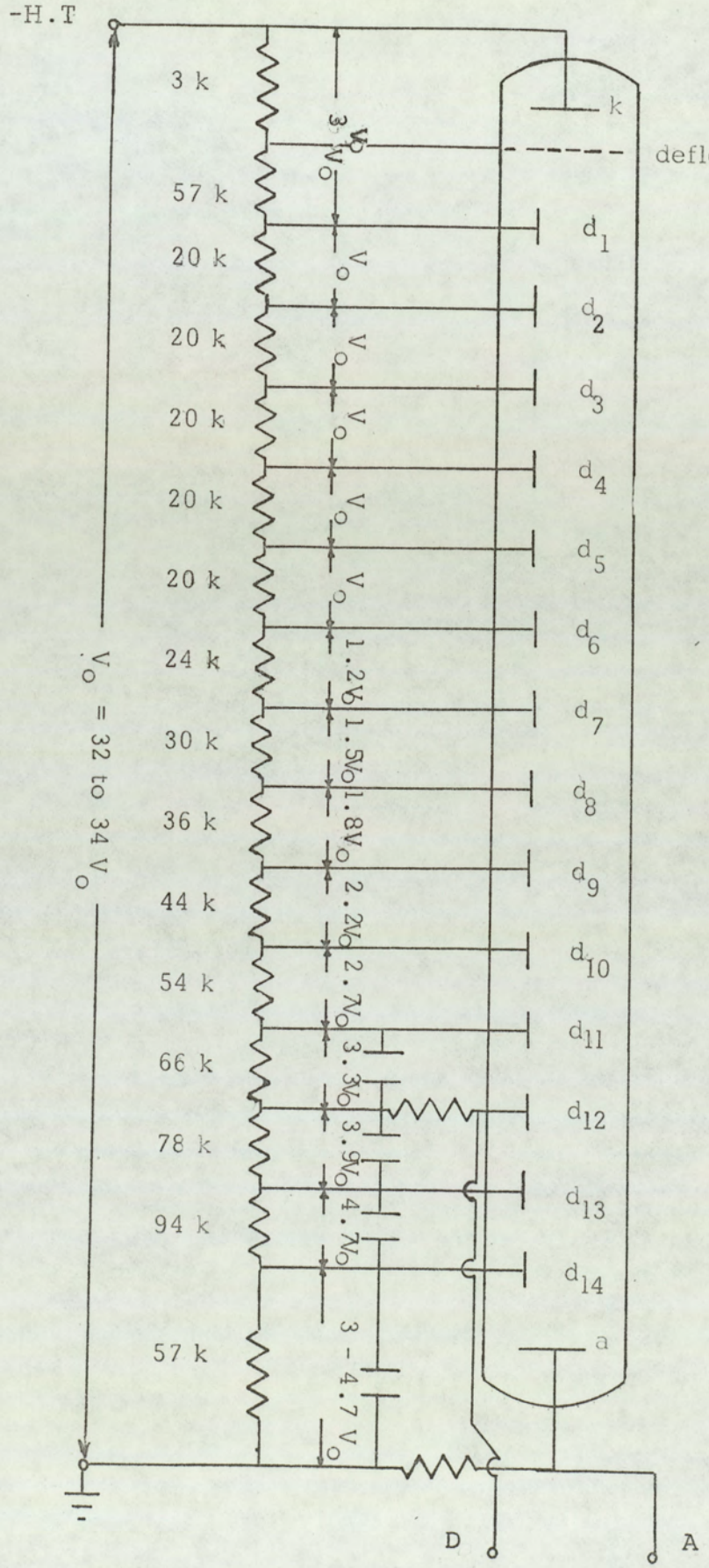

Figure (4-13) The dynode resistor chain used for the 56-AVP photomultiplier tube used in the gamma-ray detector .

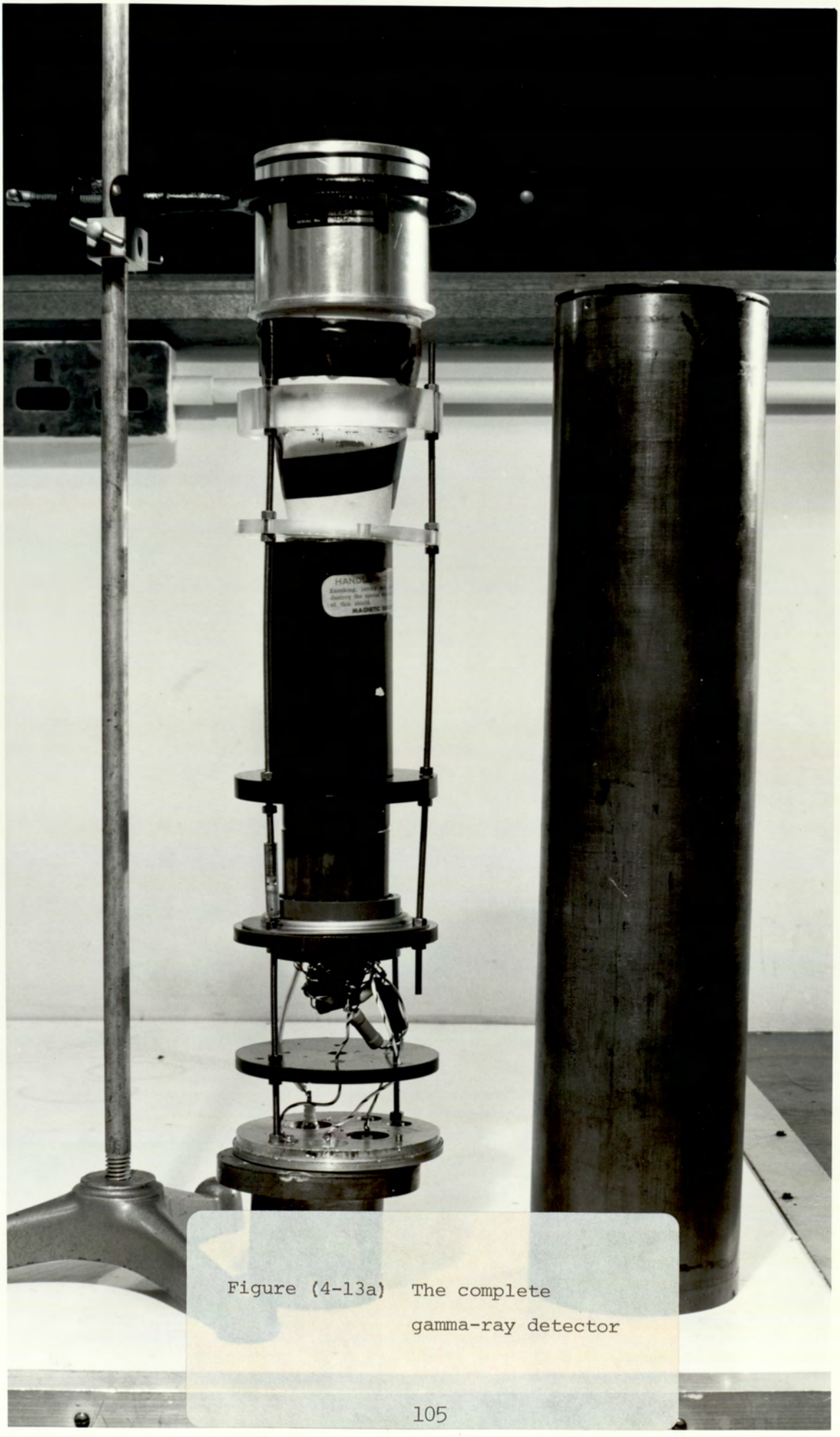

Figure (4-13a) The complete gamma-ray detector

neutron beam, there are scattered neutrons from the walls and the floor of the room which would cause a high background signal. An adequate neutron shield should satisfy the following requirements, a - moderate the fast neutrons; b - absorb slow neutrons and c - absorb the secondary penetrating radiation, e.g. gamma-rays.

a - Fast neutron moderation :- It is most important in a neutron shield to quickly moderate the fast neutrons to low energies. The most effective moderators are the elements with low atomic number, and therefore, hydrogen containing materials such as water, concrete and paraffin wax are the major components of most fast neutron shields. The elastic scattering cross-section for hydrogen is relatively large but decreases with energy as shown in Figure (4-14 a, b) where the values of the cross-section are taken from the latest ENDF B 4G.[96] As the inelastic scattering process does not occur with hydrogen and the neutron capture cross-section is negligible for fast neutrons, it follows that hydrogen has a very low secondary gamma-ray production.

b - Absorption of slow neutrons : Once the neutron has been moderated it can be eliminated through an appropriate capture reaction therefore, a second component is normally used in neutron shields either homogeneously mixed with the moderator or present as an absorbing layer near its inner surface. This additive is chosen to have the following properties i) has a high neutron capture cross-section so that the moderated neutrons will preferentially undergo

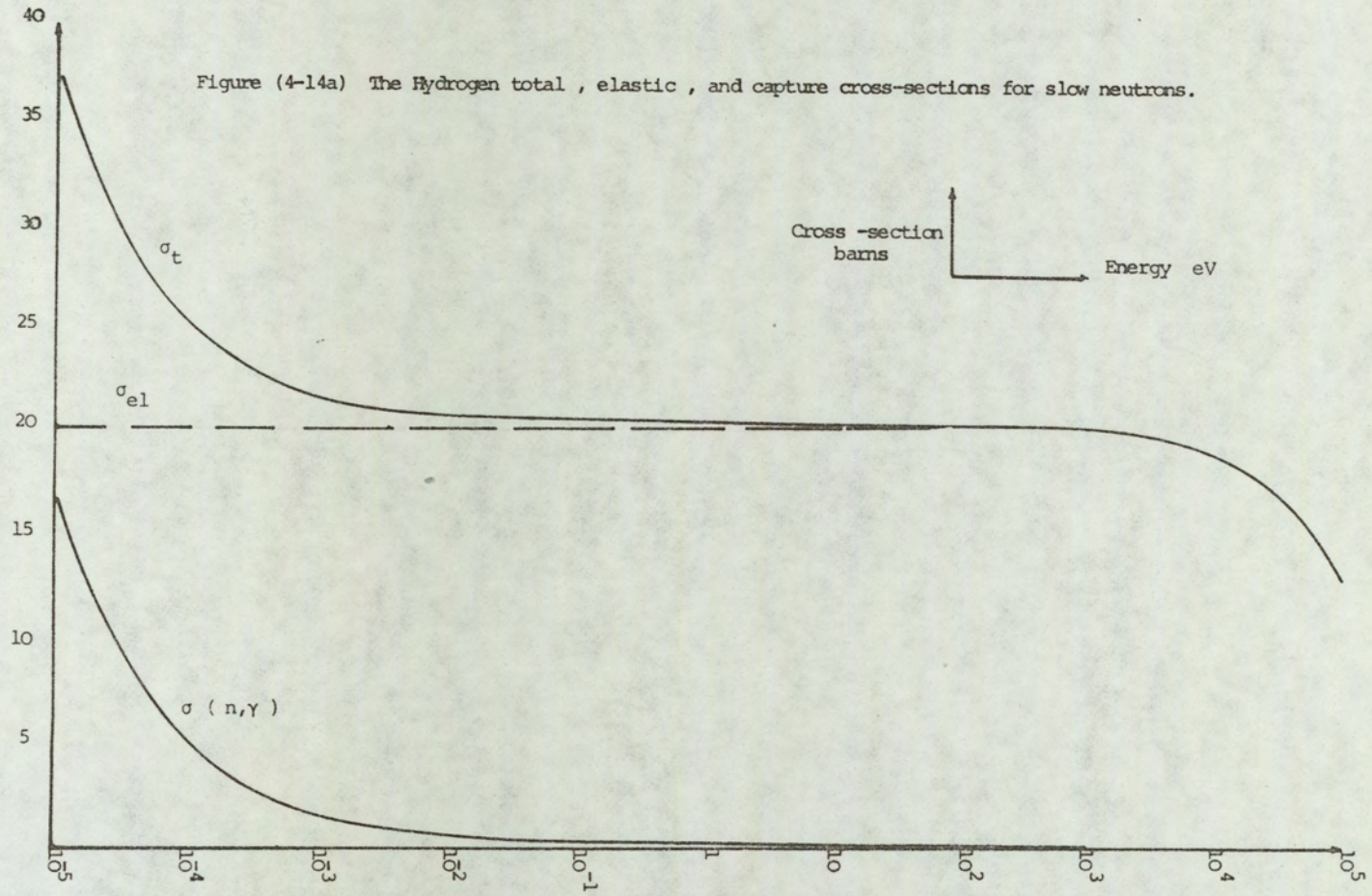

Figure (4-14a) The Hydrogen total , elastic , and capture cross-sections for slow neutrons.

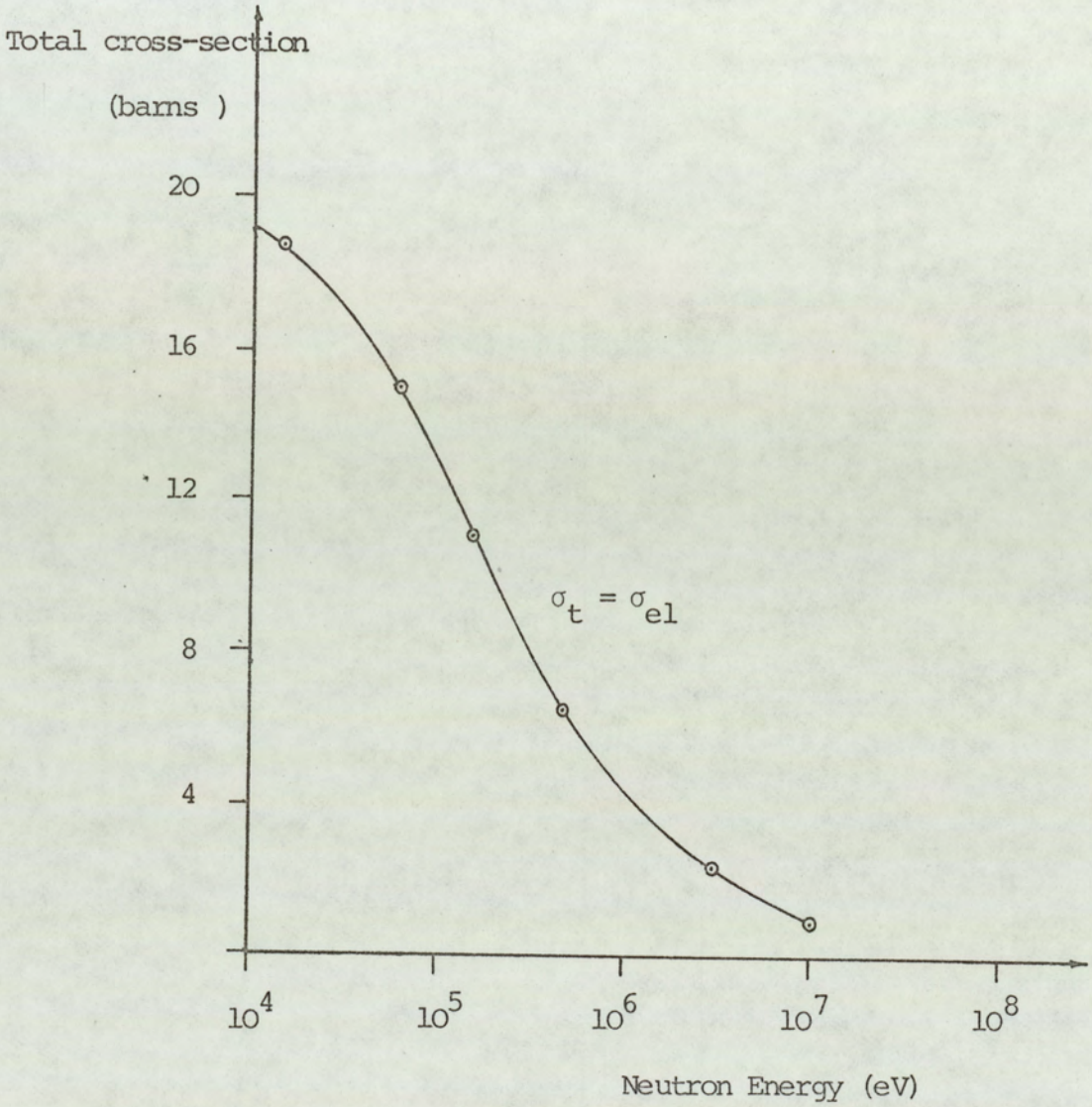

Figure (4-14b) The neutron total cross-section for hydrogen for neutron energies (10^4 - 10^8)

absorption within this material and ii) a stable reaction product or if the nucleus is unstable it should decay without the emission of penetrating gamma-rays.

Boron, B and lithium, Li are the most popular materials for shielding against slow neutrons and in slow neutron detectors for the conversion of slow neutron energies into a directly detectable particle. The reaction in Boron may be written as

$$^{10}_{5}B + {}^{1}_{0}n \longrightarrow \begin{cases} {}^{7}_{3}Li + \alpha & Q = 2.792 \text{ MeV (ground state)} \\ {}^{7}_{3}Li + \alpha & Q = 2.310 \text{ MeV (excited state)} \end{cases}$$

where the branching indicates that the reaction product $^{7}_{3}Li$ may be left in ground state or in the first excited state which quickly returns (half life 10^{-13} sec) to the ground state with the emission of 0.48 MeV gamma-rays.

The reaction in lithium is

$$^{7}_{3}Li + {}^{1}_{0}n \xrightarrow{\beta^-} {}^{3}_{1}H + \alpha \quad Q = 4.78 \text{ Mev}$$

The unstable tritium decays by β^- emission with a 12.3 yr half life to helium without gamma-ray emission.

The slow neutron cross-sections for Boron and lithium are shown in figure (4-15) where it can be seen that the thermal cross-

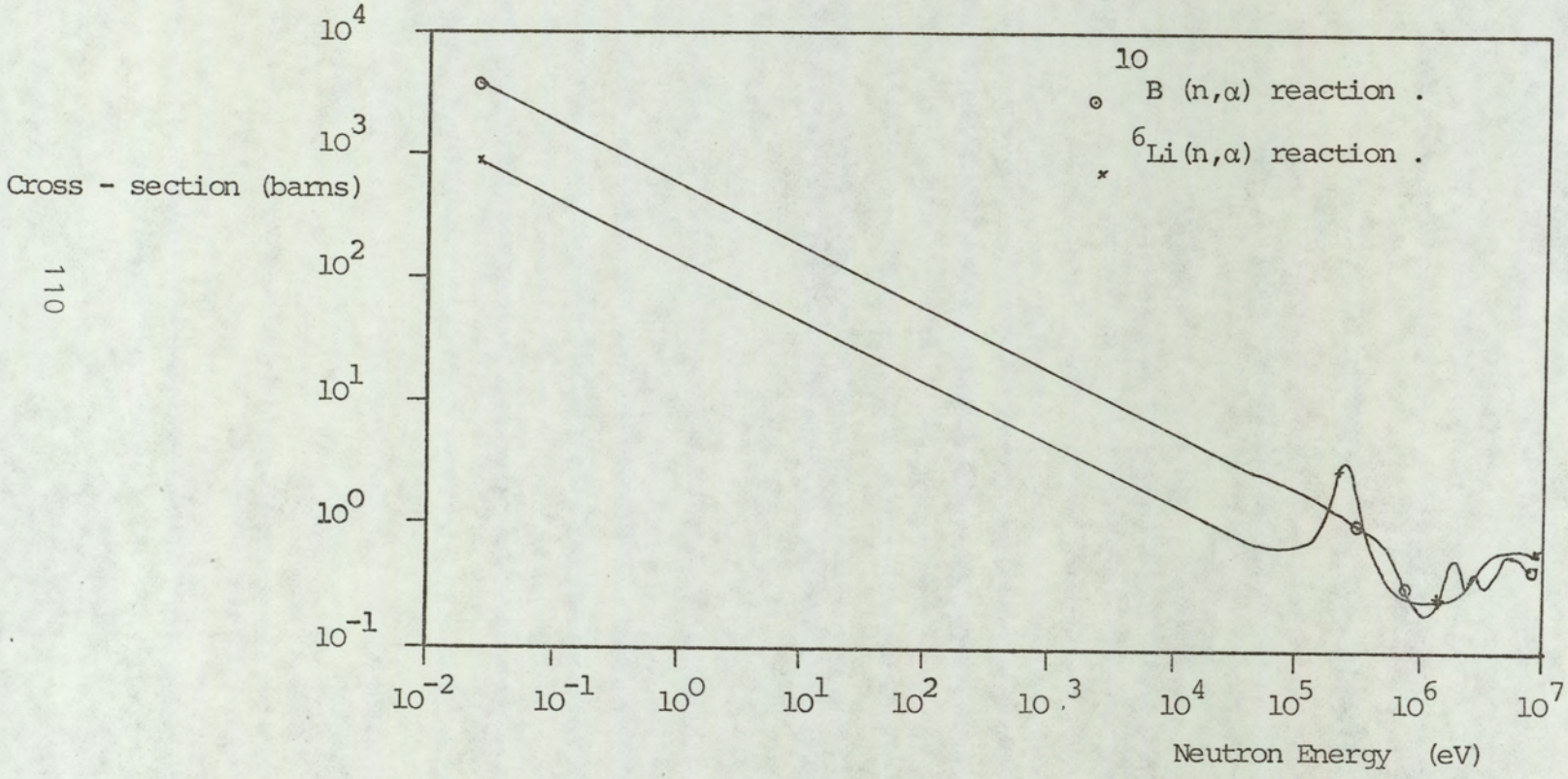

Figure (4-15) Cross-section Vs. Energy for the (n,α) reactions in Boron and Lithium .

section for Boron reaction is 3840 barns and for lithium reaction is 940 barns and both have $1/V$ variation with increasing the neutron-energy. For handling and constructional reasons, Boron and lithium are generally used in the form of a compound, some suitable compound, some suitable compounds are lithium carbonate $Li\ C\ O_3$, borax $Na_2B_4O_7LOH_2O$ and Boric oxide $B_2\ O_3$.

Cadmium is a very efficient neutron absorber in the energy range 0.01 to 1 eV, the absorption is by radiative capture, but the many hard gamma-rays emitted in a single capture process make cadmium unacceptable for use in a neutron shield requiring a low gamma-ray background.

c - Absorption of the Secondary Penetrating Radiations : The innermost part of a shield consists of a suitable gamma-ray absorbing material, lead is the most preferred material for this purpose due to its high density and high atomic number. It shields the detector from gamma-rays produced by reactions in the shielding material and the general gamma-ray background.

4.7.2. Shield Construction :-

The requirement that the shield is to be mobile imposes a limiting factor on the size and weight of the shield. Figure (4-16) shows a cross-section of the constructed shield. The weight of the assembled shield was about 225 Kg.

The lead gamma-ray shield was 55 mm thick at the side of the

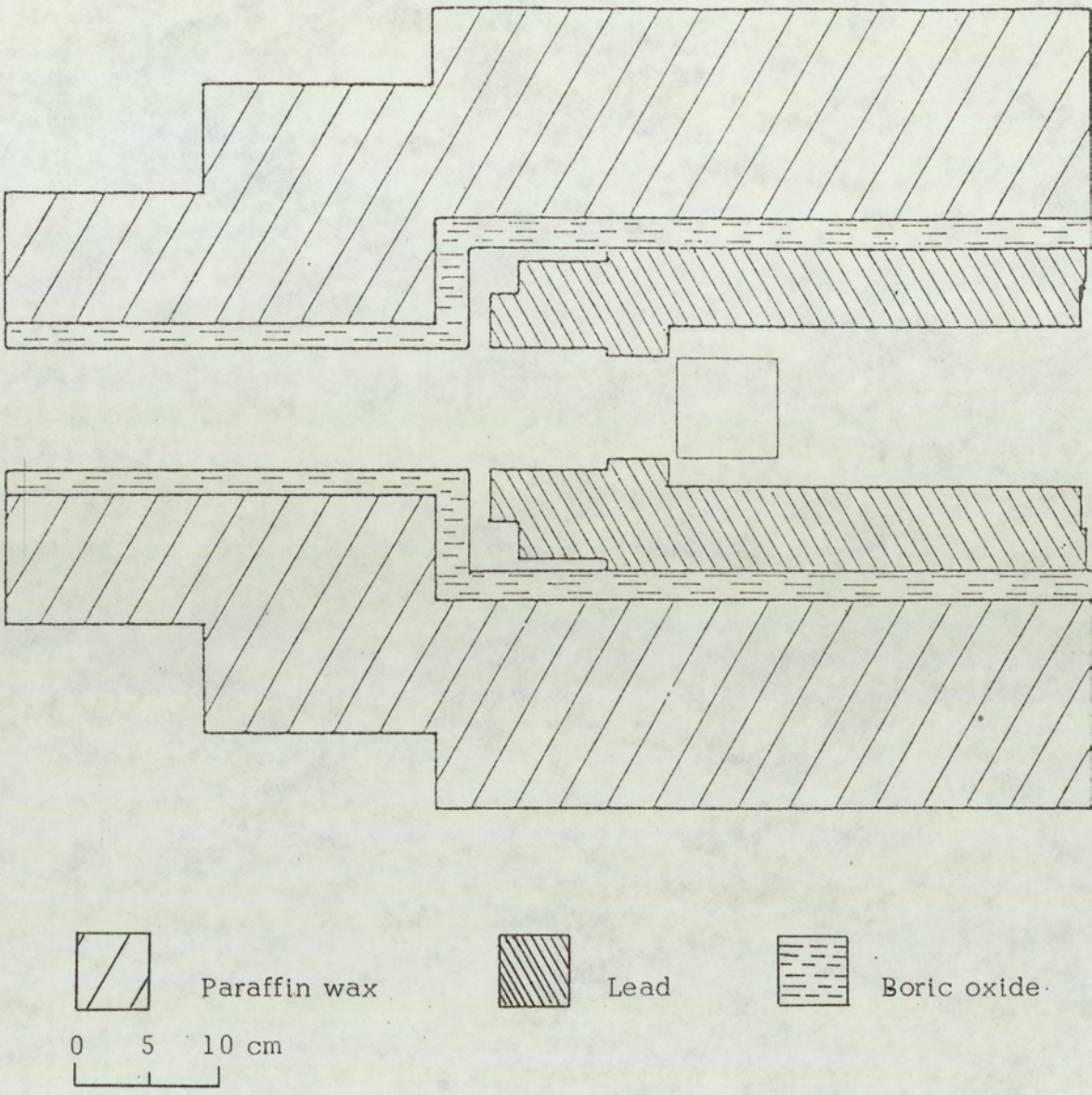

Figure 4-16. Cross-section of the neutron shield

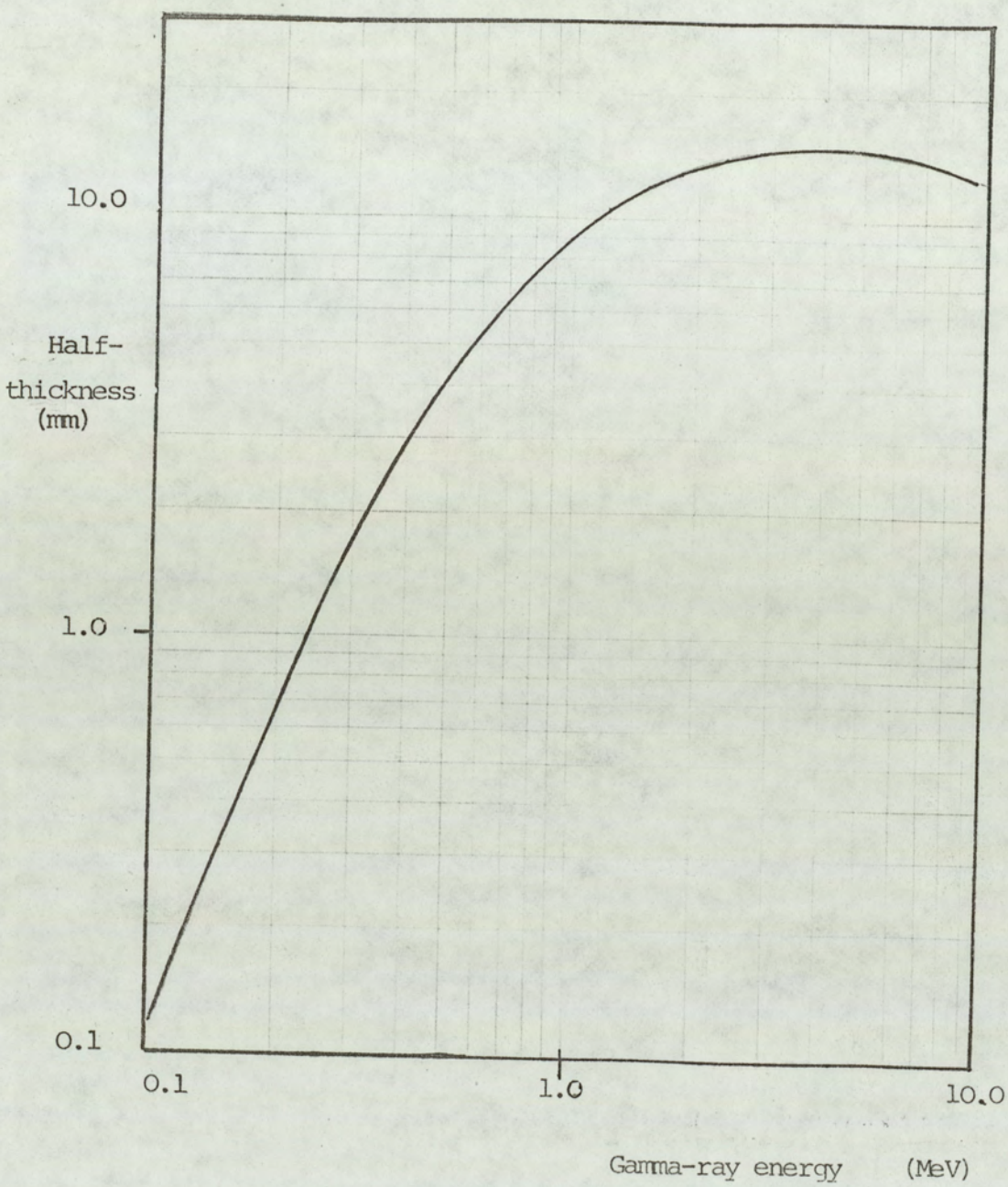

Figure (4-17) The half-thickness of lead vs. gamma-ray energy .

detector and had a maximum thickness of 125 mm in front of the crystal. Figure (4-17) shows that the half thickness of lead versus gamma-ray energy obtained from Connel [50] . The curve shows that the 3.5 MeV gamma-rays are the most penetrating with half thickness of 15 mm, so the minimum thickness of lead used was nearly four times the half thickness value.

The slow neutron shield consisted of boric oxide powder packed in a double walled cylinder made from tin plated iron, the cylinder had a 20 mm thickness surrounding the lead shield, and the effective density of the boric oxide was 1200 Kg/m^3. The thickness of 20 mm boric oxide absorbs 100% of the neutron flux upto a neutron energy of 1 eV.

The outermost part of the shield was the moderator which consisted of paraffin wax with a thickness of 150 mm at the side of the crystal and a maximum thickness of 300 mm in front of the crystal. The front of the shield was tapered so as to suspend a smaller solid angle at the neutron source.

Kerger and Mather [81] state that 200 mm of paraffin wax is considered enough to absorb most high energy neutrons.

The collimator of the shield also contained a lining of boric oxide powder packed into a sealed double walled cylinder and had a thickness of 15 mm sufficient to absorb all incident thermal neutrons. A steel frame was imbedded in the wax to support the lead and the boric oxide shields preventing them from sinking into the wax shield. Figure (4-18) shows the shield mounted on its mobile stand.

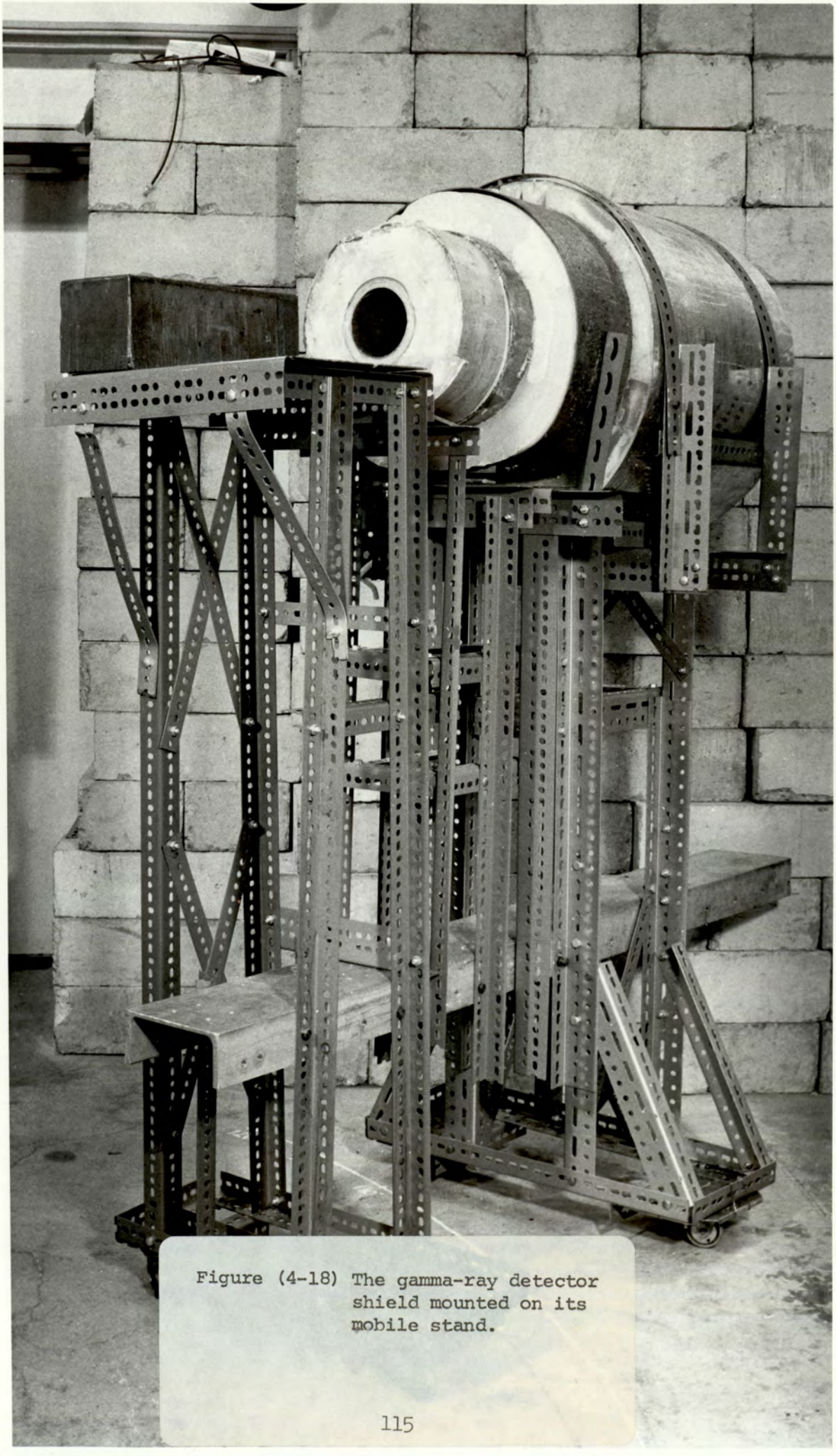

Figure (4-18) The gamma-ray detector shield mounted on its mobile stand.

4.8 Efficiency of Gamma-Ray Detector

For quantitative measurements, the efficiency of the detector as a function of gamma-ray energy must be known. One of the main advantages in using scintillation crystals for gamma-ray measurements is the fact that many standard size detectors can be mass-produced with virtually identical properties. Undoubtedly, there are more published data available on the detection efficiency of sodium iodide scintillators for gamma-ray than any other detector type or application, hence, reasonably complete data can be compiled on each of the common configurations.

However, extra care must be taken when applying the published data since efficiency is defined in a number of ways, vis;

a. The absolute total gamma ray detection efficiency $\varepsilon_{tot}(E_\gamma)$ defined as

$$\varepsilon_{abs}(E_\gamma) = \frac{\text{Number of pulses recorded (total area under the pulse heigh spectrum}}{\text{Number of radiation quanta emitted by the source}}$$

and is dependent not only on detector properties but also on the details of the details of the counting geometry.

b. The intrinsic total gamma-ray detection efficiency $\varepsilon_{int}(E_\gamma)$ defined as

$$\varepsilon_{int.}(E_\gamma) = \frac{\text{Number of pulses recorded}}{\text{Number of radiation quanta incident onto the detector}}$$

This no longer includes the solid angle subtended by the detector. The two efficiencies are simply related for isotropic sources by

$$\varepsilon_{int} = \varepsilon_{abs} \frac{4\pi}{\Delta\Omega} \qquad (4.18)$$

where $\Delta\Omega$ is the solid angle of the detector seen from the actual source position. The intrinsic total gamma-ray detection efficiency of a detector depends on the detector material, the radiation energy and the physical thickness of the detector in the direction of the incident radiation. The two efficiencies above assumes that all the gamma-ray pulses from the detector no matter how low in energy are counted, thus contributing to the total efficiency whether absolute or instrinsic.

c. The peak efficiency $\varepsilon_P (E_\gamma)$ defined as,

$$\varepsilon_{P\text{-abs}} (E_\gamma) = \frac{\text{Number of full energy events in the photo-peak}}{\text{Number of radiation quanta emitted by the source}}$$

and

$$\varepsilon_{P\text{-int}} (E_\gamma) = \frac{\text{Number of full energy events in the photo peak}}{\text{Number of radiation quanta incident onto the detector}}$$

The subscripts abs. and int. stand for absolute and intrinsic efficiencies as defined earlier.

The ratio of the peak to total efficiencies is known as the

"peak-to-total" ratio or photofraction r ie.

$$r = \frac{\varepsilon_p (E_\gamma)}{\varepsilon (E_\gamma)} \qquad (4.19)$$

which is sometimes tabulated separately.

It is often preferable from an experimental stand point to use peak efficiencies only, because the number of full energy events is not sensitive to perturbing effects such as scattering from surrounding objects or spurious noise.

In the present work equation (4.19) was used to calculate the peak efficiency as follows:

The absolute peak detection efficiency = The peak-to-total ratio X The absolute gamma-ray detection efficiency.

The peak-to-total ratio was determined experimentally for two gamma-ray energies namely 0.662 MeV and 1.28 MeV, the results were compared to the published results obtained by using a (7.62 x 7.62mm) NaI (Tl) crystal as reported by Heath[82] and other workers[83,84] the two results agreed to within 2% with the published values.

Figure (4.19) shows the photofraction or peak-to-total value obtained for (76.2 mm x 76.2 mm) Na I (Tl) crystals.

The absolute detection efficiency was calculated for the geometry used as follows. As the detector crystal face was positioned

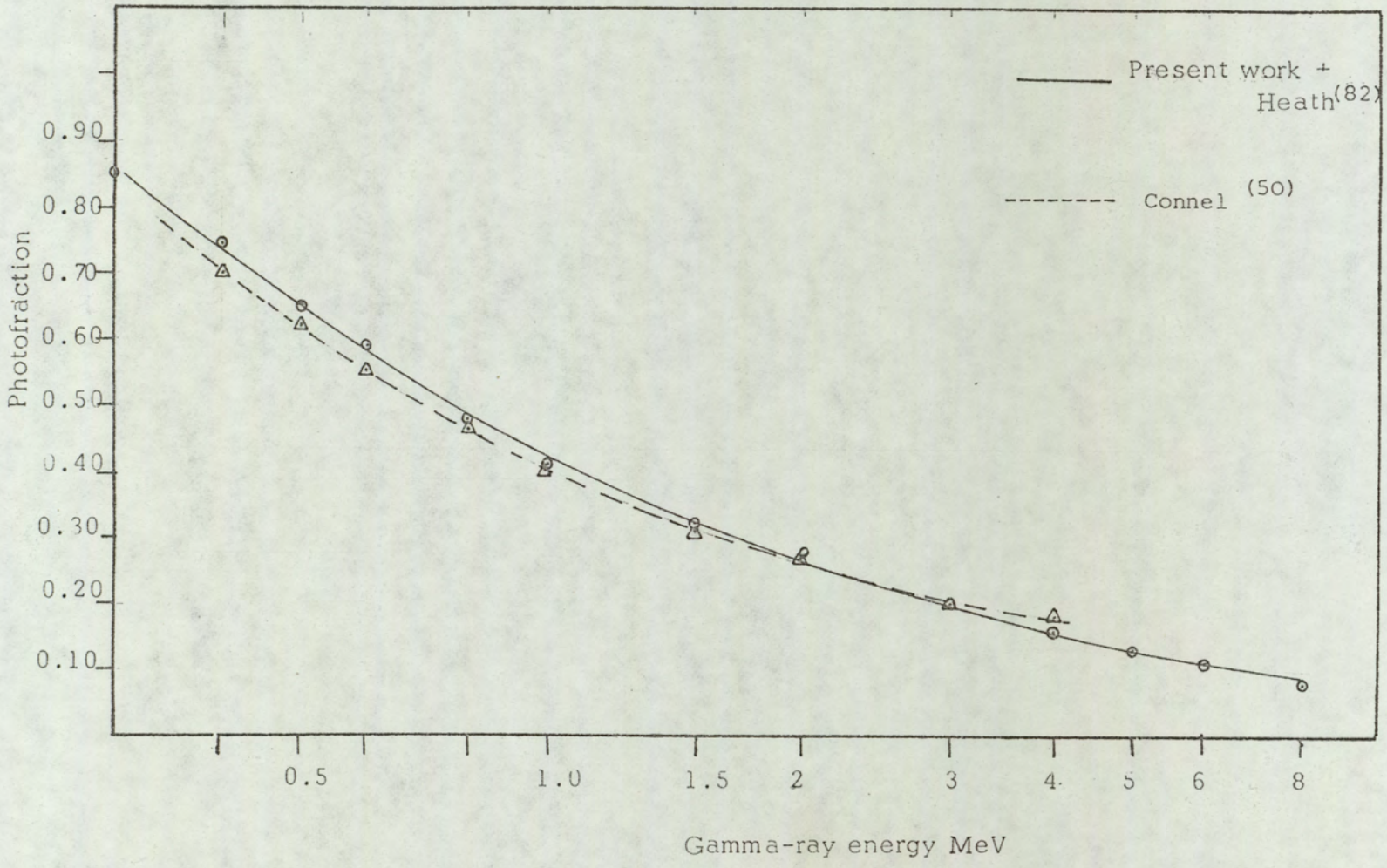

Figure (4-19) The peak-to-total rate of a (3"x3") NaI (Tl) crystal

1.40 m from the scattering sample, the solid angle subtended by the detector at the scattering sample is about 2.315×10^{-3} which is very small, hence, to a good approximation the source gamma-rays incident on the detector could be considered as a parallel beam. Assuming that the gamma-ray flux is incident normally onto the crystal face, the total efficiency is given by the fraction of interactions in the detector multiplied by the fraction of incident radiation penetrating the detector entrance window.

$$\varepsilon_{tot}(E_\gamma) = \exp.(-\mu_A X_A) . \left\{ 1 - \exp.(\mu_C X_C) \right\} \qquad (4.20)$$

where X_A, X_C are the detector entrance window quoted by the manufacturers as equivalent to 280 mg/cm^2 of aluminium, and the crystal thickness respectively and μ_A and μ_C are the respective aluminium and crystal total linear gamma-ray absorption coefficients. The values of the absorption coefficients were taken from Goldstein[85] tabulation of White's data.

Finally, the peak efficiency was determined using equations (4,19) and (4.20). The result is shown in Figure (4.20) which shows the gamma-ray peak efficiency as a function of gamma-ray energy.

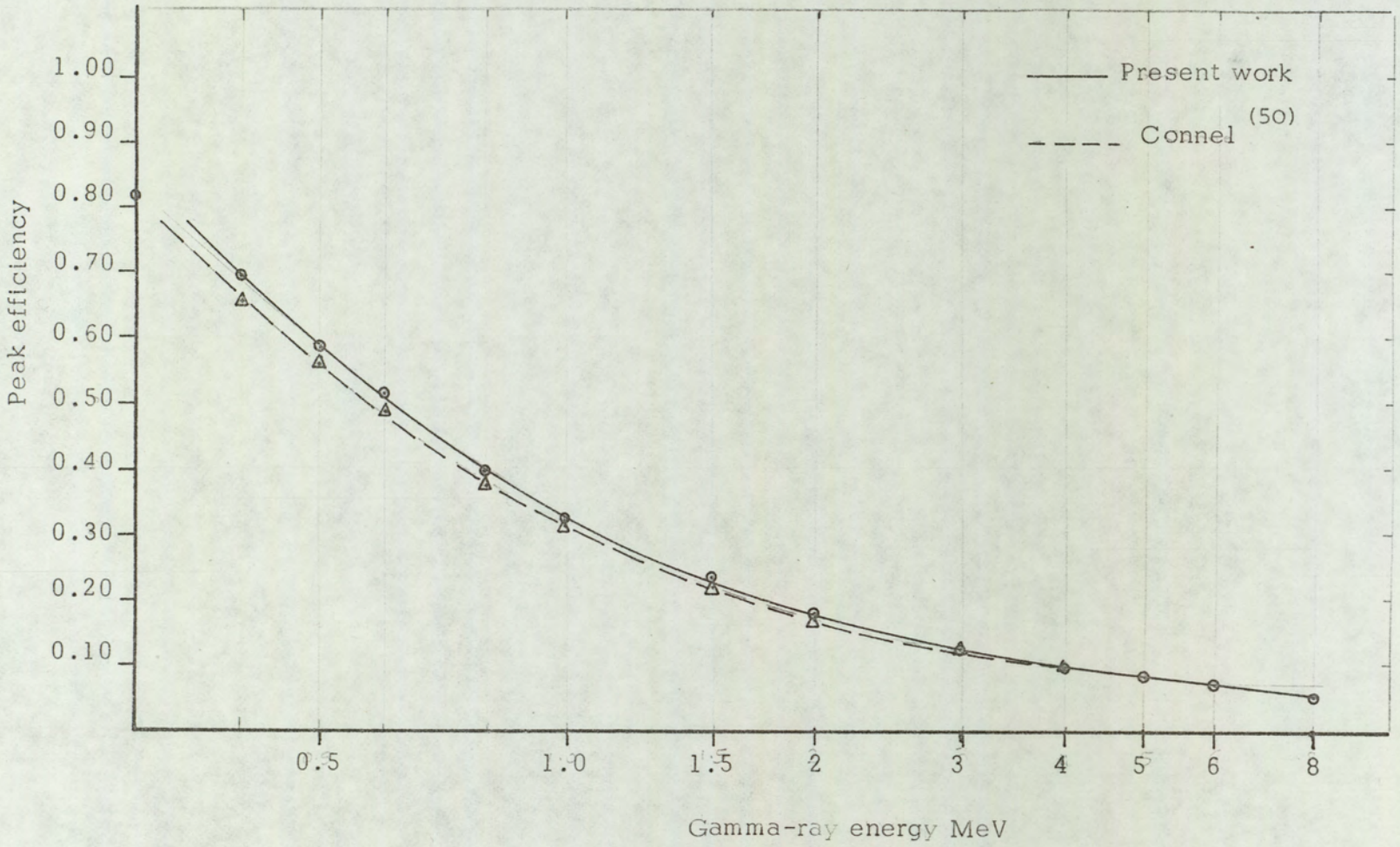

Figure (4-20) The gamma-ray peak efficiency as a function of γ-ray energy

CHAPTER FIVE

DATA ANALYSIS AND THE EXPERIMENTAL RESULTS

Using the experimental method described in Section 3-5-6, the experimental data was accumulated in the form of gamma-ray energy spectra together with the total number (time-integrated) of the incident neutrons monitored by the associated alpha particles detected during the period of each measurement.

In Part (I) of this Chapter, the derivation of the differential cross-section per unit solid angle for gamma-ray production is discussed while Part II will be devoted to the analysis of the experimental results.

PART 1

5.1. THE DIFFERENTIAL CROSS-SECTION

The probability that a particular collision process, such as elastic or inelastic scattering of a particle into a small solid angle $d\Omega$ at a certain specified angle θ with the incident beam will take place is defined in terms of the differential cross-section $d\sigma$

where $$d\sigma = \sigma(\theta)\, d\Omega \qquad (5\text{-}1)$$

consider a neutron flux of ϕ neutrons per second per unit area incident onto the scattering sample which produces G gamma-rays of energy E MeV per second in a sample containing N nuclei. The total cross per nucleus for production of a given gamma-ray is

given by

$$\sigma_E = G/\phi N \qquad (5\text{-}2)$$

σ_E has the dimentions of area and usually has the units of barns (1 barn = 10^{-24} cm^2 = 10^{-28} m^2).

The differential cross-section per unit solid angle at a scattering angle θ is given by

$$\frac{d\sigma(\theta)}{d\Omega} = g(\theta)/\phi N \qquad (5\text{-}3)$$

where $g(\theta)$ is the number of gamma-rays produced per second per unit solid angle centered on the direction θ to the neutron beam. The units of the differential cross-section are (millibarns/steradian) abbreviated (mb/st).

In principle, the number of gamma-rays produced by the incident neutrons can be obtained from the gamma-ray energy spectra, but several factors have to be taken into account. These several factors are discussed in the following sections.

5.2. Gamma-Ray Energy Spectra :-

Figure 5.1 shows an example of the gamma-ray spectrum obtained from an iron sample at a scattering angle of 50°. The following discussion illustrates the factors involved in obtaining the number of gamma-rays of a particular energy emitted by the sample at

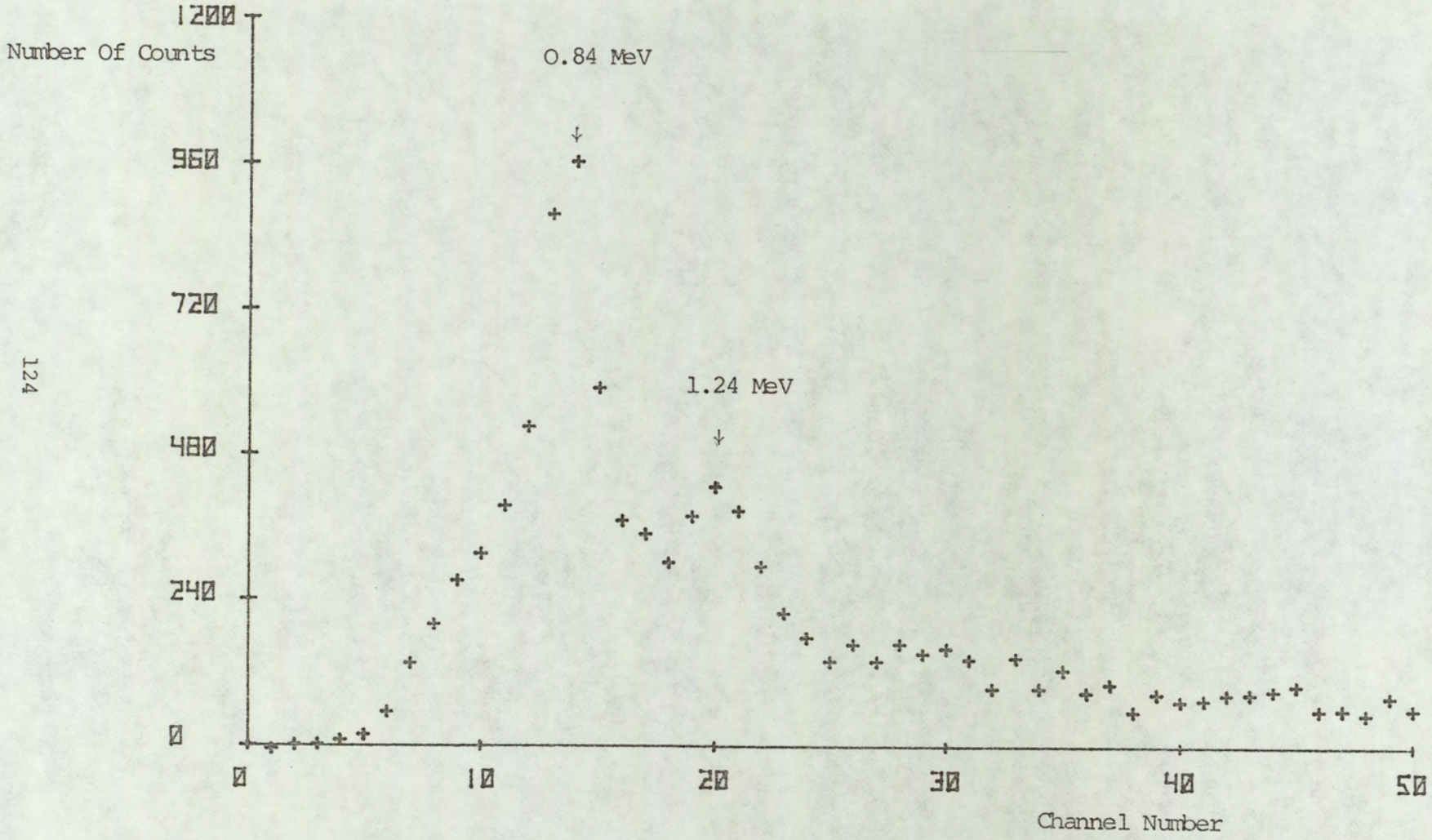

Figure (5-1) Typical gamma-ray spectrum from iron sample at scattering angle of 50^{o} . Sample thickness = 2 cm.

a particular scattering angle.

As mentioned in Section (3.4.2) it was necessary to set the gamma-ray-discriminator level above zero to eliminate the relatively high background count at low energies in order to produce an acceptable signal-to-background count at low energies, meant that not all the γ-rays in the Compton spectrum are detected, and hence, the peak efficiency rather than the total efficiency was used. In the case of Iron samples, the gamma-rays of interest had energies of 0.84 and 1.24 MeV respectively were clearly resolved. In Figure (5-1), there is also an indication of peaks corresponding to higher gamma-ray energies (e.g. 1.81 MeV). The 0.84 MeV peak is situated on the Compton backgrounds of these higher energy gamma-rays and an accurate determination of the total count in the 0.84 MeV photo-peak requires careful removal of the Compton distribution from the 1.24 MeV. This is also the case for the case of the 1.24 MeV photo-peak where the contributions from the higher energy gamma-rays must be removed.

Several methods dealing with this have been reported in the literature, two of which are outlined below.

a. The graphical stripping technique[50,82] in which the full energy peak count of the highest gamma-ray present is directly determined, as the peak base line in this case is the abscissa and the spectral shape of this gamma-ray is subtracted from the total distribution, when this is completed for this gamma-ray energy, the second highest energy gamma-ray has its

total absorption peak resting on the abscissa and its intensity can be estimated. The spectral shape corresponding to this second gamma-ray is then subtracted from the remaining distribution, and the process is continued. It is difficult to apply this method in the present work because of the small number of counts in the higher peaks.

b. Covell Method :- [87]

This method can be used to estimate the intensity of a single gamma-ray in a complicated spectrum. In this method a calibrated fraction of the area of the total absorption peak is measured and then a correction factor relating the fractional peak count to the true count is applied. This correction factor is determined experimentally by observing the gamma-ray spectra of isotopic source emitting gamma-ray near the energy of interest.

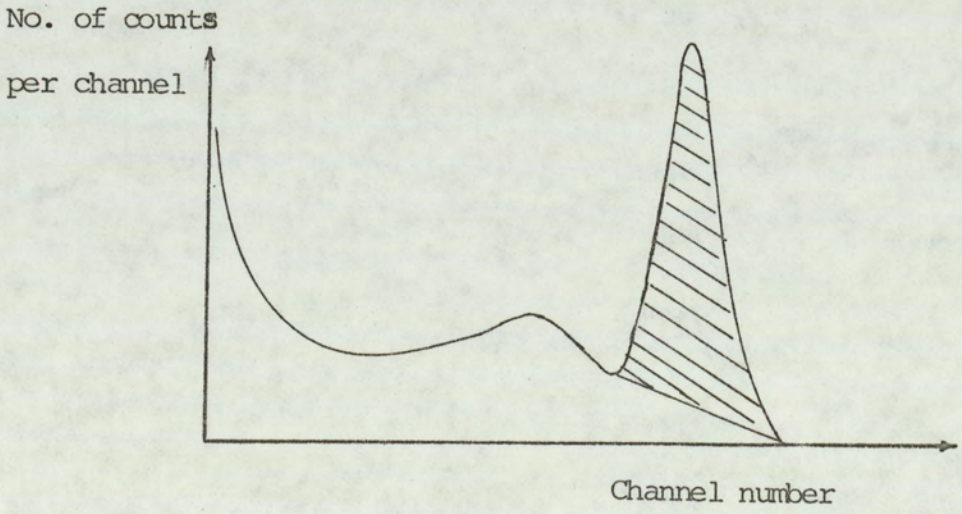

Covell's method

A modification of this method suitable for use where more than one peak is present was used in the present work for the gamma-ray spectra iron samples.

The peaks are fairly well resolved and the Compton background associated with each full energy peak is clearly seen. A standard spectral shape was measured experimentally. This was fitted to each of the full energy peaks in turn and the Compton background contribution of each was drawn in extending from the peak to the origin. The total Compton contribution at any given point was then obtained by summing these individual contributions. This summed Compton contribution was taken as background line above which the peak area was considered.

For the gamma-ray spectra obtained from concrete samples, it was not possible to determine the spectral shapes experimentally since there was not enough isotopic sources to cover the gamma-ray energies of interest. Instead the calculated response functions based on Monte-carlo calculation and formulated by Berger and Seltzer[88] were used. The continuous part of the energy deposition spectrum $C(E_o, E)$ has been expressed in terms of dimensionless functions C_j $(j = 1,2,3,4)$ which depend on dimensionless energy related variables, X, Y and Z.

For $E \leq 1.2$ MeV, they set

$$C_o(E_o, E) = C_1(E_o, X) \cdot (1 + m_o c^2/2E_o) / E_o \qquad (5\text{-}4)$$

Where $X = E\ (1 + m_o c^2/2E_o) / E_o$ (5-6)

For $E > 1.2$ MeV, they set

$$C(E_o, E) = C_2(E_o, Y) / (E_o - 2 m_o c^2), \qquad (5\text{-}7\text{-}a)$$

$$\text{for} \quad O \leq E < (E_o - 2m_o c^2)$$

$$C(E_o, E) = C_3(E_o, Z) / 2 m_o c^2 \qquad (5\text{-}7\text{-}b)$$

$$\text{for} \quad E_o - 2m_o c^2 \leq E < E - m_o c^2$$

$$C(E_o, E) = C_4(E_o, Z) / 2 m_o c^2 \qquad (5\text{-}7\text{-}c)$$

$$\text{for} \quad E_o - m_o c^2 \leq E \leq E_o$$

where

$$Y = E / (E_o - 2 m_o c^2)$$

$$Z = (E - E_o + 2 m_o c^2) / 2 m_o c^2$$

m_o = electron mass

and c = velocity of light.

The functions C_j and given in the reference. (88)

The estimated statistical accuracy of the response functions obtained in the continuum part with the use of these functions is 5-15%. The continuous parts were evaluated for gamma-ray energies 1, 2, 3, 4, 5 and 6 MeV and then normalized to the peak heights in the experi-

mentally determined spectra, hence, the Compton background contribution of each was determined. The total Compton contribution at any point was then obtained by summing these individual contributions. The Compton continuum for γ -ray energies from 1 to 6 MeV is shown in Figure (5-2) and the normalized resultant background line based on the above discussion for gamma-ray spectrum from concrete sample is shown in Figure (5-3).

5.3. The Neutron Flux Corrections

As mentioned in Section (3.5.6), the number of neutrons incident onto the sample was obtained from total count of the associated α - particles. Corrections are necessary due to the background activation considered in detail by Allenby [44], a brief account only will be given here. This correction was divided into two components.

1. The radiation produced by activation of the target and surrounding assembly is caused principally by neutron reactions of the type A (n, X) B and can be monitored by observing the count rate on the scaller immediately after switching off the beam after the run.

2. The fast neutron background which consists mainly of 14 MeV neutrons produced in the T (d,n) ^{4}He reaction leaving the target at 90° to the deutron beam which can be monitored by observing the alpha particle count rate for various values of target current, and then replacing the alpha-particle detector aperture plate by another

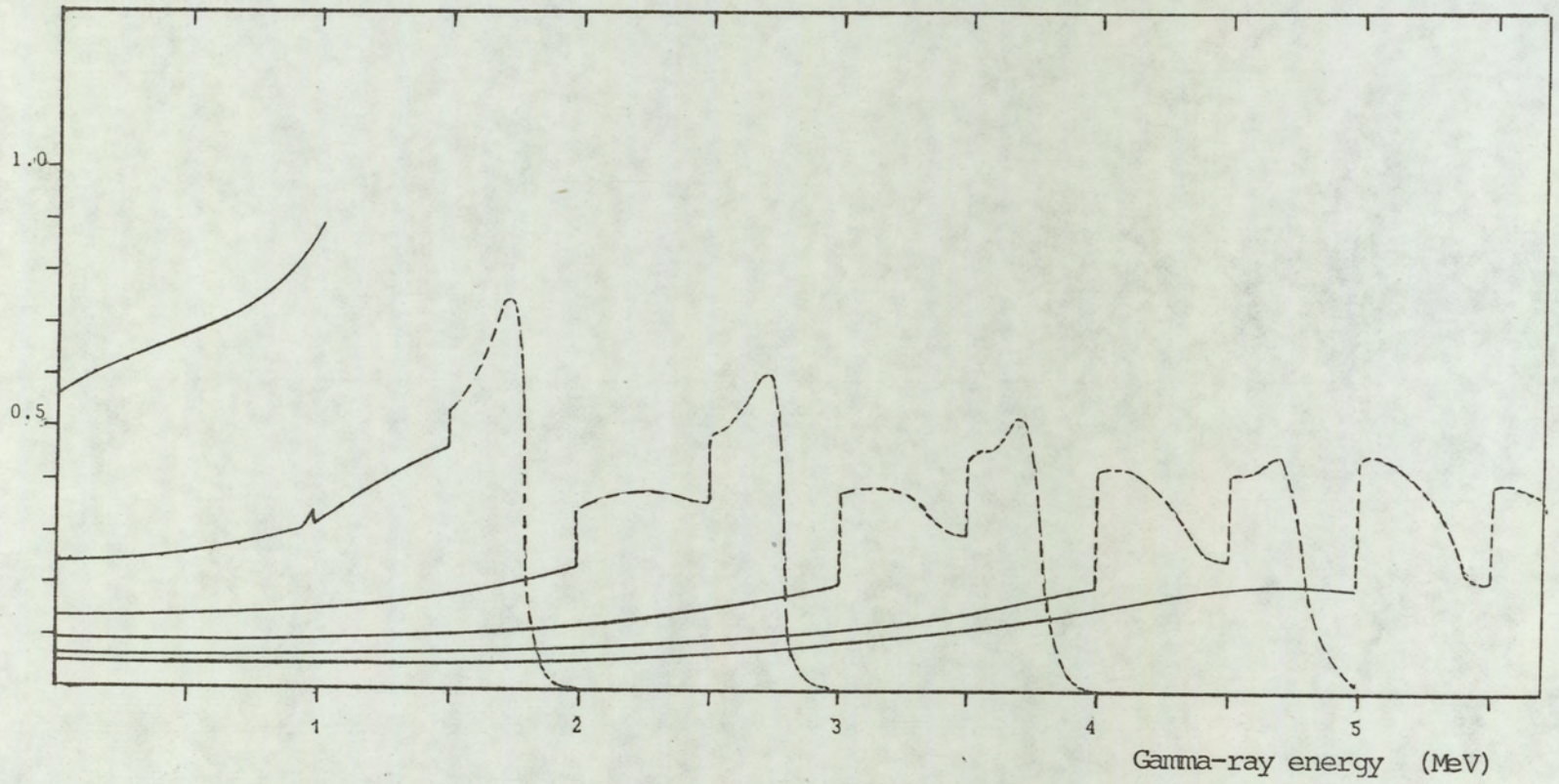

Figure (5-2) The continuous part (Compton continuum) of the response function of (3x3) NaI (Tl) detector for different gamma-ray energies .

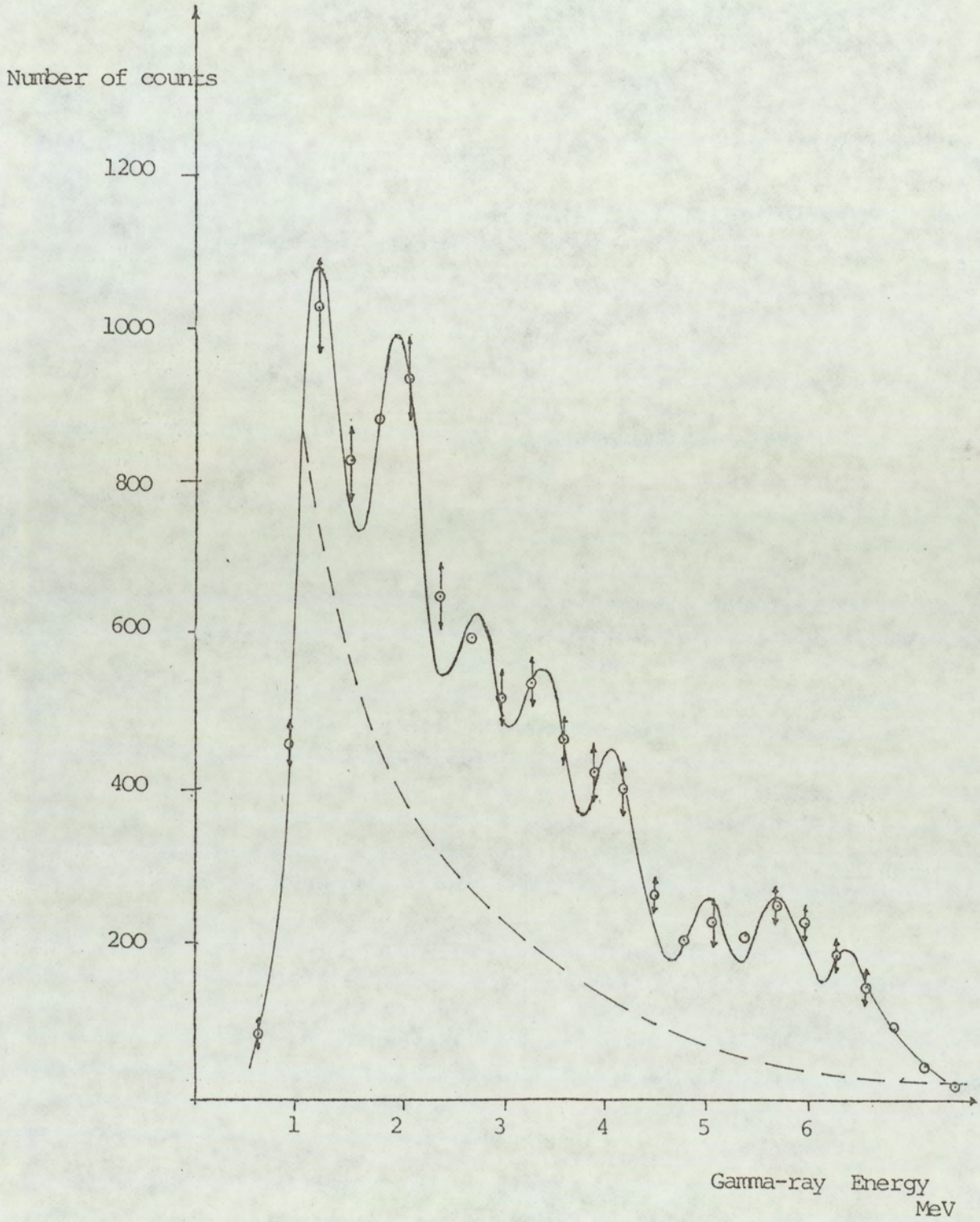

Figure (5-3) A typical typical gamma-ray spectrum from concrete sample . Sample thickness =12.5 cm. , scattering angle = 50^{o} . The broken line shows the added Compton contribution from all the gamma-ray peaks.

aluminium plate with no aperture. The 1 mm thickness of the plate is sufficient to stop the 3.5 MeV alpha-particles[44], but has negligible effect on 14 MeV neutrons. The alpha count rate is then observed for the same set of target currents. The difference between the two counts allows the correction to be estimated.

It was found that 0.055 of the count consists of this background and this is constant over the range of target currents used to within $\pm$ 0.005.

The experimental alpha-count rate is multiplied by the correction factor $F_1 = 0.945 \pm 0.005$ to give the correct alpha-count.

5.4. Neutron Absorption in the Target Assembly :-

The neutrons associated with the detected alpha-particles must be able to escape from the target assembly before reaching the scattering sample. According to the manufacturers specifications, they must pass through 2.55 mm of steel and 1.30 mm of water which is used to cool the target.

The fraction of neutrons (F_2) escaping from the target assembly can be calculated from the following formula :

$$F_2 = \exp - \left\{ \Sigma_{Fe} X_{Fe} + (\Sigma_H + \Sigma_O) X_{water} \right\} \quad (5\text{-}8)$$

where Σ_{Fe}, Σ_H and Σ_O are the macroscopic cross-sections of

iron, hydrogen and oxygen respectively, X_{Fe} and X_{water} are the thickness of stainless steel and water respectively.

Table (5-1) gives the values of all the quantities required to calculate the (F_2) correction.

Element	σ_T	X mm
Iron	2.316 b	2.50 ± 0.03
Oxygen	1.523 b	1.30 ± 0.03
Hydrogen	0.646 b	

Table (5-1) Total cross-section for neutron interactions less forward scattering for iron, oxygen and hydrogen [50] and the thickness of each in the target assembly.

The fraction escaping the target assembly is $F_2 = 0.939 \pm 0.048$. From Sections 5-3 and 5-4, the observed alpha-particle count must be multiplied by these two factors to give the corrected neutron count, i.e.

The correct integrated neutron count = the observed integrated alpha count x F_1 x F_2

$$\phi(n) = \phi_m(\alpha) \times F_1 \times F_2 \qquad (5\text{-}9)$$

5.5. Neutron Beam Attenuation in the Scattering Sample :-

Consider the neutron flux ϕ_o incident onto the sample,

The reaction rate in an element of thickness dx in the sample is given by

$$\text{The reaction rate} = \phi_o \; N \; e^{(-\Sigma_t X)} dX \qquad (5\text{-}10)$$

where

ϕ_o = Incident neutron flux

N = No. of sample nuclei/cm^3

Σ_t = Total macroscopic cross-section

X = Sample thickness

The total number of reactions is obtained by integrating the reaction rate over the whole sample

$$= \int_o^x \phi_o \; N \; e^{-\Sigma_t X} \; dX$$

$$= \frac{N \; \phi_o}{\Sigma_t} \left(1 - e^{-\Sigma_t X} \right) \qquad (5\text{-}11)$$

Since $\Sigma_t = N \sigma_t$

where

$\sigma_t \equiv$ the total microscopic cross-section

The above equation can be rewritten as

$$= \frac{\phi_o}{\sigma_t} \left(1 - e^{-\Sigma_t X} \right) \qquad (5\text{-}12)$$

If σ_γ is the total gamma-ray production cross-section from neutron inelastic scattering then,

The total gamma-ray yield (G) from neutron inelastic scattering is given by

$$G = \phi_o \left\{ 1 - e^{-N \sigma_t X} \right\} \left(\frac{\sigma_\gamma}{\sigma_t} \right) \qquad (5\text{-}13)$$

Upon using the definition of the differential gamma-ray production cross-section per unit solid angle, $\left(\frac{d \sigma (\theta)}{d \Omega} \right)$, the gamma-ray yield $G' (\theta)$ in a unit solid angle centered at an angle θ to the incident beam is given by

$$G' (\theta) = \phi_o \left(1 - e^{-N \sigma_t X} \right) \left\{ \frac{\left(\frac{d (\theta)}{d \Omega} \right)}{\sigma_t} \right\} d \Omega \qquad (5\text{-}14)$$

For very thin samples, i.e. $N \sigma_t X << 1$ or equivalently by expressing $(N \sigma_t X)$ in terms of the mean free path $\lambda = (N \sigma_t)^{-1}$ then $N \sigma_t X = \frac{X}{\lambda}$, the condition becomes, for sample thickness $X << \lambda$ the term between the brackets can be approximated by

$$\left(1 - e^{-N \sigma_t X} \right) = N \sigma_t X \qquad (X << \lambda) \qquad (5\text{-}15)$$

and equation (5-14) reduces to

$$G'(\theta) = \phi_o N X \left(\frac{d\sigma(\theta)}{d\Omega}\right) d\Omega$$

hence,

$$\frac{d\sigma(\theta)}{d\Omega} = \frac{G'(\theta)}{\phi_o N X \, d\Omega} \qquad (5\text{-}14a)$$

Table (5-2) gives the values of the factors $(1 - e^{-N\sigma_t X})$ and $N\sigma_t X$ for various iron samples to test the validity of this approximation.

Sample Thickness cm	Sample Thickness in mfp	$N\sigma_t X$	$1 - e^{-N\sigma_t X}$
2.0	0.442	0.442	0.357
1.0	0.221	0.221	0.198
0.5	0.1105	0.1105	0.1046
0.25	0.05525	0.05525	0.05375
0.125	0.027625	0.027625	0.027246

Table (5-2) The values of the factors $N\sigma_t X$ and $(1 - e^{-N\sigma_t X})$ for different sample thickness in iron.

From the above table it can be seen that for an iron sample of thickness 0.442 mfp the use of this approximation could introduce an

error of ~ 24% in the neutron attenuation factor. However, in the present case, this approximation was not justified as the samples were much thicker in order to study the multiple scattering effect on the observed cross-sections; instead the original equation (5-14) was used.

5.6. Absorption of the Gamma-rays in the Scattering Sample :-

The correction for self absorption takes into account the fact that some of the gamma-rays produced in the sample are absorbed and never reach the gamma-ray detector. The magnitude of this correction depends on the mass absorption coefficient of the sample material and on the geometry of the sample.

The formation of this correction for thin scattering samples has been given by Connel [50] and by Allenby [44]. In both cases the sample was placed at 45^{o} to the neutron beam. The sample was divided into strips of thickness d X as shown in Figure (5- 4).

The fraction of the total gamma-ray beam which is produced in the elemental strip d X is given by $\frac{d X}{b}$ where b is the sample thickness and it is assumed that the gamma-rays are produced uniformly throughout the sample.

The fraction of gamma-rays produced in the strip (d X) and escaping the sample through the face AB is given by

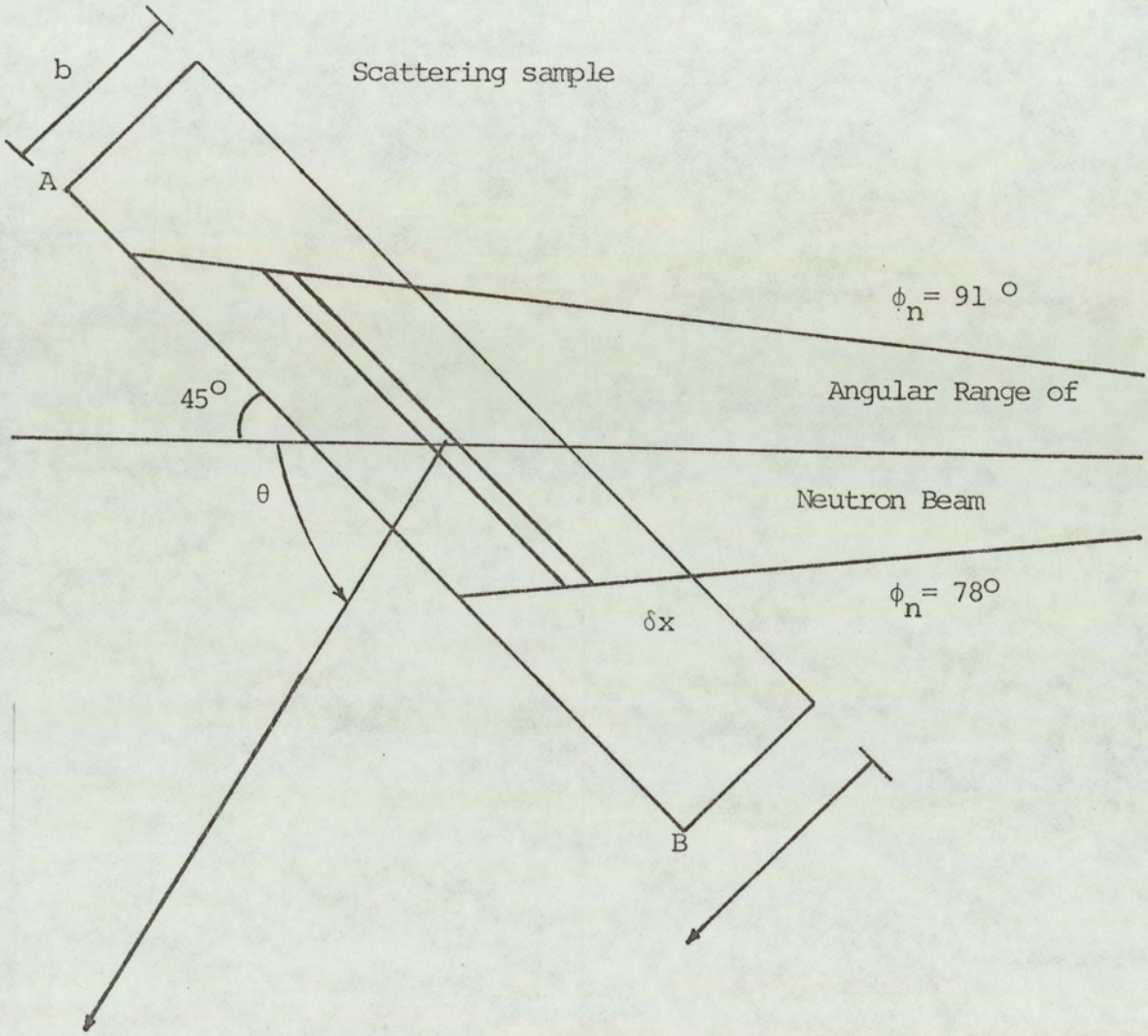

Figure (5-4) Sample geometry used by Connel [50] and Allenby[44] .

$$S'(\theta) = \exp\left(-\frac{\mu(b-X)}{\cos(\theta-45)}\right)\frac{dX}{b} \qquad (5\text{-}16)$$

where μ is the absorption coefficient which is a function of the gamma-ray energy and the sample atomic number, and θ is the gamma-ray detector angle.

Integrating equation (5-16) over the width b of the sample leads to

$$S(\theta) = \int_0^b \left(\frac{-\mu(b-X)}{\cos(\theta-45)}\right)\frac{dX}{b}$$

$$= \frac{\cos(\theta-45^\circ)}{\mu b}\left\{1-\exp\left(\frac{-\mu b}{\cos(\theta-45)}\right)\right\} \qquad (5\text{-}17)$$

This equation gives the fraction of gamma-rays produced in the sample and escape through the sample face (A B) to the detector. If the sample is placed at 90° to the neutron beam equation (5-17) still holds, the only change required is to replace 45° by 90° and hence,

$$S(\theta) = \frac{\cos(\theta-90^\circ)}{\mu b}\left\{1-\exp\left(\frac{-\mu b}{\cos(\theta-90)}\right)\right\}$$

ie.

$$S(\theta) = \frac{\cos\theta}{\mu b}\left\{1-\exp\left(\frac{-\mu b}{\cos\theta}\right)\right\} \qquad (5\text{-}18)$$

Again, this equation is correct as long as the gamma-rays are escaping through the face AB, of the sample.

Equation (5-18) can be rewritten as

$$S(\theta) = \frac{1}{\mu\,(b/\cos\theta)} \left\{ 1 - \exp - \mu\left(\frac{b}{\cos\theta}\right) \right\}$$

$$= \frac{1}{\mu B} \left\{ 1 - \exp-(\mu B) \right\} \qquad (5\text{-}19)$$

using Figure (5-4), it can be readily seen that $B = \frac{b}{\cos\theta}$ represents the actual thickness traversed by the gamma-rays in escaping from the sample in the direction θ to reach the detector. For thick samples, it is not true that all the gamma-rays reaching the detector escape through the face AB, especially at higher scattering angles so equation (5-19) needs to be modified.

For the special case of $\theta = 90^{\circ}$, the distance traversed is simply the width of the sample instead of the thickness, so B must be replaced by W and hence,

$$S(\theta)_{(\theta = 90} = \frac{1}{\mu W} \left\{ 1 - \exp - (\mu W) \right\} \qquad (5\text{-}19\text{-a})$$

The validity of equations (5-19) and (5-19-a) was checked by drawing the sample-detector geometry and measuring B through the center of the sample, the results obtained for $S(\theta)$ were compared to the values obtained using the analytical formula (5-18), the two sets of results were in agreement to better than 1% averaged over several values of θ for samples of different thicknesses as long as the gamma-rays are escaping through the sample face AB.

Figure (5-5) illustrates the case where the gamma-rays can reach the detector both through the face AB and the side DB, i.e. mixed exit for the gamma-rays reaching the detector. Here the gamma-rays produced in the shaded area, escape through the side BD while the gamma-rays produced in the rest of the sample escape through the face AB.

In order to determine the total fraction $S(\theta)$, the center of each area was determined C_F and C_S where the subscripts stand for face and side respectively, then the average distance travelled through this center to the sample boundary in the direction θ was determined by geometrical drawing. These were B_F for the face exit and B_S for the side, then the fractions $S_F(\theta)$ and $S_S(\theta)$ were determined using equation (5-19-a) i.e.

$$S_F(\theta) = \frac{1}{\mu B_F} \left\{ 1 - \exp(-\mu B_F) \right\}$$

$$S_S(\theta) = \frac{1}{\mu B_S} \left\{ 1 - \exp(-\mu B_S) \right\} \qquad (5\text{-}19\text{-}b)$$

The total fraction of gamma-rays escaping the sample was then determined by adding the weighted contributions for $S_F(\theta)$ and $S_S(\theta)$ i.e.

$$S(\theta) = \left\{ \frac{T_S}{T} \cdot (S_S(\theta)) + \frac{T_F}{T} \cdot (S_F(\theta)) \right\} \qquad (5\text{-}20)$$

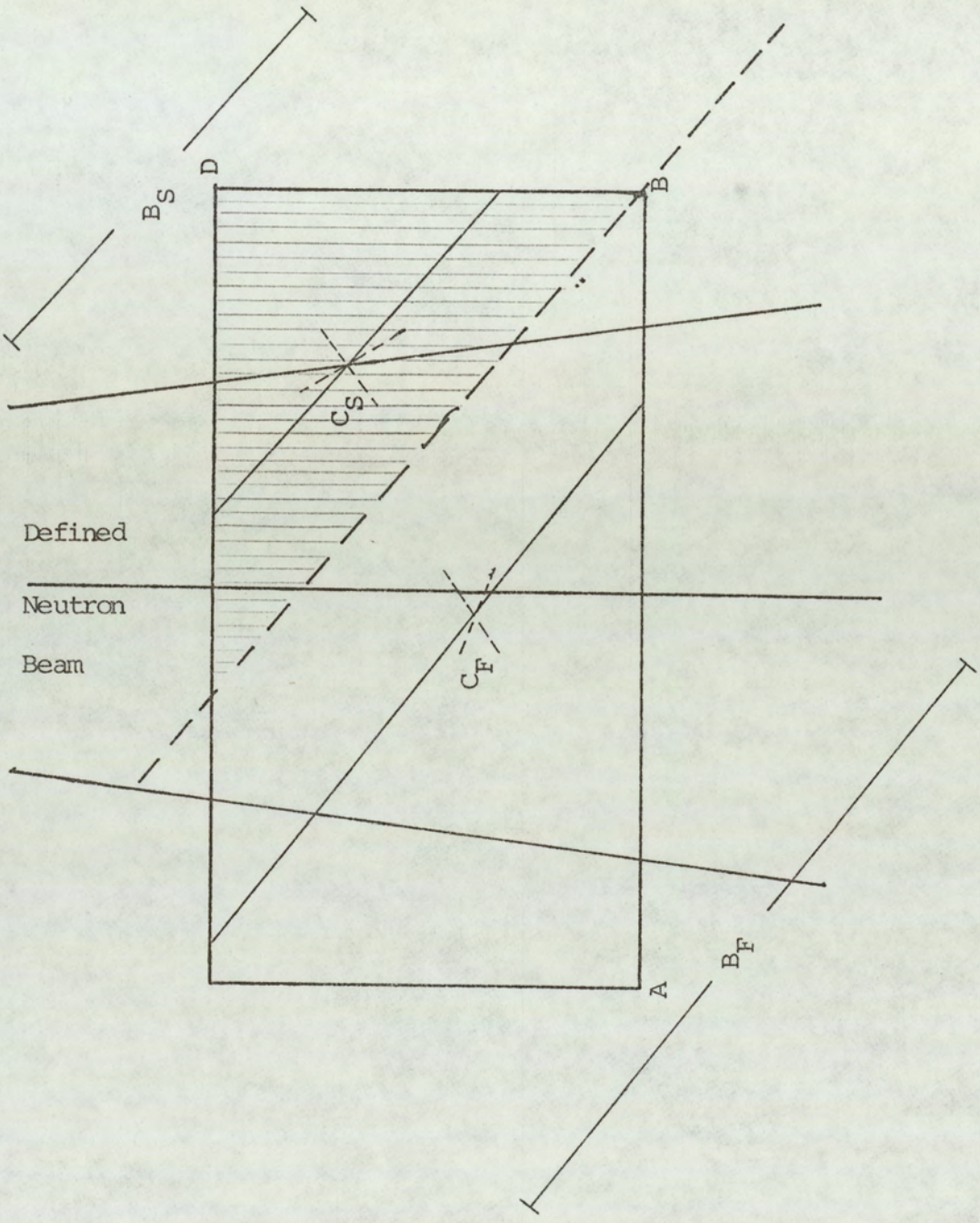

Figure (5-5) The parameters used for the calculation of S (θ) for mixed gamma-ray exit (face & side)

For each sample a separate diagram was drawn to find the side from which the gamma-rays escape from the sample and to determine the required parameters for the evaluation of S (θ).

5.7 The Solid Angle Calculation and the Geometry Factor

The solid angle subtended by the detector at the center of the sample can be calculated for a point source from

$$\Delta \Omega = \left(\frac{A}{R^2}\right) \qquad \text{Point Source} \qquad (5\text{-}21)$$

where A = the area of the detector face = $\frac{\pi D^2}{4}$

D = the crystal diameter

R = Sample-detector separation

In case of an extended source, a similar analysis to that made for the calculation of S (θ) was employed and a factor called "The Geometry Factor" was derived to take account of the fact that the gamma-rays were not coming from a point source.

The effective source area was calculated by considering the actual dimensions of the source inside the sample as determined by the defined neutron beam in both the horizontal and vertical directions. This is shown for both the side and face exit in Figure (5-6). The area of the face exit (A_F) and the area of the side exit (A_S) were calculated. Using the values of (T_F) and (T_S) defined in Section 5-6 the projected area on a plane parallel to the plane of the detector face

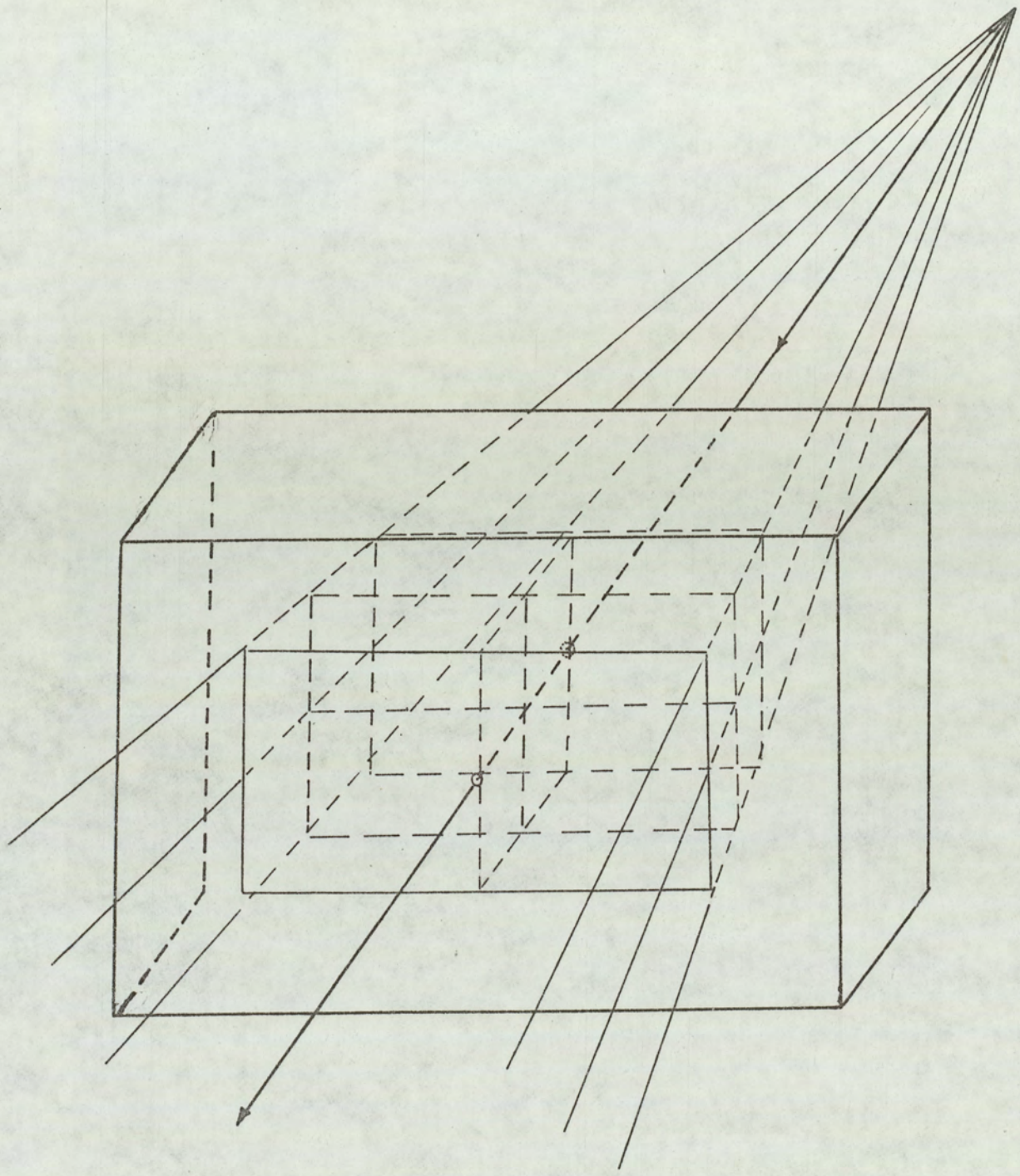

Figure (5-6) The effective gamma-ray source inside the scattering sample .

was calculated using the formula

$$A = A_F \cos(\theta) \left(\frac{T_F}{T}\right) + A_S \cos(90 - \theta)\left(\frac{T_S}{T}\right) \quad (5\text{-}22)$$

The geometry factor is then defined as

$$GF = \frac{A}{A_D}$$

Where A_D = The area of the detector face.

5.8 The Calculation of the Differential Cross-Section :-

Taking into account all the above factors, the equation used for the calculation of the differential cross-section for the production of gamma-ray of energy E_γ is given by:

$$\frac{d\sigma(\theta)}{d\Omega} = \frac{(P(\theta)/\Omega) \cdot GF}{(\phi_n(\theta) \cdot F_1 \cdot F_2)\ S(\theta, E_\gamma)\ \varepsilon(E_\gamma) \left\{\frac{1}{\sigma_t}(1 - \exp(-\Sigma_t X)\right\}} \quad (5\text{-}23)$$

where :

$(P(\theta)/\Omega)$ = No. of gamma-rays of energy E_γ per unit solid angle

GF = Geometry factor

$\phi_n(\theta)\ F_1, F_2$ = The corrected total number of neutrons incident onto the sample

$S(\theta, E_\gamma)$ = Fraction of gamma-rays of energy E_γ escaping the scattering sample without interaction.

$\varepsilon(E_\gamma)$ = The gamma-ray detector efficiency for gamma-rays of energy E_γ .

σ_t, Σ_t = The total microscopic and macroscopic cross-sections at neutron energy of 14 MeV

X = The sample thickness.

PART II

ABSOLUTE DIFFERENTIAL CROSS-SECTION MEASUREMENTS, RESULTS

5.9 The Differential Cross-Section Measurement Procedure :

The full description of the electronic system and its setting has been given in Section (3.4). The gamma-ray spectra were observed for the measurement of the differential cross-section as follows;

The electronic system was switched on for at least one hour prior to taking any measurement to allow the system to stabilise. The neutron source was run for about 45 min., before the experiment to allow the activity of the gamma-ray detector and the target assembly to reach a steady level.

Prior to the gamma-ray spectrum accumulation for each sample, a time of flight spectrum was obtained from the sample to determine the gamma-ray peak position and hence the single-channel analyser window setting to eliminate any possible error that could result from gain shift in the electronics.

The gamma-ray spectra were accumulated by performing alternate runs with the sample in position and the pulse height analyser in the "ADD" mode, followed by a run with the sample removed and the pulse height analyser in the "SUBTRACT"mode, to subtract the background from the spectrum. The runs were made for the same integrated alpha-count as monitored on the scaler, and as far as possible the same alpha-

rate as monitored on the rate-meter to keep the times and hence the effect of the activity the same for the add and subtract modes. A single data accumulation period was about 25 mins., after which the spectrum was printed out on paper. The background was then subtracted and the corrected spectrum was printed out. The cycle was then repeated until sufficient data for statistical accuracy was accumulated.

5.10 The Stability of the Neutron Beam

Considering equation (5-3) which relates the differential cross-section to the gamma-ray yield, the neutron flux and the number of nuclei in the target ie.

$$\frac{d\sigma(\theta)}{d\Omega} = \frac{g\ (\theta)}{\phi\ N} \qquad (5.3)$$

It follows that $g\ (\theta) \propto \phi$ ie. the gamma-ray signal count rate is proportional to the neutron production rate ($\phi = N_R\ (t) \cdot t$, where $N_R(t)$ is the neutron production rate.

The recorded background results from random coincidences between the background flux incident onto the gamma-ray detector and the alpha-detector pulses. These latter pulses are produced by the alpha-particles and the background activity in both the detector and the target assembly. Since the first of the two fluxes is proportional to the neutron production rate and the second to the alpha-particle production rate which is equal to the neutron production rate, it follows that the background is proportional to the square of the neutron production rate ie.

$$BG(t) \propto N_R(t)^2$$

The above discussion illustrates the necessity of keeping the neutron production rate constant during the accumulate and background runs if the correct background contribution is to be subtracted from the spectrum.

5.11. Experimental Results For the Iron Samples

5.11.1. Gamma-ray Spectra and Interpretation :

The gamma-ray spectra were accumulated at scattering angles ranging from 30° to 90° in steps of 10° for the thin iron sample (thickness 2 cm). Figure (5-1) shows typical gamma-spectrum obtained from this sample at the scattering angle of (50°).

For the thick samples, (thickness, 7.6 cm and 10.4 cm), the measurements were made at the scattering angles 30°, 50°, 70° and 90°. Typical gamma-ray spectra from these samples are shown in Figures (5-7) and (5.8) . For all the iron measurements, the gamma-ray discriminator level was set to reject pulses from gamma-rays having an energy less than 0.6 MeV. All the iron spectra show several well resolved peaks, the most intense of these being at 0.84 MeV and 1.24 MeV, other peaks can be seen at 1.81 MeV and there is an indication of higher energy peaks at 2.13 MeV and 2.78 MeV. corresponding to higher excited states in iron.

Figure (5.9a) shows the energy level scheme of the ^{56}Fe

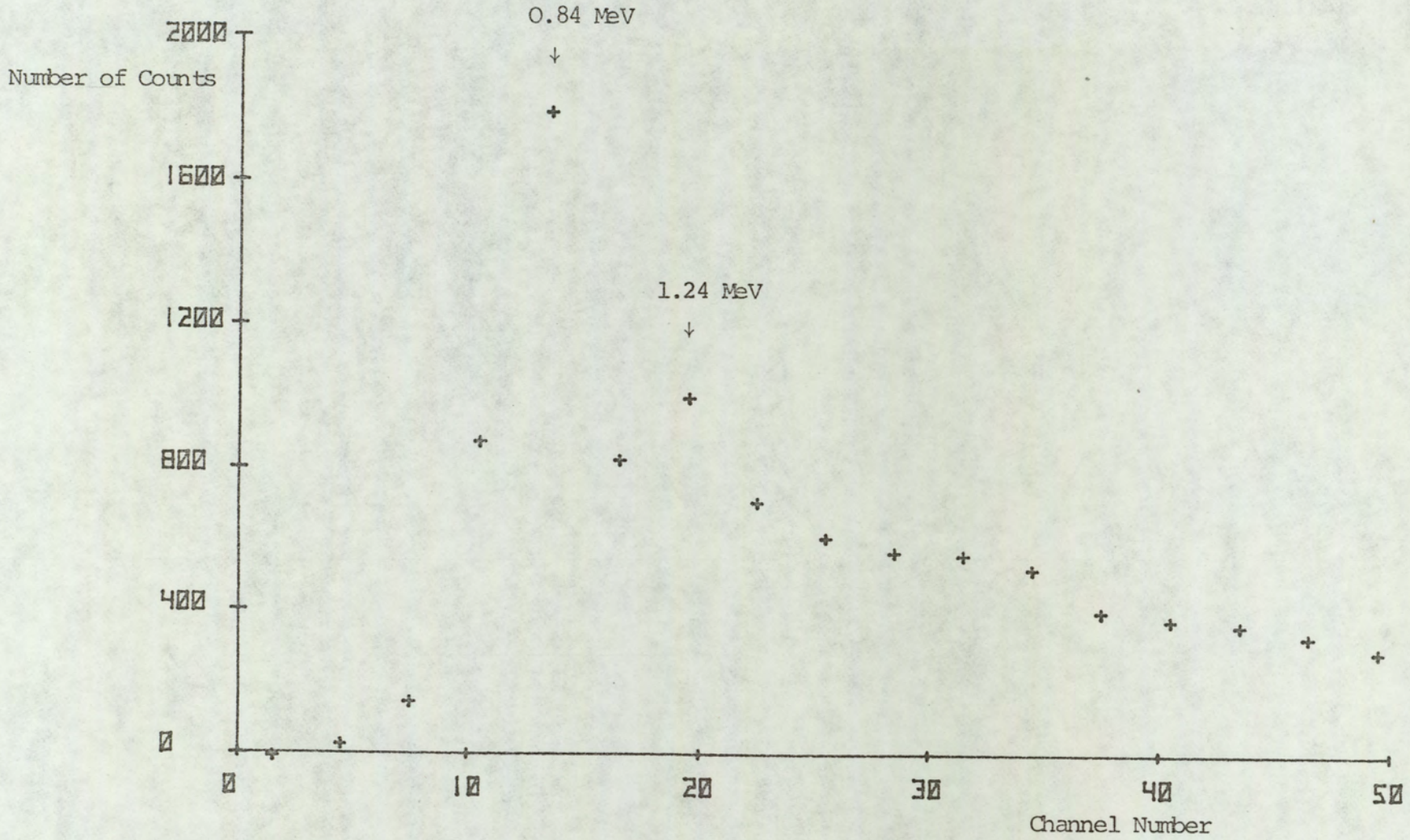

Figure (5-7) Gamma-ray energy spectrum from thick iron sample of 7.6 cm thickness at scattering angle of 30^{o} .

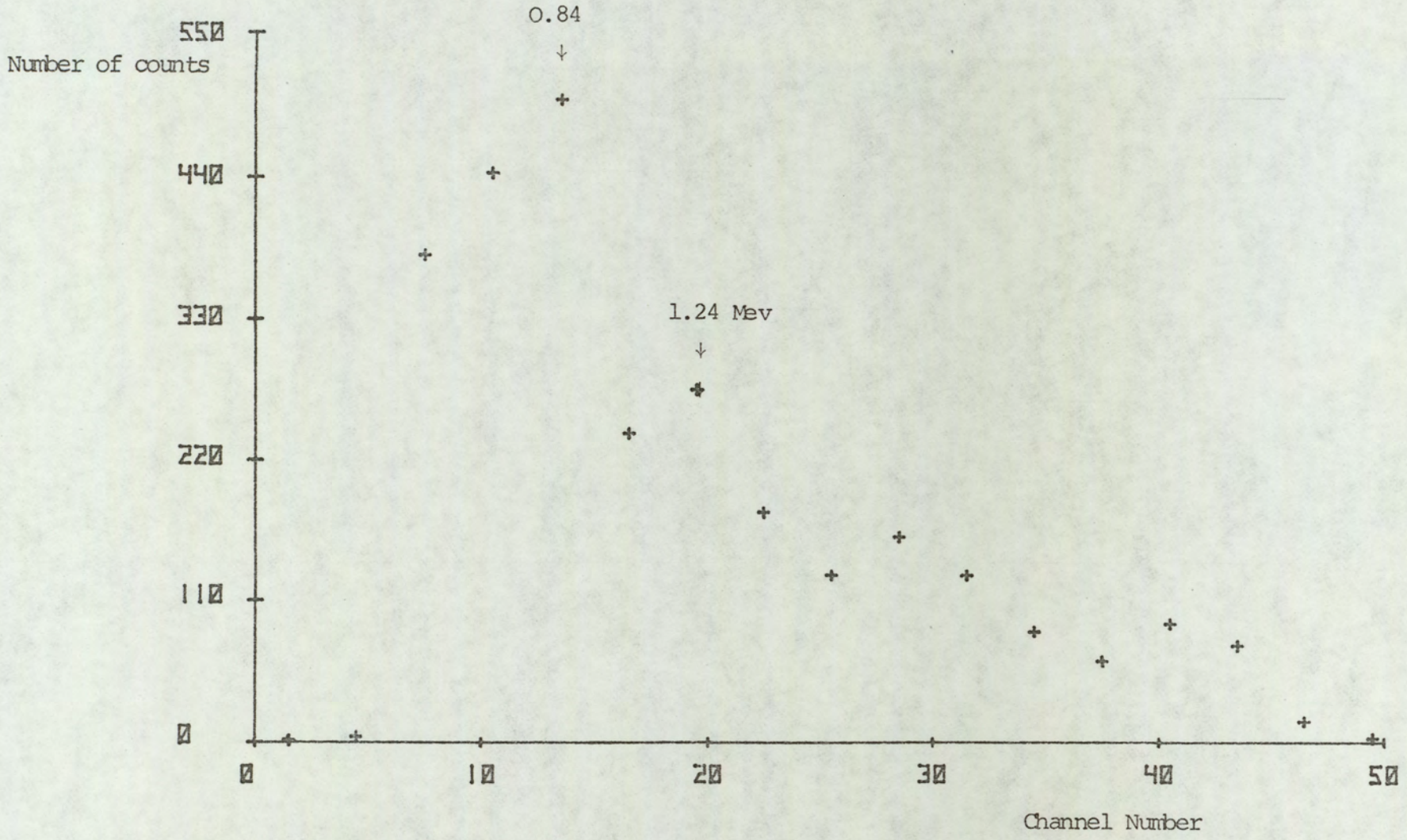

Figure (5-8) Gamma-ray energy spectrum from 10.4 cm thick iron sample at scattering angle of 90^{o} .

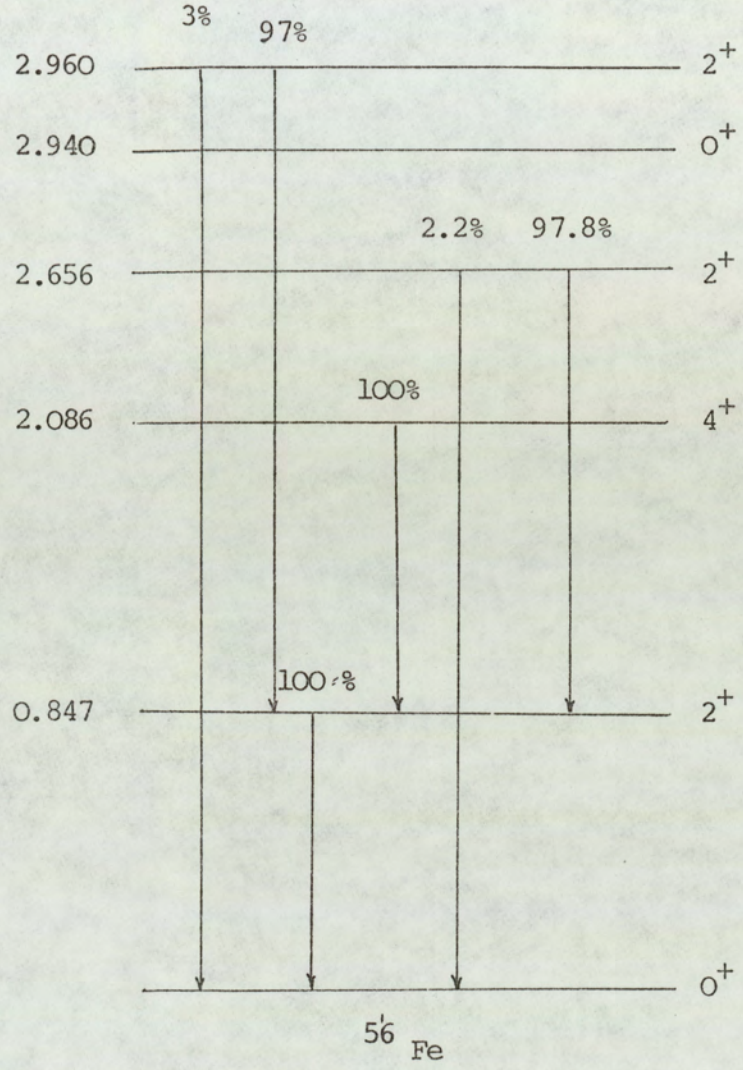

Figure (5-9a) Energy level scheme of ^{56}Fe nucleus .
Branching ratios from Rao [89]

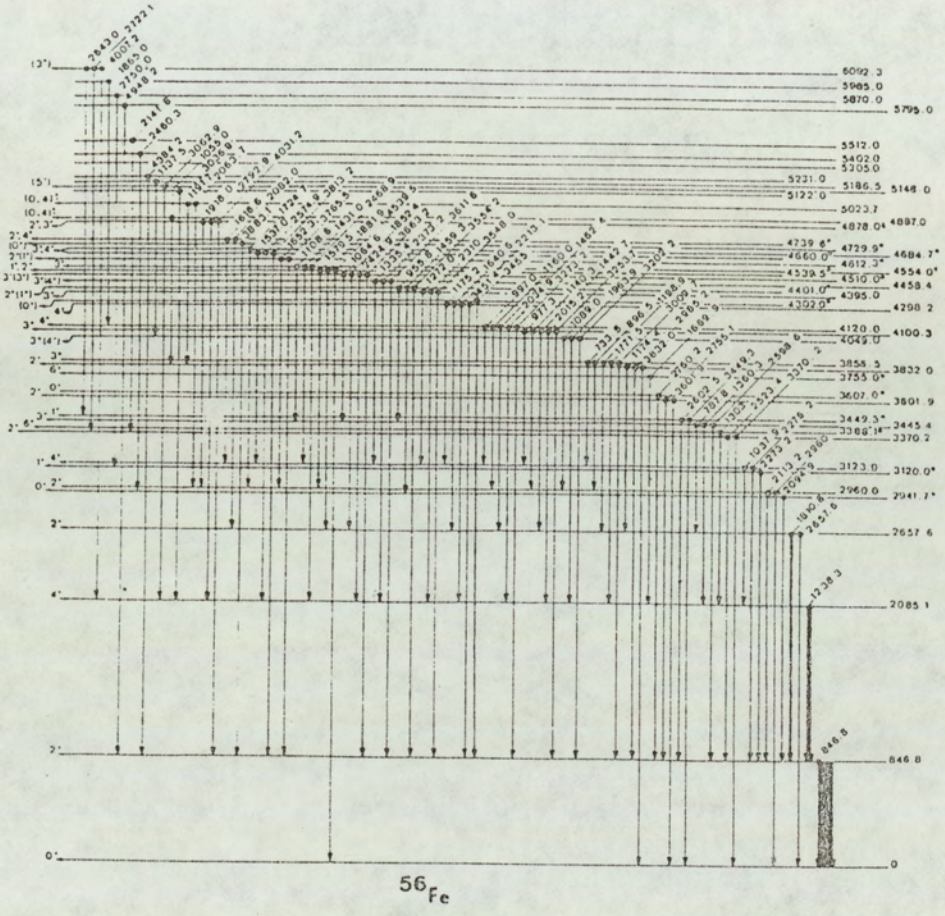

Figure (5-9b) Energy level scheme of the ^{56}Fe nucleus proposed by Lachkar et al[6].

nucleus, as reported by Roa [89] while Figure (5.9) shows a proposed energy level scheme by Lachkar et al., [6] for the same nucleus. From these figures several of the gamma-ray peaks can be identified, the 0.84 MeV is due to transition from the first excited state (2^+) to the ground state which results in the emission of gamma-rays of energy 0.8468 MeV, while the 1.24 MeV peak is the result of the transition between the second excited state (4^+) at 2.0851 MeV and the first excited state. The 1.81 MeV is due to the transition between the third excited state (2+) and the first excited state (2^+). The third level at 2.658 MeV decays with 97.8% probability to the first excited state with the emission of 1.81 MeV gamma-rays and with 2.2% probability to the ground state emitting 2.658 MeV gamma-rays [90].

The isotopic abundance of the other naturally occurring iron isotopes is 5.87% for the ^{54}Fe and 2.17% for the ^{57}Fe. The ^{57}Fe yields gamma-rays with energies below 0.7 MeV, but since these γ-rays cannot be resolved from the 0.84MeV peak or are below the gamma-ray discriminator level, and the low isotropic abundance of ^{57}Fe, the contributions from ^{57}Fe can be ignored. The ^{54}Fe yields a gamma-ray of energy 1.409 MeV [90] from the transition from the first excited state to the ground state. Although there is an indication of the presence of this peak, the statistics are not good enough to enable it to be resolved.

5.11.2. Possible Competing Reactions :

Table (5.7) below gives the values of the total non-elastic

scattering cross-sections and the total inelastic scattering cross-sections for the interaction of 14 MeV neutrons with ^{56}Fe.

Non-elastic Scattering Cross-Section	Inelastic Scattering Cross-Section	Source
1.40033 barns	0.74922 barns	ENDF BIV[96]
-	0.78	Asami et al.,[97]
1.36 $\pm$ 0.03 "	0.62 $\pm$ .16	Stehn et al.,[92]

Table 5.7. The total non-elastic and inelastic cross-sections for the interaction of 14 MeV neutrons with ^{56}Fe.

Although it is possible to interpret the observed spectrum by considering inelastic scattering only, other non-elastic scattering reactions also produce gamma-rays in the same energy range.

The (n, 2n) reaction having cross-section of (440 $\pm$ 90) mb may result in the emission of gamma-rays of energy 0.805, 0.93, 1.21 and 1.316 MeV[90] from the decay of ^{55}Fe formed in the reaction to the ground state. ^{55}Fe decays to ^{55}Mn by electron capture with a half-life of 2.6 years. The peaks due to the detection of the 0.805 and 0.930 MeV gamma-rays cannot be resolved from the 0.845 MeV peak due to the limited resolution of the Na I (Tl) detector. Engesser et al.,[98] reported the detection of 0.92 MeV gamma-rays and they attributed it to the transitions (1.32 MeV to 0.4 MeV) and (0.93 MeV to zero) in the

^{55}Fe resulting from the ^{56}Fe (n,2n) $^{55}Fe^*$ reaction, they also reported that the 1.33 MeV gamma-ray peak in the iron spectrum is the result of the reactions ^{56}Fe (n, n) $^{56}Fe^*$ followed by the decay of the 3.54 MeV level to the 2.09 MeV level and also ^{56}Fe (n,2n) $^{55}Fe^*$ and the transition 1.32 MeV to the ground state. However, Engesser et al.,[98] reported no evidence of the 0.805 and the 1.21 MeV gamma-rays. The third peak reported due to the (n,2n) reaction is at 0.41 MeV but this peak is not seen because of the discriminator level. The same results were found by Jönsson et al., [91].

The number of counts in the 0.84 MeV peak should thus be corrected for a possible contribution from the 0.93 MeV peak from the $^{55}Fe^*$, and the counts in the 1.24 MeV peak should be corrected for the contribution due to the 1.33 MeV peak from the $^{55}Fe^*$.

Table (5.8) shows the differential gamma-ray production cross-sections of the above gamma-ray energies as reported by several authors and the results of the present work.

The disagreement between Engesser and Jönsson has two possible explanations

a) The different gamma-ray detectors used, while it can be expected that the 0.93 MeV peak can be resolved completely using Ge-Li detector, it is difficult to resolve it from the 0.845 MeV peak using Na I (Tl) detector.

Table 5.8. The differential cross-sections for $^{56}Fe\ (n,n'\gamma)^{56}Fe$ for the production of different gamma-rays.

REFERENCE		$(d\sigma(\theta)/d\Omega)$ mb / Sr				NOTES
		0.845 MeV	0.93 MeV	1.24 MeV	1.33 MeV	
Engesser et al.[98]	90^{o}	56.9 ± 5.8	11.7 ± 3.9	23 ± 2.3	7.4 ± 2.5	NaI (Tl)
Jönsson et al.[91]	av (80^{o}-150^{o})	74.7 ± 0.7	4.4 ± 0.4	21.4 ± 0.6	5.2 ± 1.6[a]	Ge(Li)
	80^{o}	68.2 ± 0.7[c]	4 ± 0.4	19.6 ± 0.6	4.8 ± 1.4[b]	
Lachkar et al.[6]	80^{o}	67.0 ± 6	-	26 ± 5.2	-	Ge(Li)+ NaI(Tl)
	90^{o}	65.5 ± 6.6	-	32.3 ± 7	-	
Present work	80^{o}	65.8 ± 5.9	-	28.3 ± 2.97	-	
	90^{o}	63.8 ± 6.7	-	35.1 ± 3.69	-	NaI (Tl)

(a) E_{γ} = 1.305

(b) E_{γ} = 1.316

(c) The cross-section hasbeen corrected for the contribution from the (n, p) reaction.

b) The results of Jönsson et al., are the averages of the differential cross-sections over the range 50^{o} to 110^{o} due to the large angular acceptance of the detector, thus the angular distribution of the 0.93 MeV gamma-ray is thus not known.

However, the values of Jönsson et al.,[91] are preferred mainly because they used the Ge-Li detector with its better resolution and because of the smaller quoted uncertanties attached to the measurement.

The other reaction that would contribute to the count in the 0.845 MeV gamma-ray peak is the (n, p) reaction vs.

$$^{56}Fe\ (n,\ p)\ ^{56}Mn^{*} \xrightarrow{\beta^{-}} {}^{56}Fe^{*}$$

The total cross-section for this reaction is given in Table (5.9) as reported by several workers.

Table (5.9) The total cross section for the ^{56}Fe (n, p) reaction

σ (n, p) in (mb)	Reference	Comments
84 $\pm$ 13	Jönsson et al.,[91]	Experimental, Ge-Li detector
82 $\pm$ 7	Allan et al., [99]	Experimental
112 $\pm$ 6	Stehn et al.,[92]	
125	ENDF B IV [96]	Evaluated

Finally, the ^{56}Fe (n,d) $^{55}Mn^*$ reaction may yield gamma-rays of 0.983 MeV and 0.857 MeV due to the transitions between the second and the ground state or the first excited state. The total cross-section for this (n,d) reaction was estimated by Allenby[44] to be 36 ± 160 mb while the ENDF B IV value is given as 19 mb.

However, in the present work, it was assumed that observed spectra are mainly from the neutron inelastic scattering from the ^{56}Fe because the angular distributions of these competing reactions were not available.

5.11.3. The results of The Differential Gamma-Ray Production Cross-Section Measurements for Iron Samples

The cross-sections were calculated using equation (5-23) namely.

$$\frac{d\sigma(\theta)}{d\Omega} = \frac{P(\theta)/\Omega \quad GF}{(\phi_n(\theta)\cdot F_1 . F_2) \quad S(\theta, E\gamma).\varepsilon(E\gamma)\left\{\frac{1}{\sigma_t}(1 - e^{-\Sigma t X})\right\}} \quad (5.23)$$

where all the quantities were defined in Part I of this Chapter.

Tables (5-10) and (5-11) summarise the experimental results for the angular distributions obtained for the production of the 0.84 and the 1.24 MeV gamma-rays respectively from iron samples.

The experimental errors in the factors of equation (5.23) used for the differential cross-section calculation are listed in Table (5.12)

Table 5.10

The angular distribution for the $^{56}Fe\ (n,n'\gamma)\ ^{56}Fe$ for the production of 0.84 MeV gamma-rays

Scattering angle θ^{o}	$(d\sigma\ (\theta) / d\Omega)$ mb /Sr.		
	Sample thickness indicated in the first row below		
	2 cm = 0.441 mfp	7.6 cm = 1.68 mfp	10.4 cm = 2.3 mfp
30	73.3 ± 7.7	96.1 ± 10.1	108.8 ± 11.4
40	77.8 ± 8.2		
50	75.1 ± 7.9	92.2 ± 9.7	102.6 ± 10.8
60	71.7 ± 7.5		
70	69.1 ± 7.3	86.8 ± 9.1	101.0 ± 10.6
80	65.8 ± 6.9		
90	63. ± 6.7	77.8 ± 8.2	83.2 ± 8.7

Table (5.11)

The Angular distribution for the Production of 1.24 MeV gamma-rays From $^{56}Fe\ (n,n'\gamma)\ ^{56}Fe$

Scattering angle θ^{o}	$(d\sigma(\theta) / d\Omega)$ (mb/sr)		
	Sample thicknes in the first row below		
	2 cm	7.6 cm	10.4 cm
30	34.7 ± 3.7	53.9 ± 5.7	61.1 ± 6.4
40	39.6 ± 4.2		
50	31.8 ± 3.3	45.9 ± 4.8	52.2 ± 5.4
60	40.8 ± 4.29		
70	39.2 ± 4.1	46.6 ± 4.9	43.4 ± 4.5
80	28.3 ± 3.0		
90	35.1 ± 3.7	43.1 ± 4.5	32.3 ± 3.4

below for the iron samples.

Table (5.12)

The experimental errors in the factors of equation (5.23)

Factor	Error
$P(\theta)$	8%
$\phi_n(\theta)$	1%
$S(\theta, E_\gamma)$	2%
Ω	4%
Neutron att. factor	3%
Peak efficiency $\varepsilon(E_\gamma)$	3.5%

The values listed in the above table are the averages over the angular range of interest (30° to 90°). The total error was obtained by adding the individual errors in quadrature. The experimental errors are shown by error bars in the angular distribution curves and the curves showing the variation of the differential cross-section with thickness discussed in Sections (5.11.4) and (5.11.5) respectively.

5.11.4 The Angular Distributions For the Iron Samples

5.11.4.1. The Angular Distribution of the $^{56}Fe(n,n'\gamma)^{56}Fe$ for the Production of 0.84 MeV Gamma-Rays

The measured values of the differential cross-section for

the production of the 0.84 MeV gamma-rays in Table (5.1o) were plotted in Figures (5.10) through to (5.12) for the three iron samples used. In Figure (5.10) the results of the present work are compared with other workers' results.

In each of the above mentioned figures, the solid line represents a least squares fit to the experimental data points. The general equation representing these fits is given by

$$\frac{d\sigma(\theta)}{d\Omega} = (A_o \pm \alpha_o) + (A_2 \pm \alpha_2) \cos^2\theta + (A_4 \pm \alpha_4) \cos^4\theta \qquad (5.24)$$

and the equation for each curve is given below the figure.

The derivation of equation (5.24) is given in Appendix (B) with the computer program used to determine the coefficients A_o, A_2, and A_4 and also the errors in these coefficients, ie. α_o, α_2, and α_4 respectively.

It can be seen from Figure (5.10) that there is a good agreement between the present results and the published ones except for Abbondanno et al.,[100] results which gives lower values for the differential cross-section. A possible explanation for their results could be that they under-estimated the peak area and hence, the number of gamma-rays produced, this can be seen in Figure (5.13) which shows the gamma-ray spectrum obtained from sodium sample at scattering angle of 60^o, which was the only spectrum published in their paper [100].

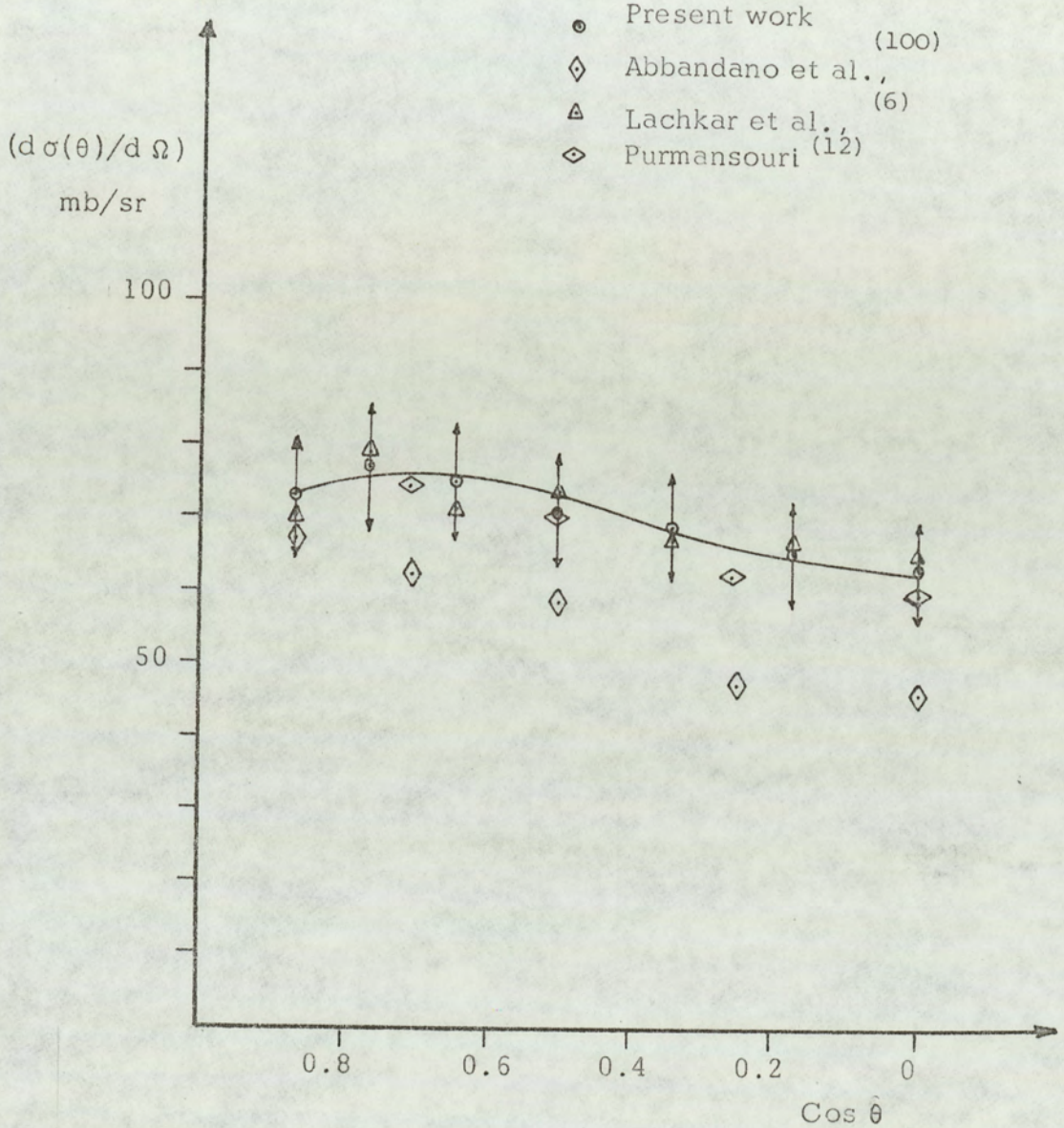

Figure (5-10). The angular distribution for the $^{56}Fe(n,n'\gamma)^{56}Fe$ 0.845 MeV gamma-rays. Sample thickness 2 Cm.

The equation describing the fitted line is

$$\frac{d\sigma(\theta)}{d\Omega} = (63.53 \pm 0.49) + (51.50 \pm 1.91)\,Cos^2\theta - (50.71 \pm 1.70)\,Cos^4\theta$$

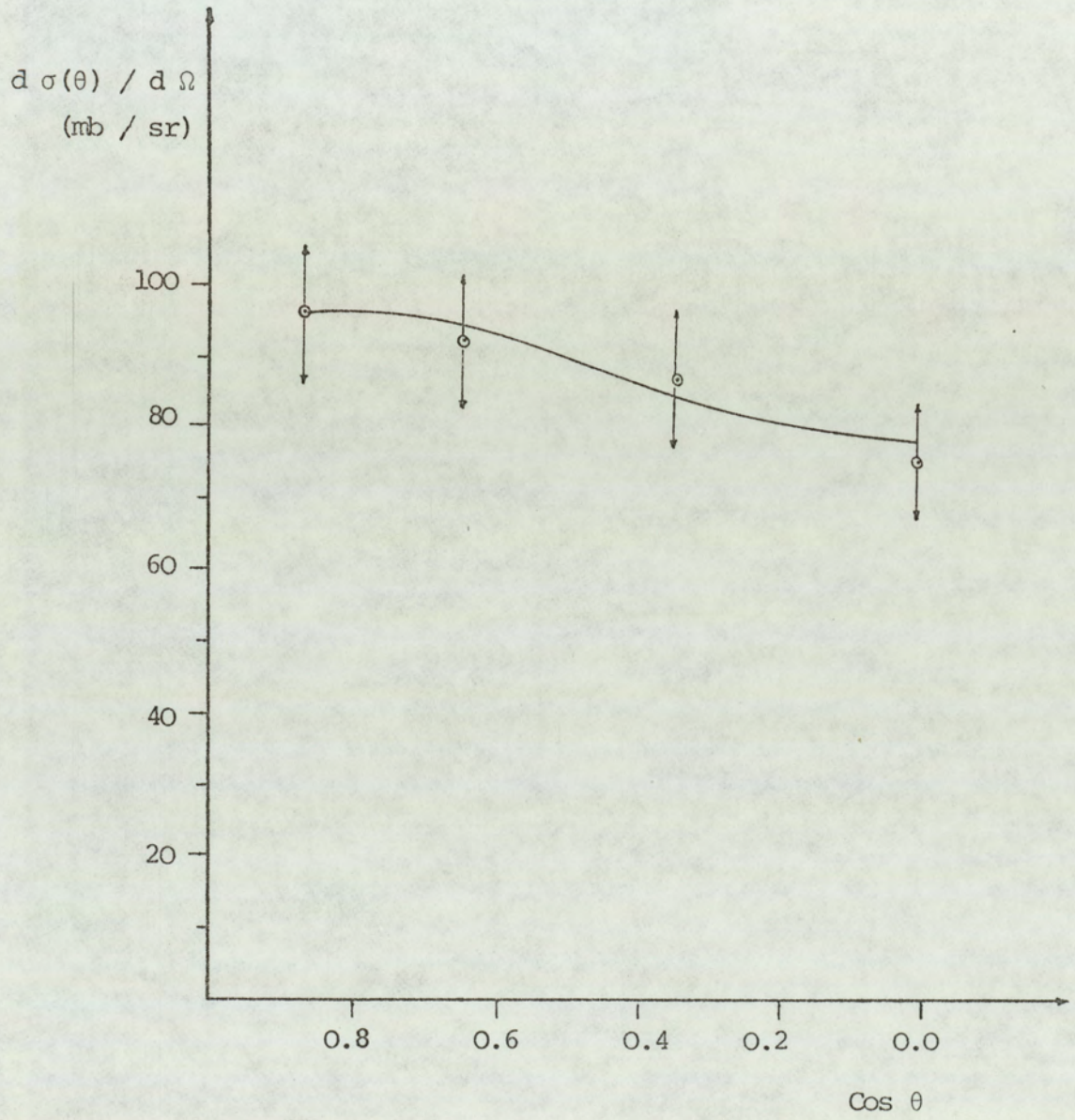

Figure (5-11) The angular distribution for the ^{56}Fe $(n,n\gamma)^{56}$Fe 0.84 MeV gamma-ray . Sample thickness = 7.6 cm.

The equation describing the fitted line is

$$d\sigma(\theta)/d\Omega = (78.52 \pm 1.58) + (58.0 \pm 4.15)\cos^2\theta - (47.37 \pm 5.49)\cos^4\theta$$

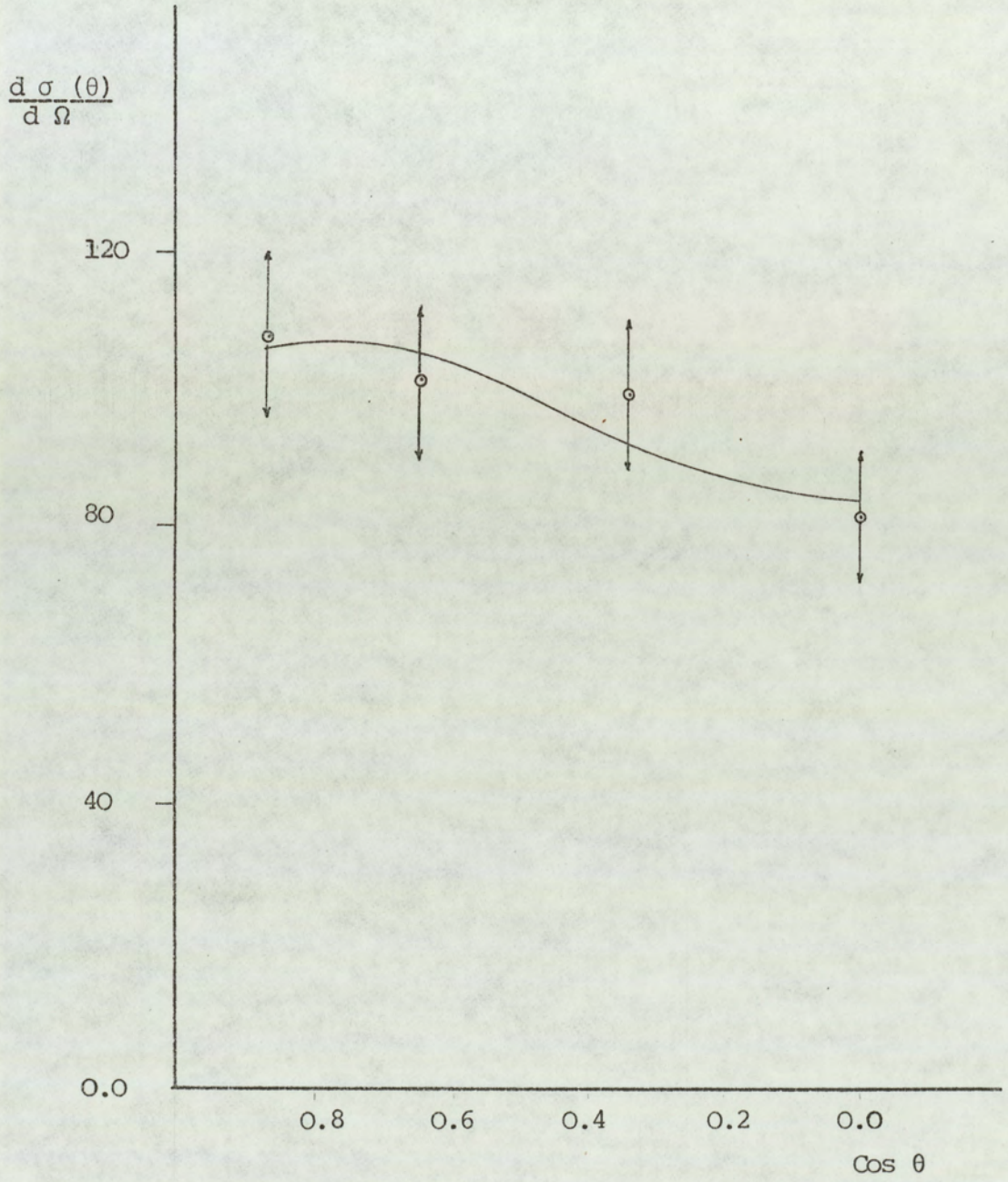

Figure (5–12) The angular distribution for the $^{56}Fe(n,n'\gamma)^{56}Fe$ 0.845 MeV gamma-ray. Sample thickness = 10.4 cm .

The equation describing the fitted line is ,

$$\frac{d\sigma(\theta)}{d\Omega} = (86.3 \pm 4.3) + (78.9 \pm 11.2)\,Cos^2\theta - (68.0 \pm 14.1)\,Cos^4\theta$$

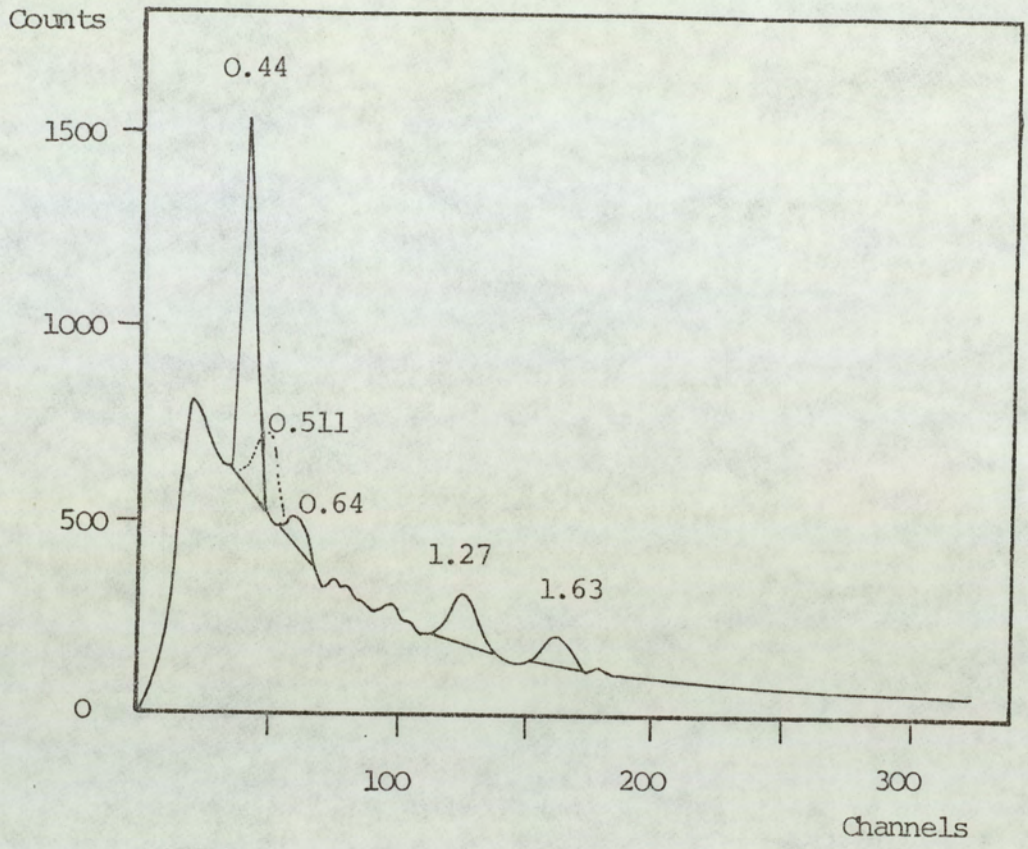

Figure (5-13) Gamma-ray spectrum obtained from Sodium sample at scattering angle 60° . Abbandanno et al [100]

5.11.4.2. The Integrated Cross-Section for the Production of 0.84 MeV Gamma-Rays By the $^{56}Fe(n,n'\gamma)^{56}Fe$ Reaction

Both compound nucleus and direct interaction theories of nuclear reaction predict that the angular distributions are symmetrical about the 90° setting angle in the centre of mass system, which is supported further by many reported gamma-ray angular distribution measurements from the interaction of 14 MeV to 15 MeV neutrons in the angular interval 0° to 180°.[5,6,102,103]

The integrated cross-section for gamma-ray production is obtained by integrating the differential cross-section over 4π solid angle, i.e.

$$\sigma(n,n'\gamma) = \int_{4\pi} \left(\frac{d\sigma_{n,n'\gamma}(\theta)}{d\Omega} \right) d\Omega$$

$$= \int_{\phi=0}^{2\pi} \int_{\theta=0}^{\pi} \left(\frac{d\sigma(\theta)}{d\Omega} \right) \sin\theta \, d\theta \, d\phi \qquad (5.25)$$

If the differential cross-section is independent of azimuth, Φ, about the incident beam direction, the integrated cross-section is given by

$$\sigma(n,n\gamma) = 2\pi \int_{0}^{\pi} \left(\frac{d\sigma_{n,n'\gamma}(\theta)}{d\Omega} \right) \sin\theta \, d\theta \qquad (5.25a)$$

upon using the fact that the distribution is symmetrical about the 90° scattering angle, equation (5.25 a) can be rewritten as

$$\sigma\ (n,n\ \gamma) \quad = \quad 4\ \pi \int_{o}^{\pi/2} \left(\frac{d\ \sigma\ n,n\gamma\ (\theta)}{d\ \Omega} \right) \text{Sin}\ \theta\ d\theta \qquad (5.25.b)$$

(38,109)

From the analysis based on a statistical compound nuclear formalism the differential cross-section can be expressed in terms of the even powers of legendre polynomials, vis

$$\frac{d\,\sigma(\theta)}{d\ \Omega} \quad = B_o + B_2\ P_2\ (\theta\ ) \ + \ B_4\ P_4\ (\ \theta) \qquad (5.26)$$

where $P_2\ (\theta\ )$ and $P_4\ (\ \theta)$ are the second and fourth order legendre polynomials and B_o, B_2 and B_4 are constants.

Equation (5.26) reduces to the form

$$\frac{d\sigma(\theta)}{d\Omega} = A_o \ + \ A_2\ \text{Cos}^{\ 2}{}_{(\theta)} \ + \ A_4\ \text{Cos}^{\ 4}{}_{(\theta)} \qquad (5.27)$$

where A_o, A_2 and A_4 are new constants.

Equation (5.25 b) can be written as

$$\sigma\ (n,n\ \gamma) \quad = \quad 4\pi \int_{o}^{\pi/2} \left\{ \ A_o \ + \ A_2\ \text{Cos}^{2}\theta \ + \ A_4\ \text{Cos}^{4}\theta \ \right\} \ \text{Sin}\theta\ d\theta \qquad (5.28)$$

$$= \quad 4\ \pi \left\{ \ A_o \ + \ \frac{A_2}{3} \ + \ \frac{R_4}{5} \ \right\} \qquad (5.28a)$$

where the A's are the calculated coefficients from the fit of the experimental results to equation (5.27).

The error in the integrated cross-section is given by

$$\delta\sigma(n,n'\gamma) = \pm 4\pi\left(\alpha_o^2 + \frac{\alpha_2^2}{4} + \frac{\alpha_4^2}{25}\right)^{\frac{1}{2}} \qquad (5.29)$$

where the α_o, α_2 and α_4 are the errors in the coefficients A_o, A_2 and A_4 respectively. A detailed discussion and the derivation of the above equations is given in Appendix (B)

The integrated cross-section for the $^{56}Fe(n,n'\gamma)^{56}Fe$ (0.84) MeV gamma-ray was calculated for each of the three iron samples from the determined values of the coefficients and the results together with the values of the coefficients is shown in Table (5.13).

From Table (5.14) in which our results are compared to the published data, it can be seen that the present result agrees with the published ones within the quoted experimental errors except in the case of Martin and Stewart's results [5, 104] where the disagreement is about 28%. The values of $\left(\frac{d\sigma(\theta)}{d\Omega}\right)$ at 90^o quoted in the literature are spread over a wide range from 30.2 ± 9.1 mb /sr [105] to 79.2 mb/sr [104] however, since some workers calculated the integrated cross-section as $4\pi \times \left(\frac{d\sigma(\theta)}{d\Omega}\right)_{\theta = 90^o}$ without measuring the actual angular distribution itisjustified to conclude that the values of the integrated cross-sections in Table (5.14) are compatible within the experimental

Table (5.13)

The integrated cross-section for the $^{56}Fe\ (n,n'\gamma)\ ^{56}Fe$ 0.84 MeV gamma-rays and the calculated coefficient for the angular distribution

Sample Thickness cm	The values of the calculated coefficients			The integrated cross-section (mb)
	$A_o \pm \alpha_o$	$A_2 \pm \alpha_2$	$A_4 \pm \alpha_4$	
2	63.53 ± 0.49	51.48 ± 1.91	-50.71 ± 1.7	886.56 ± 10.93
7.6	78.52 ± 1.58	58.00 ± 4.15	-47.37 ± 5.48	1110.61 ± 29.77
10.4	86.32 ± 4.27	78.93 ± 11.19	-68.00 ± 14.81	1244.45 ± 80.35

errors.

Table (5.14)

Comparison of the present results for the thin sample (thickness 2 cm) with the published data. (Iron)

$\left(\frac{d\sigma(\theta)}{d\Omega}\right)_{\theta=90^\circ}$ (mb/sr)	Integrated cross-section (mb)	Reference
63.8 $\pm$ 6.4	887 $\pm$ 11	Present work
75.62 $\pm$ 8.97	1138 $\pm$ 135	Martin and Stewart (5)
79.2 $\pm$ 9.7	1228 $\pm$ 150	Martin and Stewart (104)
45.6 $\pm$ 5		
45.6 $\pm$ 5	721 $\pm$ 76	Abboundanno et al., (100)
65.5 $\pm$ 6	823 $\pm$ 82*	Lachkar et al., (6)
62.28 $\pm$ 4.42	814 $\pm$ 21	Allenby (44)
60.0 $\pm$ 4.6	754 $\pm$ 57	Poormansouri (12)

(*) Calculated as $4\pi \times \left(\frac{d\sigma(\theta)}{d\Omega}\right)_{\theta=90^\circ}$

5.11.4.3. The Angular Distribution for the $^{56}Fe(n,n'\gamma)^{56}Fe$, 1.24 MeV Gamma-Rays

The values of the differential cross-section for the production of 1.24 MeV gamma-rays following the inelastic scattering of 14 MeV neutrons by the different iron samples listed in Table (5.12) were plotted in Figures (5.14), (5.15) and (5.16) for the sample thickness 2 cm, 7.6 cm and 10.4 cm respectively.

As discussed in Section (5.11.4.1) and Appendix (B), the measured cross-sections were fitted to the form of a cosine power series of legendere polynomials, i.e.

$$\left(\frac{d\sigma(\theta)}{d\Omega}\right) = (A_o \pm \alpha_o) + (A_2 \pm \alpha_2)\,\mathrm{Cos}^2\theta + (A_4 \pm \alpha_4)\mathrm{Cos}^4\theta$$

The solid line in the above Figures represent the fitted cross-sections while the circles with the error bars represent the experimental results and the error respectively. In Figure (5.15) the present result is compared to the results of other workers, but no similar experimental measurements could be found for large sample thicknesses except in the work of Pourmansouri[12] where 4 cm was the thickest sample studied. This thickness is only about 50% of the second iron sample in the present measurement, since the differential cross-section for the thick sample were calculated for energy regions one MeV wide in the spectrum rather than for energy levels of specific gamma-ray energies, Pourmansouri's results could not be compared to the present result.

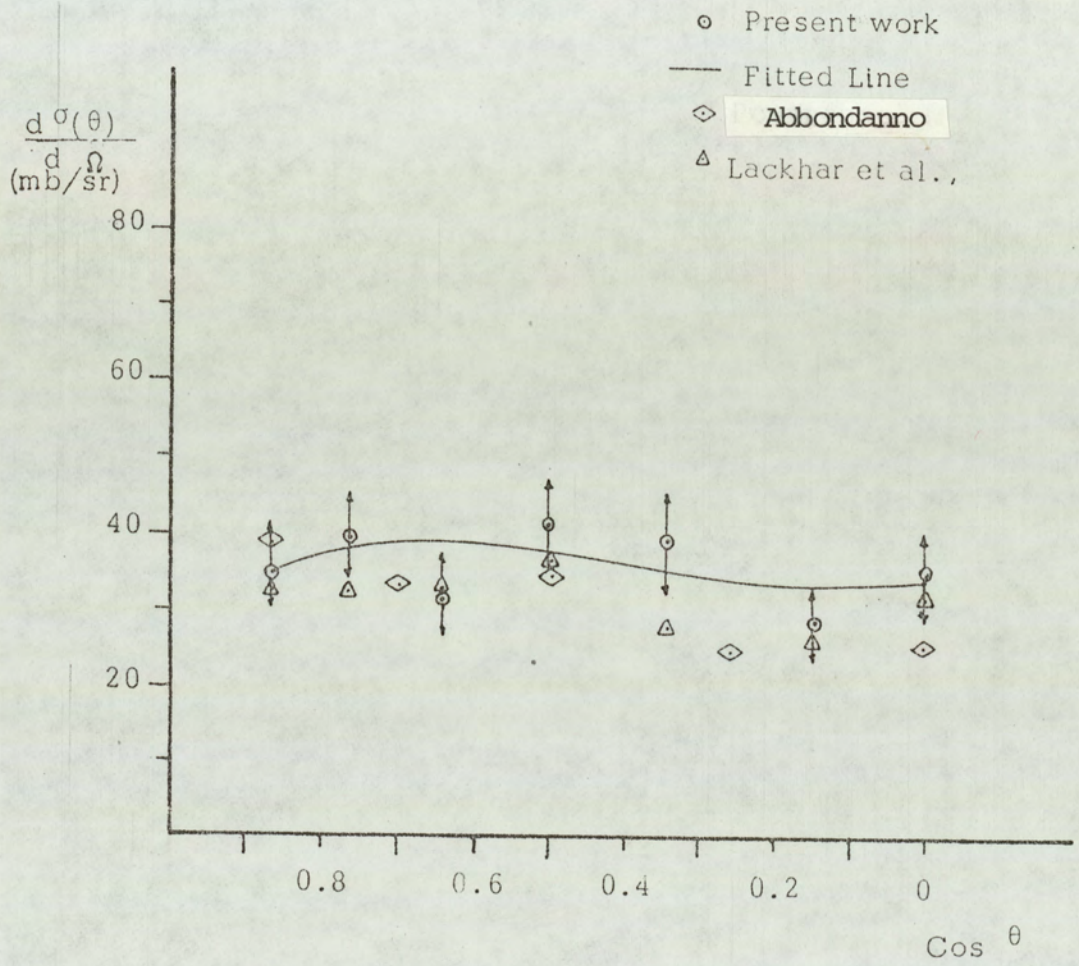

Figure (5-14) The angular distribution for the $^{56}Fe(n,n'\gamma)^{56}Fe$ 1.24 Mev gamma-ray from iron sample.

Sample thickness = 2 cm. = 0.442 mfp.

The solid line represents the fit to the equation

$$\frac{d\sigma(\theta)}{d\Omega} = (32.93 \pm 1.9) + (25.71 \pm 7.48)\,Cos^2\theta - (3.30 \pm 6.67)\,Cos^4\theta$$

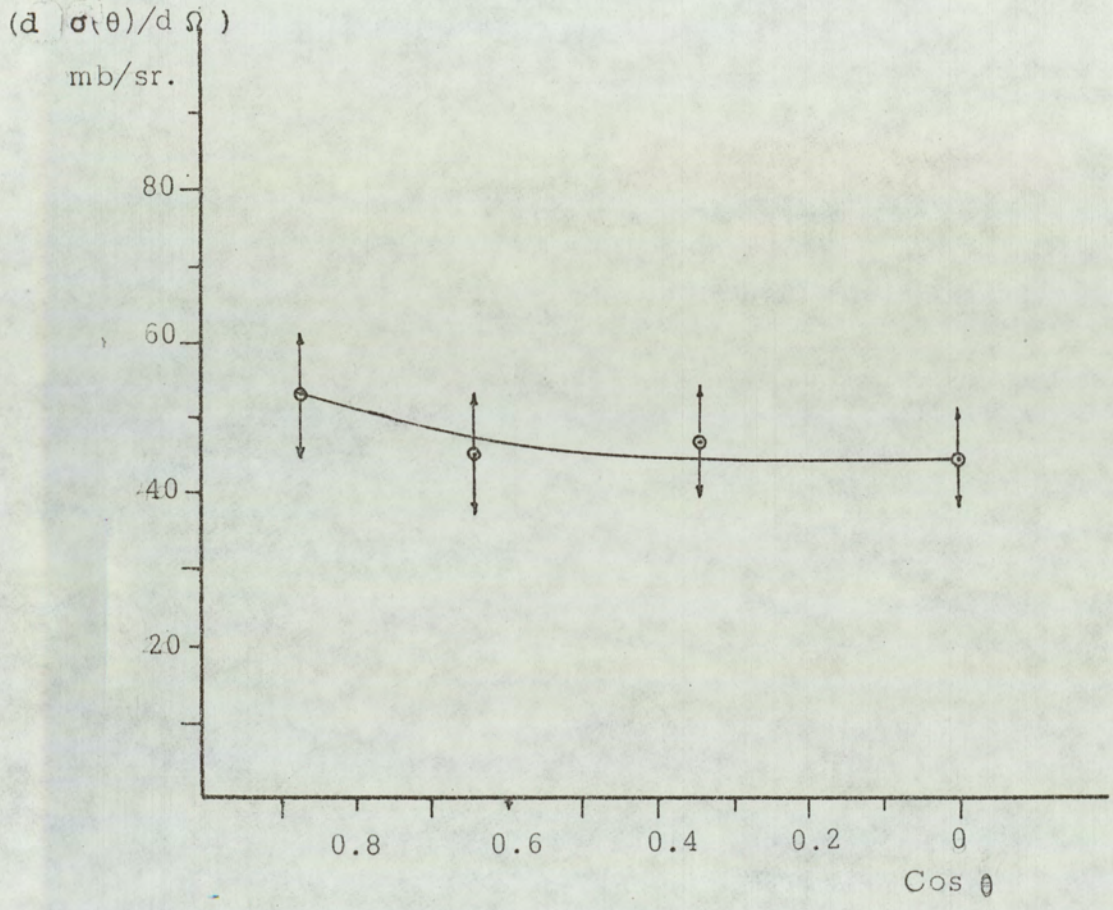

Figure (5-15) The angular distribution for the $^{56}Fe(n,n'\gamma)^{56}Fe$ 1.24 MeV gamma-rays from iron samples.
Sample thickness 7.6 cm = 1.68 mfp.
The solid line represents the fit to the equation.

$$\frac{d\sigma(\theta)}{d\Omega} = (44.48 \pm 1.35) - (2.08 \pm 3.54)\cos^2\theta + (19.22 \pm 4.69)\cos^4\theta$$

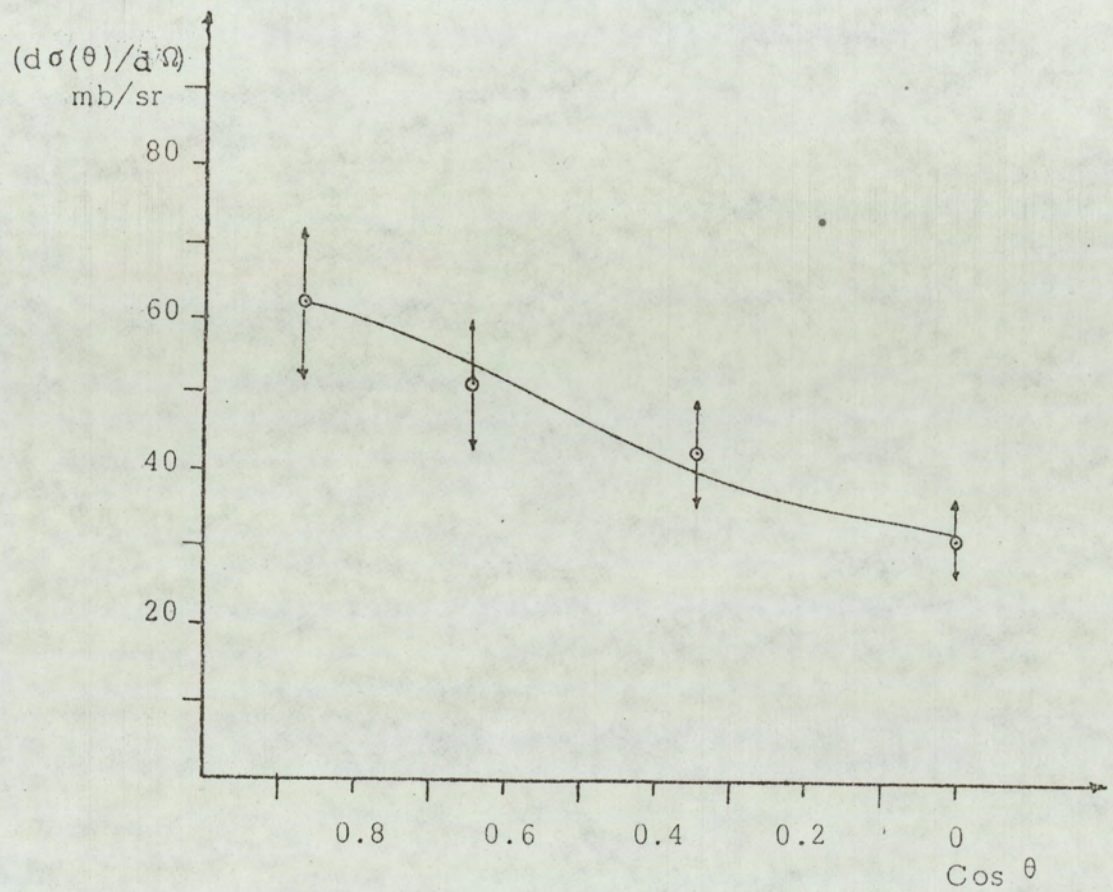

Figure (5-16) The angular distribution for the $^{56}Fe(n,n'\gamma)^{56}Fe$ 1.24 MeV gamma-rays from Iron sample.

Sample thickness = 10.4 cm = 2.3 mfp.

The solid line represent the fit to the equation

$$\frac{d\sigma(\theta)}{d\Omega} = (33.66 \pm 1.8) + (65.28 \pm 4.72)\,Cos^2\theta - (36.02 \pm 6.25)\,Cos^4\theta$$

It can be seen in Figure (5.15) that good agreement between the present results and the results of other groups, also it can be seen that Abbondanno results are systematically lower than other results as explained before.

5.11.4.4. The Integrated Cross-Section for the ^{56}Fe (n,n'γ) ^{56}Fe, 1.24 MeV Gamma-rays

The same procedure as discussed in Section (5.11.4.2) was used to calculate the integrated cross-section for the ^{56}Fe (n,n'γ) ^{56}Fe 1.24 MeV gamma-rays, using the coefficients obtained from the fit of the experimental results to equation (5.27). Table (5.15) below gives the values of the coefficients A_o, A_2 and A_4 and the integrated cross-section for each of the three iron samples used for the production of 1.24 MeV gamma-rays while in Table (5.16), our results for the thin sample (thickness 2 cm), are compared to the published results by other workers. It can be seen from Table (5.16) that the values of the integrated cross-section for the ^{56}Fe (n, n'γ) ^{56}Fe, 1.24 MeV gamma-rays are spread over the range from 289 (mb) to 695 (mb). It is difficult to attribute this disagreement to the different experimental methods since most of the above workers used Na I (Tl) detectors and the time of flight technique.

The results of the present work confirm those of Bezotosnji et al., [104] Lachkar et al., [6] and Abbondanno et al., [100]

Table (5.15)

The integrated cross-sections for the production of $^{56}Fe\ (n,n'\gamma)\ ^{56}Fe$ 1.24 MeV.

Gamma-rays and the calculated coefficients for the angular distributions

Sample Thickness cm	The values of the calculated coefficients			The Integrated cross-sections
	$A_o \pm \alpha_o$	$A_2 \pm \alpha_2$	$A_4 \pm \alpha_4$	
2	32.9 ± 1.9	25.7 ± 7.4	-31.3 ± 6.6	442 ± 42
7.6	44.4 ± 1.3	-2.0 ± 3.5	19.2 ± 4.6	598 ± 25
10.4	33.6 ± 1.8	65.2 ± 4.7	-36.0 ± 6.2	605 ± 33

Table (5.16)

The values of the differential cross-section at 90^{o} and the integrated cross-section for the $^{56}Fe\ (n,n'\gamma)^{56}Fe$ 1.24 MeV gamma-rays from the present work and as reported by other workers

$\left(\frac{d\sigma(\theta)}{d\Omega}\right)_{\theta=90^{o}}$ (mb/sr)	Integrated cross-section mb	Reference and Remarks		
35.1 ± 5.6	443 ± 43	Present work	NaI (Tl)	T. O. F.
21.4 ± 0.6 (a)	$269 \pm$ (b)	Jönsson et al.[91]	Geli	
-	695 ± 80	Martin and Stewart[104]		T. O. F.
25.2 ± 3	398 ± 44	Abbondano et al.[100]	NaI(Tl)	T. O. F.
23.0 ± 2.3	289 ± 229*	Engesser et al.[98]	"	"
-	426 ± 55**	Beľotosnyi et al.[106]		
32.3 ± 7	406 ± 88*	Lachkar et al.[6]	NaI (Tl)+Geli pulsed beam technique	

* Calculated as $4\pi \times \left(\frac{d\sigma(\theta)}{d\Omega}\right)_{\theta=90}$

** Not repeated experimental technique nor $\left(\frac{d\sigma(\theta)}{d\Omega}\right)_{\theta=90}$

(a) differential isotropic 80^{o} cross-section

(b) $4\pi \times \left(\frac{d\sigma(\theta)}{d\Omega}\right)$ Iso 80^{o}

5.11.5. The Variation of the Measured Cross-Section with the Sample Thickness

The results for the measured differential cross-sections for the three iron samples of thicknesses 2, 7.6 and 10.4 cm in the angular range studied are given in Tables (5.17) and (5.18). It can be seen from these tables that the observed cross-section increases with increasing the sample thickness, this is explained as the effect of the multiple scattering of the incident neutrons in the sample, since the 14 MeV neutron would still have enough energy after the first inelastic reaction $^{56}Fe\ (n, n'\gamma)\ ^{56}Fe$ to be involved in another inelastic reaction after travelling certain distance (related to the mean free path) in the sample. The probability of this second or further interactions generally increases with increasing the sample thickness.

Although the general form of $(d\sigma(\theta) / d\Omega)$ versus the sample thickness would imply that the variation is linear and a relation of the form

$$\frac{d\sigma(\theta)}{d\Omega} = \text{Constant} \times \text{sample thickness,}$$

which is true for single collisions only, the results were fitted to an equation of the exponential form

$$\frac{d\sigma(\theta)}{d\Omega} = \text{Constant} \cdot \text{Exp}(\beta \cdot T) \qquad (5.30)$$

where

$\frac{d\sigma(\theta)}{d\Omega}$ = The measured differential cross-section

K = The value of $(d\sigma / d\Omega)$ as the sample thickness approaches zero or equivalently the thickness where multiple scattering effect is zero.

β = Constant determined from the experimental results.

T = The sample thickness in mean free paths.

The reason for the exponential form used here is that the process of multiple scattering can be understood as a growth process in the neutron flux incident on to the target, in the sense that (N) neutrons are incident but the number of interactions in the sample are greater than (N) because each neutron would have a chance of more than one interaction.

Day [10], who used a ring scatter and 2.56 MeV neutrons reports that even with a sample thickness 0.14 cm Ξ 0.05 m.f.p. the observed cross-section would be 5% higher than the "zero-thickness" cross-section, while for a sample of 2 cm thickness, the observed cross-section would be 26% higher than the "zero-thickness" cross-section. Days experimental results were verified by Kellie et al., [11] using Monte-Carlo calculations without giving details describing the variation in the measured cross-section due to multiple scattering with thickness.

Figure (5.17) shows the logarithm of the measured Section as circles while the solid line represents a least squares fit to the logarithm of equation (5.30) i.e.

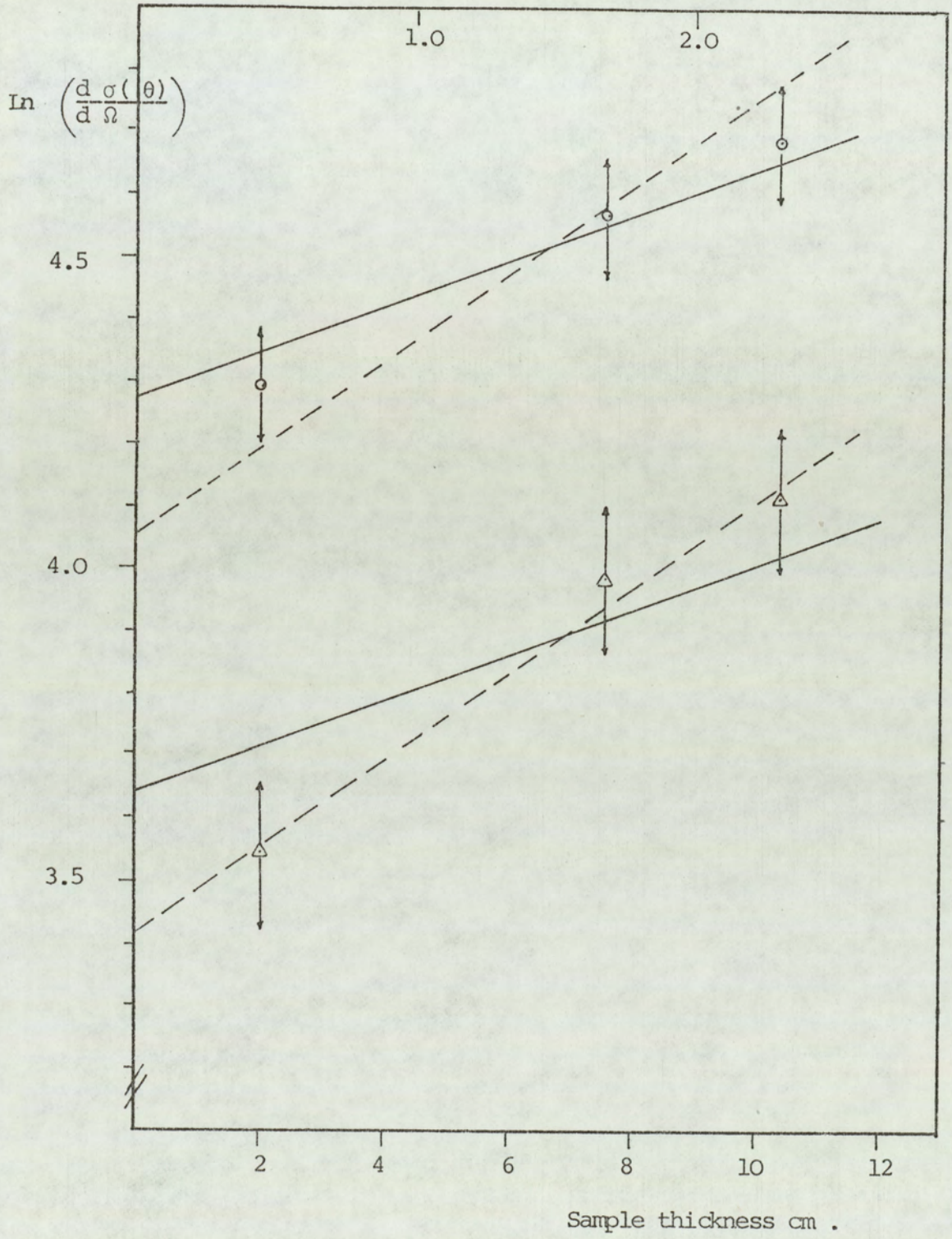

Figure (5-17) The variation of the measured differential cross-section for the production of 0.845 Mev(a) & 1.245 Mev (b) gamma-rays from iron samples with sample thickness . The lines represent least squares fit to equation (5-30 a) using β_{iron} (solid line)and the universal constant (dashed line).

Table (5.17)

The variation of the measured $\frac{d\sigma_{n,n'\gamma}(\theta)}{d\Omega}$ for the production of 0.84 MeV gamma-rays in iron with the sample thickness

Sample Thickness		$(d\sigma(\theta) / d\Omega)$ mb /Sr.			
cm	m.f.p.	$\theta = 30^{\circ}$	50°	70°	90°
2	.442	73.3 $\pm$ 8.1	75.1 $\pm$ 8.3	69.1 $\pm$ 7.6	63.8 $\pm$ 7.0
7.6	1.680	96.1 $\pm$ 10.6	92.2 $\pm$ 10.2	86.8 $\pm$ 9.6	77.8 $\pm$ 8.6
10.4	2.298	108.8 $\pm$ 12.0	102.6 $\pm$ 11.3	101.0 $\pm$ 11.1	83.2 $\pm$ 9.2

Table (5.18)

The variation of the measured $d\,(\sigma_{n,n\gamma}(\theta) / d\Omega)$ for the production of 1.24 MeV gamma-ray in iron with sample thickness

Sample Thickness		$(d\sigma(\theta) / d\Omega)$ mb / Sr.			
cm	m.f.p.	$\theta = 30^{\circ}$	50°	70°	90°
2	.442	34.7 ± 5.5	31.8 ± 5.1	39.2 ± 6.3	35.1 ± 5.6
7.6	1.680	53.9 ± 8.6	45.9 ± 7.3	46.6 ± 7.5	43.1 ± 6.9
10.4	2.298	61.1 ± 9.8	52.2 ± 8.4	43.4 ± 6.9	32.6 ± 5.2

$$\text{Log}_e\ (\text{X-sec}) = \log_e\ (\text{x-sec})_o + \beta T \qquad (5.30\ a)$$

The values of $\text{Log}_e\ (\text{x-sec})_o$ and β are obtained from the experimental results of the iron samples only.

The same treatment was performed on the concrete results to determine the value of the constant $\beta_{conc.}$ as will be discussed in the following Sections, then a universal constant was obtained by combining β_{iron} and $\beta_{conc.}$ and this constant was then used to fit both the iron and concrete results to equation (5-30a) The dashed line in Figure (5.17) represents this fit for the variation of the measured cross-section for the production of 0.845 MeV and 1.24 MeV respectively with the sample thickness, at the scattering angle 30^{o}.

Figure (5-18) shows the variation of the measured cross-sections with sample thickness for different scattering angles, and the straight lines represent in each case a least squares fit according to equation (5-30 a) using the universal constant β.

The increase in the measured cross-sections with the sample thickness is clearly seen in the above Figures and the percentage increment due to multiple scattering calculated as

$$\%\ \text{increment} = \left\{ \text{fitted} \left(\frac{d\sigma(\theta)}{d\Omega}\right)_{T=T} - \left(\frac{d\sigma(\theta)}{d\Omega}\right)_{T=0} \right\} \Big/ \left(\frac{d\sigma(\theta)}{d\Omega}\right)_{T=0} \qquad (5.31)$$

is plotted in Figure (5.19).

The results of the present work suggest lower contribution due

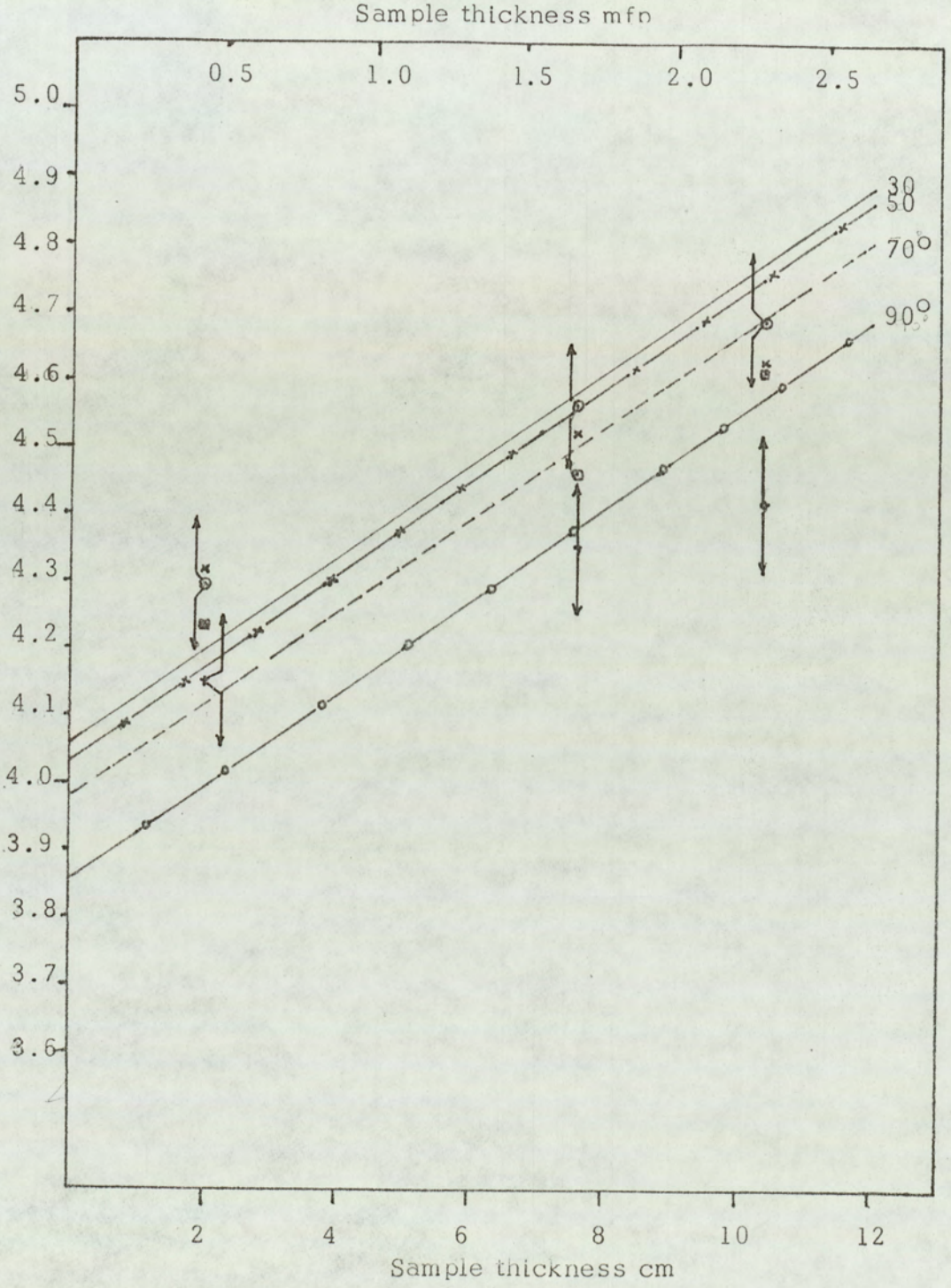

Figure (5-18) The variation of the measured differential cross-section for the production of 0.845 MeV gamma-rays from Iron with sample thickness. The lines represent least squares fit to the equation (5.30-a) using the universal constant β

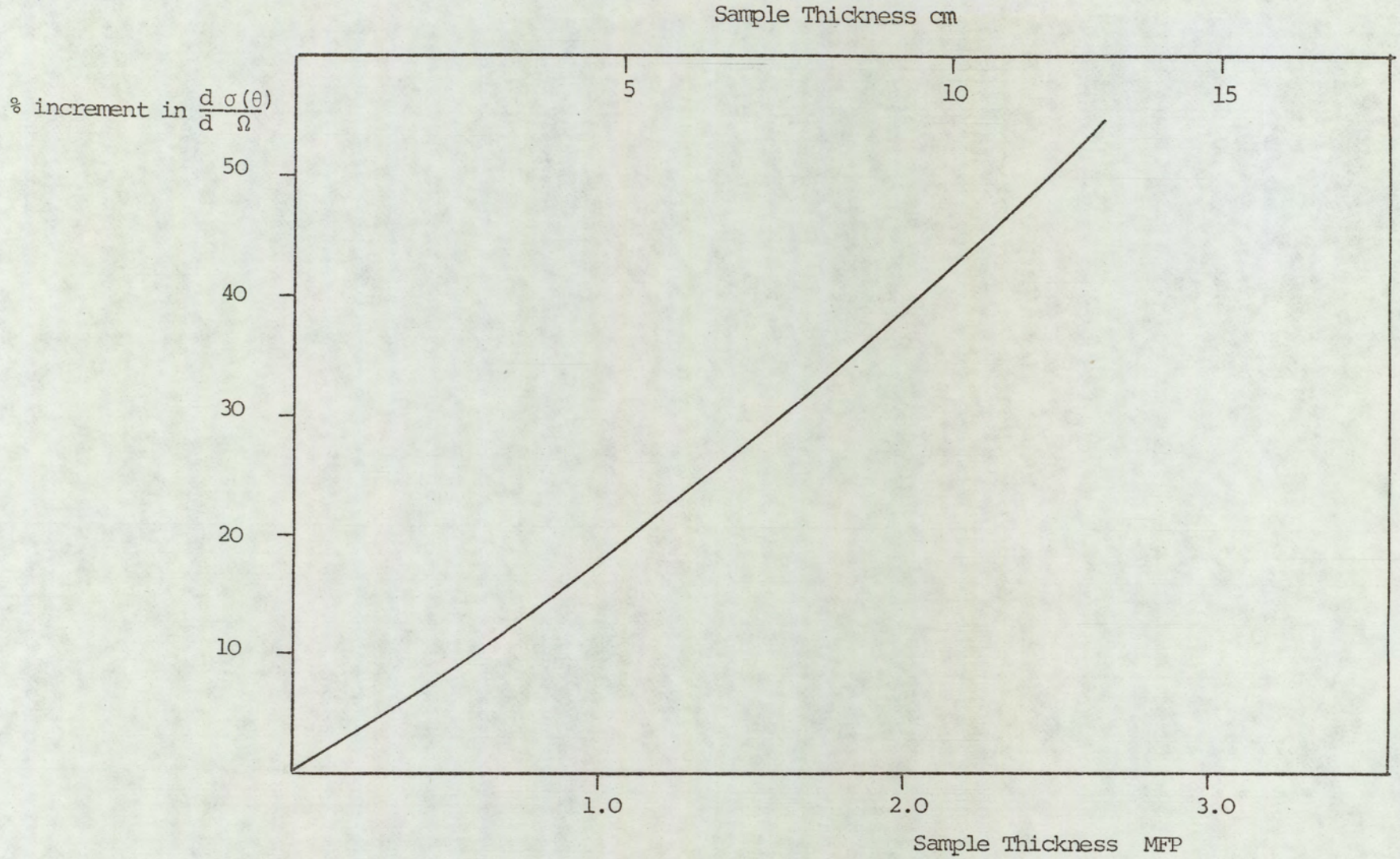

Figure (5-19) The percentage increase in the measured cross-section in iron due to multiple scattering Vs. Sample thickness .

to multiple scattering compared to the results of Day [10] and Kellie [11], a possible explanation for the disagreement is that the above authors used lower neutron energies 2.56 and 9 MeV respectively, where the main non-elastic scattering process is the inelastic scattering producing gamma-rays, while in the present work, at 14 MeV neutron energy, the particle reactions are also possible, In addition, the upper sample thickness used by Day was only 2 cm and the sample was in a disc form.

The present results suggest that the multiple scattering contribution to the gamma-ray production cross-section to be 18% and 39% at sample thicknesses of 1 and 2 mean free paths respectively.

5.12 Results for Concrete

5.12.1. The Elemental Composition of Concrete Samples

The composition of the concrete samples was briefly discussed in Section (3.4.4.2) in terms of the main compounds forming the portland cement. As this work is concerned with the gamma-ray production it was necessary to consider the elemental composition of the samples.

The concrete used in the present work was ordinary concrete type 5 or better known as (5 - Harwell concrete) and it's elemental composition in terms of gm of element/cm^3 of concrete is given in Table (5.19).

Table 5.19

Elemental densities of ordinary concrete type 5-Harwell concrete from reference [3]

Element		Concrete Composition in (gm of element/cm^3 of concrete)
Hydrogen	H	0.0220
Oxygen	O	1.2310
Carbon	C	0.0080
Sodium	Na	0.0290
Magnesium	Mg	0.0020
Aluminium	Al	0.1310
Silicon	Si	0.6300
Sulpher	S	0.0037
Potassium	K	0.0250
Calcium	Ca	0.2420
Titanium	Ti	0.0170
Iron	Fe	0.0450
Nickel	Ni	0.122

The density of the concrete was determined experimentally and it was found to be 2.504 ± 0.128 g $/cm^3$

Due to the complex composition of concrete it was difficult to analyze the gamma-ray spectra obtained from these samples in terms of

discrete gamma-ray energy levels. This may be seen from the typical gamma-ray spectrum from concrete sample shown in Figure (5.3).

5.12.2 The Experimental Results

The experimental results are expressed as differential gamma-ray production cross-section/MeV for consecutive intervals of 1 MeV in the range 1 to 6 MeV.

Equation (5.23) was used for the calculation of the differential cross-section for gamma-ray production, ie.

$$\frac{d\sigma(\theta)}{d\Omega} = \frac{\left(P(\theta) / \Omega \right) \cdot GF}{(\phi_n(\theta) \cdot F_1 \cdot F_2) \cdot S_\gamma(\theta, E\gamma) \cdot \varepsilon(E_\gamma) \cdot \frac{1}{\sigma_t} \cdot \left[1 - \exp.(-\Sigma_t X) \right]} \quad (5.23)$$

$P(\theta)$ here is the number of gamma-ray counts in the energy interval of interest and the rest of the terms are as defined before.

σ_t and Σ_t are the total microscopic and macroscopic cross-sections for concrete related by ($\Sigma_t = N \sigma_t$) where N is the number of nuclei for cm^3 in concrete.

Σ_t was determined experimentally for 14 MeV neutrons by measuring the neutron transmission through concrete samples of different thicknesses. The number of nuclei per cm^3 was determined from the published data [2, 3] for ordinary concretes and it was corrected for the density of the concrete used. The experimental results are given

in Tables (5.20) through to Table (5.24). The headings of the Tables are as follows :

S. Angle	=	Scattering angle in the laboratory system
Thickness	=	Sample thickness in inches
G. Factor	=	The Geometry factor correction
X-Section	=	Differential cross-section for gamma-ray production (mb/sr)
Errors		in (mb/sr)

The errors in the Tables are dominated by the experimental error in determining the number of gamma-ray counts in each energy group, ie. $P(\theta)$.

Table (5.25) gives the errors in the different factors excluding the error in $P(\theta)$ which is given separately in Table (5.26) for each of the energy regions considered. The total percentage error in the experimentally measured cross-sections for concrete samples was obtained by combining the above two Tables in quadrature and the final result for each energy region is shown in Table (5.27).

Table (5.20) The differential cross-section for the production of gamma-rays of energy (1-2) MeV from concrete samples in the angular range (30^{o} - 90^{o}).

S. ANGLE	THICKNESS	G-FACTOR	MEASURED X-SECTION	CORRECTED X-SECTION	ERROR
30.000	2.000	1.055	12.6	13.3	2.1
30.000	5.000	1.354	11.3	15.4	2.5
30.000	8.000	1.691	12.3	20.9	3.3
30.000	10.000	2.005	8.9	17.9	2.9
50.000	2.000	1.000	17.4	17.4	2.8
50.000	5.000	1.079	17.0	18.4	3.0
50.000	8.000	1.902	18.2	34.8	5.6
50.000	10.000	2.691	19.1	51.4	8.2
70.000	2.000	1.000	10.6	10.6	1.7
70.000	5.000	1.371	14.1	19.3	3.1
70.000	8.000	2.636	19.7	52.9	8.3
70.000	10.000	3.700	21.2	78.4	12.5

Continued.....

Table (5.20) Continued...

S. ANGLE	THICKNESS	G-FACTOR	MEASURED X-SECTION	CORRECTED X-SECTION	ERROR
90.000	2.000	1.000	11.3	11.3	1.8
90.000	5.000	1.777	17.7	31.2	5.0
90.000	8.000	3.174	23.7	75.3	12.0
90.000	10.000	4.298	18.1	77.9	12.5

Table (5.21) The differential cross-section for the production of (2-3) MeV gamma-ray from neutron interactions in concrete

S. ANGLE	THICKNESS	G-FACTOR	MEASURED X-SECTION	CORRECTED X-SECTION	ERROR
30.00	2.000	1.055	47.4	50.0	7.0
30.00	5.000	1.354	39.0	52.8	7.4
30.00	8.000	1.691	31.0	52.3	7.3
30.00	10.000	2.005	24.0	48.1	6.7
50.000	2.000	1.000	26.5	26.5	3.7
50.000	5.000	1.079	24.5	26.4	3.
50.000	8.000	1.902	29.7	56.4	7.9
50.000	10.000	2.691	27.9	75.0	10.5
70.000	2.000	1.000	25.1	25.1	3.5
70.000	5.000	1.371	26.	35.6	5.0
70.000	8.000	2.636	29.7	78.3	11.0
70.000	10.000	3.700	32.0	118.6	16.6

Continued....

Table (5.21) Continued...

S. ANGLE	THICKNESS	G-FACTOR	MEASURED X-SECTION	CORRECTED X-SECTION	ERROR
90.000	2.000	1.000	14.1	14.1	2.0
90.000	5.000	1.777	14.4	25.6	3.6
90.000	8.000	3.174	27.6	87.6	12.3
90.000	10.000	4.298	22.5	96.8	13.6

Table (5.22) The differential cross-section for the production of (3-4)MeV gamma-ray from neutron interactions in concrete.

S. ANGLE	THICKNESS	G-FACTOR	MEASURED X-SECTION	CORRECTED X-SECTION	ERROR
30.000	2.000	1.055	53.0	55.9	6.1
30.000	5.000	1.354	59.6	80.7	8.9
30.000	8.000	1.691	42.8	72.4	8.0
30.000	10.000	2.005	26.5	53.0	5.8
50.000	2.000	1.000	30.7	30.7	3.9
50.000	5.000	1.079	36.6	39.4	4.3
50.000	8.000	1.902	34.0	64.7	7.1
50.000	10.000	2.691	28.7	77.1	8.5
70.000	2.000	1.000	32.0	32.0	3.5
70.000	5.000	1.371	26.3	36.0	4.0
70.000	8.000	2.636	35.1	92.5	10.2
70.000	10.000	3.700	29.9	110.8	12.2

Continued...

Table (5.22) continued.

S. ANGLE	THICKNESS	G-FACTOR	MEASURED X-SECTION	CORRECTED X-SECTION	ERROR
90.000	2.000	1.000	13.6	13.6	1.5
90.000	5.000	1.777	18.1	32.2	3.5
90.000	8.000	3.174	20.4	64.6	7.1
90.000	10.000	4.298	16.4	70.7	7.8

Table (5.23) The differential cross-section for the production of (4-5) MeV gamma-ray from neutron interactions in concrete

S. ANGLE	THICKNESS	G-FACTOR	MEASURED X-SECTION	CORRECTION X-SECTION	ERROR
30.000	2.000	1.055	28.9	30.5	2.7
30.000	5.000	1.354	37.2	50.4	4.5
30.000	8.000	1.691	26.5	44.8	4.0
30.000	10.000	2.005	11.9	23.8	2.1
50.000	2.000	1.000	17.0	17.0	1.5
50.000	5.000	1.079	22.6	24.4	2.2
50.000	8.000	1.902	28.4	54.0	4.9
50.000	10.000	2.691	12.5	33.5	3.0
70.000	2.000	1.000	17.2	17.2	1.5
70.000	5.000	1.371	12.1	16.6	1.5
70.000	8.000	2.636	20.6	54.3	4.9
70.000	10.000	3.700	19.2	45.1	4.6

Continued.....

Table (5.23) (Continued...)

S. ANGLE	THICKNESS	G-FACTOR	MEASURED X-SECTION	CORRECTION X-SECTION	ERROR
90.000	2.000	1.000	11.8	11.8	1.1
90.000	5.000	1.777	8.8	15.6	1.4
90.000	8.000	3.174	6.7	21.1	1.9
90.000	10.000	4.298	11.6	49.8	4.5

Table (5.24) The differential cross-section for the production of (5-6) MeV gamma-ray from neurton interactions in concrete.

S. ANGLE	THICKNESS	G-FACTOR	MEASURED X-SECTION	CORRECTION X-SECTION	ERROR
30.000	2.000	1.055	25.5	26.9	2.2
30.000	5.000	1.354	31.4	42.5	3.4
30.000	8.000	1.691	25.5	43.0	3.4
30.000	10.000	2.005	11.8	23.6	1.9
50.000	2.000	1.000	13.0	13.0	1.0
50.000	5.000	1.079	21.1	22.7	1.8
50.000	8.000	1.902	32.2	61.2	4.9
50.000	10.000	2.691	11.5	30.8	2.5
70.000	2.000	1.000	14.8	14.8	1.2
70.000	5.000	1.371	11.0	15.0	1.2
70.000	8.000	2.636	19.8	52.2	4.2
70.000	10.000	3.700	13.5	49.8	4.0

Continued.....

Table (5.24) continued...

S. ANGLE	THICKNESS	G-FACTOR	MEASURED X-SECTION	CORRECTION X-SECTION	ERROR
90.000	2.000	1.000	15.4	15.4	1.2
90.000	5.000	1.777	9.1	16.2	1.3
90.000	8.000	3.174	7.8	24.9	2.0
90.000	10.000	4.298	7.1	30.7	2.5

Table (5-25)

The percentage error in the factors of equation (5-23)

Factor	% Error
$\phi_n(\theta)$	1
$S(\theta, E_\gamma)$	2
$\Delta\Omega$	4
Neutron attenuation	3
Peak efficiency	3.5

Table (5-26)

The percentage error in $P(\theta)$ for the concrete samples

Energy region (MeV)	% error in $P(\theta)$
1 - 2	15.0
2 - 3	12.5
3 - 4	10.0
4 - 5	7.5
5 - 6	5.0

Table (5.27) The total percentage error in the experimentally measured cross-sections for the concrete samples.

Energy Region (MeV)	% Total Error
1 - 2	16
2 - 3	14
3 - 4	11
4 - 5	9
5 - 6	8

5.12.3. The Angular Distributions for the Gamma-ray Production from Concrete Samples

The measured angular distributions for the different gamma-ray energy intervals are shown in Figures (5.20) through to (5.24). Each figure gives angular distributions for each energy range each of which corresponds to one sample thickness. The solid line in these figures represent a least squares fit of the experimental data points to the general equation representing these curves which is given by

$$\frac{d\sigma(\theta)}{d\Omega} = (A_o \pm \alpha_o) + (A_2 \pm \alpha_2)\cos^2\theta + (A_4 \pm \alpha_4)\cos^4\theta$$

The equation for each curve is given in Table (5.28).

The most noticeable feature of these curves is that the angular distributions from the 5 and 12.5 cm samples are similar in shape and as the increment in the value of $\left(\frac{d\sigma(\theta)}{d\Omega}\right)$ is not very large, these two curves could be replaced by another curve representing the average

TABLE (5-28)

The equations for the fitted lines in figures (5-20) through to (5-24)

Figure No. + Energy Range	Scat. Angle	Sample Thickness	The fitted line $\frac{d\sigma(\theta)}{d\Omega} = A_o + A_2 x^2 + A_4 x^4$, $X = \cos\theta$		
		mfp	$A_o \pm \alpha_o$	$A_2 \pm \alpha_2$	$A_4 \pm \alpha_4$
(5-20) 1-2 MeV	30	0.57	9.5 ±1.4	33.0 ±3.7	-37.3 ±5.0
	50	1.43	29.0 ±2.8	- 53.0 ±7.3	48.2 ±9.7
	70	2.29	73.1 ±3.7	-149.9 ±9.7	110.0 ±12.9
	90	2.86	79.8 ±2.4	- 37.1 ±6.4	-61.9 ±8.4
(5-21) 2-3 MeV	30	0.57	17.7 ±3.5	10.0 ±9.3	42.8 ±12.3
	50	1.43	31.1 ±5.1	-43.3 ±13.4	95.2 ±17.7
	70	2.29	89.4 ±1.3	-122.5 ±3.6	98.5 ± 4.8
	90	2.86	105.8 ±10.1	-16.8 ±26.6	-84.5 ±35.3
(5-22) 3-4 MeV	30	0.57	19.0 ±5.7	30.4 ±15.1	22.5 ±20.0
	50	1.43	35.7 ± 2.7	-51.6 ±7.2	149.3 ± 9.6
	70	2.29	74.9 ±11.0	4.5 ±28.8	-14.9 ±38.2
	90	2.86	81.2 ±13.1	103.6 ±34.5	-195.5 ±45.6
(5-23) 4-5 MeV	30	0.57	13.9 ±1.9	-3.1 ± 5.1	33.1 ± 6.8
	50	1.43	16.6 ± .7	-16.8 ± 1.8	83.0 ±2.4
	70	2.29	25.9 ±7.4	174.4 ±19.6	-204.4 ±25.9
	90	2.86	50.1 ±0.2	-48.4 ± 0.7	18.1 ±1.0
(5-24) 5-6 MeV	30	0.57	16.7 ±1.0	-38.2 ± 2.6	69.4 ±3.5
	50	1.43	16.3 ± .6	-14.5 ± 1.5	66.6 ±2.0
	70	2.29	26.2 ±4.6	202.9 ±12.1	-245.4 ±16.0
	90	2.86	36.6 ±6.9	28.7 ±18.1	-64.7 ±23.9

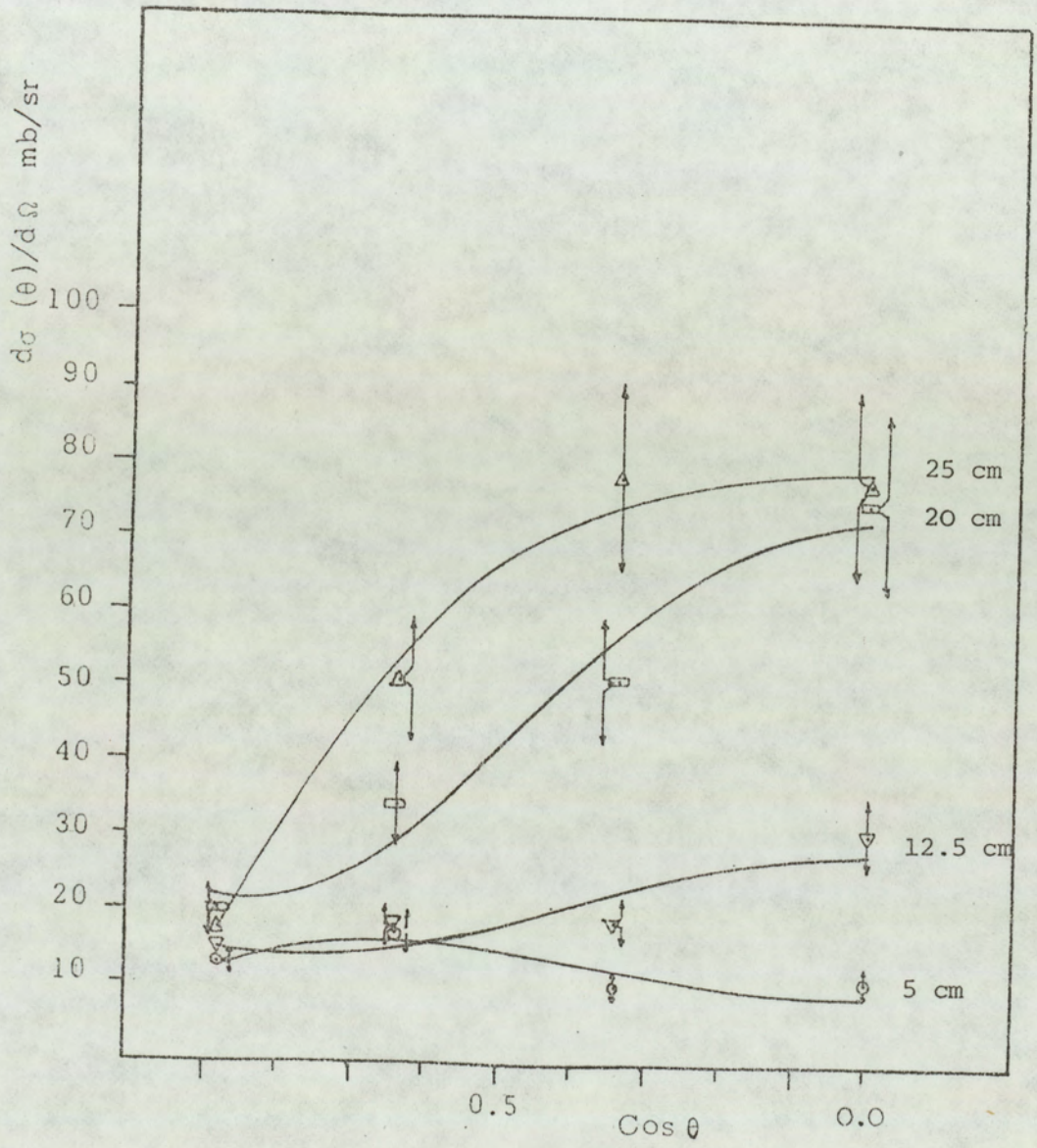

Figure (5-20) The angular distribution for the production of (1-2) MeV gamma-rays from concrete samples .

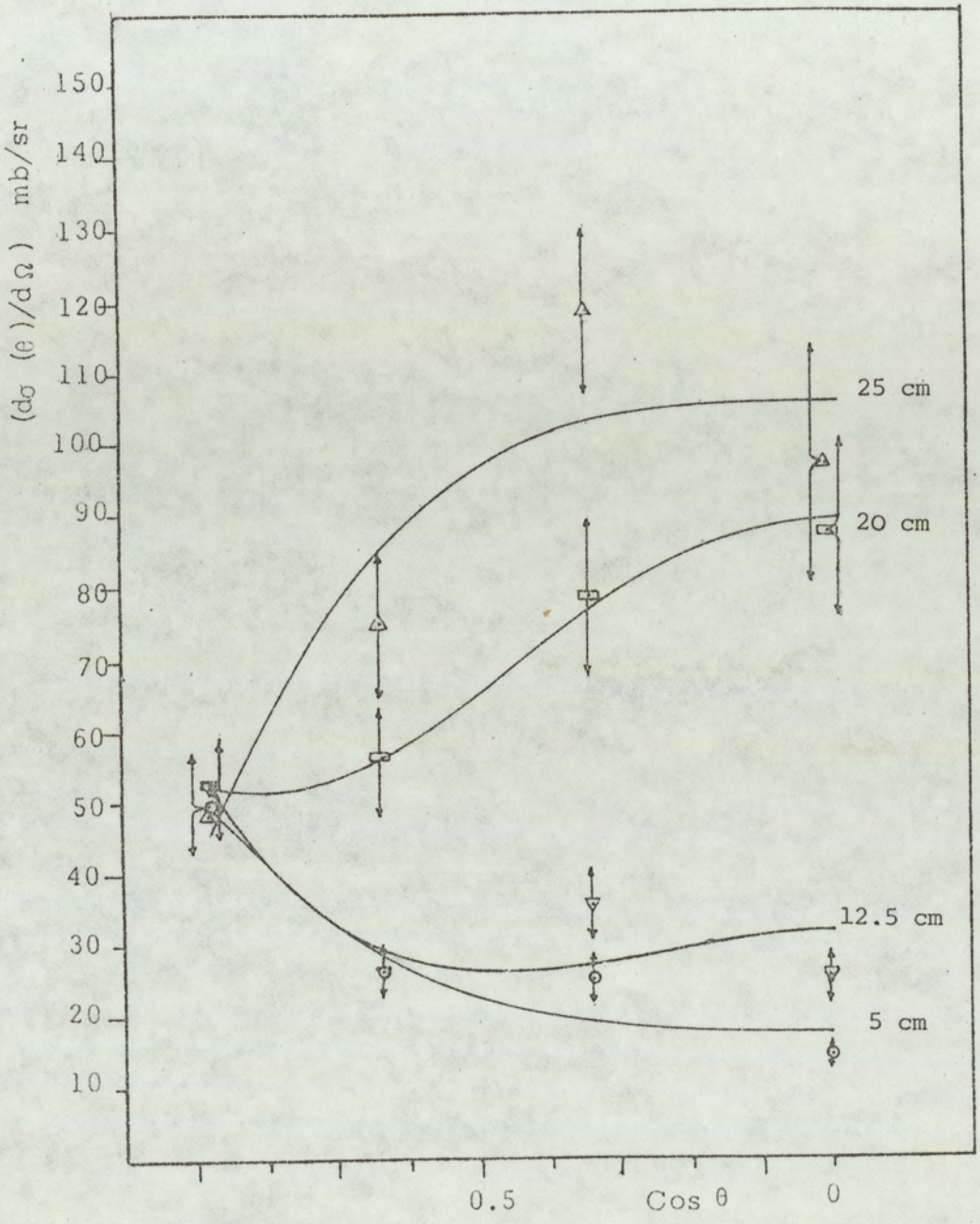

Figure (5.21) The angular distribution for the production of 2-3 MeV gamma-rays from concrete.

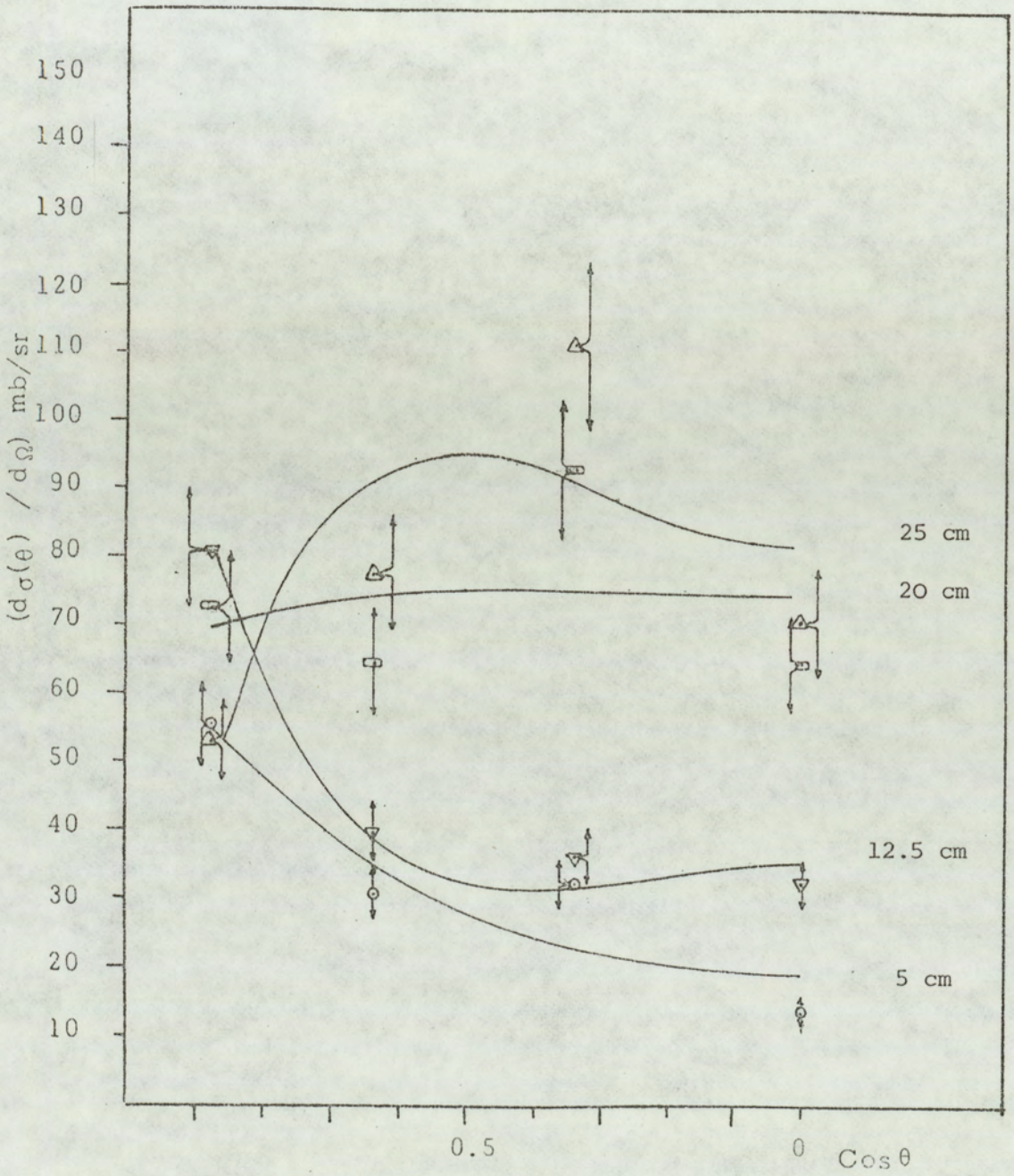

Figure (5-22) The angular distribution for the production of (3-4) MeV gamma-rays from concrete

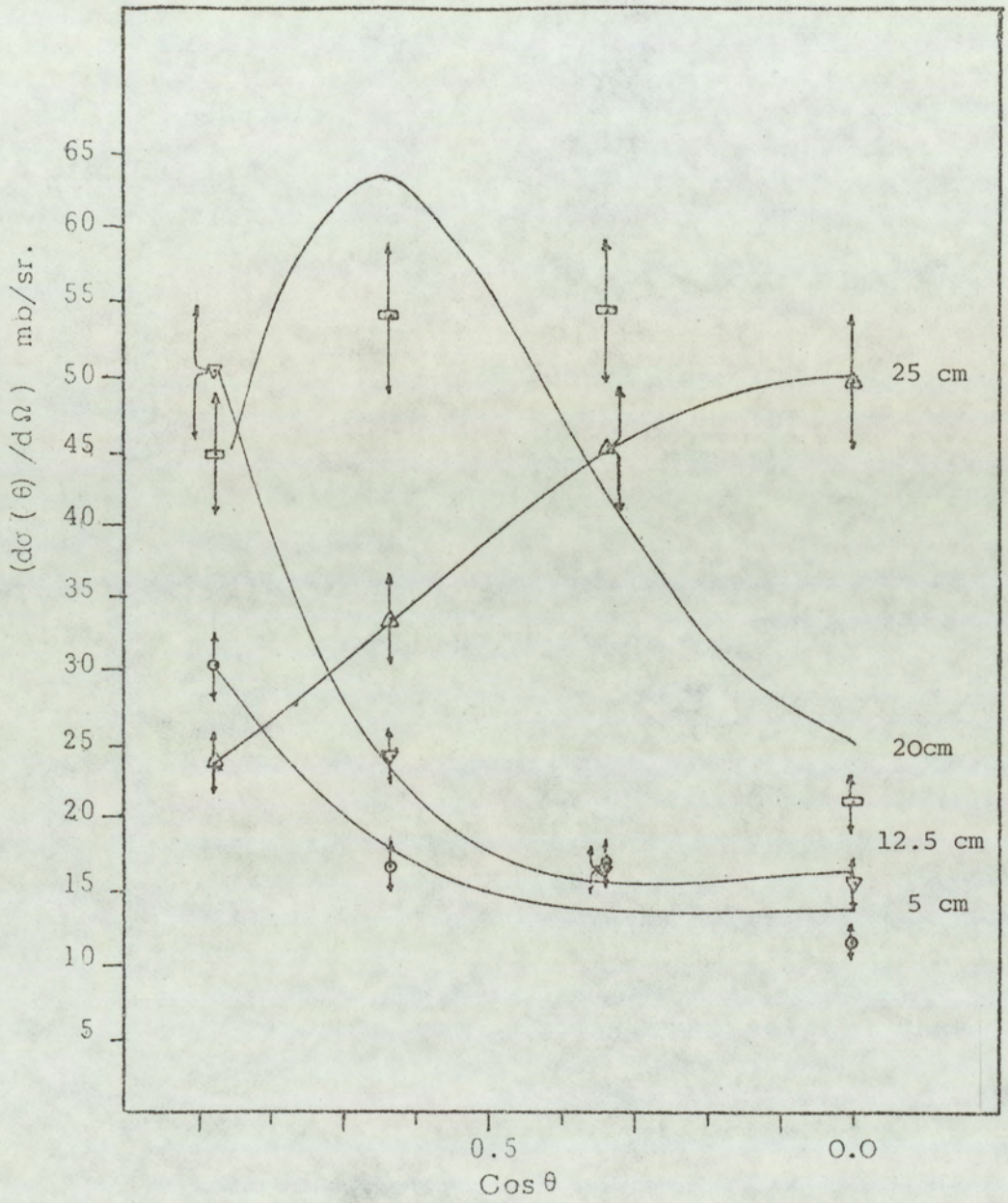

Figure (5-23) The angular distribution for the production of 4.5 MeV gamma-rays from concrete samples .

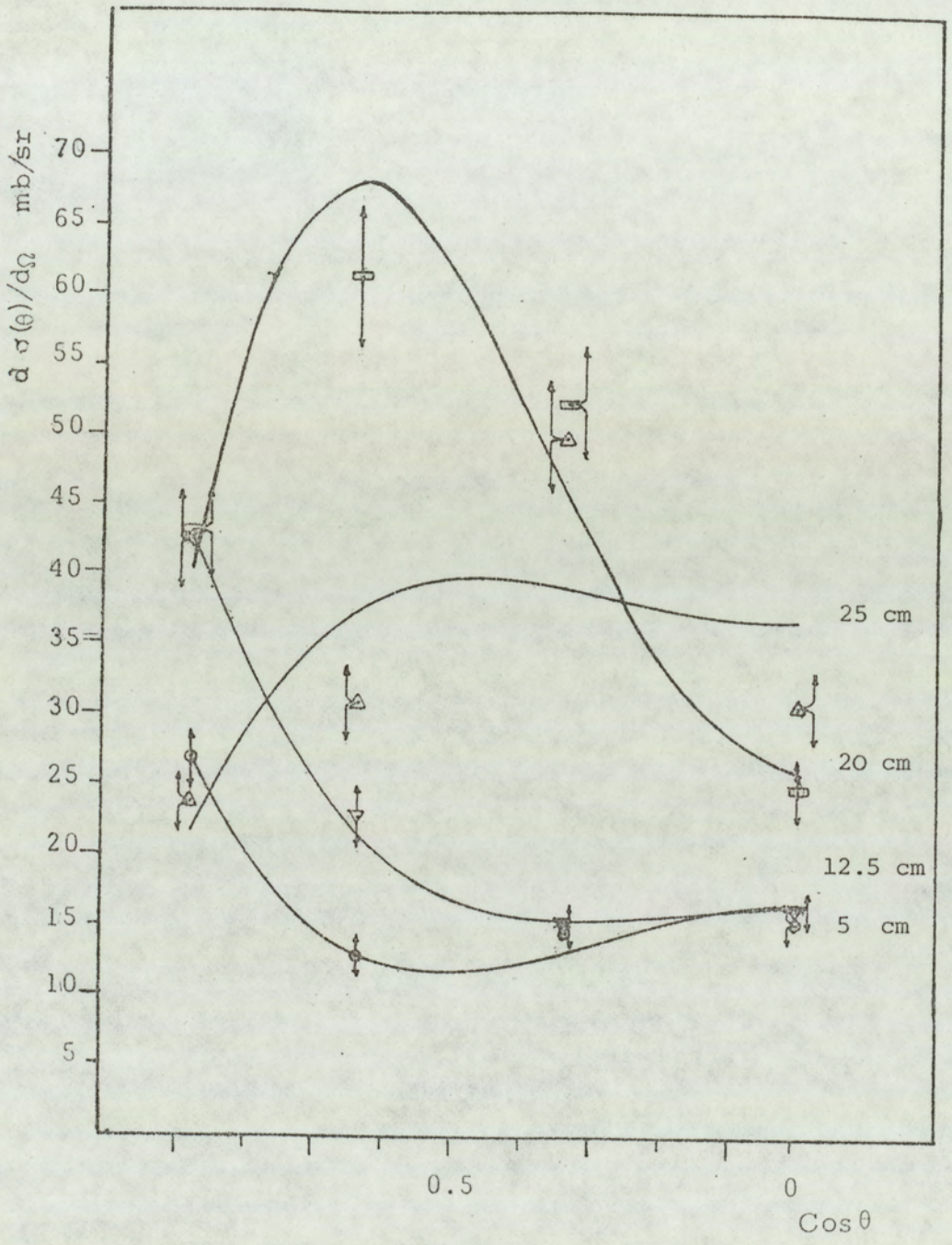

Figure (5-24) The angular distribution for the production of (5-6) MeV γ-rays from concrete

angular distribution for the two samples. A similar argument holds for the 20 and 25 cm samples.

The mean free path for 14 MeV neutrons in the concrete is about 10 cm which means that the different sample thicknesses are 0.5, 1.25, 2 and 2.5 mean free paths. From the above argument it seems reasonable to conclude that angular distributions from the concrete samples will have the same shape for all samples having any thickness in intervals of one mean free path width, i.e. (0-1), (1-2) etc.

No similar measurements were found in the published literature hence, it was not possible to compare our results with others. However, using the major elements constituting concrete, ie. oxygen, calcium, silicon and aluminium, and from the published data on the relevant cross-sections, it was possible to construct the total cross-section for concrete and the differential cross-sections for gamma-ray production. The sets of data considered were those of Dickens et al., [7,110,111,112] Orphan et al., [113] Caldwell et al., [48] Drake et al., [39] Thompson et al., [108] Perkin et al., [114] and Engesser et al., [98] It must be emphasized that there is a considerable disagreement among these data sets and none of these data contains the cross-section for the four elements nor the complete angular distributions, since the measurements were performed at only one or two angles usually 90° and 125°. The following table shows the source of data for each element considered.

Element	Data Source	Angle at which the cross-section was measured
Oxygen	Calwell[48], Thompson[108], Orphan[113], Drake[39], Perkin[114], Dickens[115]	90°
Calcium	Dickens[111]	125°
Silicon	Dickens[112]	90°
Aluminium	Dickens[113]	90°

The equation used for the evaluation of the concrete cross-sections was used by Schmidit[2] for the evaluation of the removal cross-sections for concrete using the data for the elements constituting concrete. The equation for evaluating the total macroscopic cross-section Σ_t from which the microscopic cross-section can be found using the relation $\Sigma_t = N \sigma_t$ was

$$\Sigma_t = \sum_i \rho_i \left(\Sigma_t / \rho \right)_i \qquad (5\text{-}32)$$

where

Σ_t = Macroscopic cross-section for concrete.

ρ_i = Partial density of the constituent i in (gm/cm^3)

$(\Sigma / \rho)_i$ = The total cross-section per unit density of the i^{th} constituent.

The result of this evaluation for the differential cross-section

for the production of the different gamma-rays considered at 90^{o} is compared to the experimental results in Table (5.29).

From Table (5.29) and in view of the inherent uncertainties in the composition of concrete and the used cross-section, it can be seen that the experimentally measured and the estimated values of the differential cross-sections are in reasonably good agreement.

5.12.4. The Integrated Cross-Sections For the Production of Gamma-Rays From the Interaction of 14 MeV Neutrons in Concrete

The principles of evaluating the integrated cross-section from the measured angular distribution has been discussed in Section (5.11.4.2). The general equation describing the angular distributions is given by

$$\frac{d\sigma(\theta)}{d\Omega} = (A_o \pm \alpha_o) + (A_2 \pm \alpha_2) \cos^2\theta + (A_4 \pm \alpha_4) \cos^4\theta$$

where all the terms are as defined earlier.

The equation for each angular distribution for concrete samples is given in Table (5.28) where the values of the coefficients A_o, A_2 and A_4 together with the associated error in each coefficient can be found.

The integrated cross-sections for the production of gamma-rays of different energies following the inelastic scattering of 14 MeV neutrons in concrete are given in Table (5.30).

The integrated cross-sections for each gamma-ray energy group from the four concrete samples were fitted to equation (5.30) namely

Table (5-29) The extrapolated values $\frac{d\sigma(90^o)}{d\Omega}$ and the synthesised values from the published data.

Gamma-ray Energy MeV	$\frac{d\sigma(90)}{d\Omega}$ (*)		$\frac{d\sigma(90)}{d\Omega}$	From L.S.F. to the experimental results (+)	Synthesized cross-sections based on equation (5-31) (**)
	$\beta_1 = 0.4584$ (a)	$\beta_2 = 3112$ (b)	β (c)	$\frac{d\sigma(90)}{d\Omega}$	
1-2	18.05 ± 2.89	24.58 ± 3.93	0.8844	7.79 ± 1.28	14.78 ± 3
2-3	20.21 ± 2.83	27.72 ± 3.88	0.9192	8.08 ± 1.13	7.13 ± 1.5
3-4	17.19 ± 1.89	23.16 ± 2.54	0.7457	9.89 ± 1.09	9.49 ± 1.95
4-5	9.50 ± 0.86	12.68 ± 1.14	0.5765	7.50 ± 0.68	4.04 ± 1.00
5-6	9.30 ± 0.74	12.01 ± 0.96	0.3202	11.78 ± 0.94	10.66 ± 2.5

(*) The values of β shown are those used for fitting the experimental results to equation (5-30)

(a) $\beta_1 = 0.4594$ from concrete measurements

(b) $\beta_2 = 0.3117$ universal constant from iron and concrete measurements

(c), (+) The values of β from L.S.F. for the experimental measurements at 90^o for the concrete samples

(**) The elements considered are oxygen, calcium, silicon and aluminium with partial densities 1.231, 0.242, 0.63 and 0.131 respectively.

Table (5-30)

The integrated cross-sections for the production of different energy gamma-rays in concrete, for different sample thicknesses.

Gamma-ray energy range MeV	The integrated cross-sections for the production of E MeV gamma-rays from concrete samples in (mb) the first row below gives the sample thickness			
	5 cm	12.5 cm	20 cm	25 cm
1 - 2	165 ± 27	264 ± 53	560 ± 70	692 ± 46
2 - 3	373 ± 67	450 ± 96	859 ± 26	1047 ± 192
3 - 4	424 ± 109	608 ± 52	923 ± 207	964 ± 249
4 - 5	245 ± 37	347 ± 13	543 ± 141	473 ± 6
5 - 6	225 ± 19	312 ± 11	563 ± 87	418 ± 130

$$\left(\frac{d\sigma(\theta)}{d\Omega}\right)_T = \left(\frac{d\sigma(\theta)}{d\Omega}\right)_{T=0} \cdot \exp(\beta \cdot T)$$

(where a detailed discussion of this equation is given in Sections (5.11.5) and (5.12.5)), to find $(\sigma_{int})_{T=0}$ and the results are shown in Table (5.31) together with the estimated cross-sections from the published data [7] and the values of $4\pi\left(\frac{d\sigma(\theta)}{d\Omega}\right)_{\theta=90^\circ,\ T=0}$

It can be seen from that table that the agreement between the estimated values and the experimental measured $4\pi\left(\frac{d\sigma(\theta)}{d\Omega}\right)_{\theta=90^\circ,\ T=0}$ is quite good. The value of the extrapolated σ_{int} for thickness $T = 0$ and the estimated values are not in good agreement and this implies that the angular distributions for the gamma-ray production in the gamma-ray energy considered are not isotropic. Consequently the assumption that the integrated cross-section is equal to $4\pi \times \left(\frac{d\sigma(\theta)}{d\Omega}\right)_{\theta=90^\circ}$ does not hold, except for the gamma-ray in the energy range (5-6) MeV where it can be seen that $(\sigma_{int})_{T=0}$, the estimated value $4\pi\left(\frac{d\sigma(90)}{d\Omega}\right)_{Published}$ and the experimentally determined $4\pi \times \left(\frac{d\ (90^\circ)}{d\ \Omega}\right)_{T=0}$ are in a very good agreement.

5.12.5. The variation of Measured Cross-Section with the Sample Thickness in Concrete

The experimental results for the differential cross-section for gamma-ray production from the four concrete samples in the angular range studied are presented in tables (5-20) through to (5-24). These

Table (5-31)

Comparison of the experimentally predicted integrated cross-sections for gamma-ray production in concrete and the estimated values from the published data.

Gamma-ray energy range MeV	Experimental Results		Estimated σ_{int} from the published data* $\sigma_{int} = 4\pi \times \left(\frac{d\sigma(\theta)}{d\Omega}\right)_{90}$
	Extrapolated σ_{int} for zero thickness using $\beta_{conc.}$	$\sigma_{int} = 4\pi \times \left(\frac{d\sigma(90^{o})}{d\Omega}\right)_{T=o}$	
1 - 2	162 ± 49	98 ± 29	185 ± 31
2 - 3	276 ± 69	100 ± 25	90 ± 15
3 - 4	306 ± 61	124 ± 25	119 ± 20
4 - 5	172 ± 26	94 ± 14	50 ± 9
5 - 6	161 ± 16	148 ± 15	133 ± 23

* Errors calculated as 17% from Dickens

results were analysed in the same way as the iron results (Section 5.11.5).

Figure (5.24) shows a typical concrete result for the variation of the measured cross-section with sample thickness, where the lines represent a least squares fit to the natural logarithm of equation (5-30)

$$\text{Log}_e\left(\frac{d\sigma(\theta)}{d\Omega}\right) = \text{Log}_e\left(\frac{d\sigma(\theta)}{d\Omega}\right)_{T=0} + \beta T \qquad (5.30)$$

All the quantities in the above equation have been defined in Section (5.11.5), with β being the universal constant obtained as the average of the values of β from the iron and concrete sresults.

Figure (5.25) shows the variation of the differential cross-section for the production of (3-4) MeV gamma-rays from concrete with the sample thickness (expressed in mean free paths) in the angular range studied. No similar measurements were found in the literature and hence, it was not possible to compare our results with others. Figure (5.26) shows the variation for two different gamma-ray groups namely (2-3) MeV and (5-6) MeV, at the scattering angle $\theta = 90^{o}$. The continuous line for the (2-3) MeV represents the maximum error in the fit obtained using the universal constant β, with the value of ($\chi^2 = 0.36$) while the broken line for the (5-6) MeV represents the minimum error in the fit using the same universal constant, the value of χ^2 for the later case is ($\chi^2 = 0.01$).

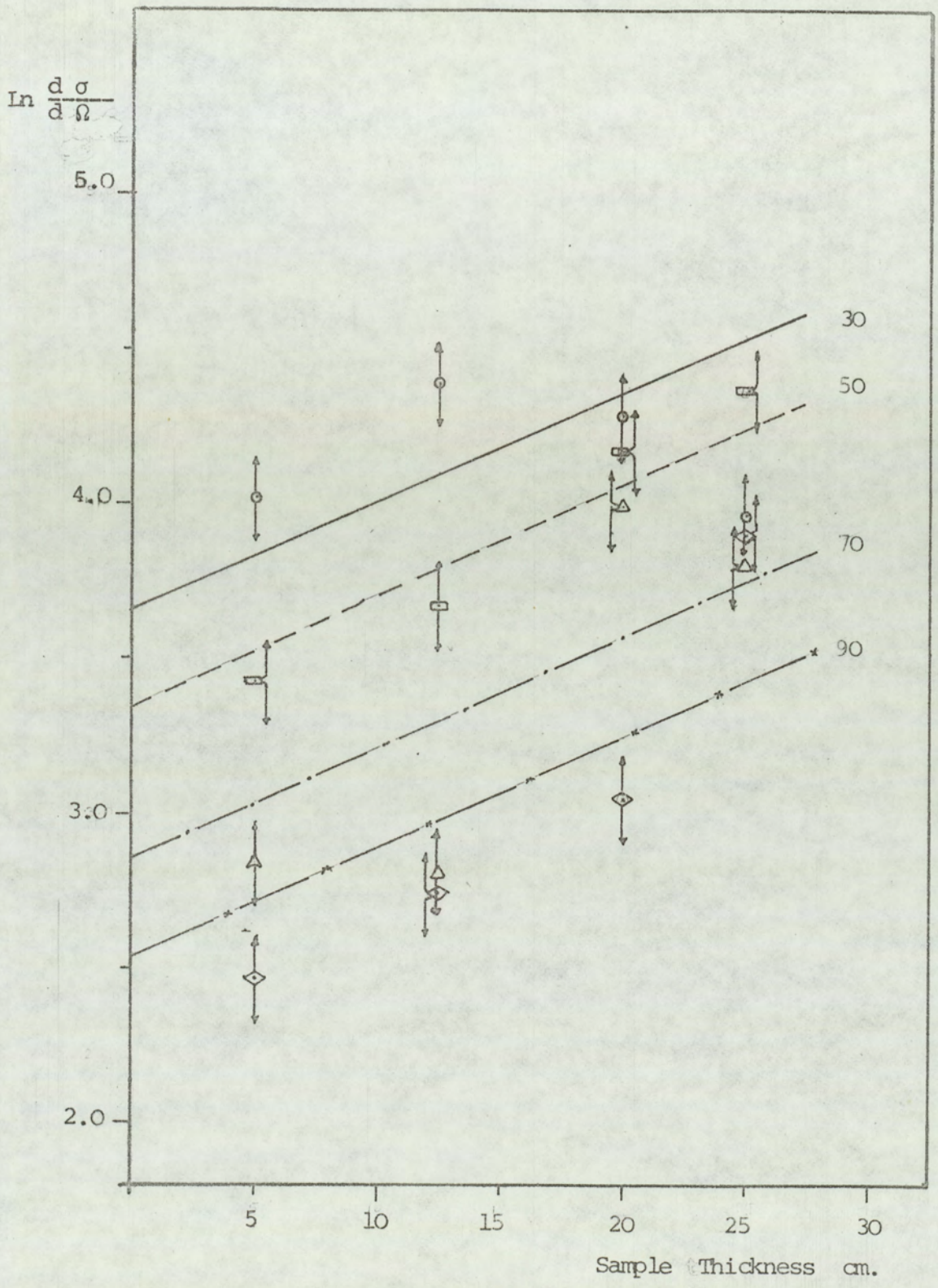

Figure (5-25) The variation of the measured differential cross-section for the production of (3-4) MeV gamma-ray from concrete samples with sample thickness .

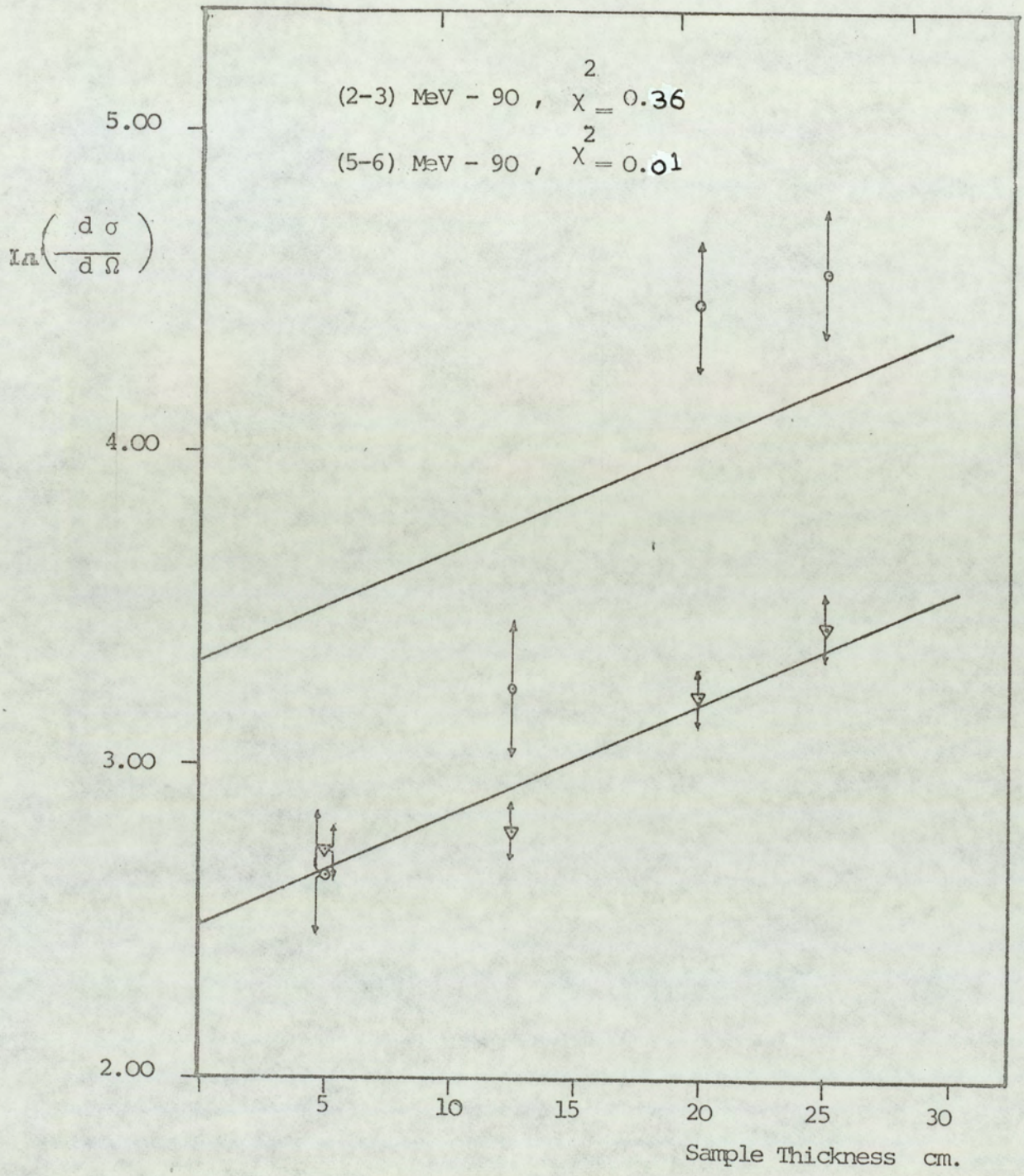

Figure (5-26) The maximum and minimum error in the fit using the universal constant β

The values of χ^2 for all the gamma-ray groups from the different concrete samples in the angular range studied are given in table (5-32). The χ^2 values correspond to the fits to the logarithm of equation (5-30) using both the universal constant β and the value of $\beta_{conc.}$ from the concrete results only.

Table (5-32) The values of χ^2 per point for the fit of the measured cross-sections to the logarithm of equation (5-30)

Gamma-ray Energy (MeV)	Scattering angle	(χ^2)	
		β = 0.3112 univ.	β = 0.4584 conc.
1-2	30	0.03	0.10
	50	0.05	0.03
	70	0.35	0.20
	90	0.34	0.22
	Integrated X-S	0.07	0.03
2-3	30	0.08	0.17
	50	0.06	0.03
	70	0.13	0.06
	90	0.36	0.22
	Integrated X-S	0.02	0.01
3-4	30	0.10	0.19
	50	0.01	0.004
	70	0.09	0.04
	90	0.20	0.10
	Integrated X- S	0.005	0.01
4-5	30	0.22	0.32
	50	0.08	0.07
	70	0.14	0.10
	90	0.12	0.06
	Integrated X-S	0.01	0.02
5-6	30	0.17	0.26
	50	0.19	0.15
	70	0.19	0.12
	90	0.01	0.03
	Integrated X-S	0.02	0.03

* X-S ≡ Crsoss- section .

CHAPTER SIX

COMPARISON OF THE RESULTS WITH THEORY

6.1 Multiple Scattering of Neutrons In An Extended Sample

The general assumption made when calculating the differential cross-section for gamma-ray production following the inelastic scattering of neutrons is that the gamma-ray yield is due to neutrons that have interacted once only in the scattering sample, consequently, the neutron flux falls exponentially through the sample.

However, there is often a good chance that a neutron will be scattered again, elastically or inelastically before finally leaving the scattering sample or being thermalized. Neutron elastic scattering is very forward peaked and neutrons interacting by this process (or through this channel) lose a very small amount only of their energy except for scattering from light nuclei with ($A < 12$). The probability of multiple scattering depends on the dimensions of the scattering sample and on the scattering cross-section of the sample material. The effects of multiple scattering on the gamma-ray production cross-section are :-

a) To cause an increase in the gamma-ray yield due to the effective increase in the neutron flux, consequently the calculated cross-section from the experiment is artificially high and,

b) Changing the incident neutron energy by elastic scattering[115] so that the neutron energy distribution through the sample will

be continuous from the source energy to zero energy. This has the effect of increasing the measured cross-section since generally, the cross-section for gamma-ray production decreases with increasing the neutron energy from a few MeV above the threshold. This can be seen in the measurements of Lachkar et al.,[6] on iron, Orphan et al.,[113] and Nordborg et al.,[41], on oxygen and Dickens, al.,[116] on calcium.

Day[10] measured the 0.84 MeV gamma-ray production cross-section following the inelastic scattering of 2.6 MeV neutrons from different iron samples. In each case, the cross-section was calculated by two methods :

i) Ignoring the multiple scattering, and

ii) By including a correction term for the increased gamma-ray yield from the second neutron scattering events.

Figure (6-1) shows the results of Day's[10] work where it can be seen that multiple scattering is appreciable even for thin scattering samples. For sample thickness of between 0.1 and 0.2 mfp, the multiple scattering contibutions are 8.7% and 14% respectively. These results were verified theoretically by Kellie et al.[11], using Monte-Carlo calculations. The two sets of results were in agreement to within 1% of each other. Figure (6-2) shows the percentage of the gamma-ray yield due to multiple scattering at different neutron energies according to Kellie et al.[11] calculations. This is in contrast to Walt

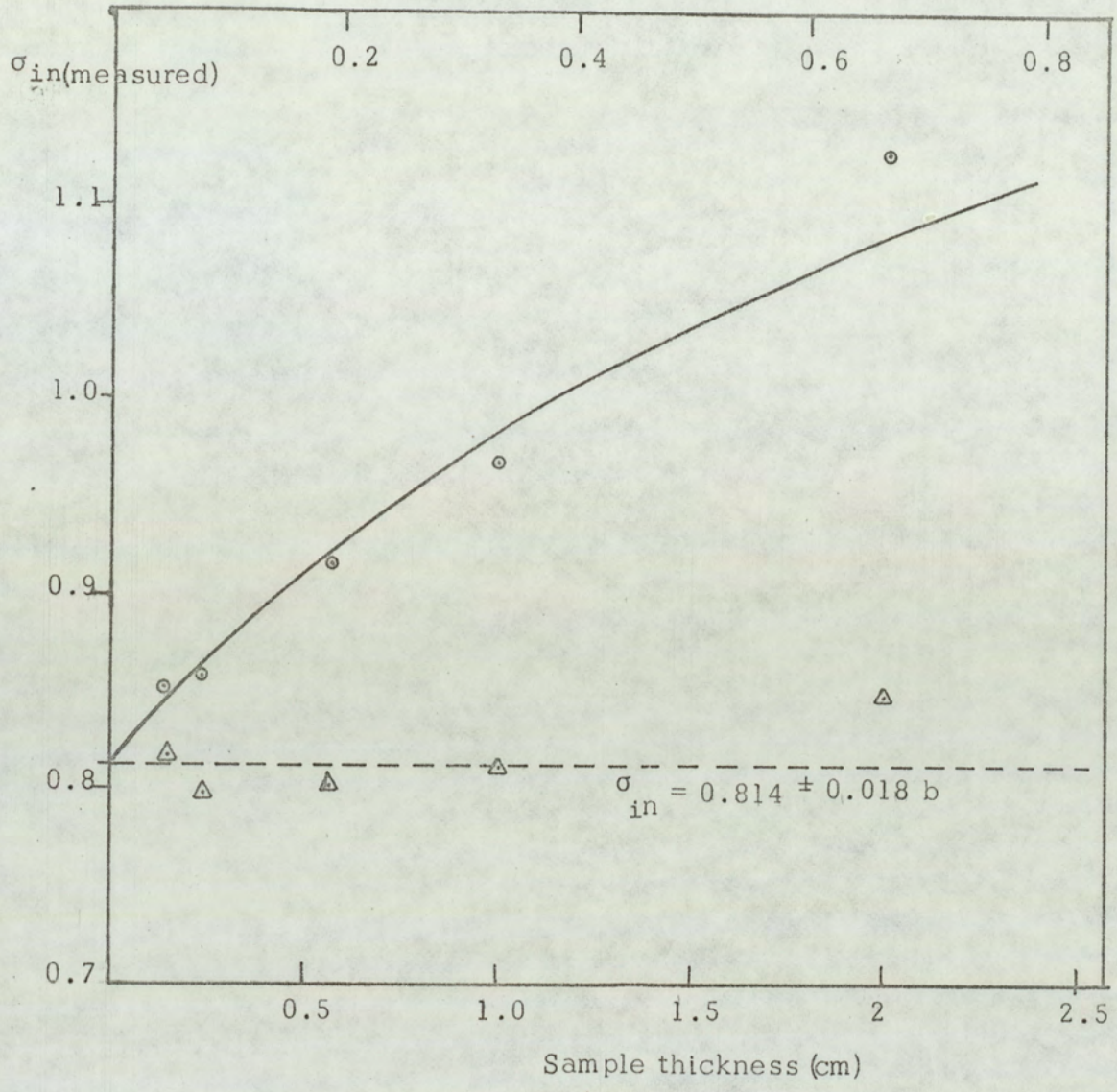

Figure (6.1) The effect of multiple scattering on the gamma-ray production cross-section with different sized samples for ^{56}Fe (n,n)^{56}Fe 0.845 MeV level.

O O O Experimental Results

Δ Δ Δ Corrected cross-section

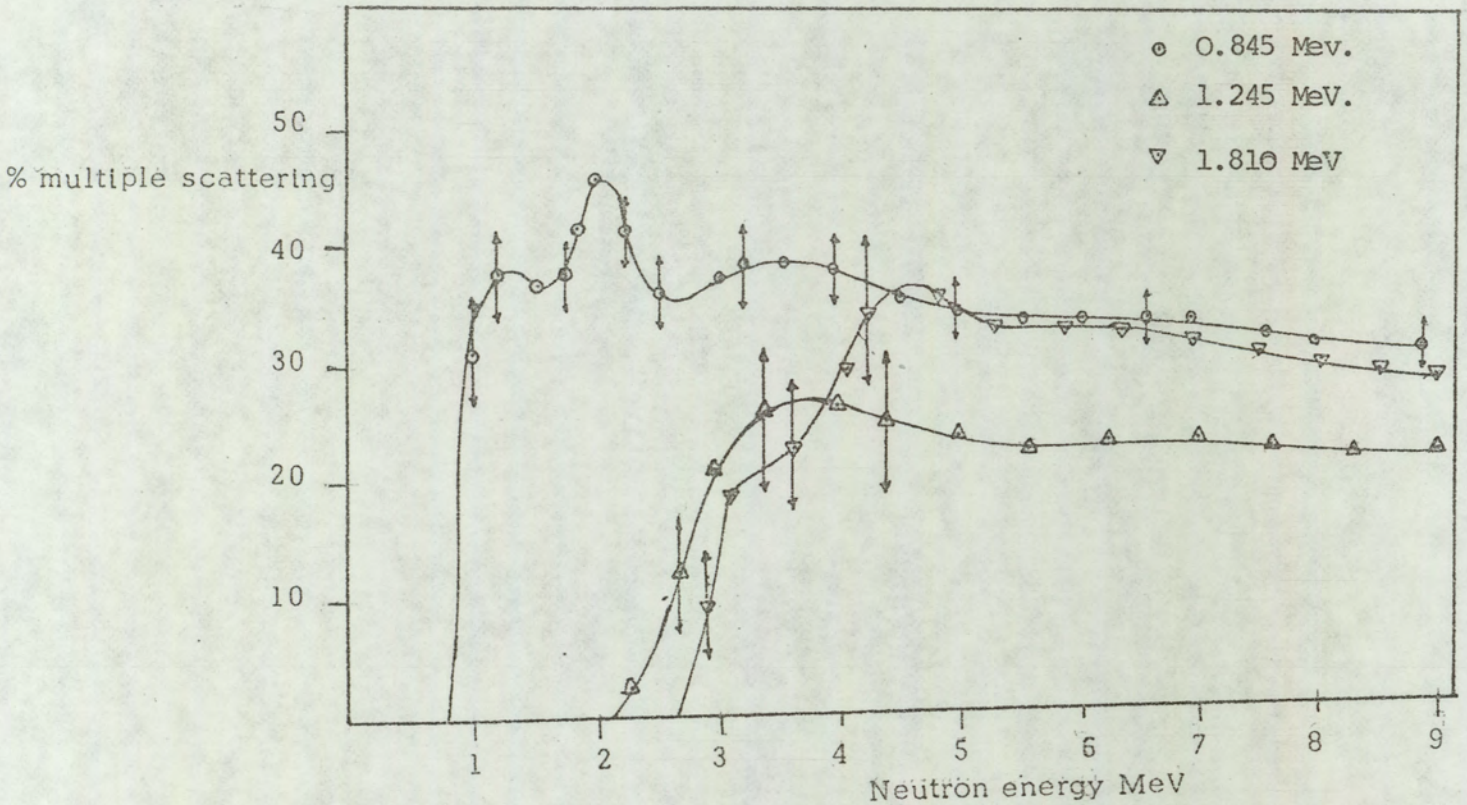

Figure 6-2 Percentage of the yield of the 0.845, 1.24 and 1.81 MeV dexitation gamma-rays from ^{56}Fe resulting from multiple scattering in a disc shaped scattering sample (11)

[38] who states that multiple scattering is not appreciable for sample thickness less than 0.2 mfp.

Since multiple scattering correction requires a great deal of tedious computing, Day[10] suggested that provided the sample thickness has a neutron transmission $\geq$ 70%, the multiple scattering correction could be neglected if the neutron flux is assumed to be constant throughout the sample; i.e. the increased gamma-ray yield is exactly compensated by neglecting the neutron beam attenuation. The validity of this approximation was verified by Day[10] and by Nishimura[117] who found that cross-sections measurements agreed within 2% for different sized samples at incident neutron energies of 2.5 MeV. Martin and Stewart[118] and Allenby[44] also obtained good agreement for cross-sections measurements with different sample thickness at incident neutron energies of 14 MeV.

However, in the present work the thickness and dimensions of the scattering samples are sufficiently large that the above criteria cannot be employed and the multiple scattering process has to be taken into account.

The usual theoretical technique for calculating the effect of multiple scattering is the Monte-Carlo technique which will be briefly discussed in the following section.

6.2 The Monte-Carlo Method :

This method in all its forms involves some sort of random sampling process. Samples are drawn from some "Parent Population" through sampling procedures governed by specified probability laws. Statistical data are collected from the samples and through analysis of these data, one is lead to inferanse concerning the parent population.

For the multiple scattering process, the Monte-Carlo method consists of performing a theoretical experiment with a large number of neutrons incident onto the scattering sample and following the history of each neutron in the sample. The machine is programmed to decide when a neutron suffers a collision, the direction in which it is scattered and what its subsequent history might be, when the process is carried out for a very large number of neutrons. This process gives a satisfactory statistical sample. If a high speed computer is available, then the usefulness of the technique can be improved greatly since it is possible to increase the number of trials, hence allowing more precise simulation of the actual process and hence, yielding greater accuracy.

Because of the complexity of neutron interactions, the transport of neutrons in the reactor shields and the asociated secondary gamma-rays produced are usually handled by using Monte-Carlo technique [119, 120] which has proved to be a useful, if not versatile, tool for calculating the theoretical bases to experimental data.

The utility of the Monte-Carlo Computer Programmes has been significantly restricted by the large computing effort required, although several Monte-Carlo multiple scattering programmes are in use (121,122,123) none of them are suited to the present use because of the considerable number of revisions to adapt these programmes to the present problem and to the computer available at the university, hence, a simpler method working from the principles of continuous slowing down of neutrons in the sample has been adopted.

6.3. The Calculation Procedure Based on The Continuous Slowing Down Model

The following model is an attempt to produce a semi-analytical approach towards the first neutron scattering interaction in the sample which could be extended to take into account the second and further multiple scattering processes involved. The model is based on the continuous slowing down model and the fermi age equation to determine the neutron spatial energy distribution inside the sample and then predicting the gamma-ray yield at each detector position using this distribution.

The following conditions are assumed to hold ;

i) The scattering sample consists of nuclei other than the very light nuclei, i.e. hydrogen and deterium.

ii) The average decrement in the logarithm of the neutron energy per collision (ξ) is independent of the neutron energy.

Under this condition, the behaviour of the neutrons can be reasonably represented by an average, and the logarithmic energy decrement per collision is small. As a result during the slowing down process, it can be assumed that the neutron loses energy continuously rather than discontinuously as is actually the case.

With the above conditions, the differential equation representing the slowing down behaviour in a non-absorbing medium is given by [120]

$$\nabla^2 q = \left\{ \frac{\xi \Sigma_s}{D} \right\} \cdot \frac{dq}{du} \qquad (6\text{-}1)$$

where

q = the slowing down density.

ξ = the average logarithmic energy decrement per collision,

Σ_s = Macroscopic scattering cross-section

D = Diffusion coefficient

u = Neutron lethergy = $\ln (E_o/E_1)$ where E_o and E_1 are the neutron energies before and after the collision respectively.

Upon introducing a new variable $\tau(u)$ defined by

$$\tau(u) = \int_o^u \frac{D}{\xi \Sigma_s} \, du \qquad (6\text{-}2)$$

and making the transformation which replaces u by $\tau(u)$ equation (6-1) reduces to

$$\nabla \, q(u) = \frac{\partial q(u)}{\partial \tau(u)} \qquad (6\text{-}3)$$

Equation (6-3) is known as Fermi age equation.

The quantity τ (u) is called the fermi age of the neutron and has the units of (length)^2. The fermi age is related to the chronological age t which is the time required by the neutron to slow down on the average from its original source energy E_o to the energy E_1 or equivalently as the time between the neutron leaving the source and its attainment of the lethergy (u) by the following relation :

$$\tau(u) = \overline{D}_o \, t \qquad (6\text{-}4)$$

where $\overline{D}_o$ is the average diffusion coefficient over the time t.

The solution of equation (6-3) enables the evaluation of $q(u)$ at any point in the medium, in other words, it enables the determination of the spatial distribution of the neutrons inside the scattering sample. In the present case the large scattering sample has been divided into slices of rectangular shape having thickness of 0.5 cm. From the experimental arrangement the neutrons contributing to the interactions are those defined by the associated cone of alpha particles as shown in Figure (6-3), hence, the neutron source can be considered as a plane source, emitting (S) (neutrons/(cm^2.sec)) of monoenergetic neutrons located at the surface of the scattering sample.

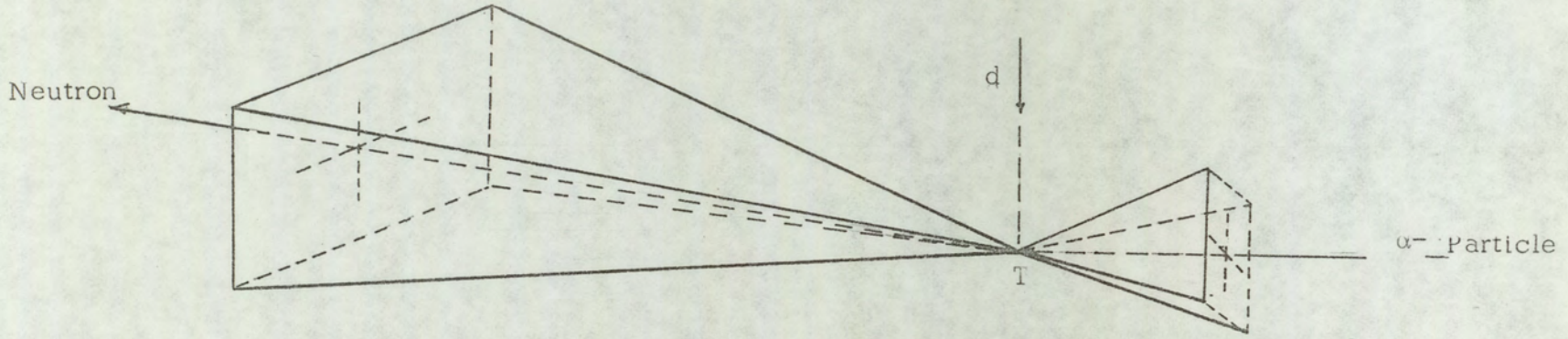

Figure 6-3. The Experimental geometry showing the neutron source on the surface of the scattering sample. Not to scale.

Suppose that the neutron source lies in the Y-Z plane passing through the origin, then fermi age equation (6-3) reduces to

$$\nabla^2 q(x,\tau) = \frac{\partial q(x,\tau)}{\partial \tau} \qquad \text{for } x \neq 0 \qquad (6.5)$$

At the source, the age of the neutron is zero and the source condition can be written as

$$q(x,0) = S \cdot \delta(x) \qquad (6.6)$$

where $\delta(x)$ is the Dirac delta function.

Equation (6-5) can be solved by using a laplace transform or by separating the variables x and τ, by using a solution of the form

$$q(x,\tau) = X(x) \cdot T(\tau) \qquad (6\text{-}7)$$

On substituting equation (6-7) in equation (6-5) and using the boundary conditions, the final solution for Fermi age equation for the slowing down density is

$$q(x,\tau) = \left(\frac{S}{\sqrt{4\pi\tau(u)}}\right) \cdot \left\{\exp\left(-x^2/4\tau(u)\right)\right\} \qquad (6\text{-}8)$$

In the present work, the neutron age $\tau(u)$ has been calculated by using the published data for the neutron age between two known

energies and using the formula

$$\tau(u) = K_o \ln (E_o/E_1) \qquad (6\text{-}9)$$

to determine the proportionality constant K_o.

For the iron samples, the neutron age has been determined by Gerasva et al ,[123] equal to 745 cm^2 for fission neutrons with average energy 2 MeV down to indium resonance energy of 1.46 eV. For concrete, Grimeland and Dönv old[124] measured the age of neutrons produced from the (D,D) reaction with incident deutron of 0.15 MeV at 90^o (resulting in source neutron energy of 2.5 MeV) down to 1.44 eV, they found that the value ($\tau(u) = 297\ cm^2$) gives a good fit to the experimental points. The calculated value for the neutron age from $E_o = 2.5$ MeV to $E_1 = 1.44$ eV in concrete by Grimeland et al.,[124] using the equation

$$\tau(u) = \frac{1}{6} \frac{\int_o^\infty A(r)\, r^4\, dr}{\int_o^\infty A(r)\, r^2\, dr} \qquad (6\text{-}10)$$

was equal to ($444 \pm 11\ cm^2$), and by using the equation

$$\tau(u) = \int_0^u \frac{du}{\sum_i 3\,\Sigma_i\,(1-\bar{\mu}_i) \sum_i (\Sigma_i\,\xi_i)} \qquad (6\text{-}11)$$

where Σ_i is the macroscopic scattering cross-section; of element i .

$\bar{\mu}_i$ is the average cosine of the scattering angle and the rest of the terms have the same meaning as defined before. They calculated the value for $\tau(u)$ using values of the cross-sections taken from BNL-325.

The neutron age from E_o = 2.5 MeV to 1.44 eV has been calculated for their concrete is

$$\tau(u) = 224 \text{ cm}^2$$

The experimental value of $\tau(u)$ determined by Grimeland et al.,[124] was 297 cm^2 for the same concrete. Comparison of the experimental and theoretical values reflects the uncertainty with which composition of concrete is known.

In the present work, the value for the neutron age was taken as the experimentally determined value, i.e. 297 cm^2. This value was used to determine the value of the constant K_o for concrete.

Equation (6-8) was then used to determine the values of the slowing down density $q(u, x)$ for neutrons having energies E_n defined by $0.01 \leq E_n \leq 14$ MeV, which after being normalized so that the sum $q(u, x)$ equals S gives the number of neutrons which have been slowed down past a certain energy E_1 in each slice of the sample. To determine the number of gamma-ray produced at each slice, the number of neutrons still having an energy above the threshold for producing a particular gamma-ray was multiplied by the inelastic cross-

section and divided by the total cross-section, i.e.

$$\text{No. of gamma-rays produced in each slice} = \sum_{E_n = E_{th}}^{E_n = 14\ \text{MeV}} N_i(E) \left(\frac{\sigma\gamma\ (E_n, E\gamma)}{\sigma_t\ (E)} \right) \qquad (6.12)$$

The total number of gamma-rays produced in each sample was obtained by summing the contributions from each slice, i.e;

$$\text{Total number of gamma-rays produced in a sample} = \sum_{\text{All the slices}} \sum_{E_n = E_{th}}^{E_n = 14\ \text{MeV}} N_i\ (E) . \left(\frac{\sigma_{\gamma(En, E_\gamma)}}{\sigma_t\ (En)} \right) \qquad (6.13)$$

The correction terms discussed in Chapter 5, which were introduced to determine the differential cross-section were again used to determine the number of gamma-rays reaching the detector and counted in the spectrum, namely :-

a) The neutron attenuation, for each slice the fraction of the neutron beam which has not interacted was used as the source strength; for the first slice $S = \quad \phi\ (n)$.

b) Self absorption in the sample has been corrected for using the values of $S(\theta)$ defined in Section ($5 - 6$).

c) Solid angle subtended by the detector and

d) the detector efficiency.

The final equation used for calculating the number of gamma-rays produced in the sample and reaching the detector to be counted was

$$P(\theta) = S \left\{ 1 - \exp(-\Sigma_t x) \right\} \cdot q(E_n, x) \cdot \left(\frac{\sigma_\gamma(E_n, E_\gamma)}{\sigma_t(E_n)} \right) \cdot \left. \begin{array}{l} \\ \\ \\ S(\theta, E_\gamma) \cdot \quad \varepsilon(E_\gamma) \cdot \Delta\Omega \end{array} \right\} \quad (6\text{-}14)$$

where all the factors involved have been defined earlier.

6.4. Comparison of Experimental Results and Theoretical Predictions For The Iron Samples :

Figures (6-4) through to Figure (6-6) show the experimental results for the number of gamma-rays of energy 0.84 MeV and 1.24 MeV produced from the iron samples under neutron bombardment. Compared with the number of gamma-rays obtained from the theory. For comparison of the two results, the number of gamma-rays was normalized to the same integrated neutron-flux. The solid line represents the theoretical predictions without considering the neutron attenuation in the sample, while the dotted line represents the theoretical predictions taking neutron attenuation into account. As the theory used provides the gamma-ray yield from the first interaction only, it can be seen that the predicted yield is systematically lower than the experimental measurement but has the same angular distribution.

For the first iron sample of thickness 2 cm, the neutron trans-

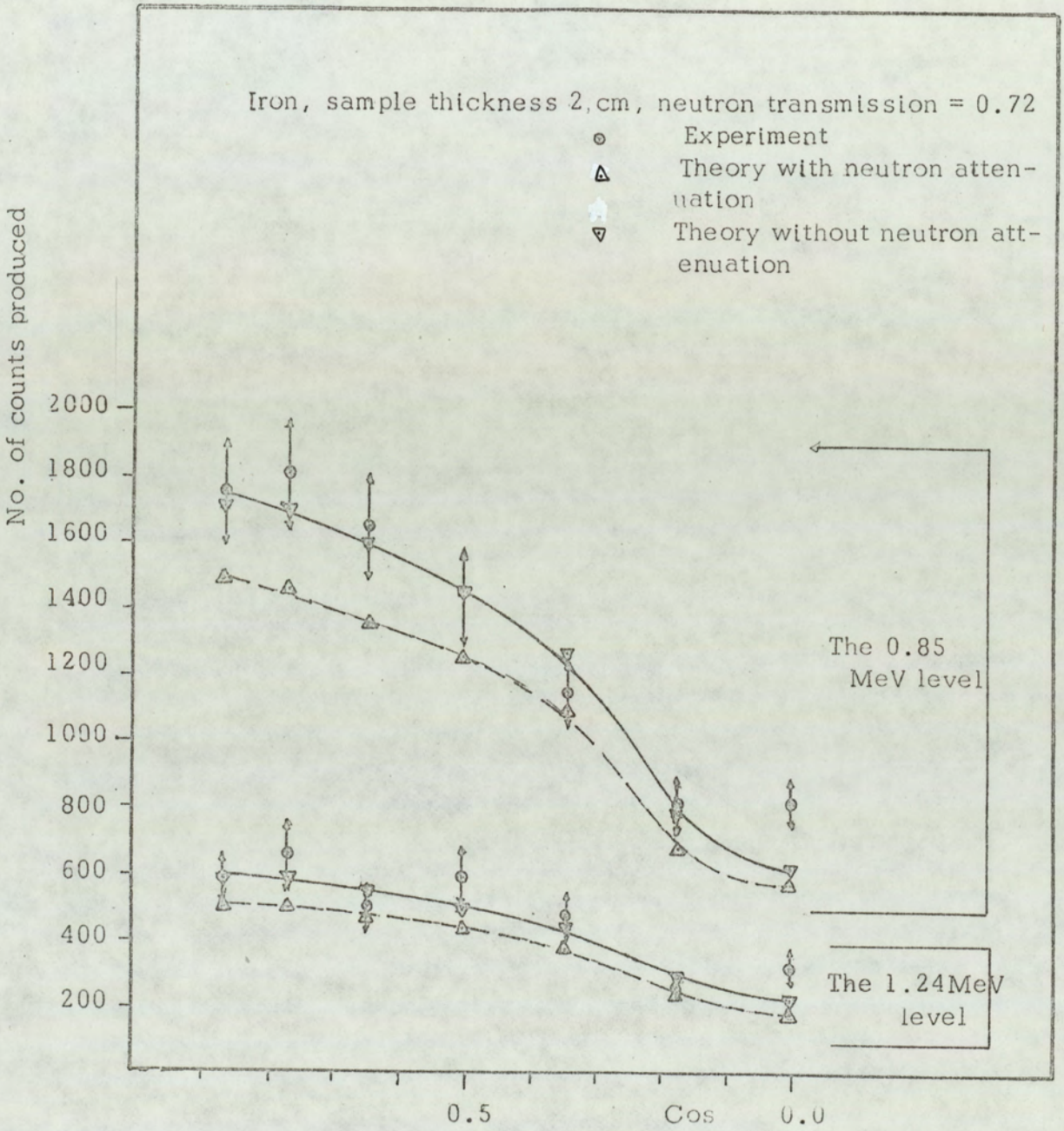

Figure 6-4

Comparison of the experimentally determined number of gamma rays of 0.84 and 1.24 MeV with the theoretical prediction of the model.

All spectra are normalized to total integrated neutron count of 3×10^8 neutrons.

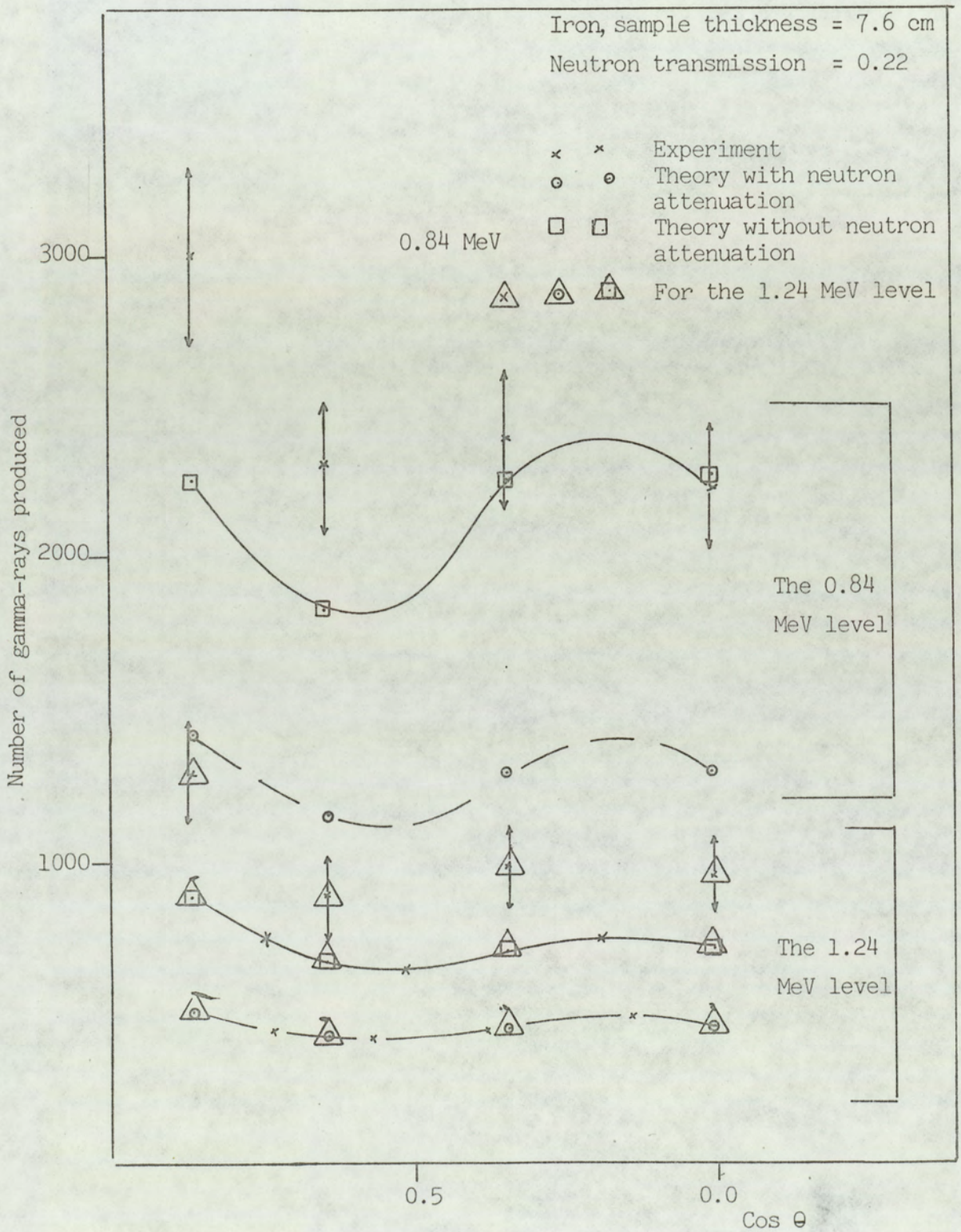

Figure (6-5) The number of 0.84 MeV and 1.24 MeV gamma-ray produced from the 7.6 cm sample as measured experimentally compared to the theoretically predicted values for the angular range (30-90).

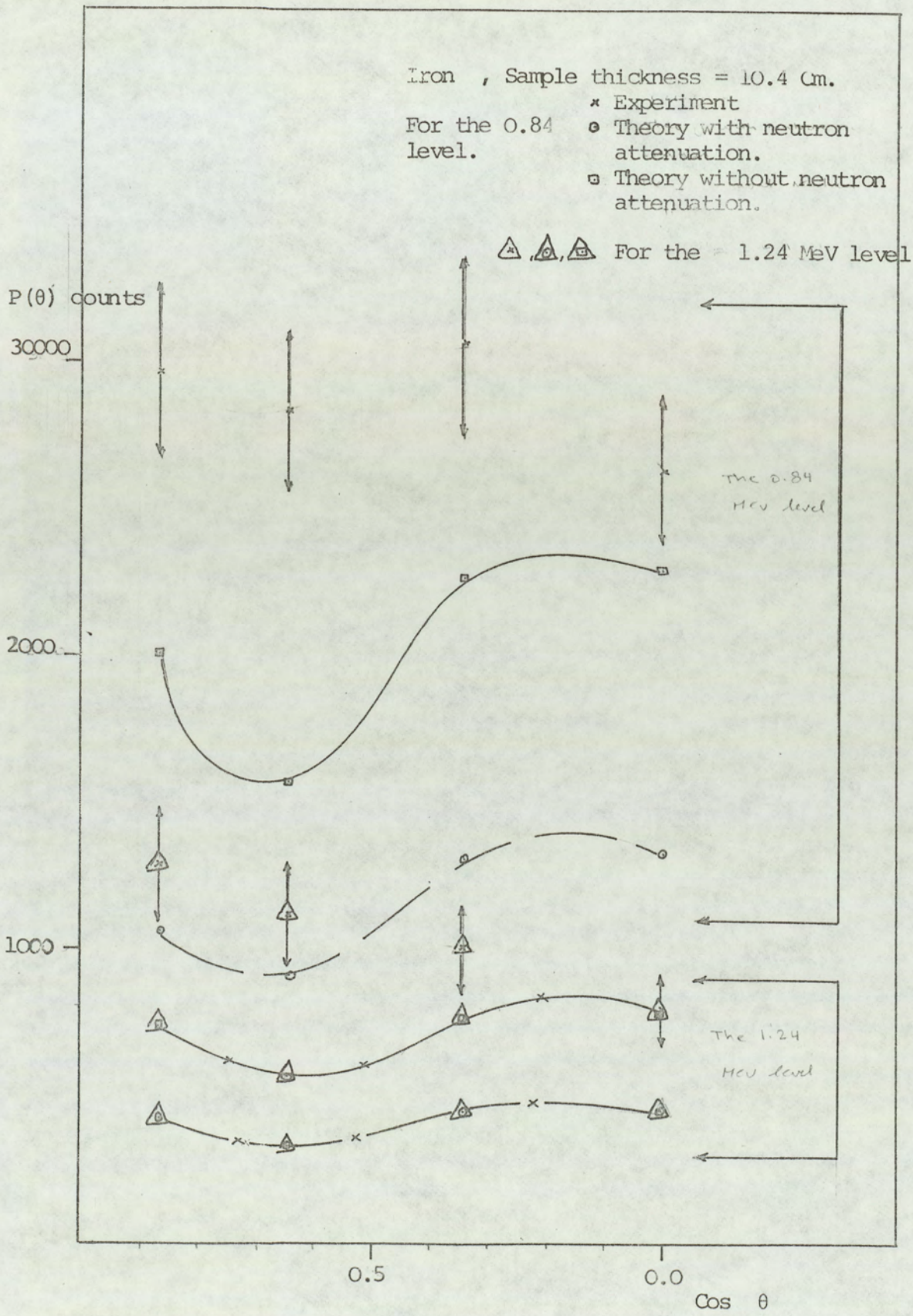

Figure (6-6) Same as figures (6-3) & (6-4) for the 10.4 Cm. thickness in iron.

mission is 0.72, and it can be seen from Figure (6-4) that the multiple scattering correction is completely balanced by ignoring the neutron flux attenuation. For the thicker samples 7.6 cm and 10.4 cm, it can be seen in Figures (6-5) and (6-6) that the multiple scattering correction required is higher than the correction used by ignoring the neutron attenuation. The errors in the experimental results do not include the statistical error which averaged over the set of all the results is about $\pm$ 5%.

6.5. Comparison of Experimental Results and Theoretical Predictions For the Concrete Samples

Figure (6-7) and (6-8) shows the results for the concrete obtained from different samples from the experiments and the theory for the production of gamma-rays between (1-2) MeV and (5-6) MeV.

In order to compare the two results, the number of gamma-rays produced has been normalized to the same integrated neutron count of 3.6×10^8. It can be seen that the agreement between the theoretical predictions and the experiment for the production of (1-2) MeV gamma-rays from concrete is acceptable in the light of the following points.

1 - The hydrogen content of the concrete seriously affects the validity of fermi age theory.

2- The total cross-section for gamma-ray production used in equation (6-13) was calculated as $4 \pi \times (\frac{d\sigma(\theta)}{d\Omega})_{90}$, which

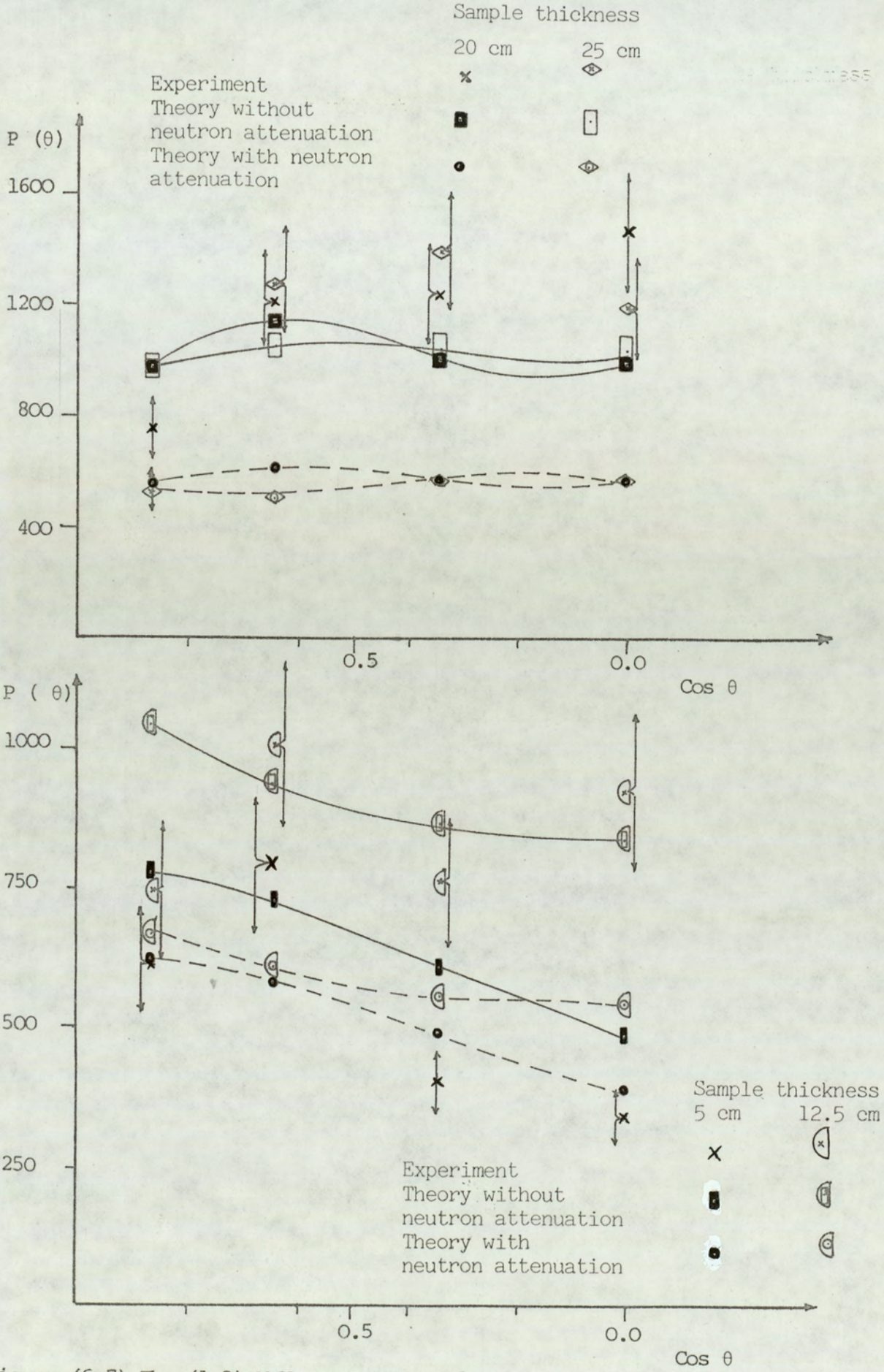

Figure (6-7) The (1-2) MeV gamma-ray production from different concrete samples in the angular range 30^{o}- 90^{o} as measured experimentally compared to the theoretically calculated values .

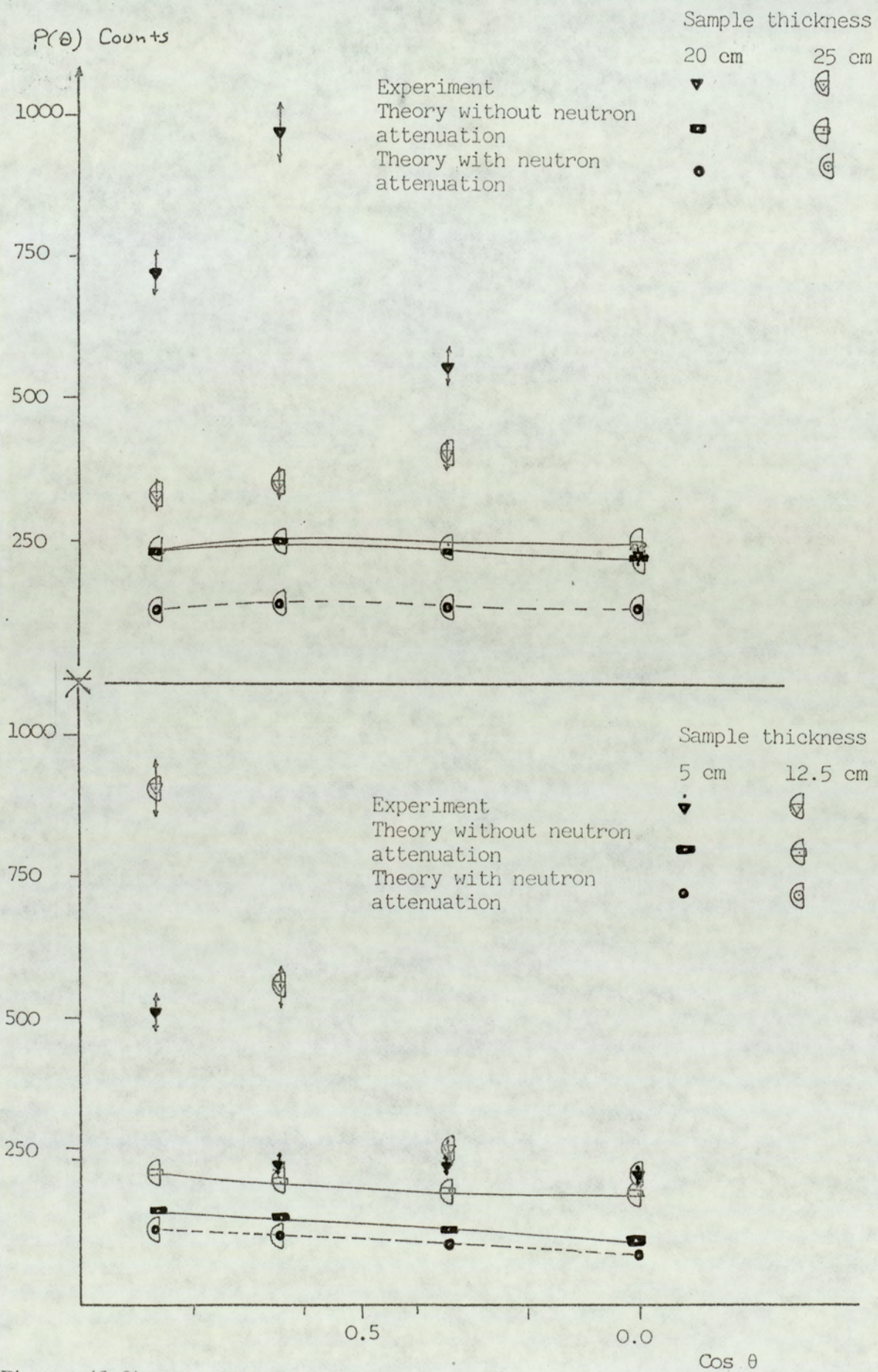

Figure (6-8) The (5-6) MeV gamma-ray production from different concrete samples in the angular range 30^{o}-90^{o} as measured experimentally compared to the theoretically calculated values .

uses the assumption that the angular distributions are isotropic while in fact, they are not, but due to the lack of angular distributions for the elements present in concrete, one has to use this assumption which is used through in the ENDF B IV when evaluating the cross-sections. However, the predicted values at 90^{o} correspond well to the quoted measurement 90^{o} cross-section, as it can be seen from the Figures (6-7) and (6-8) and from table (6-1).

Table (6-1)

The number of gamma-rays with energies between (1-2) MeV produced from the concrete samples at 90^{o} as measured experimentally and the corresponding theoretical predictions.

No. of Counts Produced	Sample Thickness			
	5 cm	12.5 cm	20 cm	25 cm
Experiment	340	925	1470	1179
Theory without Neutron Attenuation	481	841	989	1037
Theory with Neutron Attenuation	387	539	539	567

The errors associated with the above number of counts are estimated as about 15 %, without including the statistical error.

3 - The value used for the neutron age taken from the literature correspond to different concrete from the one used in the present work, but due to the lack of complete set of data required to evaluate the neutron age in concrete these values were used after correcting them to take the variation of the density of the present concrete into account according to the equation from Lamarsh [4]

$$\tau(\rho) = \tau(\rho_o) \cdot (\rho_o/\rho)^2 \qquad (6\text{-}15)$$

where ρ_o and ρ are the densities of the two concretes, $\tau(\rho_o)$ and $\tau(\rho)$ are the corresponding neutron ages.

The disagreement between the theory and experiment increases with increasing the gamma-ray energy as can be seen in Figure (6-8) which can be attributed to the fact that the theory is not a good approximation to the slowing down in concrete because of the hydrogen content as discussed before.

CHAPTER SEVEN

CONCLUSIONS

The results obtained illustrate that the time of flight spectrometer used is well capable of observing the gamma-rays produced in the interactions of 14 MeV neutrons and that the absolute differential cross-sections may be measured with reasonable accuracy.

The main advantages of using the time of flight associated particle technique over the pulsed beam technique are the elimination of the complicated and costly instrumentation required for the latterand the more efficient use of the beam.

The gamma-ray detector can be modified to achieve better light collection and energy resolution by using a larger photomultiplier tube, for example, the Philips 58 AVP Photomultiplier tube which has a photocathode diameter of 110 mm, which would remove the need for the light guide. Furthermore, the 58 AVP Photomultiplier tube has a much better energy resolution than the 56 AVP used. Pourmansouri reported peak to valley ratio for a 76.2 mm x 76.2 mm NaI (Tl) crystal coupled to a 58 AVP tube as 3 to 1 which is superior to the 1.17 to 1 obtained in the present work using a 56 AVP tube. This improvement would allow for smaller sample-detector separation leading to better statistical accuracy in the accumulated spectra.

The present results for the angular distribution from thin iron sample were in a good agreement with the published data as discussed in Chapter

5. The measured spectra from thick iron samples with thicknesses up to ~ 2.5 mfp. showed well defined gamma-ray peaks thus enabling the determination of angular distributions for specific gamma-ray levels from thick samples. This is an improvement as it was reported by Pourmansouri to be difficult to resolve individual peaks in the spectrum, he therefore, was able to report angular distributions per MeV only.

The angular distributions obtained from the concrete samples where no similar measurements have been reported provide a good example of the possibility of studying complex compounds with a reasonable accuracy using the time of flight technique. This is further supported by the good agreement between the measured differential cross-sections at the scattering angle of 90^{o} and the synthesized ones obtained from the published data.

The constant β obtained from the experiments for the variation of the measured cross-section with thickness and the formula used to describe this variation seems to give a good fit to the experimental results. The constants β_{iron} and $\beta_{conc.}$ obtained for iron and concrete separately gave better fits to the iron results and concrete results individually, nevertheless, the universal constant β gave a good fit to both iron and concrete results and it is hoped would also describe the behaviour in any material in the light to medium heavy range, ie. $(3 < A < 70)$, since the materials studied represent this range. This needs to be studied experimentally.

The simple theory developed satisfactorily predicted the gamma-ray production in thin samples and with further modification to include the effects of further scattering events, it could predict the production from thick samples.

It would be interesting to test the results and conclusions of this work by using the same or similar system to study the angular distributions and the effects of multiple scattering on the measured differential cross-sections in different materials. Suitable materials could include carbon, nickel and lead for two reasons a) as they represent a wide range of elements, their behaviour could be a good representative over a wide range of interest and b) they have a relevance to the possible fusion reactor systems.

APPENDIX A

THE KINETICS OF NUCLEAR REACTION

Consider the nuclear reaction

$$M_1 + M_2 \longrightarrow M_3 + M_4 \qquad \text{(A-1)}$$

From the conservation of energy

$$M_1 C^2 + M_2 C^2 + E_1 + E_2 = M_3 C^2 + M_4 C^2 + E_3 + E_4 \qquad \text{(A-2)}$$

If the target is initially at rest, $E_2 = 0$, it follows that

$$(M_1 + M_2 - M_3 - M_4) C^2 = (E_3 + E_4 - E_1) = Q \qquad \text{(A-3)}$$

From the conservation of momentum P,

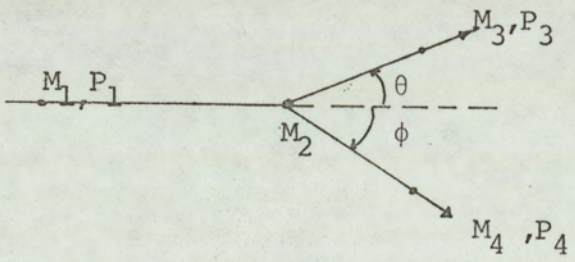

$$P_1 = P_3 \text{ Cos } \theta + P_4 \text{ Cos } \phi$$

$$0 = P_3 \text{ sin } \theta - P_4 \text{ Cos } \phi \qquad \text{(A-4)}$$

From the above equations, the equation for the energy of the light particle, E_3 is given by (127)

$$E_3 = \frac{M_1 M_2 E_1}{(M_3 + M_4)^2} \left[2 \cos^2 \theta + \frac{M_4(M_3+M_4)}{M_1 M_3} \left(\frac{Q}{E_1} - \frac{M_1}{M_4} + 1 \right) \right.$$

$$\left. \pm 2 \cos\theta \left\{ \cos^2 \theta + \frac{M_4(M_3 + M_4)}{M_1 M_3} \left(\frac{Q}{E_1} - \frac{M_1}{M_4} + 1 \right)^{\frac{1}{2}} \right\} \right] \quad \text{(A-5)}$$

where

M_1 = Mass of incident particle

M_2 = Mass of target

M_3 = Mass of light product

M_4 = Mass of heavy product

E_1 = Energy associated with M_1

θ = Laboratory angle of light product

Q = Energy released in reaction

Defining the quantities

$$E_T = E_1 + Q$$

$$A_o = (M_1 + M_2)(M_3 + M_4)$$

$$A = \frac{M_1 M_4}{A_o} \quad \frac{E_1}{E_T}$$

$$B = \frac{M_1 M_3}{A} \quad \frac{E_1}{T}$$

$$C = \frac{M_2 M_3}{A_o} \left[1 + \frac{M_1 Q}{M_2 E_T} \right]$$

$$D = \frac{M_2 M_4}{A_o} \left[1 + \frac{M_1 Q}{M_2 E_T} \right]$$

Equation (A-5) can be rewritten as

$$E_3 = E_T B \left[\text{Cos}\,\theta + (D/B - \text{Sin}^2\,\theta)^{\frac{1}{2}} \right]^2 \qquad \text{(A-6)}$$

The energy of the heavy product, E_4 in the laboratory is given by

$$E_4 = E_T A \left[\text{Cos}\,\phi + \left(\frac{C}{A} - \text{Sin}^2\,\phi \right)^{\frac{1}{2}} \right]^2 \qquad \text{(A-7)}$$

The angle of emission of the heavy and light products in the laboratory system are related by

$$\text{Sin}\,\phi = \left[\frac{M_3 E_3}{M_4 E_4} \right]^{\frac{1}{2}} \text{Sin}\,\theta$$

Considering the reaction in the centre of mass system and densting the angle of emission of the light and heavy products by θ_c and ϕ_c respectively, the energy of the light product is given by

$$E_3 = E_T \left[(B + D) + (2AC)^{\frac{1}{2}} \text{Cos}\,\theta_c \right] \qquad \text{(A-9)}$$

and the energy of the heavy product, E_4 in the laboratory is given by

$$E_4 = E_T \left[(A + C) + (2AC)^{\frac{1}{2}} \cos \phi_c \right] \qquad \text{(A-10)}$$

The centre of mass and laboratory angles of the light product are related by

$$\sin \theta_c = \left[\frac{E_3}{E_T D} \right]^{\frac{1}{2}} \sin \theta \qquad \text{(A-11)}$$

APPENDIX B

LEAST SQUARES FIT

The equation describing the angular distribution in the X(a,b) Y reaction has the form

$$\frac{d\sigma(\theta)}{d\Omega} = A_o + A_2 \cos^2\theta + A_4 \cos^4\theta \qquad \text{(B-1)}$$

In fitting a curve to differential cross-section measurements, the assumption is made that there is no error in the value of the scattering angle thus, an experimental error exists only in the values of the differential cross-section.

Let $Y_i = \frac{d\sigma(\theta)}{d\Omega}$ and $X_i = \cos\theta$ then equation (B-1) becomes

$$Y_i = A_o + A_2 X_i^2 + A_4 X_i^4 \qquad \text{(B-2)}$$

The coefficients of the polynomial can be estimated using the least squares principle, by minimizing

$$\sum_{i=1}^{n} \left[Y_i - (A_o + A_2 X_i^2 + A_4 X_i^4) \right]^2 \qquad \text{(B-3)}$$

for n data points (X_i, Y_i).

Differentiating equation (B-3) partially with respect to A_o, A_2 and A_4, equating the partial derivatives to zero and letting a_i be the best estimate of A_i gives

$$\sum Y_i = n\, a_o + a_2 \sum X_i^2 + a_4 \sum X_i^4$$

$$\sum Y_i X_i^2 = a_o \sum X_i^2 + a_2 \sum X_i^4 + a_4 \sum X_i^6 \qquad \text{(B-4)}$$

$$\sum Y_i X_i^4 = a_o \sum X_i^4 + a_2 \sum X_i^6 + a_4 \sum X_i^8$$

where the summation extends from i to n in each case. The coefficients a_o, a_2 and a_4 of the polynomials fitted to the measured angular distributions were calculated using equation (B-4).

Estimation of error in fitted curve

If the fitted polynomial to the measured angular distribution is given by

$$Z_i = a_o + a_2 X_i^2 + a_4 X_i^4 \qquad \text{(B-5)}$$

then the residuals, d_i are given by

$$d_i = Y_i - (a_o + a_2 X_i^2 + a_4 X_i^4) \qquad \text{(B-6)}$$

The standard error, α , in the expression

$$Y_i - (a_o + a_2 X_i^2 + a_n X_i^4)$$

is given by

$$\alpha^2 = \frac{\sum_{i=1}^{n} d_i^2}{n - m} \qquad \text{(B-7)}$$

where m is the number of calculated coefficients, and in this case $m = 3$.

If α_i is the standard error in a_i, then from Topping[128] the errors α_i is given by

$$\frac{\alpha_o^2}{\begin{vmatrix} X_4 & X_6 \\ X_4 & X_8 \end{vmatrix}} = \frac{\alpha_2^2}{\begin{vmatrix} n & X_4 \\ X_4 & X_8 \end{vmatrix}} = \frac{\alpha_4^2}{\begin{vmatrix} n & X_2 \\ X_2 & X_4 \end{vmatrix}} = \frac{\alpha^2}{\Delta} \qquad (B.8)$$

where

$$\Delta = \begin{vmatrix} n & X_2 & X_4 \\ X_2 & X_4 & X_6 \\ X_i & X_6 & X_8 \end{vmatrix} \quad , \quad X_2 = \sum X_i^2 \quad , \quad X_4 = \sum X_i^4$$

$$X_6 = \sum X_i^6 \quad \text{and} \quad X_8 = \sum X_i^8 \quad , \quad \text{and where the}$$

summations, $\sum$, in equations (B-7) and (B-8) are from 1 to n.

The equation for the angular distribution is then given by

$$\frac{d\sigma(\theta)}{d\Omega} = (a_o + \alpha_o) + (a_2 + \alpha_2)\,\mathrm{Cos}^2\theta + (a_4 + \alpha_4)\,\mathrm{Cos}^4\theta$$

L.S.FIT (T-X CONC.)

```
READY.

 110 PRINT "LEAST SQUARES FIT"
 120 FOR I=1TO20
 130 READW,W1
 140 PRINTCHR$(1) "FOR THE ENERGY BAND (";W"-";W+1")MEV";W1"DEG."
 150 PRINT:PRINT
 160 PRINTSPC(3)"T CM."SPC(6)"T MFP."SPC(6)"X-SEC"SPC(7)"LN(X-S"
 170 PRINTSPC(3)"====="SPC(6)"======"SPC(6)"====="SPC(7)"======"
 180 O=4
 190 C=0
 200 D=0
 210 E=0
 220 F=0
 230 FOR P=1 TO O
 240 READX1,N
 250 X=(X1*.1145)
 260 Y=LOG(N)
 270 A=X*Y
 280 B=X*X
 290 C=C+X
 300 D=D+Y
 310 E=E+A
 320 F=F+B
 330 M=(O*E-(C*D))/(O*F-C*C)
 340 G=(D*F-(C*E))/(O*F-C*C)
 350 G1=EXP(G)
 360 Z=X1:GOSUB460:PRINTU$ SPC(4)
 370 Z=X :GOSUB460:PRINTU$ SPC(4)
 380 Z=N :GOSUB460:PRINTU$ SPC(4)
 390 Z=Y :GOSUB460:PRINTU$
 400 NEXT P
 410 PRINT:PRINT
 420 PRINT,CHR$(1)"Y=";M"*X+";G
 430 PRINT
 440 PRINT CHR$(1)"X0-SEC=";G1
 450 NEXTI
 460 Z=INT(Z*1000+.5)
 470 Q$=STR$(Z):L=LEN(Q$)
 480 R$=LEFT$(Q$,L-3)
 490 K$=RIGHT$(Q$,3)
 500 J$=R$+"."+K$:H$="        "+J$
 510 U$=RIGHT$(H$,8)
 520 RETURN
 530 STOP
 535 REM"============ 1-2 MEV ========="
 540 DATA 1,30,  5,13.298,12.5,15.426,20,20.860,25, 17.869
 550 DATA1,50,5,17.422,12.5,18.438,20,34.776,25,51.422
 560 DATA1,70, 5,10.592,12.5,19.289,20,51.932,25,78.429
 570 DATA1,90, 5,11.269,12.5,31.206,20,75.297,25,77.949
 575 REM"============ 2-3 MEV ========="
 580 DATA 2,30,  5,49.985,12.5,52.798,20,52.353,25,48.142
 590 DATA2,50,5,26.538,12.5,26.419,20,56.398,25,75.017
 600 DATA2,70, 5,25.148,12.5,35.606,20,78.300,25,118.555
 610 DATA2,90, 5,14.115,12.5,25.603,20,87.555,25,96.791
 615 REM"========== 3-4 MEV ========="
 620 DATA 3,30,5,55.885,12.5,80.716,20,72.395,25,53.042
 630 DATA3,50,5,30.686,12.5,39.446,20,64.729,25,77.135
 640 DATA3,70, 5,32.033,12.5,36.044,20,92.537,25,110.800
 650 DATA3,90,5,13.558,12.5,32.151,20,64.639,25,70.651
 660 REM"========= 4-5 MEV ========="
 670 DATA 4,30,5,30.798,12.5,50.396,20,44.808,25,23.847
```

LEG.POL.FIT FOR THE CONC.RESULTS

```
READY.

 100 OPEN1,4:CMD1
 110 PRINTCHR$(1)"24-3-81 LEG.POL.FIT FOR THE CONC.RESULTS": PRINT
 120 PRINTCHR$(1)"**** AFTER  GF CORRECTION ****"
 130 FOR T=1TO20
 140 X1=0:X2=0:X3=0:X4=0:X5=0
 150 Y1=0:R1=0:L1=0
 160 READ  S1,S2
 170 PRINTCHR$(1)"THE ENERGY BAND (";S1"-";S1+1")MEV":PRINT
 180 PRINTCHR$(1)"THE SAMPLE THICKNESS =";S2"CM."
 190 M=4
 200 FOR I=1TOM
 210 READX(I):NEXT
 220 FOR I=1TOM
 230 READY(I):NEXT
 240 PRINTCHR$(1)" MEASURED X-SECTIONS "
 250 FOR I=1TOM
 260 PRINTX(I)SPC(6)Y(I)
 270 NEXTI
 280 FOR I=1TOM
 290 N=M
 300 X1(I)=COS(X(I)*π/180)
 310 X1(I)=INT(X1(I)*1000 +.5)/1000
 320 X1=X1+X1(I)
 330 X1   =INT(X1*1000 +.5)/1000
 340 X2(I)=X1(I)↑2
 350 X2=X2+X2(I)
 360 X2   =INT(X2*1000 +.5)/1000
 370 X3(I)=X1(I)↑4
 380 X3   =X3+X3(I)
 390 X3   =INT(X3*1000 +.5)/1000
 400 X4(I)=X1(I)↑6
 410 X4   =X4+X4(I)
 420 X4   =INT(X4*1000 +.5)/1000
 430 X5(I)=X1(I)↑8
 440 X5   =X5+X5(I)
 450 X5   =INT(X5*1000 +.5)/1000
 460 Y1=Y1+Y(I)
 470 R(I)=Y(I)*X2(I)
 480 R1=R1+R(I)
 490 R1=INT(R1*1000+.5)/1000
 500 L(I)=Y(I)*X3(I)
 510 L1=L1+L(I)
 520 L1=INT(L1*1000+.5)/1000
 530 NEXTI
 540 IFS2>5THEN:GOTO640
 550 PRINT"SIGMA COS=              X1= ";X1
 560 PRINT"SIGMA COS↑2=            X2=";X2
 570 PRINT"SIGMA COS↑4=            X3= ";X3
 580 PRINT"SIGMA COS↑6=            X4= ";X4
 590 PRINT"SIGMA COS↑8=            X5= ";X5
 600 PRINT"=========================="
 610 PRINT"SIGMA D-X-S=            Y1=   ";Y1
 620 PRINT"SIGMA((D.X)*(COS↑2))=    R1=";R1
 630 PRINT"SIGMA((D.X)*(COS↑4))=    L1=";L1
 640 Z1=(Y1*X2-R1*N)*(X3*X3-X2*X4)-(R1*X3-L1*X2)*(X2*X2-N *X3)
 650 Z2=(X3↑2-X2*X4)*(X2*X3-N*X4)-(X3*X4-X2*X5)*(X2*X2-X2*X4)
 660 Z=Z1/Z2
 670 Y=((Y1*X2-R1*N)-(X2*X3-N*X4)*Z)/(X2↑2-N*X3)
```

```
680 X9=(Y1-X2*Y-X3*Z)/Y1
690 H1=(Y1*X4-R1*X3)*(X3*X5-X4↑2)
700 H2=(R1*X5-L1*X4)*(X2*X4-X3↑2)
710 H3=(N*X4-X2*X3)*(X3*X5-X4↑2)
720 H4=(X2*X5-X3*X4)*(X2*X4-X3↑2)
730 B0=(H1-H2)/(H3-H4)
740 B2=((Y1*X4-R1*X3)-(N*X4-X2*X3)*B0)/(X2*X4-X3↑2)
750 B4=(L1-(X3*B0+X4*B2))/X5
760 PRINT
770 PRINTCHR$(1)SPC(5) " THE COEFFICIENTS ":PRINT
780 PRINT"B0=";B0:PRINT"B2=";B2:PRINT"B4=";B4
790 PRINT
800 PRINT:PRINTCHR$(1)SPC(4)"THE FITTED X-SECTIONS "
810 PRINT
820 FOR E=30TO90 STEP 5
830 V=COS(E*π/180)
840 V1=INT(V*1000+.5)/1000
850 XS=B0+B2*(V↑2)+B4*(V↑4)
860 XS=INT(XS*100 +.5)/100
870 PRINTE SPC(5)V1,XS
880 NEXTE
885 PRINT"=========================="
890 FOR E=30TO90 STEP20
900 V=COS(E*π/180)
910 V1=INT(V*1000+.5)/1000
920 XS=B0+B2*(V↑2)+B4*(V↑4)
930 XS=INT(XS*100 +.5)/100
940 PRINTE SPC(5)V1,XS
950 NEXTE
960 PRINT:PRINT:PRINT
970 IF T=4THEN:PRINT:PRINT:PRINT:PRINT:PRINT:PRINT:PRINT:PRINT:PRINT:PRINT
980 IF T=8THEN:PRINT:PRINT:PRINT:PRINT:PRINT:PRINT:PRINT:PRINT:PRINT:PRINT
990 IF T=12THEN:PRINT:PRINT:PRINT:PRINT:PRINT:PRINT:PRINT:PRINT:PRINT:PRINT
1000 IF T=16THEN:PRINT:PRINT:PRINT:PRINT:PRINT:PRINT:PRINT:PRINT:PRINT:PRINT
1010 IF T=20THEN:PRINT:PRINT:PRINT:PRINT:PRINT:PRINT:PRINT:PRINT:PRINT:PRINT
1020 NEXT T
1030 REM"========== (1-2 MEV)========"
1040 DATA 1,5
1050 DATA 30   ,50   ,70  ,90
1060 DATA 13.298,17.422,10.592,11.269
1070 DATA 1,12.5
1080 DATA 30   ,50   ,70  ,90
1090 DATA15.426,18.438,19.289,31.206
1100 DATA 1,20
1110 DATA 30   ,50   ,70  ,90
1120 DATA20.860,34.776,51.932,75.297
1130 DATA 1,25
1140 DATA 30   ,50   ,70  ,90
1150 DATA17.869,51.422,78.429,77.949
1160 REM"========== (2-3 MEV)========"
1170 DATA 2,5
1180 DATA 30   ,50   ,70  ,90
1190 DATA49.985,26.538,25.148,14.115
1200 DATA 2,12.5
1210 DATA 30   ,50   ,70  ,90
1220 DATA52.798,26.419,35.606,25.603
1230 DATA 2,20
1240 DATA 30   ,50   ,70  ,90
1250 DATA52.353,56.398,78.300,87.555
1260 DATA 2,25
1270 DATA 30   ,50   ,70  ,90
1280 DATA48.142,75.017,118.555,96.791
1290 REM"========== (3-4 MEV)========"
1300 DATA 3,5
1310 DATA 30   ,50   ,70  ,90
1320 DATA55.885,30.686,32.033,13.558
```

C. T. G.

```
READY.

 100 OPEN1,4:CMD1
 110 PRINTCHR$(1)"4-4-81 CONCRETE TOTAL GAMMA PRODUCTION"
 120 DIM M1(50),MX(50),M(50),  I(100),FR(100),N(50),MS(50)
 130 DIM M2(40),M3(40),M4(40),M5(40)
 140 DIM Q1(50),F1:100),E1(50),A(50),T(50),Q(50),F2(50),FF(50),N9(50)
 150 MU=.1145
 160 INPUT AA,NA
 170 WW=1
 180 PRINTCHR$(1)SPC(2)"GAMMA PRODUCTION (";AA-1"-";AA")MEV."
 190 NN=3.8E5
 200 IF WW=1THEN:GOTO250
 210 PRINTCHR$(1),"E0= 14"SPC(2)"MU=";MU
 220 PRINTCHR$(1)"NO. OF SOURCE NEUTRONS =360000"
 230 PRINT SPC(6)"E1(N)"SPC(9)"A(N)"SPC(7)"T(N)"SPC(7)"Q(N)"SPC(9)"FF"SPC(9)"Q1"
 240 PRINT SPC(6)"====="SPC(9)"===="SPC(7)"===="SPC(7)"===="SPC(9)"=="SPC(9)"=="
 250 E0=14
 260 IF WW=1THEN:GOTO290
 270 PRINT SPC(6)"E MEV"SPC(6)"0.INT.XS"SPC(3)"N.TOT.MIC XS"SPC(3)"N.MAC.XS"
 280 PRINT SPC(6)"====="SPC(6)"========"SPC(3)"============"SPC(3)"========"
 290 FOR N=1TO14:READE1(N):NEXT
 300 FOR N=1TO12:READX1(N):NEXT
 310 FOR N=1TO12:READX2(N):NEXT
 320 FOR N=1TO12:READX3(N):NEXT
 330 FOR N=1TO12:READX4(N):NEXT
 340 FOR N=1TO12:READX5(N):NEXT
 350 FOR N=1TO12:READMX(N):NEXT
 360 IF AA>2THEN:GOTO 420
 370 FOR N=1TO12
 380 Z=14-N :GOSUB1930:PRINTR$SPC(1)
 390 Z=MX(N):GOSUB1930:PRINTR$SPC(1)
 400 PRINTX1(N);X2(N);X3(N);X4(N);X5(N)
 410 NEXTN
 420 PRINTCHR$(1),"NA=";NA*1E22
 430 PRINT SPC(7)"X CM."SPC(7)"FRAC."SPC(4)"NO.N.INT"SPC(5)"NO.G.PR"SPC(5)"AC.N
 440 PRINTSPC(7)"====="SPC(7)"====="SPC(4)"========"SPC(5)"======="SPC(5)"====="
 442 PRINT:PRINT
 445 PRINTSPC(7)"X CM."SPC(4)"FRAC.INT"SPC(4)"FRAC.REM"
 446 PRINTSPC(7)"====="SPC(4)"========"SPC(4)"========"
 447 PRINT
 450 FOR X=.5TO25  STEP.5
 460 QT=0
 470 GOTO 1009
1009 NN=NN
1010 FF=ABS(EXP(-.1145*X)-EXP(-.1145*(X-.5)))*100
1011 FF=INT(FF*1000+.5)/1000
1020 READ FR
1021 N9=NN*FR
1025 Z=X     :GOSUB1930:PRINTR$SPC(1)
1026 Z=FF    :GOSUB1930:PRINTR$SPC(1)
1027 Z=FR    :GOSUB1930:PRINTR$
1030 Q0=0
1040 M=14
1050 FOR N=1 TOM-AA
1060 A(N)=LOG(E0/E1(N))
1070 T(N)=39.5*A(N)
1080 Q(N)=(1/.868719468 )*1/(EXP(.25/(4*T(N)))*SQR(4*π*T(N)))
1090 Q0=Q0+Q(N)
1100 MS(N)=MX(N)*1E24  /(NA*1E22)
1110 IFAA=6THEN:GOTO1160
1120 IFAA=5THEN:GOTO1180
```

```
1130 IFAA=4THEN GOTO1200
1140 IFAA=3THEN GOTO1220
1150 IFAA=2THEN GOTO1240
1160 Q1(N)=N9*Q(N)*(FF/100)*(X5(N)/MX(N))
1170 IFAA=6THEN GOTO1250
1180 Q1(N)=N9*Q(N)*(FF/100)*(X4(N)/MX(N))
1190 IFAA=5THEN GOTO1250
1200 Q1(N)=N9*Q(N)*(FF/100)*(X3(N)/MX(N))
1210 IFAA=4THEN GOTO1250
1220 Q1(N)=N9*Q(N)*(FF/100)*(X2(N)/MX(N))
1230 IFAA=3THEN GOTO1250
1240 Q1(N)=N9*Q(N)*(FF/100)*(X1(N)/MX(N))
1250 QT=QT+Q1(N)
1260 QA=QA+Q1(N)
1270 IF WW=1THEN  GOTO1340
1280 Z=E1(N) GOSUB1930:PRINTR#SPC(1)
1290 Z=A(N) GOSUB1930:PRINTR#SPC(1)
1300 Z=T(N) GOSUB1930:PRINTR#SPC(1)
1310 Z=Q(N)*100  GOSUB1930:PRINTR#SPC(1)
1320 Z= FF    GOSUB1930:PRINTR#SPC(1)
1330 Z=Q1(N)  GOSUB1930:PRINTR#
1340 NEXTN
1350 IF X=5 THEN GOTO1430
1360 IF X<5 THEN GOTO1370
1370 IF X=12.5 THEN GOTO1430
1380 IF X<12.5 THEN GOTO1390
1390 IF X=20   THEN GOTO1430
1400 IF X<20   THEN GOTO1410
1410 IF X=25   THEN GOTO1430
1420 IF X<25   THEN GOTO1490
1430 PRINT"ACC. Q=";QQ
1440 Z=  X    GOSUB1930:PRINTR#SPC(1)
1450 Z=FF GOSUB1930:PRINTR#SPC(1)
1460 Z=N9*FF/100:GOSUB1930:PRINTR#SPC(1)
1470 Z=QT   GOSUB1930:PRINTR#SPC(1)
1480 Z=QA   GOSUB1930:PRINTR#
1490 IFX=5THEN PRINT:PRINT:PRINTCHR#(1)SPC(4)"END OF SAMPLE NO.(1)":PRINT:PRINT
1500 IFX=12.5THEN PRINT:   PRINTCHR#(1)SPC(4)"END OF SAMPLE NO. (2) ":PRINT:PRI
NT
1510 IFX=20 THEN PRINT:  PRINTCHR#(1)SPC(4)"END OF SAMPLE NO. (3) ":PRINT:PRINT
1520 IFX=25 THEN PRINT:  PRINTCHR#(1)SPC(4)"END OF SAMPLE NO. (4) ":PRINT:PRINT
1530 NEXTX
1540 STOP
1550 REM"*******************************"
1560 REM" ======== NEUTRON ENERGY ===="
1570 DATA 13,12,11,10,9,8,7,6,5,4,3,2,1,.01
1580 REM"====== GAMMA TOTAL X-SEC =="
1590 REM"====== X1(N) (1-2) MEV  =="
1600 DATA.186,.193,.199,.185,.185,.166,.176,.171,.168,.153,.116,.078
1610 REM"====== X2(N) (2-3) MEV  =="
1620 DATA.090,.095,.098,.092,.086,.080,.074,.061,.044,.024,.016,.003
1630 REM"====== X3(N) (3-4) MEV  =="
1640 DATA.119,.139,.141,.145,.141,.101,.051,.049,.029,.02,.0007,.0001
1650 REM"====== X4(N) (4-5) MEV  =="
1660 DATA.051,.036,.034,.032,.027,.027,.020,.010,.005,.001,.0001,.0001
1670 REM"====== X5(N) (5-6) MEV  =="
1680 DATA.134,.110,.110,.082,.133,.132,.103,.027,.0015,.0001,.0001,.0001
1690 REM"====== TOTAL X-SEC -CONC. =="
1700 DATA1.74,1.72,1.75,1.70,1.58,1.55,1.24,1.29,1.67,1.55,2.23,1.63
1820 REM"***** FRACTION REMAINING ****"
1830 DATA1,.944,.892, .842,.795,.751,.709,.670,.633,.597
1840 REM"============================="
1850 DATA .564,.533,.503,.475,.449,.424,.400,.378,.357,.337,.318,.301,.284,.268
1860 REM"============================="
1870 DATA .253,.239,.226,.213,.201,.190,.179,.170,.160,.151,.143,.135
1880 DATA .127,.120,.114,.107
```

```
1890 REM"============================="
1900 DATA .101,.096,.090,.085,.081,.076,.072,.068,.064,.060
1910 REM"============================="
1920 REM"*****************************"
1930 Z=INT(Z*1000 +.5)
1940 B$=STR$(Z):L=LEN(B$)
1950 D$=LEFT$(B$,L-3):J$=RIGHT$(B$,3)
1960 P$=D$+","+J$:O$="              "+P$
1970 R$=RIGHT$(O$,11)
1980 RETURN
1990 STOP
3000 REM" ===== FRACTION INT.  ===="
3010 DATA 5.564,5.255,4.962,4.686,4.425,4.179,3.947,3.727,3.52,3.324
3020 REM"==== END OF SAMPLLE NO(1)===="
3030 DATA 3.139,2.964,2.799,2.644,2.496,2.358,2.226,2.102,1.986,1.875,1.771
3040 DATA 1.672,1.579,1.491,1.408
3050 REM"=====END OF SAMPLE NO.(2)===="
3060 DATA 1.330,1.256,1.186,1.120,1.058,.999,.943,.891,.841,.794,.750,.709
3070 DATA .669,.632,.597
3080 REM"==== END OF SAMLE NO.(3)===="
3090 DATA .563,.532,.503,.475,.448,.423,.4,.356,.337,.318
3100 REM" ====== END OF SAMPLE NO.4==="
READY.
```

P(#) TH. & EXP.

```
READY.

 10 OPEN1,4:CMD1
 100 PRINTCHR$(1)"=====  MODIFIED P(#) =        ====="
 110 PRINT
 120 REM"==== CONCRETE ALL ENERGIES ====="
 130 PRINTCHR$(1)SPC(3)"CONCRETE  ALL ENERGY GROUPS "
 140 PRINT
 150 PRINTCHR$(1),"AFTER GF. CORRECTION"
 160 PRINT
 170 FOR MM=1TO5
 180 IFMM=1THEN:PRINTSPC(10)CHR$(1)"==== (1-2) MEV. NA=7E22    ===="
 190 IFMM=2THEN:PRINTSPC(10)CHR$(1)"==== (2-3) MEV. NA=7E22===="
 200 IFMM=3THEN:PRINTSPC(10)CHR$(1)"==== (3-4) MEV. NA=7E22===="
 210 IFMM=4THEN:PRINTSPC(10)CHR$(1)"==== (4-5) MEV. NA=7E22===="
 220 IFMM=5THEN:PRINTSPC(10)CHR$(1)"==== (5-6) MEV. NA=7E22===="
 230 IF MM=1THEN:EF=.315
 240 IF MM=2THEN:EF=.230
 250 IF MM=3THEN:EF=.135
 260 IF MM=4THEN:EF=.130
 270 IF MM=5THEN:EF=.125
 280 PRINTCHR$(1)"EFFICIENCY=";EF
 290 FOR L=30TO90 STEP20
 300 PRINT
 310 PRINT"FOR THETA =";L"DEG."
 320 PRINTSPC(4)"T CM."SPC(8)"S(#)"SPC(6)"PT(#)"SPC(8)"GF"SPC(7)"PTG"
 330 PRINTSPC(58)"P(#)EX."SPC(5)"(PEX/PT)%"
 340 PRINTSPC(4)"====="SPC(8)"===="SPC(6)"====="SPC(8)"=="SPC(7)"==="
 350 PRINTSPC(58)"======="SPC(5)"========="
 360 FOR I=1TO4
 370 K=2.315E-3
 380 READ  N,GF,T,P1,S
 390 N1=N*S*EF*K/(4*π)
 400 NG=INT(N1 +.5)
 410 GG=NG/GF
 415 GG=INT(GG +.5)
 420 FA=P1/NG
 430 Z=T:GOSUB550:PRINTF$SPC(1)
 440 Z=S:GOSUB550:PRINTF$SPC(1)
 450 Z=NG:GOSUB550:PRINTF$SPC(1)
 460 Z=GF:GOSUB550:PRINTF$SPC(1)
 470 Z=GG:GOSUB550:PRINTF$SPC(1)
 480 Z= P1:GOSUB550:PRINTF$SPC(1)
 490 Z=FA:GOSUB550:PRINTF$
 500 NEXT I
 510 PRINT:PRINT:PRINT
 520 NEXT L
 530 PRINT:PRINT:PRINT
 540 NEXTMM
 550 Z=INT(Z*1000 +.5)
 560 A$=STR$(Z):D=LEN(A$)
 570 R$=LEFT$(A$,D-3)
 580 U$=RIGHT$(A$,3)
 590 H$=R$+"."+U$:P$="          "+H$
 600 F$=RIGHT$(P$,10)
 610 RETURN
 620 REM" ===========(1-2)MEV=========="
 630 REM"========== 30 DEG. ========"
 640 DATA 12908181,1.055,5.612,.832,17949886,1.354,12.5,744,.641
 650 DATA 18837240,1.691,20.757,.510,18968186,2.005,25.540,.48
 660 REM"========== 50 DEG. ========"
```

REFERENCES

1. Hunt S.E. Fission Fusion and The Energy Crisis C Pergamon Press (1974)

2. Schmidt F.A.R. Nucl. Eng. Des. 10 308-324 (1969)
O.R.N.L. - RSIC - 26 (1969)

3. Jaeger R.G. (editor) Engineering Compendium on Radiation Materials Vol. II Springer-Verlag Berlin - Germany (1975)

4. Lamarsh J.R. Introduction to Nuclear Engineering rd printing Addison - Wesley Publishing Company (1977)

5. Martin P.W., and Stewart D.T., Jr. of Nucl. Energy A/B 19 447 (1965)

6. Lachkar J., Sigaud J., Patin Y., and Haugat G. Nucl. Sci., Eng. 55 168-187 (1974)

7. Dickens J.K., Morgan G.L., Chapman G.T., Love T.A., Newman E., and Perey F.G. Nucl. Sci. Eng. 62 515-531 (1977)

8. Lane R.D. and Miller W.F., Nucl. Inst. Meth. 16 1-16 (1962)

9. Minetti B., Pasquarelli A. Nucl. Inst. Meth. 120 509-514 (1974)

10. Day R.B., Phys. Rev. 102 767 (1956)

11. Kellie J.D., Islam M. N., and Crawford G.I. Nucl. Phys. A 208 545 (1973)

12. Pourmansouri Ph.D Thesis, University of Aston, in Birmingham (1975)

13. Marka, H., Palfalvi, J. and Verles., P. Health Phys. 26 29-39 (1974)

14. Kocol H., Plott W.F., Mc.Neus D.N., and Moghissi Health Phys. 26 114-116 (1974)

15. Bozyap O., and Day L.R., Health Phys. 28 101-109 (1975)

16. Chilton A.B. Health Phys. 29 (313-314) (1975)

17. Bohr N. Nature 137 344 (1936)

18. Mathur S.C., Nucl. Phys. 81 468 (1965)

19. Cranberg L. Phys. Rev. 159 969 (1967)

20. Benjamin R.W., Buchanon P.S., and Morgan I.L. Nuclear Phys. 79 241 (1966)

21. Glendenring N.K., Phys. Rev. 114, 1297 (1955)

22. Clark R.L. and Cross W.G. Nucl. Phys. 53 177 (1964)

23. Stelson P.H. Nucl. Phys. 68 97 (1965)

24. Hauser W. and Feshbach H., Phys. Rev. 87 366 (1952)

25. Weisskopf V.F. Rev. Mod. Phys. 29 174 (1957)

26. Feshbach H. Ann. Phys. (N.Y) 5 357 (1958)

27. Feshbach H. Ann. Phys. (N.Y) 19 287 (1960)

28. Feshbach H. Rev. Mod. Phys 36 1076 (1964)

29. Satchler, G.R. Phys. Rev. 104 1198 (1956)

30. Phillips G.C., Paul E.B., Ferguson A.T.G., Whitehead A.B., Grjebine T., Moreau R. and Olkowsky B. Nucl. Inst. 3, 43 (1958)

31. Turner C.M. and Bloom S.D. Rev. of Sci. Inst. 29 480 (1958)

32. Meuhlause C.O., Bloom S.D., Wegner H.E. and Glasoe G.N. Phys. Rev. 103, 720 (1956)

33. Snyder C.W. and Parker V.E. Phys. Rev. 95 635 (1953)

34. Parker V.E. and King R.F. Bull. Am. Phys. Soc., 1 70 (1956)

35. Mobley R.C. Phys. Rev. 88 360 (1952)

36. Stelson P.H., Robinson H., Kin. J., Rapapori J., and Satchler. Nucl. Phys. 68 97 (1965)

37. Oliver C.J., Collinge B. and Kaye G. Nucl. Inst. Meth. 50 109 (1967)

38. Marion J.B. and Foweler J., (Editors) "Fast Neutron Physics" Interscience Publisher Ltd. N.Y. 542 (1960)

39. Drake D.M., Hopkins J.C. and Young C.S. Nucl. Sci. Eng. 40 294-305 (1970)

40. Drake D.M., Arther E.D. and Sitbert M.G., 65 49-64 (1978)

41. Nordberg, C. and Nelson L. Nucl. Sci. Eng. 66 75-83 (1978)

42. Scherrer V.E., Thews R., and Faust W.R. Phys. Rev. 89 1268 (1953)

43. McDonald W.J., Robson J.M., and Malcolm. Nucl. Phys. 75 353-370 (1966)

44. Allenby K., PhD Thesis University of Aston in Birmingham (1974)

45. Fewel T.R., Nucl. Inst. Meth. 61 61-71 (1968)

46. Huber P. Lewandowski Z., Platter R.C. Poppel B., and Wagner R., Nucl. Inst. Meth. 14 131-137 (1961)

47. Haught R.C., and Dalgas D.R., Nucl. Inst. Meth. 165 55-56 (1979)

48. Caldwell R.L., Mills W.R., (Jr.) and Hickman J.B., (Jr.) Nucl. Sci., Eng. 8 173 (1960)

49. Vanpatter D.M., Nath N., Shafroth S.M., Malik S.S., and Rothman M.A., "Phys. Rev. 128 1246 (1962)

50. Connel K.A., PhD Thesis University of Aston in Birmingham (1972)

51. Morgan G.L., Love T.A., Dickens J.K. and Perey F.G., O.R.N.L-T.M. - 3702
Oak-Ridge National Laboratory (1973)

52. Baynham D.E., PhD Thesis University of Aston in Birmingham (1971)

53. Connor, J.P., Bonner T.W. and Smith J.R., Phys. Rev. 468 (1952)

54. Argo H.V. et al., Taschek R.F., Agnew H.M., Hemmendinger A and Leland W.T. Phys. Rev. 87 612 (1952)

55. Allan D.L Poole M.J. Proc. Royal Soc., A204 500 (1951)

56. Benvensite, J., and Zenger J., UCRL - 4266 (1954)

57. Reynolds H.K. Dunbar N.F. Wenzel W.A. Haling W., Phys. Rev. 92 742 (1953)

58. McDonald W., and Gedcke D., Nucl. Inst. Meth. 55 1, (1967)

59. Schwarz Schild, A. Nucl. Inst. Meth. 21 1, (1963)

60. Evans R.D., The Atomic Nucleus McGrew-Hill NY (1955)

61. Shafroth S.M., (Editor) Scintillation Spectrometry of Gamma-Ray Radiation, Gordon and Breach Inc. C (1964)

62. Knoll G.F., Radiation Detection and Measurement, John Wiley & Sons, U.S.A. (1979)

63. White G.R., U.S. National Bureau of Standards NBS - 1003 (1952)

64. Adams, F., and Dams, R. Applied Gamma-Ray Spectrometry, 2nd Edition and Revision of the Original Publication by C.E. Crouthamel Pergamon Press, Oxford (1970)

65. Van Leof, J.J., and Lind, D.A., Phys. Rev. 102 767 (1956)

66. Neutron Cross-Sections BNL-325 Sup. No. 2 (1964)

67. Grosher L.V. etal., Atlas of Gamma-Ray Spectra from Radiative Capture of Thermal Neutrons. Pergamon Press (1959)

68. Neutron Cross-Sections BNL-325 3rd ed. Vol. 1. (1973)

69. Aitken J.H., and Dixon W.R., Nucl. Phys. 67 395 (1965)

70. Chasman, C., Jones, K., and Ristinen, Nucl. Inst. Meth. 37 1, (1965)

71. Bunting R.L., and Kranshaar, J.J., Nucl. Inst. Meth. 118 565 (1974)

72. Budder, R., Patzner, W., and Wohlfarth, 117 609 (1974)

73. Ryan R.D., IEEE Trans. Nucl. Sci. NS 20, 1 473 (1973)

74. Langly R.A., Nucl. Inst. Meth. 113 109 (1973)

75. Stelson P.H., Dickens J.K., Raman S., and Tramell, Nucl. Inst. Meth. 98 481 (1972)

76. Kraner H.W., Phel R.H., and Haffer E.E., IEEE, Trans. Nucl. Sci. NS.22 No. 1. 149 (1975)

77. Goulding F.S., and Phel R.H., IEEE, Trans. Nucl. Sci. NS 19 No.1 91 (1972)

78. Engstrom R.W., et al., Nucleonics 10 No. 4 58 (1952)

79. Conner R., and Hussain M. Nucl. Inst. Meth., 6 337 (1960)

80. Kent et al., Phys. Rev. 125 331 (1962)

81. Kreger W.E., and Mather R.L., Scintillation Spectroscopy of Gamma-Radiation (Editor) S.M. Shaharof Gondon and Breach Inc. (1964)

82. Heath R.L., AEC Reports IDO 16408 (1957)

IDO 16880 (1964)

83. Snyder B.J. Nucl. Inst. Meth. 46 173 (1967)

84. Zerby C.D., and Morgan H.S. Nucl. Inst. Meth. 14 115 (1961)

85. Goldstein H., Fundamental Aspects of Reactor Shielding, Pergamon Press 233-236 (1959)

86. Neville A.M. Properties of Concrete , Pitman -London (1963)

87. Covel D.F., Anal. Chem. 31 1785 (1959)

88. Berger M.J., and Seltzer S.M., Nucl. Inst. Meth. 104 317-332 (1972)

89. Rao M.N., Nucl. Data Sheets B3-5 6-87 (1970)

90. Lederer C.M., Hollander J.M., and Perlman, Table of Isotopes Wiley (1967)

91. Jönsson B., Nyberg K., and Bergqvist I., Arkiv För Fysik 32 (20) 295 (1969)

92. Stehn J.R., et al., BNL-325 TID - 4500 2nd Ed. (1964)

93. Nyberg. Ponnet K., et al., Physica Scripta 4 165 (1971)

94. Goldberg M.D., May V.M. and Stehn J.R., BNL 400 2nd ed. Brookhaven National Laboratory (1962)

95. Stamp A., & Rook J., Nucl. Phys. 53 657 (1964)

96. ENDF B IV Nuclear Data Bank France

97. Asami T., and Tanaka S., JAERI. M. 8136 March (1979)

98. Engesser F.C., and Thompson W.E., J. Nucl. Energy 21 487 (1967)

99. Allan, D.L., Nucl. Phys. 24 274 (1961)

100. Abbondanno U., Giacomich R., Lagonegro M., and Pauli G. J. Nucl. Energy 27 227 (1973)

101. Sheldon, E., and Van Patter D.M., Rev. Mod. Phys. 38 143 (1966)

102. Benetskii B.A., Yu P., Bettn 0 and Ya Gonzatko, Soviet Phys. Jept. 18 640 (1964)

103. Benvensite J., Mitchell A.C., Schrader and Zenger J.H., Nucl. Phys. 19 448 (1960)

104. Martin P.W., and Stewart Can. J. Phys. 46 1657 (1968)

105. Arya A.P., Bull. Am. Phys. Soc. 12 124 (1967)

106. Bezotosnyi V.M., Vershinin V.G., Surov L.M., and Shvetsov M.S. Sov. J. Nucl. Phys. 5 632 (1966)

107. Grgutakis,E Nuclear Data Bank France, Private Communication

108. Thompson L.C., and Risser J.R. Phys. Rev. 94 941-943 (1954)

109. Roger V.C., Hendengren D.C., Orphan V.J., and Hoot C.G., Trans. Am. Nucl. Soc. 14 297-849 (1971)

110. Dickens J.K. et al., ORNL-TM-4232 (1973)

111. Dickens J.K., et al., ORNL-TM-4252 (1973)

112. Dickens J.K., et al., ORNL-TM-4389 (1973)

113. Orphan V.J., Hoot C.G., and Joseph John Nucl. Sci. Eng. 42 352-366 (1970)

114. Perkin J.L. Nucl. Phys. 60 561-580 (1964)

115. Dickens J.K., and Percy F.G., Nucl. Sci. Eng. 40 (1970)

116. Dickens et al., Nucl. Sci. Eng. 53 277 (1974)

117. Nishimura K., Kano K.O and Kikuchi, Nucl. Phys. 70 421 (1965)

118. Martin P.W., & Stewart D.T. Nucl. Phys. 60, 349 (1964)

119. Spanier J., and Gelband E.M. "Monte Carlo Principles and Neutron Transport Problems" Addison Wesley Publishers C (1969)

120. Glasstone S. and Edlund M.C. "The Elements of Nuclear Reactor Theory", Princeton N.J. Van Nostrand (1952)

121. Parker J.B., Towel J.H., and Sans D., and Jones Nucl. Inst. Meth. 14 1 (1961)

122. Parker J.B., Towel J.H., Sams D., Gilboy W.B., Purnell A.D., and Stevens H.J. Nucl. Inst. Meth. 30 77 (1964)

123. Geraseva L.A., & Wavilov. J. Nucl. Energy. A/B 16 123 (1962)

124. Grimeland G. and Dövold S. Nucl. Sci. Eng. 19 245 (1964)

125. Goldstein H. et al., Report (ORNL-2639) (1961)

126. Paschall R.K., J. Nucl. Energy A/B 20 25 (1966)

127. Marion J.B. and Young. F.C. "Nuclear Reaction Analysis" North Holland Publishing Company. (1968)

128. Topping J. "Errors of observation and their treatment". The Institute of Physics and the Physical Soc. Monograph.